

Annexe bibliographique

I	MÉCANIQUE STATISTIQUE HORS D'ÉQUILIBRE	1
A	Un système perpétuellement hors d'équilibre : l'annihilation balistique	3
	E. Trizac, <i>Phys. Rev. Lett.</i> 88 , 160601 (2002).	5
	J. Piasecki, E. Trizac and M. Droz, <i>Phys. Rev. E</i> 66 , 066111 (2002).	9
B	Gaz granulaires : des petites échelles vers les grandes	23
	T. van Noije, M. Ernst, E. Trizac, I. Pagonabarraga, <i>Phys. Rev. E</i> 59 , 4326 (1999).	25
	I. Pagonabarraga, E. Trizac, T. van Noije, M. Ernst, <i>Phys. Rev. E</i> 65 , 011303 (2002).	41
	A. Barrat, T. Biben, Z. Rácz, E. Trizac, F. van Wijland, <i>J. Phys. A</i> 35 , 463 (2002).	61
C	Gaz granulaires : dynamique des systèmes vibrés	79
	A. Barrat and E. Trizac, <i>Phys. Rev. E</i> 66 , 051303 (2002).	81
	A. Barrat and E. Trizac, <i>Gran. Matter</i> 4 , 57 (2002).	95
II	MATIÈRE MOLLE ET FLUIDES COMPLEXES	102
A	Qu'est-ce qu'une dispersion colloïdale?	103
	E. Trizac, M. Eldridge and P. Madden, <i>Molecular Physics</i> 90 , No. 4, 675 (1997) . . .	105
B	Compacité et polydispersité optimale	109
	J. Zhang, R. Blaak, E. Trizac, J. Cuesta, D. Frenkel, <i>J. Chem. Phys.</i> 110 , 5318 (1999).	111
C	Renormalisation de charge pour les colloïdes en suspension	119
	E. Trizac, L. Bocquet and M. Aubouy, <i>Phys. Rev. Lett.</i> 89 , 248301 (2002).	121
	E. Trizac, M. Aubouy and L. Bocquet, <i>J. Phys: Condens. Matter</i> 15 , S291 (2003).	125
D	Interactions effectives entre poly-ions de même charge	131
	E. Trizac, <i>Phys. Rev. E</i> 62 , R1465 (2000).	133
	G. Téllez and E. Trizac, <i>J. Chem. Phys.</i> 118 , 3362 (2003).	137
E	Macroions anisotropes et effet d'écran	143
	Trizac, Bocquet, Agra, Weis, Aubouy, <i>J. Phys.: Condens. Matter</i> 14 , 9339 (2002).	145

Chapitre A

Un système perpétuellement hors d'équilibre : l'annihilation balistique

Kinetics and Scaling in Ballistic Annihilation

Emmanuel Trizac*

Laboratoire de Physique Théorique (UMR 8627 du CNRS), Bâtiment 210, Université de Paris-Sud, 91405 Orsay Cedex, France
(Received 23 January 2002; published 8 April 2002)

We study the simplest irreversible ballistically controlled reaction, whereby particles having an initial continuous velocity distribution annihilate upon colliding. In the framework of the Boltzmann equation, expressions for the exponents characterizing the density and typical velocity decay are explicitly worked out in arbitrary dimension. These predictions are in excellent agreement with the complementary results of extensive Monte Carlo and molecular dynamics simulations. We finally discuss the definition of universality classes indexed by a continuous parameter for this far from equilibrium dynamics with no conservation laws.

DOI: 10.1103/PhysRevLett.88.160601

PACS numbers: 05.20.Dd, 05.70.Ln, 73.23.Ad, 82.20.Nk

Systems with reacting particles model a rich variety of phenomena and provide prominent situations to develop and test the foundations of nonequilibrium statistical mechanics. In this context, the diffusion controlled first order annihilation process ($A + A \rightarrow \emptyset$) has been extensively studied and the corresponding decay kinetics is well understood. On the other hand, much less is known in the contrasting case where the reactants move ballistically between the collision events, despite the relevance of such motion for growth and coarsening processes [1,2]. A few theoretical results are available in $d = 1$ dimension for such irreversible kinetic processes with discrete initial velocity distributions. In a pioneering work, Elskens and Frisch show from combinatorial considerations that the particle density $n(t)$ decays like $1/\sqrt{t}$ for the simplest binary velocity distribution [3]. Powerful generalizations of this result were obtained still in 1D, either for a larger class of stochastic ballistic annihilation and coalescence models [4,5] or from kinetic theory for discrete multivelocity distributions [6,7]. No exact results could be obtained for the generic case of continuous distributions, where the decay exponents have been computed numerically [8–10]. Recently, however, Krapivsky and Sire considered the latter situation in the framework of the Boltzmann equation (relying on the so-called “molecular chaos” factorization [11]) and derived bounds for the exponents as well as their leading large d behavior. The existing body of literature has essentially focused numerically on the one-dimensional case, and no accurate predictions seem to be available for the decay exponents.

In this Letter, we obtain predictions for the decay exponents and velocity distribution (assumed initially continuous), revisiting Boltzmann kinetic theory in arbitrary dimension, with the explicit inclusion of non-Gaussian corrections to velocity distributions. These predictions are compared both with the existing numerical results in 1D and the expressions derived in [8,10], and further tested against extensive numerical simulations in dimensions 2 and 3, following two complementary routes: we first solve the mean-field nonlinear Boltzmann equation describing the annihilation process by means of a Monte Carlo scheme,

which validates the analytical expressions obtained within the molecular chaos framework; second, we go beyond mean field and investigate the exact decay kinetics by implementing molecular dynamics simulations. The two numerical approaches yield the same exponents in dimension 2 or higher, in excellent agreement with the analytical prediction. Finally, we address the question of universality in this process [9] by partitioning the possible continuous velocity distributions into groups associated with the same asymptotic dynamic scaling behavior, akin to equilibrium universality classes.

We consider an assembly of identical spherical particles with radius σ in dimension d , with initial velocity distribution $f(\mathbf{v}, t = 0)$ and random initial positions. Particles follow free flight motion until a collision occurs which results in the removal of both partners. We are interested in the time evolution of density $n(t) = \int f(\mathbf{v}, t) d\mathbf{v}$ and typical velocity $\bar{v}(t)$, related to the kinetic temperature $T(t)$ defined as the variance of the velocity distribution

$$T(t) = \frac{1}{n(t)} \int \mathbf{v}^2 f(\mathbf{v}, t) d\mathbf{v} = (\bar{v})^2. \quad (1)$$

Insight into the decay kinetics may be gained by writing the rate equations for n and T

$$\frac{dn}{dt} = -\omega(t)n, \quad (2)$$

$$\frac{d(nT)}{dt} = -\omega(t)nT_{\text{coll}} = -\alpha\omega(t)nT, \quad (3)$$

where the first line stands for a definition of the instantaneous mean collision frequency ω , while T_{coll} is the time dependent total kinetic energy of a colliding pair, which is thus dissipated in a binary encounter, as stated by the right-hand side equality in Eq. (3). On dimensional grounds, the collision frequency is expected to scale like the inverse time, which together with Eqs. (2) and (3) implies an algebraic time decay for n and \bar{v} , as well as a time-independent energy dissipation parameter α [defined in Eq. (3) as $\alpha = T_{\text{coll}}/T$]. We therefore introduce two exponents ξ and γ such that $n(t) \propto t^{-\xi}$ and $\bar{v} \propto t^{-\gamma}$ (and $T \propto t^{-2\gamma}$). With a ballistic dynamics controlled by the

mean-free-path $\ell \propto 1/(n\sigma^{d-1})$, the collision frequency may be written as the ratio \bar{v}/ℓ . From $\omega \propto 1/t$, we obtain the scaling relation $\xi + \gamma = 1$ [8–10,12], which may be combined with the ratio of Eqs. (2) and (3) to give

$$\xi = \frac{2}{1 + \alpha} \quad \text{and} \quad \gamma = \frac{\alpha - 1}{\alpha + 1}. \quad (4)$$

Since particles with a higher velocity are likely to disappear with a higher rate than the average particle with temperature T , we expect $\alpha = T_{\text{coll}}/T$ to be larger than 1, so that the typical velocity should decrease with time [$\gamma > 0$ from Eq. (4)]. This, moreover, explains the failure of the naive mean-field picture where the density decay rate is written $\dot{n} \propto -n^2$, so that $n(t) \propto 1/t$. This transparency limit would hold in the absence of collisional correlations ($\alpha = 1$) which becomes only asymptotically exact in the limit of infinite dimension d .

We now turn to the computation of α within the molecular chaos framework, which is *a priori* an uncontrolled approximation. It will, however, be shown to capture the essential collisional correlations missed by the naive mean-field argument, and to provide decay exponents in excellent agreement with their numerical counterparts. The corresponding Boltzmann equation reads

$$\frac{\partial f(\mathbf{v}, t)}{\partial t} = -f(\mathbf{v}, t) \int d\mathbf{w} |\mathbf{v} - \mathbf{w}| f(\mathbf{w}, t), \quad (5)$$

which implies that if the initial distribution behaves like a power law $|v|^\mu$ near the velocity origin, this property is preserved at subsequent times by the dynamics, which in turn should affect the exponents ξ and γ , expected to depend explicitly on μ (as appears on the analytical predictions of Ben-Naim *et al.* [8] $\xi = (2d + 2\mu)/(2d + 2\mu + 1)$, or on the bounds derived by Krapivsky and Sire [10]). Looking for a scaling solution of the kinetic equation (5), we introduce a rescaled velocity $\mathbf{c} = \mathbf{v}/\bar{v}$ and rescaled single particle distribution function φ through

$$f(\mathbf{v}, t) = \frac{n(t)}{\bar{v}^d} \varphi(\mathbf{c}, t), \quad (6)$$

so that $\varphi(\mathbf{c}, t)$ is the probability distribution function of the velocity \mathbf{c} at time t , satisfying the constraints $\int \varphi d\mathbf{c} = 1$ and $\int c^2 \varphi d\mathbf{c} = 1$ at any time. If $f(\mathbf{v}, t)$ evolves into a self-similar decay state, the only relevant time dependence occurs via $n(t)$ and $\bar{v}(t)$, so that $\varphi(\mathbf{c}, t)$ no longer depends on time and the evolution equation for f (assumed isotropic) translates into

$$\left[1 + \left(\frac{1 - \alpha}{2} \right) \left(d + c_1 \frac{d}{dc_1} \right) \right] \varphi(c_1) = \varphi(c_1) \int d\mathbf{c}_2 \times \frac{c_{12}}{\langle c_{12} \rangle} \varphi(c_2), \quad (7)$$

where $\langle (\dots) \rangle = \int (\dots) \varphi(c_1) \varphi(c_2) d\mathbf{c}_1 d\mathbf{c}_2$ so that $\langle c_{12} \rangle \equiv \langle |\mathbf{c}_1 - \mathbf{c}_2| \rangle$ denotes the rescaled collision frequency.

Equation (7) may be considered as an eigenvalue problem for α , which has been computed numerically in 1D

[10]. However, it is useful to reformulate Eq. (7) into an infinite hierarchy of consistency relations obtained by computing the corresponding moment of order p :

$$\alpha = 1 + \frac{2}{p} \left(\frac{\langle c_{12} c_1^p \rangle}{\langle c_{12} \rangle \langle c_1^p \rangle} - 1 \right). \quad (8)$$

Note that the special case $p = 2$ coincides with the definition of α through the kinetic energy dissipation as expressed by Eq. (3): $\alpha = T_{\text{coll}}/T = \langle c_{12} c_1^2 \rangle / (\langle c_{12} \rangle \langle c_1^2 \rangle)$. We look for explicit solutions by expanding φ in a basis of Sonine functions [13]

$$\varphi(\mathbf{c}) = \mathcal{M}(\mathbf{c}) \left[1 + \sum_{n=1}^{\infty} a_n S_n(c^2) \right], \quad (9)$$

where the polynomials S_n are orthogonal with respect to the Gaussian weight $\mathcal{M}(\mathbf{c})$. Computing the averages involved in (8) from the functional expression (9) provides a system of equations for the coefficients a_n .

In practice, only a few terms are required in the expansion (9) in order to get a precise estimation for α , provided relations of lowest order p as possible are retained among the hierarchy (8). In this respect, taking the limit of vanishing velocity of (7) yields the “optimal” relation involving α and moments of φ of order 1:

$$\alpha = 1 + \frac{2}{\mu + d} \left(1 - \frac{\langle c_1 \rangle}{\langle c_{12} \rangle} \right), \quad (10)$$

that we consider as the first equation of (8) corresponding to the limit $p \rightarrow 0^+$. At Gaussian order for φ [i.e., truncating (9) at order $n = 0$], it is straightforward to get

$$\alpha = \alpha_0 = 1 + \frac{2}{d + \mu} \left(1 - \frac{\sqrt{2}}{2} \right) \quad (11)$$

which, together with Eq. (4) yields the zeroth order estimation for ξ :

$$\xi_0 = \frac{2d + 2\mu}{2(d + \mu + 1) - \sqrt{2}}. \quad (12)$$

It is noteworthy that in the limit of large dimension, we obtain $\xi_0 \sim 1 - d^{-1}(1 - 1/\sqrt{2}) + \mathcal{O}(1/d^2)$ irrespective of μ , which has been shown to be the exact $1/d$ behavior within Boltzmann molecular chaos framework [10]. The first non-Gaussian correction is carried by a_2 (a_1 identically vanishes from the definition of temperature [14]) and this coefficient is related to the kurtosis of the velocity distribution: a_2 is proportional to the fourth cumulant $\langle c_i^4 \rangle - 3\langle c_i^2 \rangle^2$, where c_i is a given Cartesian coordinate of \mathbf{c} . After a lengthy calculation performed at linear order in a_2 , we obtain

$$a_2 = 8 \frac{\mu + d(3 - 2\sqrt{2})}{4d^2 + 6\mu + d(6 + 4\mu - \sqrt{2})}, \quad (13)$$

$$\alpha_2 = \alpha_0 + \frac{\sqrt{2}}{16d} a_2. \quad (14)$$

The above predictions rely on a perturbative expansion starting from the Maxwellian \mathcal{M} (regular at $\mathbf{v} = \mathbf{0}$) and

are therefore expected to be particularly relevant for μ close to 0. The agreement with the existing numerical data is excellent; an accurate estimation has been reported in 1D within molecular chaos for the much studied $\mu = 0$ case [10]: $\xi = 0.769(5)$ whereas we obtain at zeroth order $\xi_0 = 0.773$ from (12) and at second order $\xi_2 = 2/(1 + \alpha_2) = 0.769(3)$ from Eq. (14). This exponent is compatible with its counterpart extracted from the exact dynamics (0.78 in [9]). Moreover, we have investigated numerically the annihilation dynamics in higher dimensions by means of (a) the direct simulation Monte Carlo procedure [15] (DSMC) solving the nonlinear homogeneous Boltzmann equation (5) and (b) molecular dynamics simulations (MD) implementing the exact dynamics with periodic boundary conditions [16]. The DSMC technique provides precise data for the velocity distributions and decay exponents, and allows one to test the validity of the analytical truncated expansion of the scaling form φ , leading to (11) or (14). Alternatively, MD results assess the reliability of the molecular chaos ansatz, but are more demanding on computer resources: on the one hand, the system needs to reach very low densities in order to develop the self-similar decay stage where $f(\mathbf{v}, t)$ takes the scaling form (6), but on the other hand, the mean free path ℓ which increases with time like t^ξ must remain smaller than the simulation box size L , which provides a lower bound for $n(t)$ or equivalently an upper bound for accessible times before finite size effects hinder the precise determination of ξ and γ . In practice, we considered systems with $N = 10^5 - 5 \times 10^5$ particles in MD and $N = 10^6 - 10^7$ in DSMC where it is further possible to average over 10^3 to 10^4 replicas to increase the statistics of the velocity distributions, which is crucial for computations at large times with a concomitant low number of particles left.

The results of two-dimensional simulations are shown in Fig. 1 where it appears that the MD data are fully compatible with DSMC, although less precise. For $\omega_0 t \approx 10^3$, the MD density and temperature tend to saturate, which corresponds to the upper time limit where $\ell \approx L$, and the subsequent evolution is discarded. The predictions $\xi_0 = 0.872$ and $\xi_2 = 0.870$ for $\mu = 0$ (indistinguishable in Fig. 1) are in good agreement with the simulations, irrespective of the initial $f(\mathbf{v})$ chosen (we considered several distributions with the constraint $\mu = 0$, see the discussion below concerning universality). The above exponent is compatible with that reported in the context of a multiparticle lattice gas method (0.87 [17]). Moreover, the initial spatial configuration is irrelevant (the long time dynamics and rescaled velocity distributions are the same starting from a fluidlike structure or from various crystalline arrays), and the scaling relation $\xi + \gamma = 1$ is seen to be well obeyed in the asymptotic regime (inset of Fig. 1). The same scenario holds in dimensions 3 and 4, where the predictions at zeroth and second order are very close, and indistinguishable from the numerics ($\xi_0 \approx 0.91$ in 3D and 0.93 in 4D for $\mu = 0$). However, the agreement is expected to become worse as μ deviates from 0 (with

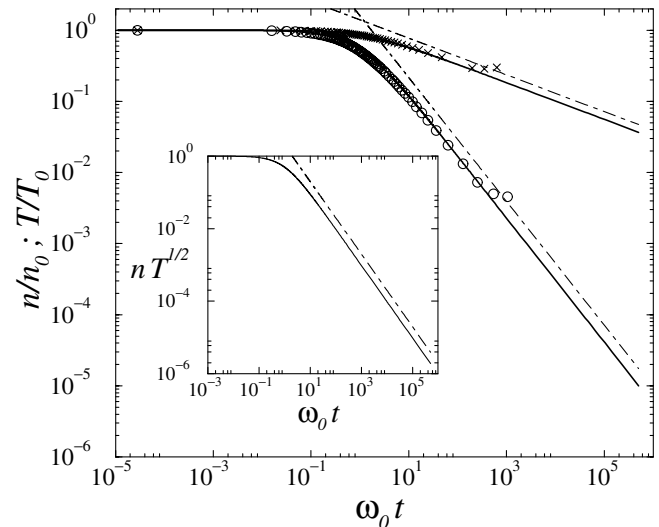


FIG. 1. Evolution of the density (lower sets) and kinetic temperature (upper sets), normalized by their initial values. At $t = 0$, the velocity distribution is Maxwellian ($\mu = 0$), with a collision frequency denoted ω_0 . MD results are shown by symbols (circles for n and crosses for T) and DSMC by continuous curves. The dashed lines have slopes given by the theoretical predictions. Inset: check of the scaling relation $\xi + \gamma = 1$ where $n\sqrt{T}$ is expected to scale like $t^{-\xi-\gamma}$; the dashed line has slope -1 .

$\mu > -d$ to ensure proper normalization). This is confirmed in Tables I and II, which summarize the results obtained for various μ , with comparison to the theoretical prediction of Ben-Naim *et al.* [8] (coinciding with the lower bound for ξ obtained in [10], the upper bound being 1). For $\mu = 0$, the non-Gaussian parameter a_2 is small [with an even smaller correction to α due to the prefactor $\sqrt{2}/16d$ in (14)]. This fourth cumulant, however, rapidly increases with μ , so that inclusion of higher order terms [$n = 3 \dots$ in (9)] would be required to obtain the same level of accuracy as for regular distributions near the velocity origin.

In the remainder, we consider the possibility to define universality classes for ballistic annihilation kinetics, in the following sense: does μ completely specify the asymptotic velocity distribution and decay exponents, irrespective of further details concerning the initial conditions [9]? To answer this question we have run several simulations (MD and Monte Carlo) corresponding to different initial conditions sharing the same μ , for several values of this parameter. The corresponding decay exponents ξ and γ are monitored, which provides a first test, however quite insensitive to possible non Gaussianities (see above the numerical proximity between ξ_0 and the non-Gaussian corrected ξ_2). A more sensitive and severe probe is provided

TABLE I. Decay exponent ξ in one dimension.

(1D) values of μ	$-4/5$	$-1/2$	0
Prediction [8,10]	0.28	0.5	0.666
Numerics [8,10]	0.32/0.37	0.56/0.60	0.769
ξ_2 from Eq. (14)	0.32	0.60	0.769

TABLE II. Exponent ξ in 2D; the simulation data are the Monte Carlo results of the present work.

(2D) values of μ	-1	-1/2	0	3
Prediction [8,10]	0.66	0.75	0.800	0.91
Simulation	0.75	0.83	0.870	0.97
ξ_2 from Eq. (14)	0.76	0.84	0.870	0.95

by the kurtosis a_2 , which may be computed in two different ways: first from its definition involving the fourth cumulant $\langle c_i^4 \rangle - 3\langle c_i^2 \rangle^2$, or alternatively from the direct computation of $\varphi(c)/\mathcal{M}(c)$, which may further be compared to the analytical expansion $1 + a_2 S_2(c^2)$ with a_2 given by Eq. (13) (recall that $a_1 \equiv 0$). The latter method is illustrated in Fig. 2 where the four initial distributions shown in the inset evolve after a transient towards the same attractor, that is furthermore in quantitative agreement with the Sonine prediction. Moreover, the same values of ξ and γ are measured within statistical inaccuracy for the 4 distributions. We have observed the same phenomenology for $\mu \neq 0$, which points to the relevance of defining universality classes of initial conditions as distributions having the same regularity exponent μ , as conjectured in 1D for $\mu = 0$ [9].

In conclusion, we have shown that the nontrivial dynamic scaling behavior of ballistic annihilation may be investigated within Boltzmann kinetic theory, and accurate decay exponents have been explicitly worked out. Their evaluation (12) at zeroth order turns out to be straightforward,

but follows from a kinetic equation and is therefore specific to the precise model considered here. A more versatile approach that would apply to any ballistically controlled reaction (including coalescence with arbitrary conservation laws, with or without stochasticity in the reactions) consists in reconsidering the rate equations (2) and (3), and identifying the proper energy dissipation parameter α before approximating it assuming a Gaussian velocity distribution. This “model-independent” approach gives $\alpha = 1 + 1/(2d)$ in the particular case of pure annihilation, which corresponds to $\xi = 4d/(4d + 1)$ (i.e., 0.8, 0.89, and 0.92 in dimensions 1, 2, and 3) in reasonable agreement with the exponents mentioned above (0.77, 0.87, and 0.91, respectively). We conjecture that the exponent $\xi = 4d/(4d + 1)$ becomes exact when the particles annihilate with probability p (and collide elastically otherwise), in the limiting case $p \rightarrow 0^+$ (whereas $p = 1$ for “pure” annihilation). This hopefully provides an illustration of the central role played by the energy dissipation parameter α in ballistically controlled reactions, and calls for further investigations with more involved reactions.

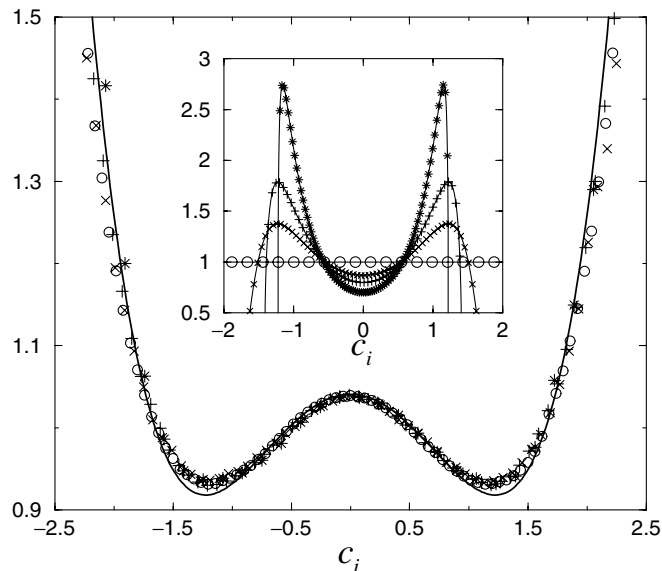


FIG. 2. Plots of $\varphi(c_i)/\mathcal{M}(c_i)$ versus c_i in 2D. The inset shows 4 different initial distributions with $\mu = 0$, one of them being Gaussian [thus corresponding to the flat curve (circles)]. These distributions having very different a_2 at $t = 0$ collapse onto a master curve in the asymptotic scaling regime (main graph). The thick curve is the prediction $1 + a_2 S_2(c_i^2)$ where a_2 is given by Eq. (13) and $S_2(x) = x^2/2 - 3x/2 + 3/8$. The symbols (stars, crosses, pluses, and circles) refer to the same distributions at late times (main graph) and at $t = 0$ (inset). The results have been obtained by averaging over 10^4 replicas of a system with $N = 5 \times 10^6$ particles.

- *Electronic address: Emmanuel.Trizac@th.u-psud.fr
- [1] J. Krug and H. Spohn, Phys. Rev. A **38**, 4271 (1988).
 - [2] M. Gerwinski and J. Krug, Phys. Rev. E **60**, 188 (1999).
 - [3] Y. Elskens and H. L. Frisch, Phys. Rev. A **31**, 3812 (1985).
 - [4] R. A. Blythe, M. R. Evans, and Y. Kafri, Phys. Rev. Lett. **85**, 3750 (2000).
 - [5] Y. Kafri, J. Phys. A **33**, 2365 (1999).
 - [6] J. Piasecki, Phys. Rev. E **51**, 5535 (1995).
 - [7] M. Droz, P. A. Rey, L. Frachebourg, and J. Piasecki, Phys. Rev. Lett. **75**, 160 (1995).
 - [8] E. Ben-Naim, S. Redner, and F. Leyvraz, Phys. Rev. Lett. **70**, 1890 (1993); E. Ben-Naim, P. L. Krapivsky, F. Leyvraz, and S. Redner, J. Phys. Chem. **98**, 7284 (1994).
 - [9] P. A. Rey, M. Droz, and J. Piasecki, Phys. Rev. E **57**, 138 (1998).
 - [10] P. L. Krapivsky and C. Sire, Phys. Rev. Lett. **86**, 2494 (2001).
 - [11] P. Résibois and M. de Leener, *Classical Kinetic Theory of Fluids* (John Wiley and Sons, New York, 1977).
 - [12] Incidentally, the relation $\xi + \gamma = 1$ equally applies to the homogeneous cooling stage of (inelastic) granular matter where density is conserved ($\xi = 0$ so that $T \propto t^{-2}$, as observed; see, e.g., J. Dufty, cond-mat/0108444, and references therein).
 - [13] L. Landau and E. Lifshitz, *Physical Kinetics* (Pergamon Press, New York, 1981).
 - [14] T. P. C. van Noije and M. H. Ernst, Granular Matter **1**, 57 (1998).
 - [15] G. Bird, *Molecular Gas Dynamics* (Oxford University Press, New York, 1976); *Molecular Gas Dynamics and the Direct Simulation of Gas Flows* (Clarendon Press, Oxford, 1994).
 - [16] M. P. Allen and D. J. Tildesley, *Computer Simulations of Liquids* (Clarendon Press, Oxford, 1987).
 - [17] B. Chopard, A. Masselot, and M. Droz, Phys. Rev. Lett. **81**, 1845 (1998).

Dynamics of ballistic annihilationJarosław Piasecki,¹ Emmanuel Trizac,² and Michel Droz³¹*Institute of Theoretical Physics, University of Warsaw, Hoza 69, 00-681 Warsaw, Poland*²*Laboratoire de Physique Théorique,* Bâtiment 210, Université de Paris–Sud, 91405 Orsay, France*³*Département de Physique, Université de Genève, CH-1211 Genève 4, Switzerland*

(Received 23 May 2002; published 10 December 2002)

The problem of ballistically controlled annihilation is revisited for general initial velocity distributions and an arbitrary dimension. An analytical derivation of the hierarchy equations obeyed by the reduced distributions is given, and a scaling analysis of the corresponding spatially homogeneous system is performed. This approach points to the relevance of the nonlinear Boltzmann equation for dimensions larger than 1 and provides expressions for the exponents describing the decay of the particle density $n(t) \propto t^{-\xi}$ and the root-mean-square velocity $\bar{v} \propto t^{-\gamma}$ in terms of a parameter related to the dissipation of kinetic energy. The Boltzmann equation is then solved perturbatively within a systematic expansion in Sonine polynomials. Analytical expressions for the exponents ξ and γ are obtained in arbitrary dimension as a function of the parameter μ characterizing the small velocity behavior of the initial velocity distribution. Moreover, the leading non-Gaussian corrections to the scaled velocity distribution are computed. These expressions for the scaling exponents are in good agreement with the values reported in the literature for continuous velocity distributions in $d=1$. For the two-dimensional case, we implement Monte Carlo and molecular dynamics simulations that turn out to be in excellent agreement with the analytical predictions.

DOI: 10.1103/PhysRevE.66.066111

PACS number(s): 05.70.Ln, 05.20.Dd, 73.23.Ad, 82.20.Nk

I. INTRODUCTION

Ballistically controlled reactions provide simple examples of nonequilibrium systems with complex kinetics. They consist of an assembly of particles with a given velocity distribution, moving freely between collisions in a d -dimensional space. In the simplest version of these models consider here, when two particles meet, they instantaneously annihilate each other and disappear from the system. Despite its apparent simplicity, this problem is highly nontrivial and has attracted substantial interest during the past years [1–10]. The one-dimensional case where the particles can only have two velocities $\pm c$ has been studied in a pioneering work by Elskens and Frisch [1]. In particular, they proved that for a symmetric initial velocity distribution, the particle density is decreasing, in the long-time limit, as $n(t) \propto t^{-\xi} \propto t^{-1/2}$. The case of general distributions in dimension $d=1$ was discussed by Piasecki [2], who reduced exactly the annihilation dynamics to a single closed equation for the two-particle conditional probability. Moreover, it was shown in the particular bimodal situation of a discrete velocity distribution ($\pm c$) that in one dimension, important dynamical correlations are developing during the time evolution, invalidating mean-field or Boltzmann-like approaches. This exact approach was applied to the case of a three-velocity distribution by Droz *et al.* [3], with the result that the dynamical exponents were strongly depending upon the details of the initial velocity distribution.

No analytical solutions could be found for continuous velocity distributions. In one dimension, Ben-Naim *et al.* [4,5] have shown that the exponent ξ could depend on the behav-

ior near the origin of the initial velocity distribution. This problem has been revisited by Rey *et al.* [6]. Based on the exact theoretical approach [2,3], a dynamical scaling theory was derived and its validity supported by numerical simulations for several velocity distributions. This leads to the conjecture that all continuous velocity distributions $f(v)$ that are symmetric, regular, and such that $f(0) \neq 0$ are attracted in the long-time regime towards the same distribution, and thus belong to the same universality class. This conjecture was reinforced by numerical simulations in two dimensions [10].

The case of a continuous velocity distribution has also been approached recently by Krapivsky and Sire [9]. Starting from a Boltzmann equation, they investigated the decay of the particle density $n(t) \sim t^{-\xi}$ and the root-mean-square velocity $\bar{v} \propto t^{-\gamma}$. They derived upper and lower bounds for the exponents as well as their leading expansion in $1/d$, valid in high dimension. The main question with such an approach concerns the validity of a Boltzmann equation. This is not justified in the one-dimensional (1D) case and remains an open problem in higher dimensions.

The purpose of this paper is to give a first-principles answer to this type of question. The paper is organized as follows. In Sec. II, an original analytical derivation of the equations governing the dynamics of ballistic annihilation is given. The hierarchy equations obeyed by the reduced distributions are obtained. It is shown that in the Grad limit, the hierarchy formally reduces to a Boltzmann-like form for $d > 1$. If the initial reduced distributions factorize, the whole hierarchy reduces to one nonlinear equation. In Sec. II, a scaling analysis of the exact spatially homogeneous hierarchy is performed. The exponents ξ and γ are shown to depend only on one parameter α related to the dissipation of energy. This scaling analysis turns out to be invalid for the case $d=1$ with discrete velocity distributions, but correct in

*Unité Mixte de Recherche 8627 du CNRS.

the continuous case. Strong arguments are given in favor of the validity of the Boltzmann approach for the case $d > 1$ in the long-time limit. The Boltzmann equation is then solved within a systematic approximation based on an expansion in Sonine polynomials (Sec. III). The first non-Gaussian corrections to the scaled velocity distribution are computed and predictions for the exponents ξ and γ are explicitly worked out as functions of the dimension d and the parameter μ characterizing the small velocity behavior of the initial velocity distribution: $[f(\mathbf{v}, t=0) \propto |\mathbf{v}|^\mu \text{ for } |\mathbf{v}| \rightarrow 0]$. These predictions for ξ and γ are asymptotically exact for large dimensions, and reproduce the $1/d$ correction to the mean-field values. In 1D, they are in very good agreement with the exponents reported in the literature [9] at the Boltzmann level. In 2D, we implement extensive direct simulation Monte Carlo methods (DSMC), where the nonlinear Boltzmann equation is solved, and molecular dynamics (MD) simulations, where the exact equations of motion are integrated (Sec. IV). The agreement between the MD and DSMC routes confirms the validity of the Boltzmann approach, and the decay exponents measured are in exceptionally good agreement with the Sonine prediction. Conclusions are drawn in Sec. V. A preliminary account of part of the results presented here has been published elsewhere [10].

II. EXACT RESULTS

A. Derivation of the hierarchy

Let Ω be a region of finite measure in R^{2d} . We denote by

$$\mu_k^\Omega(\mathbf{r}_1, \mathbf{v}_1, \dots, \mathbf{r}_k, \mathbf{v}_k; t) \quad (1)$$

the probability density for finding (at time t) exactly k particles within Ω in the states $(\mathbf{r}_j, \mathbf{v}_j) \in \Omega$, $j=1, 2, \dots, k$, where \mathbf{r}_j and \mathbf{v}_j are the position and the velocity vectors, respectively. The knowledge of the densities μ_k^Ω for all $\Omega \in R^{2d}$ and $k=0, 1, 2, \dots$ defines entirely the state of the system. For a given region Ω , the normalization condition reads

$$\begin{aligned} \mu_0^\Omega(t) + \sum_{k=1}^{\infty} \int_{\Omega} d\mathbf{r}_1 d\mathbf{v}_1 \cdots \int_{\Omega} d\mathbf{r}_k d\mathbf{v}_k \\ \times \mu_k^\Omega(\mathbf{r}_1, \mathbf{v}_1, \dots, \mathbf{r}_k, \mathbf{v}_k; t) = 1, \end{aligned} \quad (2)$$

where $\mu_0^\Omega(t)$ is the probability of finding the region- Ω void of particles at time t .

A necessary condition for the occurrence of a pair of particles at the phase space points $(\mathbf{r}_j, \mathbf{v}_j), (\mathbf{r}_i, \mathbf{v}_i)$ at time $t > 0$ is that $\mathbf{r}_{ij} = \mathbf{r}_i - \mathbf{r}_j, \mathbf{v}_{ij} = \mathbf{v}_i - \mathbf{v}_j$ belong to the region of the phase space with the characteristic function

$$\begin{aligned} \chi(\mathbf{r}_{ij}, \mathbf{v}_{ij}; t) = \theta(|\mathbf{r}_{ij}| - \sigma) \{ 1 - \theta(\mathbf{r}_{ij} \cdot \mathbf{v}_{ij}) \\ \times \theta(\sigma - \sqrt{|\mathbf{r}_{ij}|^2 - (\mathbf{r}_{ij} \cdot \hat{\mathbf{v}}_{ij})^2}) \\ \times \theta(|\mathbf{v}_{ij}|t - \mathbf{r}_{ij} \cdot \hat{\mathbf{v}}_{ij}) \\ + \sqrt{\sigma^2 - |\mathbf{r}_{ij}|^2 + (\mathbf{r}_{ij} \cdot \hat{\mathbf{v}}_{ij})^2} \}, \end{aligned} \quad (3)$$

where σ denotes the particle diameter, $\hat{\mathbf{v}}_{ij}$ is a unit vector in the direction of the relative velocity, and θ denotes the Heaviside distribution. Indeed, moving backward in time, the particles collide during the time interval $(0, t)$ if and only if the following three conditions are simultaneously satisfied: (i) $\mathbf{r}_{ij} \cdot \mathbf{v}_{ij} > 0$ (particles approach each other), (ii) $\sigma > \sqrt{|\mathbf{r}_{ij}|^2 - (\mathbf{r}_{ij} \cdot \hat{\mathbf{v}}_{ij})^2}$ (the impact parameter is smaller than σ), (iii) $|\mathbf{v}_{ij}|t > \mathbf{r}_{ij} \cdot \hat{\mathbf{v}}_{ij} - \sqrt{\sigma^2 - |\mathbf{r}_{ij}|^2 + (\mathbf{r}_{ij} \cdot \hat{\mathbf{v}}_{ij})^2}$ (the time t is long enough for the overlapping configuration to occur). Hence, $\chi(\mathbf{r}_{ij}, \mathbf{v}_{ij}; t) = 1$ if and only if no overlapping takes place during the time interval $(0, t)$.

At time t , particles $1, 2, \dots, k$ occupy in Ω the one-particle states

$$(\mathbf{r}_1, \mathbf{v}_1), (\mathbf{r}_2, \mathbf{v}_2), \dots, (\mathbf{r}_k, \mathbf{v}_k), \quad (4)$$

with probability density (1). Using the characteristic function (3), we can construct the probability density for finding the same particles in the phase space configuration

$$(\mathbf{r}_1 + \mathbf{v}_1 dt, \mathbf{v}_1), (\mathbf{r}_2 + \mathbf{v}_2 dt, \mathbf{v}_2), \dots, (\mathbf{r}_k + \mathbf{v}_k dt, \mathbf{v}_k) \quad (5)$$

at time $(t + dt), dt > 0$. It reads

$$\left[\prod_{i < j}^k \chi(\mathbf{r}_{ij} + \mathbf{v}_{ij} dt, \mathbf{v}_{ij}; t + dt) \right] \mu_k^\Omega(\mathbf{r}_1, \mathbf{v}_1, \dots, \mathbf{r}_k, \mathbf{v}_k; t). \quad (6)$$

In the limit $dt \rightarrow 0^+$, the above expression takes the asymptotic form

$$\begin{aligned} \mu_k^\Omega(\mathbf{r}_1, \mathbf{v}_1, \dots, \mathbf{r}_k, \mathbf{v}_k; t) \left[1 + \sum_{i, j, i < j}^k \left(\frac{\partial}{\partial t} + \mathbf{v}_{ij} \cdot \frac{\partial}{\partial \mathbf{r}_{ij}} \right) \right. \\ \left. \times \chi(\mathbf{r}_{ij}, \mathbf{v}_{ij}; t) dt \right]. \end{aligned} \quad (7)$$

Using definition (3), we find

$$\begin{aligned} \left(\frac{\partial}{\partial t} + \mathbf{v}_{ij} \cdot \frac{\partial}{\partial \mathbf{r}_{ij}} \right) \chi(\mathbf{r}_{ij}, \mathbf{v}_{ij}; t) \\ = (\hat{\mathbf{r}}_{ij} \cdot \mathbf{v}_{ij}) \delta(|\mathbf{r}_{ij}| - \sigma) [1 - \theta(\mathbf{r}_{ij} \cdot \mathbf{v}_{ij})], \end{aligned} \quad (8)$$

where $\hat{\mathbf{r}}_{ij} = \mathbf{r}_{ij} / |\mathbf{r}_{ij}|$. We denote by $T^v(i, j)$ the right-hand side of Eq. (8) and rewrite it in the form

$$T^v(i, j) = \sigma^{d-1} \int d\hat{\boldsymbol{\sigma}} (\hat{\boldsymbol{\sigma}} \cdot \mathbf{v}_{ij}) \theta(-\hat{\boldsymbol{\sigma}} \cdot \mathbf{v}_{ij}) \delta(\mathbf{r}_{ij} - \sigma \hat{\boldsymbol{\sigma}}). \quad (9)$$

Here $\hat{\boldsymbol{\sigma}}$ is the unit vector along the line passing through the centers of the spheres at contact. The integration with respect to the measure $d\hat{\boldsymbol{\sigma}}$ is thus the angular integration over the solid angle in d -dimensional space. The θ function in Eq. (9) restricts this angular integral to the hemisphere corresponding to precollisional configurations.

Our aim is to construct the probability density μ_k^Ω at time $(t + dt)$ for $dt \rightarrow 0^+$:

$$\begin{aligned}
& \mu_k^\Omega(\mathbf{r}_1 + \mathbf{v}_1 dt, \mathbf{v}_1, \dots, \mathbf{r}_k + \mathbf{v}_k dt, \mathbf{v}_k; t + dt) \\
&= \mu_k^\Omega(\mathbf{r}_1, \mathbf{v}_1, \dots, \mathbf{r}_k, \mathbf{v}_k; t) + \left(\frac{\partial}{\partial t} + \sum_{j=1}^k \mathbf{v}_j \cdot \frac{\partial}{\partial \mathbf{r}_j} \right) \\
& \quad \times \mu_k^\Omega(\mathbf{r}_1, \mathbf{v}_1, \dots, \mathbf{r}_k, \mathbf{v}_k; t) dt. \quad (10)
\end{aligned}$$

To this end, we have still to add to the term (7) the probability weights of two events. The first corresponds to the presence at time t of $(k+2)$ particles within Ω in the states

$$(\mathbf{r}_1, \mathbf{v}_1), (\mathbf{r}_2, \mathbf{v}_2), \dots, (\mathbf{r}_k, \mathbf{v}_k), (\mathbf{r}_{k+1}, \mathbf{v}_{k+1}), (\mathbf{r}_{k+2}, \mathbf{v}_{k+2}). \quad (11)$$

The state (11) is then transformed into Eq. (4) at time $(t + dt)$ as the result of an annihilating collision between the particles $(k+1)$ and $(k+2)$, during the time interval $(t, t + dt)$. According to Eqs. (7) and (8), the rate of the occurrence of binary collisions between pairs (i, j) is obtained by applying the operator $[-T^v(i, j)]$ defined in Eq. (9) to the corresponding distribution. Hence, when $dt \rightarrow 0^+$, the $(k+1, k+2)$ annihilation process contributes to the density (10) the term

$$\begin{aligned}
& - \int_{\Omega} d(k+1) \int_{\Omega} d(k+2) T^v(k+1, k+2) \\
& \quad \times \mu_{k+2}^\Omega(1, 2, \dots, k, k+1, k+2; t) dt, \quad (12)
\end{aligned}$$

where the shorthand notation $dj \equiv d\mathbf{r}_j d\mathbf{v}_j$ for $j=1, 2, \dots$ has been used.

Finally, we have to take into account the effects of the free flow of particles across the boundary $\partial\Omega$ of the region Ω . Indeed, the k -particle state can be created or destroyed by an additional particle $(k+1)$ leaving or entering the considered region. Denoting by $\hat{\mathbf{n}}$ the unit vector normal to $\partial\Omega$ oriented outwards, we get the term

$$\begin{aligned}
& \int d\mathbf{v}_{k+1} \int_{\partial\Omega} dS (\hat{\mathbf{n}} \cdot \mathbf{v}_{k+1}) \mu_{k+1}^\Omega(1, \dots, k, k+1; t) dt \\
&= \int_{\Omega} d(k+1) \mathbf{v}_{k+1} \cdot \frac{\partial}{\partial \mathbf{r}_{k+1}} \mu_{k+1}^\Omega(1, \dots, k, k+1; t) dt. \quad (13)
\end{aligned}$$

Here dS is the measure of the surface area, and the equality (13) follows from Gauss' theorem.

The enumerated events combine together to create the complete rate of change of the probability density μ_k^Ω . As equivalent events have the same probability measure, we can equate Eq. (10) with the sum of contributions (7), (12), and (13), thus obtaining the hierarchy equations ($k=1, 2, \dots$)

$$\begin{aligned}
& \left(\frac{\partial}{\partial t} + \sum_{j=1}^k \mathbf{v}_j \cdot \frac{\partial}{\partial \mathbf{r}_j} - \sum_{i,j,i < j}^k T^v(i, j) \right) \mu_k^\Omega(1, \dots, k; t) \\
&= - \int_{\Omega} d(k+1) \int_{\Omega} d(k+2) T^v(k+1, k+2) \\
& \quad \times \mu_{k+2}^\Omega(1, 2, \dots, k+2; t) + \int_{\Omega} d(k+1) \\
& \quad \times \mathbf{v}_{k+1} \cdot \frac{\partial}{\partial \mathbf{r}_{k+1}} \mu_{k+1}^\Omega(1, \dots, k, k+1; t). \quad (14)
\end{aligned}$$

Finally, the evolution equation for μ_0^Ω follows from the normalization condition (2). This completes the derivation of the infinite hierarchy of equations satisfied by the probability densities μ_k^Ω .

From Eq. (14), one can derive in a straightforward way the hierarchy satisfied by the reduced distributions $f_k(1, 2, \dots, k; t)$. They are relevant for the evaluation of physical parameters, as $f_k(1, 2, \dots, k; t) d1 \dots dk$ represents the measure of the number of k -particle phase space configurations, with k particles occupying the one-particle states $(\mathbf{r}_1, \mathbf{v}_1), (\mathbf{r}_2, \mathbf{v}_2), \dots, (\mathbf{r}_k, \mathbf{v}_k)$ at time t . The distributions f_k are related to the probability densities μ_k^Ω by the equation (see Ref. [11])

$$\begin{aligned}
f_k(1, 2, \dots, k; t) &= \sum_{p=0}^{\infty} \frac{(k+p)!}{p!} \int_{\Omega} d(k+1) \dots \int_{\Omega} d(k+p) \\
& \quad \times \mu_{k+p}^\Omega(1, \dots, k, k+1, \dots, k+p; t). \quad (15)
\end{aligned}$$

Note that $f_k(1, 2, \dots, k; t)$ do not depend on Ω .

In order to derive the evolution equation for f_k , one has thus to consider hierarchy equation (14), with k replaced by $(k+p)$, and use relation (15). One finds

$$\begin{aligned}
& \left(\frac{\partial}{\partial t} + \sum_{j=1}^k \mathbf{v}_j \cdot \frac{\partial}{\partial \mathbf{r}_j} - \sum_{i < j}^k \sum_{i < j}^k T^v(i, j) \right) f_k(1, \dots, k; t) \\
&= \sum_{p=0}^{\infty} \frac{(k+p)!}{p!} \int_{\Omega} d(k+1) \dots \int_{\Omega} d(k+p) \\
& \quad \times \left\{ \left[- \sum_{j=k+1}^{k+p} \mathbf{v}_j \cdot \frac{\partial}{\partial \mathbf{r}_j} + \sum_{j=1}^k \sum_{i=k+1}^{k+p} T^v(i, j) \right. \right. \\
& \quad \left. \left. + \sum_{k+1 \leq i < j}^{k+p} T^v(i, j) \right] \mu_{k+p}^\Omega(1, \dots, k+p; t) \right. \\
& \quad \left. - \int_{\Omega} d(k+p+1) \int_{\Omega} d(k+p+2) T^v(k+p+1, \right. \\
& \quad \left. \times k+p+2) \mu_{k+p+2}^\Omega(1, \dots, k+p+1, k+p+2; t) \right. \\
& \quad \left. + \int_{\Omega} d(k+p+1) \left(\mathbf{v}_{k+p+1} \cdot \frac{\partial}{\partial \mathbf{r}_{k+p+1}} \right) \right. \\
& \quad \left. \times \mu_{k+p+1}^\Omega(1, \dots, k+p+1; t) \right\}. \quad (16)
\end{aligned}$$

It is then a question of inspection to see that on the right-hand side of Eq. (16), only the term

$$\begin{aligned} & \sum_{p=1}^{\infty} \frac{(k+p)!}{p!} \int_{\Omega} d(k+1) \cdots \int_{\Omega} d(k+p) \\ & \times \sum_{j=1}^k \sum_{i=k+1}^{k+p} T^v(i,j) \mu_{k+p}(1, \dots, k+p; t) \\ & = \int d(k+1) \sum_{j=1}^k T^v(j, k+1) f_{k+1}(1, \dots, k, k+1; t) \end{aligned} \quad (17)$$

survives. All the remaining terms exactly cancel out.

The hierarchy equations satisfied by the reduced distributions f_k describing the annihilation dynamics thus read

$$\begin{aligned} & \left(\frac{\partial}{\partial t} + \sum_{j=1}^k \mathbf{v}_j \cdot \frac{\partial}{\partial \mathbf{r}_j} - \sum_{i < j} \sum_{i < j} T^v(i,j) \right) f_k(1, \dots, k; t) \\ & = \int d(k+1) \sum_{j=1}^k T^v(j, k+1) f_{k+1}(1, \dots, k, k+1; t). \end{aligned} \quad (18)$$

Consider now Eqs. (18), supposing that the state of the system is spatially homogeneous. In this case the distribution f_1 does not depend on the particle position. Let us formally take the Grad limit

$$\sigma \rightarrow 0, \quad n(t) \rightarrow \infty, \quad n(t) \sigma^{d-1} = \lambda^{-1} = \text{const}, \quad (19)$$

where

$$n(t) = \int d\mathbf{v} f_1(\mathbf{v}; t).$$

The fixed mean free path λ introduces a relevant length scale, so we pass to dimensionless positions, putting

$$\mathbf{r}_j = \lambda \mathbf{x}_j, \quad j = 1, 2, \dots \quad (20)$$

With this change of variables, the collision operator (9) takes the form

$$\begin{aligned} T^v(i,j) &= [n(t) \sigma^d]^{d-1} \frac{1}{\lambda} \int d\hat{\boldsymbol{\sigma}} (\hat{\boldsymbol{\sigma}} \cdot \mathbf{v}_{ij}) \theta(-\hat{\boldsymbol{\sigma}} \cdot \mathbf{v}_{ij}) \\ & \times \delta[\mathbf{x}_{ij} - n(t) \sigma^d \hat{\boldsymbol{\sigma}}]. \end{aligned} \quad (21)$$

We conclude that the term on the left-hand side of Eq. (18) involving the collision operators (21) vanishes in the Grad limit for $d > 1$, because the dimensionless parameter $n(t) \sigma^d$ tends to zero. Note that this term induces dynamical correlations, hindering the propagation of the molecular chaos factorization. On the other hand, using the definition of $T^v(j, k+1)$, we find that the term on the right-hand side equals

$$\begin{aligned} & \frac{1}{\lambda} \sum_{j=1}^k \int d\mathbf{v}_{k+1} \int d\hat{\boldsymbol{\sigma}} (\hat{\boldsymbol{\sigma}} \cdot \mathbf{v}_{j(k+1)}) \\ & \times \theta(-\hat{\boldsymbol{\sigma}} \cdot \mathbf{v}_{j(k+1)}) f_{k+1}(1, \dots, j, \dots, k, \\ & \mathbf{r}_{k+1} = \mathbf{r}_j - \sigma \hat{\boldsymbol{\sigma}}, \mathbf{v}_{k+1}; t) / n(t), \end{aligned} \quad (22)$$

and its prefactor $1/\lambda$ remains finite in the same limit. So, formally the hierarchy equation (18) at a given time t reduces pointwise in the Grad limit to the Boltzmann-like hierarchy,

$$\begin{aligned} & \left(\frac{\partial}{\partial t} + \sum_{j=1}^k \mathbf{v}_j \cdot \frac{\partial}{\partial \mathbf{r}_j} \right) f_k^B(1, \dots, k; t) \\ & = \int d(k+1) \sum_{j=1}^k T^v(j, k+1) \\ & \times f_{k+1}^B(1, \dots, k, k+1; t) \quad (k=1, 2, \dots). \end{aligned} \quad (23)$$

The hierarchy (23) propagates the factorization of the reduced distributions

$$f_k^B(1, \dots, k; t) = \prod_{j=1}^k f_k^B(j; t). \quad (24)$$

Hence, if the initial state is factorized, the whole hierarchy (23) reduces to a nonlinear equation

$$\left(\frac{\partial}{\partial t} + \mathbf{v}_1 \cdot \frac{\partial}{\partial \mathbf{r}_1} \right) f^B(1; t) = \int d2 T^v(1, 2) f^B(1; t) f^B(2; t). \quad (25)$$

Equation (25) is the Boltzmann kinetic equation corresponding to the annihilation dynamics. In the following section, we shall see that the formal Grad limit taken here, where $n \rightarrow \infty$, is relevant for the description of the annihilation dynamics at late times, even if the density $n(t)$ decreases with increase in time.

B. Scaling analysis of the hierarchy

The evolution of the annihilation kinetics shares a common feature with the Grad limit: The ratio of particle diameter to mean free path $\lambda = 1/(n\sigma^{d-1})$, which is related to the packing fraction, vanishes in both cases. To be more specific, we perform a scaling analysis of the exact *homogeneous* hierarchy equations and look for self-similar reduced distributions where the time dependence has been absorbed into the density $n(t)$, with the velocities \mathbf{v} and positions \mathbf{r} renormalized by the typical (root-mean-squared) velocity $\bar{v}(t)$ and mean free path, respectively. We define the reduced variables

$$\mathbf{c} = \frac{\mathbf{v}}{\bar{v}} \quad \text{and} \quad \mathbf{x} = \frac{\mathbf{r}}{\lambda},$$

with

$$(\bar{v})^2 = \frac{1}{n(t)} \int v^2 f_1(\mathbf{v}; t) d\mathbf{v}. \quad (26)$$

For the one-body distribution, we therefore introduce the reduced function \tilde{f}_1 , such that

$$f_1(\mathbf{v}; t) = \frac{n(t)}{\bar{v}(t)^d} \tilde{f}_1(\mathbf{c}) = \frac{n(t)}{\bar{v}(t)^d} \tilde{f}_1\left(\frac{\mathbf{v}}{\bar{v}(t)}\right). \quad (27)$$

By definition, the moments of order 0 and 2 of \tilde{f}_1 are constrained to unity. Requiring that the k -body distribution f_k factorizes into $\prod_{i=1}^k f_1(i)$ in the limit of infinite relative separations between the particles, we consistently obtain the

$$\omega(t) = n(t) \bar{v}(t) \int d\mathbf{c}_1 d\mathbf{c}_2 d\hat{\sigma} (-\hat{\sigma} \cdot \mathbf{c}_{12}) \theta(-\hat{\sigma} \cdot \mathbf{c}_{12}) \tilde{f}_2(\mathbf{c}_1, \mathbf{c}_2, \sigma \hat{\sigma}), \quad (31)$$

$$\alpha = \frac{\int d\mathbf{c}_1 d\mathbf{c}_2 d\hat{\sigma} (\hat{\sigma} \cdot \mathbf{c}_{12}) \theta(-\hat{\sigma} \cdot \mathbf{c}_{12}) c_1^2 \tilde{f}_2(\mathbf{c}_1, \mathbf{c}_2, \sigma \hat{\sigma})}{\left[\int c^2 \tilde{f}_1(\mathbf{c}) d\mathbf{c} \right] \left[\int d\mathbf{c}_1 d\mathbf{c}_2 d\hat{\sigma} (\hat{\sigma} \cdot \mathbf{c}_{12}) \theta(-\hat{\sigma} \cdot \mathbf{c}_{12}) \tilde{f}_2(\mathbf{c}_1, \mathbf{c}_2, \sigma \hat{\sigma}) \right]}. \quad (32)$$

Equation (32) is valid for general velocity rescalings. Definition (26) chosen here implies that the term $\int c^2 \tilde{f}_1(\mathbf{c}) d\mathbf{c}$ in the denominator equals unity. The coefficient α may be seen as the ratio of the kinetic energy dissipated in a typical collision normalized by the average kinetic energy, and is time independent in the scaling regime. It is convenient to introduce the internal ‘‘clock’’ \mathcal{C} of the dynamics counting the number of collisions, such that $d\mathcal{C} = \omega dt$. With this variable, Eqs. (29) and (30) integrate into

$$n(t) = n_0 \exp[-\mathcal{C}(t)]$$

and

$$\bar{v}^2(t) = \bar{v}_0^2 \exp[-(\alpha - 1)\mathcal{C}(t)], \quad (33)$$

where the time origin with density n_0 and kinetic energy density $n_0 \bar{v}_0^2$ has been chosen to coincide with $\mathcal{C} = 0$. Knowledge of the \mathcal{C} dependence of n and \bar{v} allows one to relate absolute time t to the number of accumulated collisions: From Eq. (31), we have

$$\frac{d\mathcal{C}}{dt} = \omega_0 \frac{n}{n_0} \frac{\bar{v}}{\bar{v}_0} = \omega_0 \exp[-\mathcal{C}(1 + \alpha)/2], \quad (34)$$

where $\omega_0 \equiv \omega(t=0)$, so that

scaling form

$$f_k(\mathbf{r}_1, \mathbf{v}_1, \dots, \mathbf{r}_k, \mathbf{v}_k; t) = \left(\frac{n}{\bar{v}^d}\right)^k \tilde{f}_k(\mathbf{x}_1, \mathbf{c}_1, \dots, \mathbf{x}_k, \mathbf{c}_k). \quad (28)$$

The evolution equations of $n(t)$ and kinetic energy density $n\bar{v}^2(t)$ follow from integrating Eq. (18) with weights $d\mathbf{v}_1$ and $v_1^2 d\mathbf{v}_1$, respectively, for $k=1$. We obtain

$$\frac{dn}{dt} = -\omega(t)n, \quad (29)$$

$$\frac{d(n\bar{v}^2)}{dt} = -\alpha\omega(t)n\bar{v}^2, \quad (30)$$

where the collision frequency ω and kinetic energy dissipation parameter α read

$$\mathcal{C} = \frac{2}{1 + \alpha} \ln\left(1 + \frac{1 + \alpha}{2} \omega_0 t\right). \quad (35)$$

The corresponding time evolution is

$$\frac{n}{n_0} = \left[1 + \frac{1 + \alpha}{2} \omega_0 t\right]^{-2/(1 + \alpha)}, \quad (36)$$

$$\frac{\bar{v}}{\bar{v}_0} = \left[1 + \frac{1 + \alpha}{2} \omega_0 t\right]^{(1 - \alpha)/(1 + \alpha)}. \quad (37)$$

Without knowing the detailed form of the one-particle distribution function f_1 , it is thus possible to conclude about the time decay of n and \bar{v} , which appear to obey algebraic laws in the long-time limit [$n(t) \propto t^{-\xi}$ and $\bar{v}(t) \propto t^{-\gamma}$, with $\xi = 2/(1 + \alpha)$ and $\gamma = (\alpha - 1)/(\alpha + 1)$]. The exponents ξ and γ are consequently simply related to the unknown quantity α , for which a perturbative expansion will be put forward in Sec. III before a numerical investigation in Sec. IV. Moreover, if the initial velocity distribution is of finite support (i.e., vanishes outside a sphere of given velocity v^*), \bar{v} fulfills the bound $\bar{v} \leq v^*$ so that γ is necessarily positive (or $\alpha \geq 1$). In the framework of Boltzmann’s equation, it will be shown in Appendix A that the quantity α is necessarily larger

than 1. For the specific initial condition where all particles have the same kinetic energy at $t=0$, $\bar{v}^2 = \langle v^2 \rangle$ is time independent, and Eq. (37) implies that $\alpha=1$. From Eq. (36), we therefore obtain the time evolution for this situation,

$$\frac{n}{n_0} = \frac{1}{1 + \omega_0 t}, \quad (38)$$

which is exact within the scaling theory. This relation *a priori* holds in any dimension, except for $d=1$ where the corresponding initial velocity distribution is the symmetric discrete bimodal function $\pm c$, for which the scaling ansatz underlying our approach fails (see the discussion at the end of the present section).

Inserting the scaling forms (27) and (28) into the first equation of the hierarchy (18) imposes the following constraint on the decay exponents: $\xi + \gamma = 1$. This scaling relation may be simply obtained by elementary dimensional analysis [4–6,9,10], and may be considered as the compatibility condition of the hierarchy with the self-similar scaling solutions [12]. It is, moreover, identically fulfilled by expressions (36) and (37). Under the constraint $\xi + \gamma = 1$, the remaining equations of the hierarchy ($k > 1$) turn out to be compatible with Eq. (28) with the additional information that the collision term on the left-hand side of Eq. (18) decays like $t^{-\gamma-d\xi}$, whereas the remaining terms are associated with a power $1/t$. Given that $\gamma + d\xi = 1 + (d-1)\xi \geq 1$, this collision term is asymptotically irrelevant except in one dimension where it remains of the same order as the dominant ones ($1/t$). We therefore recover the conclusions obtained by considering the formal Grad limit, with distribution functions expected to obey a Boltzmann-like equation. This analysis points to the relevance of Boltzmann equation for $d > 1$, a point that is further corroborated by the numerical results given in Sec. IV.

It is interesting to note that both Eq. (38) and the relation $\xi + \gamma = 1$ do not hold in 1D for discrete initial velocity distributions. In the symmetric situation of a bimodal distribution, the average kinetic energy per particle is conserved (so that $\gamma=0$), whereas the density decays as $1/\sqrt{t}$ (i.e., $\xi = 1/2$ [1]). The scaling assumption (28) is consequently incorrect in the specific situation of discrete distributions in 1D, but valid for continuous distributions [6]. To be more specific, the scaling form (28) implies that the collision frequency scales with time, like $\omega \propto n\bar{v}$. On the other hand, from the analytical solution of the bimodal $\pm c$ situation [1], we obtain $\omega \propto n^2\bar{v}$ with $\bar{v} = c$. This discrepancy is the signature of dynamical correlations in the latter discrete case. These correlations are responsible for the breakdown of Eq. (28), and in addition, violate molecular chaos. For continuous velocity distributions, again in 1D, molecular chaos also breaks down while the scaling (28) is correct. As a consequence, the exponents obtained at the Boltzmann level differ from the exact ones (see the discussion in the last paragraph of Sec. III), whereas the relation $\xi + \gamma = 1$ holds.

III. BOLTZMANN KINETIC EQUATION

This section is devoted to the analysis of the decay dynamics within the molecular chaos framework [13] of the homogeneous nonlinear Boltzmann equation. No exact solution could be obtained, and our goal is to derive accurate approximate predictions for the scaling exponents ξ and γ of the density and root-mean-squared velocity.

Before considering the kinetic equation obeyed by the rescaled distribution function, it is instructive to rewrite the original homogeneous Boltzmann equation (25) in the form

$$\frac{\partial f_1(\mathbf{v};t)}{\partial t} = -\nu(\mathbf{v};t)f_1(\mathbf{v};t),$$

with

$$\nu(\mathbf{v}_1;t) = \left[\sigma^{d-1} \int d\hat{\boldsymbol{\sigma}} (\hat{\boldsymbol{\sigma}} \cdot \hat{\mathbf{v}}_{12}) \theta(\hat{\boldsymbol{\sigma}} \cdot \hat{\mathbf{v}}_{12}) \right] \int d\mathbf{v}_2 |\mathbf{v}_{12}| f_1(\mathbf{v}_2;t), \quad (39)$$

where in the last equation, the term in brackets may be computed explicitly as a function of dimension (it is understood that the unit vector $\hat{\mathbf{v}}_{12}$ denotes an arbitrary direction). For our purpose, it is sufficient to notice that at all times, the collision frequency $\nu(\mathbf{v};t)$ of the population having velocity \mathbf{v} remains finite in the limit $v \rightarrow 0$, provided the first moment of f_1 exists. In this situation, Eq. (39) implies that $f_1(\mathbf{v};t)/f_1(\mathbf{v};0)$ admits a finite limit for $v \rightarrow 0$, or equivalently, it may be stated that if the initial velocity distribution behaves like v^μ near the velocity origin, this feature is preserved by the Boltzmann dynamics. Previous works have shown accordingly that the scaling exponents ξ and γ depend on the exponent μ [4,6,9,10].

Making use of relations (29) and (30), insertion of the scaling form (27) into the Boltzmann equation leads to

$$\left[1 + \left(\frac{1-\alpha}{2} \right) \left(d + c_1 \frac{d}{dc_1} \right) \right] \tilde{f}_1(c_1) = \tilde{f}_1(c_1) \int dc_2 \frac{c_{12}}{\langle c_{12} \rangle} \tilde{f}_1(c_2), \quad (40)$$

where we have assumed an isotropic velocity distribution [$\tilde{f}_1(\mathbf{c}) = \tilde{f}_1(c)$] and introduced the average $\langle (\dots) \rangle = \int (\dots) \tilde{f}_1(c_1) \tilde{f}_1(c_2) d\mathbf{c}_1 d\mathbf{c}_2$. $\langle c_{12} \rangle$ is therefore the rescaled collision frequency. Once μ has been chosen, Eq. (40) admits a solution for a unique value of α . We show in Appendix A that the inequality $\alpha > 1$ necessarily holds.

Irrespective of α , the large velocity behavior of \tilde{f}_1 may be obtained following similar lines as in Refs. [4,5,9,14,15]: it is possible to integrate formally Eq. (40) and cast \tilde{f}_1 into

$$\frac{\tilde{f}_1(c)}{\tilde{f}_1(c')} = \left(\frac{c}{c'} \right)^{-[2+d(1-\alpha)]/(1-\alpha)} \times \exp \left[\frac{2}{1-\alpha} \frac{1}{\langle c_{12} \rangle} \int_{c'}^c \frac{\tilde{\nu}(c'')}{c''} dc'' \right]. \quad (41)$$

In this equation, \tilde{v} is itself a functional of \tilde{f}_1 ;

$$\tilde{v}(c_1) = \int c_{12} \tilde{f}_1(c_2) d\mathbf{c}_2, \quad (42)$$

such that $\tilde{v}(c)/c$ goes to a finite limit for $c \rightarrow \infty$. We therefore obtain the large velocity tail

$$\tilde{f}_1(c) \propto c^{-[2+d(1-\alpha)]/(1-\alpha)} \exp\left(-\frac{2}{\alpha-1} \frac{c}{\langle c_{12} \rangle}\right) \quad \text{for } c \rightarrow \infty. \quad (43)$$

In one dimension, we recover the results of Refs. [4] and [9]. In Refs. [4,5], an approximation was derived for α [or equivalently, $\xi = 2/(1+\alpha)$] by assuming that the large velocity behavior of \tilde{f}_1 could hold for the whole velocity spectrum. In this picture, the power of c appearing on the right-hand side of Eq. (43) is equated to the exponent μ characteristic of the small velocity behavior (imposed by the initial distribution chosen, see above), with the result

$$\alpha = 1 + \frac{2}{\mu+d} \quad \text{or} \quad \xi = \frac{2d+2\mu}{2d+2\mu+1}. \quad (44)$$

This prediction encodes the correct dependence on μ and dimension (ξ increases when μ or d increase), and turns out to have an accuracy of order 10% when compared to the numerical results [10]. In the limit of large dimension, we obtain from Eq. (44) $\xi \sim 1 - (2d)^{-1}$, whereas Krapivsky and Sire have shown that $\xi \sim 1 - d^{-1}(1 - 1/\sqrt{2})$, also in the framework of the Boltzmann equation. The remainder of this section is devoted to the derivation of a more precise value for α , which furthermore coincides with the exact $1/d$ correction for $d \rightarrow \infty$.

Invoking the identity

$$\int d\mathbf{c} c^p \left(d + c \frac{d}{dc} \right) \tilde{f}_1(\mathbf{c}) = -p \langle c^p \rangle, \quad (45)$$

the energy dissipation parameter α may be given as the set of equivalent expressions:

$$\alpha = 1 + \frac{2}{p} \left(\frac{\langle c_{12} c_1^p \rangle}{\langle c_{12} \rangle \langle c_1^p \rangle} - 1 \right), \quad \forall p \geq 0. \quad (46)$$

A particularly useful relation between α and moments of \tilde{f}_1 follows from considering the limit $c_1 \rightarrow 0$ of Eq. (40); we get

$$\alpha = 1 + \frac{2}{\mu+d} \left(1 - \frac{\langle c_1 \rangle}{\langle c_{12} \rangle} \right). \quad (47)$$

The (infinite) family of relations (47) and (46) is equivalent to the original integro-differential equation (40), and well suited to a perturbative analysis. To this end, a systematic approximation of the isotropic function \tilde{f}_1 can be found by expanding it in a set of Sonine polynomials [16]:

$$\tilde{f}_1(c) = \mathcal{M}(c) \left[1 + \sum_{n=1}^{\infty} a_n S_n(c^2) \right]. \quad (48)$$

These polynomials are orthogonal with respect to the Gaussian weight,

$$\mathcal{M}(c) = \left(\frac{d}{2\pi} \right)^{d/2} e^{-dc^2/2}, \quad (49)$$

and the first few read

$$S_0(x) = 1, \quad (50)$$

$$S_1(x) = \frac{d}{2}(-x+1), \quad (51)$$

$$S_2(x) = \frac{d^2}{8}x^2 - \frac{d(d+2)}{4}x + \frac{d(d+2)}{8}. \quad (52)$$

The coefficients a_n follow from the orthogonality relation $\int S_n(c^2) S_m(c^2) \mathcal{M}(c) d\mathbf{c} \propto \delta_{nm}$. In particular,

$$a_1 = \frac{2}{d} \langle S_1(c^2) \rangle = \frac{2}{d} (1 - \langle c^2 \rangle) = 0, \quad (53)$$

as obtained from the definition of rescaled velocities (26). The first non-Gaussian correction is thus embodied in a_2 , which is proportional to the fourth cumulant (kurtosis) of the velocity distribution:

$$a_2 = \frac{d^2}{3} [\langle c_i^4 \rangle - 3\langle c_i^2 \rangle^2] = \frac{d}{d+2} \langle c^4 \rangle - 1, \quad (54)$$

with c_i a Cartesian component of \mathbf{c} . Upon truncating Eq. (48) at a finite order n , we obtain a regular velocity distribution near $c=0$. We consequently restrict our analysis to the case $\mu=0$ (the dependence on μ has been considered in Ref. [10]).

It is also noteworthy that any truncation of Eq. (48) at arbitrary order n leads to a Gaussian high-energy behavior, incompatible with the result (43) corresponding to an overpopulated tail with respect to the Maxwellian. However, it will be shown in Sec. IV that the difference between the truncated expansion (48) and the numerical velocity distribution becomes manifest far in the tail, where the distribution has reached very low probabilities. Consequently, when the moment involved in Eqs. (46) and (47) are evaluated from the truncation of Eq. (48), the accuracy of the result is expected to be better for low orders of p in Eq. (46). Hence the privileged role is played by Eq. (47), which is of lower order than any of the identities (46). In practice, upon truncating Eq. (48) at order n , the n unknowns α, a_2, \dots, a_n are computed evaluating the corresponding moments appearing in Eq. (47) and in $n-1$ of the relation (46), among which it is convenient to retain the $n-1$ even values of p ($p=0$ excluded). Truncation of Eq. (48) at order $n=2$ yields precise predictions for α and \tilde{f}_1 , and already at Gaussian order, α turns out to be very close to its numerical counterpart. Set-

ting $n=0$ (or equivalently, $n=1$ since $a_1 \equiv 0$) in Eq. (48), we obtain immediately the zeroth-order approximation

$$\alpha = \alpha_0 = 1 + \frac{2}{d} \left(1 - \frac{\sqrt{2}}{2} \right), \quad (55)$$

which corresponds to

$$\xi = \xi_0 = \frac{2}{1 + \alpha_0} = \frac{2d}{2(d+1) - \sqrt{2}}. \quad (56)$$

For large dimensions, this estimation goes to unity, with the exact $1/d$ correction computed in Ref. [9],

$$\xi = 1 - \frac{1}{d} \left(1 - \frac{\sqrt{2}}{2} \right) + \mathcal{O}\left(\frac{1}{d^2}\right). \quad (57)$$

This behavior turns out to be “universal,” in the sense that the μ dependence does not appear at this order [10].

We shall also be interested in the non-Gaussian features of the velocity distribution, which we quantify by the fourth cumulant a_2 . The (cumbersome) calculations at second order in Sonine expansion are detailed in Appendix B. We obtain

$$a_2 = 8 \frac{d(2\sqrt{2}-3)}{4d^2 + d(6-\sqrt{2})}, \quad (58)$$

$$\alpha_2 = \alpha_0 + \frac{\sqrt{2}}{16d} a_2. \quad (59)$$

The corresponding density exponent follows from $\xi_2 = 2/(1 + \alpha_2)$ as before. For $d \rightarrow \infty$, $a_2 \sim 2(3 - 2\sqrt{2})d^{-1}$ irrespective of μ [10], which reinforces the universal nature of large d . The correction to ξ carried by a_2 behaves as $1/d^2$ in this limit, and does not affect the $1/d$ terms that still coincide with the exact behavior (57). Both predictions (55) and (59) are such that $\alpha > 1$, which is required to obtain a normalizable distribution in Eqs. (41) and (43).

The second-order expansion considered here may be improved by consideration of higher-order Sonine terms and inclusion of nonlinear terms in a_2 . In the related context of inelastic hard spheres, the limitation of working at linear order in a_2 with neglect of Sonine terms of order $n \geq 3$ may be found in Ref. [17]. Alternatively, keeping nonlinear terms in a_2 and neglecting again Sonine terms of order $n \geq 3$ leads to multiple solutions. A stability analysis is then required to determine which one is stable, as discussed in Ref. [18].

Here, the value obtained for a_2 is quite small (see below). Our approximate expressions are accurate when compared to the full numerical solution of Boltzmann’s equation, so that we did not calculate any higher-order coefficients, nor did we consider nonlinear terms in a_2 . The existing literature reports, within the Boltzmann framework, numerical exponents in 1D, which are in excellent agreement with our predictions, already at zeroth order. For the case $\mu=0$, expressions (56) and (59) give $\xi_0 \approx 0.773$ and $\xi_2 \approx 0.769$, whereas the numerical result obtained in Ref. [9] is $\xi \approx 0.769$. These exponents are close to their counterparts ex-

tracted numerically from the exact dynamics (0.785 ± 0.005 in Ref. [6], and more recently 0.804 in [19]). The difference between the exact exponents and those obtained assuming molecular chaos is consistent with the conclusion of Sec. II: In one dimension, the factorization of the two-body distribution \tilde{f}_2 underlying Boltzmann ansatz is not an exact property of the distributions obeying hierarchy (18). On the other hand, for $d > 1$, the molecular chaos exponents are expected to become exact. This property is illustrated in the following section.

IV. SIMULATION RESULTS

The numerical results presented in this section correspond to the situation $\mu=0$, unless stated. We refer to Ref. [10] for the case of diverging ($\mu < 0$) or depleted ($\mu > 0$) velocity distributions near $v=0$.

A. The numerical methods

We follow two complementary numerical routes. First, we solve the time-dependent homogeneous Boltzmann equation by means of the direct simulation Monte Carlo method (DSMC), originally developed to study ordinary gases [20]. This scheme, where a suitable Markov chain is constructed, has been extended to deal with inelastic collisions [21,22] and is easily modified to describe the situation under study here, which does not conserve the total number of particles. Restricting to a spatially homogeneous system, the algorithm is especially easy to implement, and may be summarized as follows: among N_0 initial particles having a given velocity distribution, a pair (i,j) is chosen at random, and removed from the system with a probability proportional to $|\mathbf{v}_{ij}|$. The (suitably renormalized) time variable is then incremented by the amount $(N^2 |\mathbf{v}_{ij}|)^{-1}$, where N is the number of particles remaining in the system before another pair is drawn, etc. This scheme provides the numerical exact solution of Eq. (39), and allows to test the validity of the approximations put forward in Sec. III [essentially, truncation at second order in expansion (48) supplemented with calculations performed at linear order in the fourth cumulant a_2 (see Appendix B)]. A precise analysis of the late time dynamics (and especially the computation of velocity distributions) suffers from the concomitant low number of particles left, and the statistical accuracy is improved by averaging over independent realizations.

The second numerical method (molecular dynamics [23]) consists of integrating the exact equations of motion for an assembly of spheres confined in a (hyper)cubic box with periodic boundary conditions. This route assesses the validity of the approach relying on the homogeneous Boltzmann equation, but does not offer the same accuracy as DSMC, nor the possibility to follow the evolution over comparable times. In particular, once the mean free path λ , which grows rapidly as t^ξ , becomes of the order of the box size L , the subsequent evolution suffers from finite size effects and should be discarded. When $\lambda > L$, the algorithm used is unable to find collision events for those particles that make more than one free flight round on the torus topologically

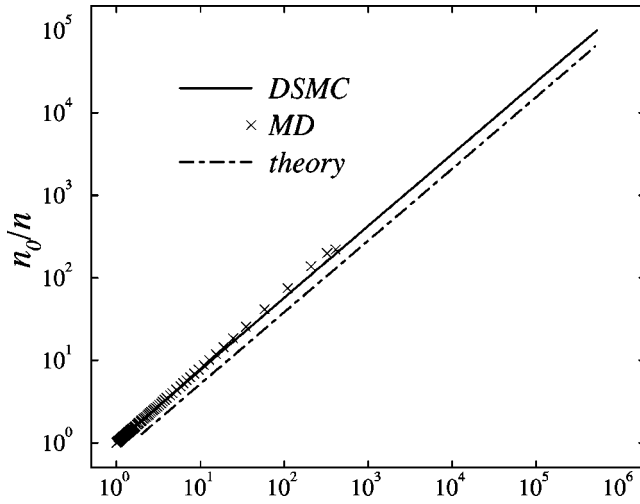


FIG. 1. Inverse density n_0/n versus $n_0\bar{v}_0/(n\bar{v})$, for $d=2$. The dotted line has slope $\xi_2=0.87$ [see Eq. (56)]. Initial number of particles: 5×10^6 (with a further average over 10^3 independent replicas) for DSMC and 2×10^5 for MD. In both cases, the initial velocity distribution is Gaussian ($\mu=0$), and the initial configuration used for MD is that of an equilibrium hard disk fluid with packing fraction $\phi=0.1$ (chosen low enough to avoid finite packing effects).

equivalent to the simulation box, which causes a spurious slowing down of the dynamics. It is then tempting to reduce λ by increasing the particle diameter σ , but then finite (and necessarily transient) density effects—incompatible with the scaling assumption (28)—may also arise if the packing fraction ϕ , proportional to $n\sigma^d$, is not low enough. Simulating explicitly the limit of point particles, the DSMC scheme considered here is free of this defect. The initial number of particles considered in MD needs to be large to allow the system to enter the scaling regime before finite size effects become dominant, we considered systems with $N=(5 \times 10^4) - (5 \times 10^5)$ spheres initially (compared to $N=10^6-10^8$ in DSMC).

B. Dynamic scaling behavior

The results of two-dimensional DSMC and MD simulations are shown in Fig. 1, where the quantity on the x axis is expected to scale like real time t from the scaling relation $\xi + \gamma = 1$. This log-log plot is a direct probe of the exponent ξ , from the slope measured. Both MD and DSMC methods give compatible results, with the possibility to follow the dynamics over a longer time interval in DSMC. The departure observed for $n_0/n \approx 200$ corresponds to the slowing down of MD resulting from finite size effects (see Fig. 2 below). The theoretical predictions at zeroth and second order are very close ($\xi_0=0.872$ and $\xi_2=0.870$), and in excellent agreement with the simulation results over several decades. On a similar graph as Fig. 1, the kinetic “temperature” \bar{v}^2 exhibits a power law behavior (not shown) with an exponent -2γ , in good agreement with the theoretical prediction ($\gamma \approx 0.13$ in 2D). Moreover, the exponents obtained analytically and numerically are compatible to

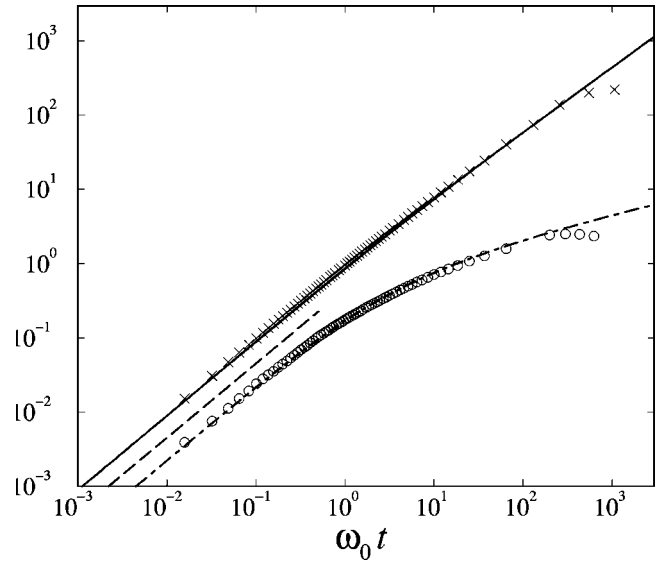


FIG. 2. Plots of $(n_0/n) - 1$ [upper curve corresponding to DSMC, compared to its MD counterpart (crosses)] and $(\bar{v}_0^2/\bar{v}^2) - 1$ (lower dashed curve for DSMC, circles for MD) as a function of time. The dotted line at short times has slope 1.

those reported in the literature ($\xi \approx 0.89$ in Ref. [4] and $\xi \approx 0.87(5)$ using a multiparticle lattice gas method [24]).

The time evolution of inverse density and inverse typical velocity square is shown in Fig. 2, where considering $n_0/n - 1$ and $\bar{v}_0^2/\bar{v}^2 - 1$ instead of n_0/n and \bar{v}_0^2/\bar{v}^2 allows one to probe the short time behavior. Unless stated, the initial velocity distribution is an isotropic Gaussian. From Eqs. (29) and (30), n and \bar{v}^2 evolve linearly with t for $\omega_0 t \ll 1$ [see also Eqs. (36) and (37)]; the same holds for inverse density and inverse typical velocity squared, which is indeed observed in Fig. 2. MD and DSMC results superimpose, except at late times where MD suffers from the slowing down discussed previously. For both numerical methods, the scaling relation $\xi + \gamma = 1$ is well obeyed, in principle at late times only, in the scaling regime. Special combinations of n and \bar{v} can, however, be constructed with the requirement to match the short time evolution with the scaling behavior. One of these quantities is displayed in Fig. 3, with a resulting scaling regime extending over more than ten decades in time. In Fig. 4, we not only test the validity of the theoretical scaling exponents, but also the full time dependence as predicted by Eqs. (36) and (37). In order to improve the agreement between theory and simulation (which holds over more than six orders of magnitude in time), the system has been left to time to enter the scaling regime. The time origin $t=0$ has been chosen when 80% of the particles originally present have disappeared. The corresponding reference configuration (with subscripts 0) thus differs from the ones considered previously.

C. Velocity distribution in the scaling regime

In order to understand the reasons for the good agreement between our theoretical predictions and the simulations, we now consider the velocity distribution, restricting to Monte Carlo results (leading to similar conclusions, MD is much

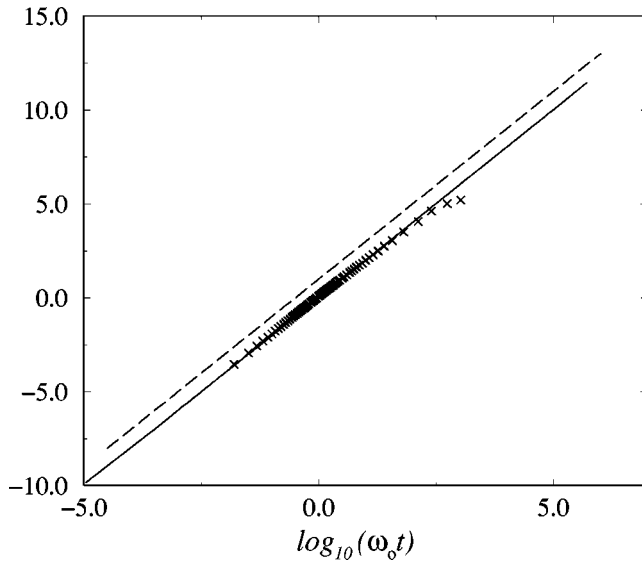


FIG. 3. Plot of $\log_{10}[n_0/n-1] + \log_{10}[n_0\bar{v}_0^2/(n\bar{v}^2)-1]$ on a logarithmic time scale ($d=2$). DSMC results are represented by the continuous curve, while the crosses correspond to MD. The dashed line has slope 2. At late times, the quantity displayed is expected to behave as $2 \log_{10}(\omega_0 t)$ from the scaling relation $\xi + \gamma = 1$. At short times, the same behavior is observed, for a different reason [see Eqs. (36) and (37)]. The ultimate MD slowing down is again visible.

more demanding on CPU time and does not allow to investigate detailed features of \tilde{f}_1 with the same accuracy). After a transient where the probability distribution function \tilde{f}_1 evolves with time, a well-defined scaling regime is reached with a time independent $\tilde{f}_1(\mathbf{c})$ shown in Fig. 5 together with

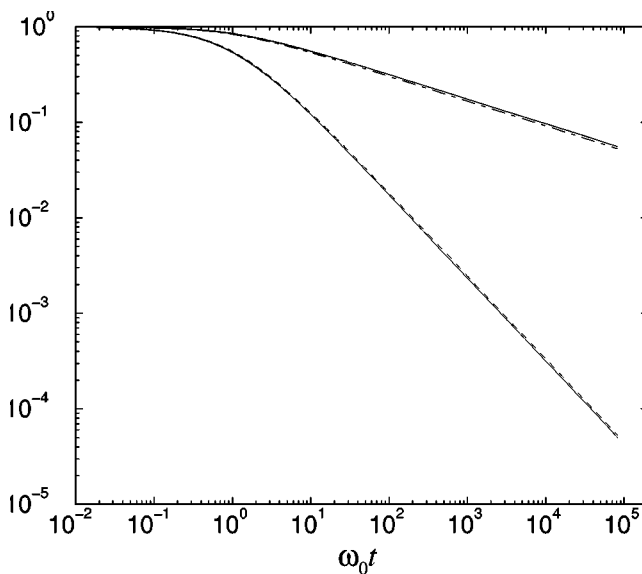


FIG. 4. Time dependence of n (lower curve) and \bar{v}^2 (upper curve) obtained in Monte Carlo, compared to the dashed curves corresponding to the theoretical predictions (36) and (37), where the energy dissipation coefficient α is calculated at second order in Sonine expansion [$\alpha_2 \approx 1.297$ from Eq. (59)].

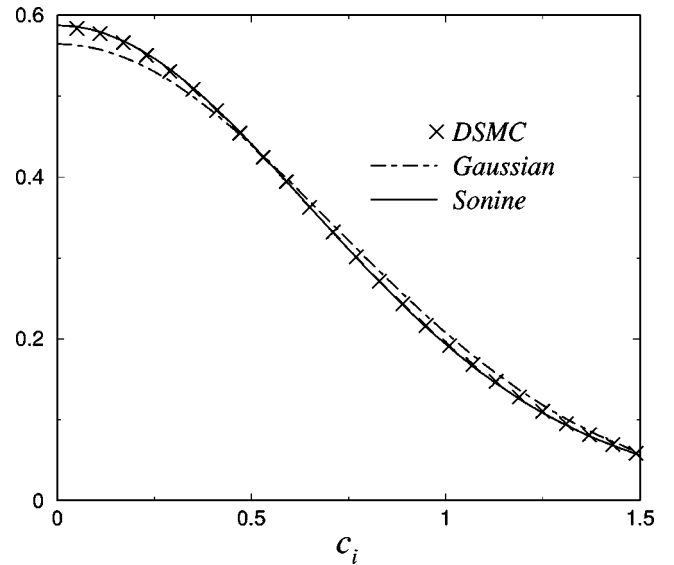


FIG. 5. Probability distribution function $\tilde{f}_1(c_i)$ of a given Cartesian component c_i of the rescaled two-dimensional velocity \mathbf{c} . The time-independent distribution obtained in DSMC simulations at late times is compared to the Gaussian \mathcal{M} and the Sonine expansion truncated at $n=2$, with the fourth cumulant given by Eq. (58) ($a_2 \approx 0.109$ for $d=2$ and $\mu=0$). All distributions have variance $1/2$, so that $\langle c^2 \rangle = 1$. The results have been obtained by averaging over 50 replicas of a system with initially $N=40 \times 10^6$ particles.

the Sonine prediction pushed at second order. The agreement is remarkable, and it is also observed that the Gaussian approximation is already close to the asymptotic rescaled velocity distribution, which is quite surprising in a kinetic process extremely far from equilibrium, with furthermore no conservation laws. Given that our perturbative analytical work relies on the calculation on low order moments of \tilde{f}_1 , this explains the accuracy of the zeroth-order predictions α_0 and ξ_0 . From Eq. (43), we expect the differences between the Sonine expansion and the numerical distribution to become visible in the high-energy tail, which is confirmed in Fig. 6. As predicted, \tilde{f}_1 is overpopulated with respect to the Gaussian, and displays a high velocity tail of the form (43) (see the inset of Fig. 6).

D. Evolution towards the asymptotic solutions

Before the scaling regime is attained, \tilde{f}_1 is time dependent, as shown in Fig. 7, where the distributions at different times have been renormalized by \mathcal{M} to emphasize the building up of non-Gaussianities. The evolution towards the scaling solution $1 + a_2 S_2$ can be observed. With respect to the Gaussian, \tilde{f}_1 is at all times overpopulated both at large and small velocities (which may be related to the positive sign of a_2 for the latter case); normalization is ensured by an underpopulation at intermediate velocities. Figures 5–7 show that the indirect measure of a_2 through the non-Gaussian character of \tilde{f}_1/\mathcal{M} agrees with the theoretical prediction, but it is also possible to compute directly a_2 in the simulations through its definition as a fourth cumulant [Eq. (54)]. It turns out that both methods are numerically fully compatible.

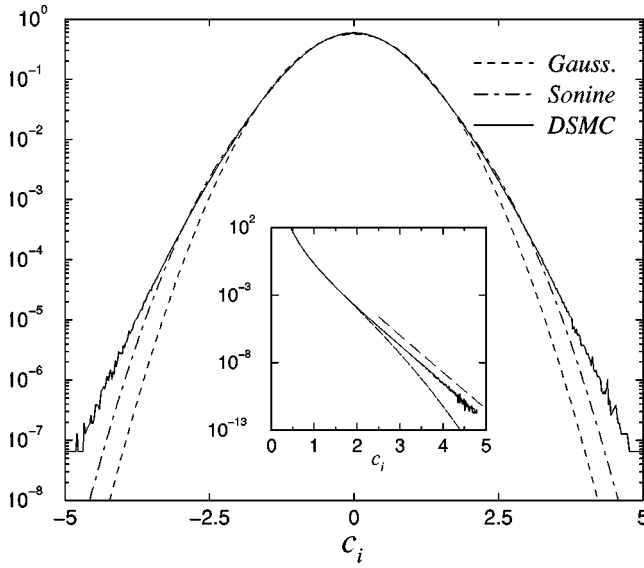


FIG. 6. Same as Fig. 5, on a linear-log scale to probe the tails of the distributions. In the inset showing $c_i^{-4.7}\tilde{f}_1(c_i)$ as a function of c_i , the dashed curve corresponds to the Gaussian [$c_i^{-4.7}\mathcal{M}(c_i)$] while the straight line is a guide for the eye evidencing a pure exponential behavior. For $d=2$ and $\mu=0$, the exponent $d+2/(1-\alpha)$ appearing in Eq. (43) is close to -4.7 and has been used to rescale the quantity plotted on the y axis in the inset.

Moreover, the Sonine expansion (48) truncated at $n=2$ holds at any time, even in the transient regime, with the time-dependent fourth cumulant a_2 measured from Eq. (54) (see Fig. 8). This result is not *a priori* expected and points to the relevance of expansion (48). We did not try to solve analytically the homogeneous time-dependent Boltzmann equation within the same framework as in the scaling regime, so that we do not have any prediction for the (transient) time depen-

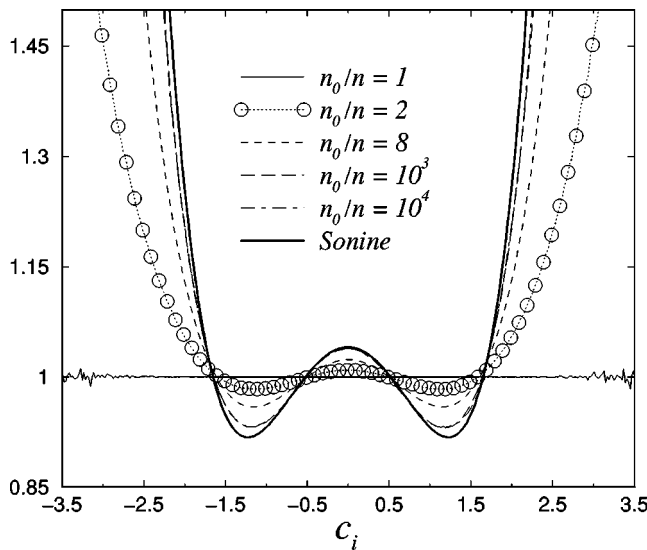


FIG. 7. Plots of $\tilde{f}(c_i)/\mathcal{M}(c_i)$ versus c_i , at different times corresponding to the indicated densities. The initial distribution is Gaussian (thus corresponding to the flat curve) and the thick curve is Sonine solution $1+a_2S_2$, with a_2 given by Eq. (58).

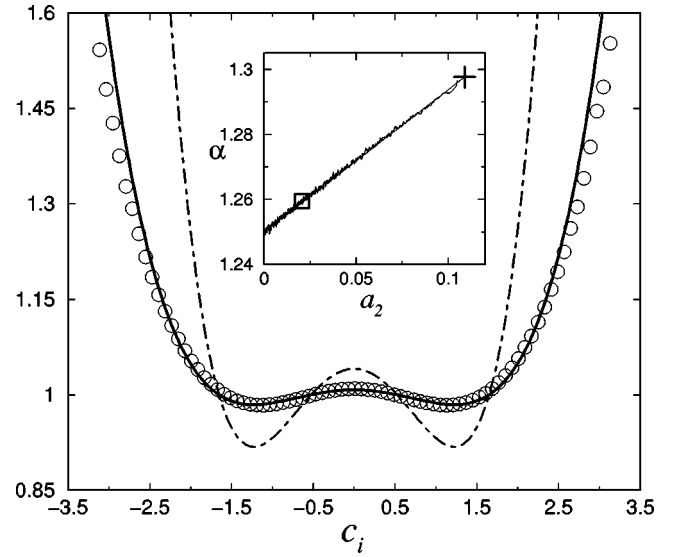


FIG. 8. Plot of $\tilde{f}(c_i)/\mathcal{M}(c_i)$ as a function of c_i , at the particular time $t_{1/2}$ where the density is exactly half the initial one, with the same initial distribution as in Fig. 7 [the circles (DSMC measure) thus show the same distribution as the circles of Fig. 7]. The thick curve shows $1+a_2(t_{1/2})S_2$, with $a_2(t_{1/2})$ measured from its definition (54). The dashed curve is the Sonine prediction in the scaling regime (i.e., the thick curve of Fig. 7). Inset: α as a function of a_2 (see main text). The DSMC measure is compared to the prediction (B10) shown by the straight line ending at the point—indicated by a cross—of coordinates (0.109, 1.297) as predicted by Eqs. (58) and (59). The square located at (0.0207, 1.2595) corresponds to the numerical measure of α and a_2 made at time $t_{1/2}$ for which the velocity distribution is displayed in the main graph.

dence of a_2 and α . However, as shown in the inset of Fig. 8, relation (B10) [which reads in 2D as $\alpha=(5/4)+(7a_2/16)$] remarkably holds for all times. Here, the energy dissipation parameter α has been computed through the ratio $\langle c_{12}c_1^2 \rangle / (\langle c_{12} \rangle \langle c_1^2 \rangle) = \langle c_1^2 \rangle_{\text{coll}} / \langle c_1^2 \rangle$, where $\langle c_1^2 \rangle_{\text{coll}}$, the mean energy dissipated in a collision, is computed in the simulations and normalized by the time-dependent mean kinetic energy per particle, $\langle c_1^2 \rangle$.

E. A final remark: Identification of “isobestic” points

For $\mu=0$, Fig. 7 indicates that during the transient evolution towards scaling, the distributions of reduced velocities have fixed points (for a given initial velocity distribution, all the curves corresponding to \tilde{f}_1 at different times pass through common points that we called isobestic points). This feature has been observed for all initial distributions investigated and appears to be a systematic property of the dynamics, which still holds for nonvanishing values of μ (see Fig. 9). We have no analytical explanation for this observation.

V. CONCLUSION

An analytical derivation of the equations governing the dynamics of an infinite system of spherical particles in a d -dimensional space, moving freely between collisions and annihilating in pairs when meeting, has been obtained. The

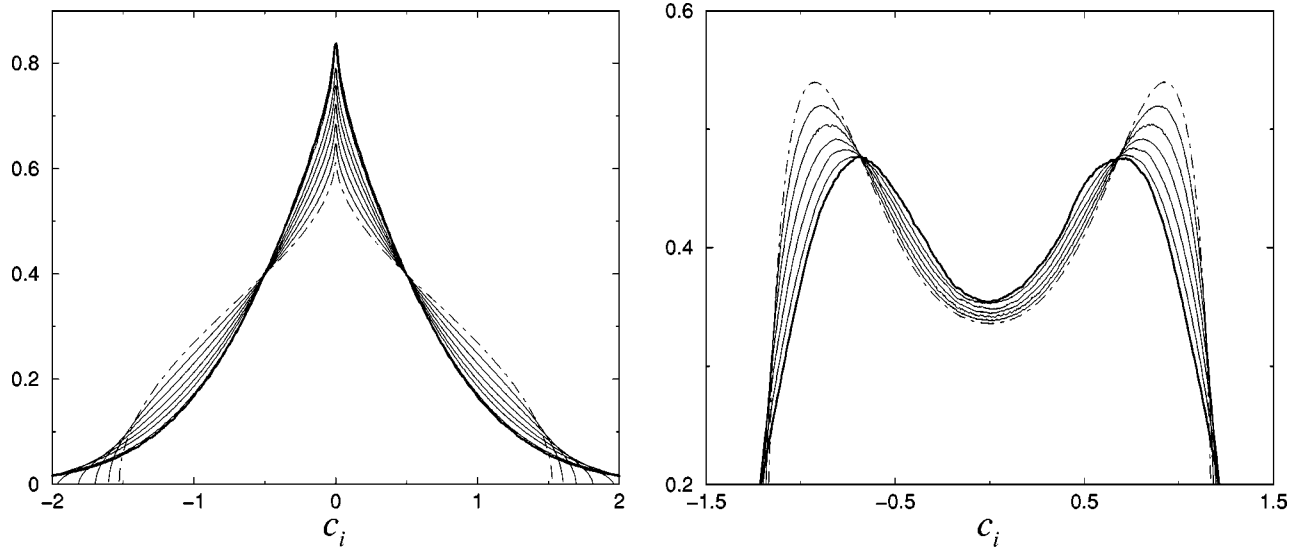


FIG. 9. Plots of $\tilde{f}_1(c_i)$ as a function of c_i at different times. The left graph corresponds to an initial velocity distribution with $\mu = -3/2$ while $\mu = 3$ for the right graph. On both graphs, the initial distribution is shown by the dashed curve, whereas the thick curves display the asymptotic distributions approached in the scaling regime.

hierarchy equations obeyed by the reduced distributions $f_k(1, 2, \dots, k; t)$ have been derived. In the Grad limit, this hierarchy formally reduces to a Boltzmann-like hierarchy for dimensions $d > 1$. If these reduced distributions f_k^B factorize at the initial time, this factorization remains valid for all times, and the whole hierarchy reduces to a nonlinear equation.

In the long-time limit, the ratio of the particle radius to the mean free path vanishes. A scaling analysis of the exact homogeneous hierarchy equations has been performed. Self-similar reduced distributions in which the time dependence has been absorbed into the density $n(t)$ and the root-mean-square velocity $\bar{v}(t)$ were introduced. As a result, the exponents ξ and γ describing the decay with time of $n(t)$ and $\bar{v}(t)$ depend only upon one single parameter α , related to the dissipation of energy. Moreover, it turns out that in dimension higher than 1, the terms responsible for the violation of molecular chaos are asymptotically irrelevant. Therefore, we recover the conclusions reached in the formal Grad limit, and thus, the Boltzmann equation becomes exact in the long-time limit in dimensions higher than 1. The above arguments give a first-principles justification for the use of the Boltzmann equation approach for $d > 1$, as well as its limitations, in ballistic annihilation problems, an issue that has been overlooked so far. However, as discussed above, this scaling analysis is incorrect for a one-dimensional system with discrete initial velocity distribution, a situation for which the scaling assumption underlying our approach fails.

The Boltzmann equation has been solved within an expansion in Sonine polynomials S_n . Truncation to order $n = 2$ provides the first non-Gaussian corrections to the scaled velocity distribution, and leads to analytical predictions for the exponents ξ and γ as a function of d . For large dimension d , these predictions coincide with the exact $1/d$ correction to the naive mean-field values ($\xi = 1$ and $\gamma = 0$), calculated in Ref. [9]. The above analytical predictions are in

remarkable agreement with the results of extensive numerical simulations we have performed for two-dimensional systems (implementing the complementary Monte Carlo and molecular dynamics techniques). In 1D, for regular continuous velocity distributions, it is noteworthy that they are in excellent agreement with the numerical solution of the Boltzmann equation, and quite close to the exact values obtained with molecular dynamics (4% difference). This last point was unexpected since molecular chaos breaks in 1D. Finally, the time dependence of the reduced velocity distribution function shows an unexplained and a remarkable feature, with the existence of fixed (“isobestic”) points, irrespective of initial conditions.

ACKNOWLEDGMENTS

We would like to thank F. Coppex for a careful reading of the manuscript, and T. van Noije, A. Barrat, F. van Wijland, and A. Santos for useful discussions. E.T. acknowledges the hospitality of the Theoretical Physics Department (Geneva) where part of this work was performed. J.P. and E.T. benefited from the financial support of the “Program d’Action Intégrée Franco-Polonais Polonium” (Contract No. 03990WF). M.D. acknowledges the support of the Swiss National Science Foundation and of the CNRS.

APPENDIX A

Within Boltzmann’s kinetic equation, we show in this appendix that $\alpha > 1$. To this end, Eq. (40) is rewritten in the form

$$\tilde{f}_1(c_1) + \left(\frac{1-\alpha}{2}\right) \text{div}_{\mathbf{c}_1}[\mathbf{c}_1 \tilde{f}_1(c_1)] = \tilde{f}_1(c_1) \int d\mathbf{c}_2 \frac{c_{12}}{\sqrt{c_{12}}} \tilde{f}_1(c_2), \quad (\text{A1})$$

and integrated with weight $\psi(c_1)d\mathbf{c}_1$, where we choose $\psi(c) = c^{2/(1-\alpha)}$. Assuming that the moment $\int \psi \tilde{f}_1$ exists, we obtain after integration by parts (neglecting surface terms),

$$0 = \int d\mathbf{c}_1 d\mathbf{c}_2 \psi(c_1) \frac{c_{12}}{\langle c_{12} \rangle} \tilde{f}_1(c_1) \tilde{f}_1(c_2). \quad (\text{A2})$$

The right-hand side of Eq. (A2) is a strictly positive quantity [except when $\tilde{f}_1(c) = \delta(c)$], which leads to a contradiction. We therefore conclude that the quantity $\int \psi \tilde{f}_1$ does not exist. Remembering that $\psi(c) \tilde{f}_1(c) \sim c^{\mu+2/(1-\alpha)}$ near the velocity origin, the divergence of $\int \psi \tilde{f}_1$ implies

$$\frac{2}{1-\alpha} + d - 1 + \mu < -1. \quad (\text{A3})$$

Supplementing this condition with the normalization constraint $\mu > -d$, we obtain $\alpha > 1$. The physical meaning of this condition is that the typical kinetic energy dissipated per particle in a collision is larger than the average kinetic energy of the system at the same time. The temperature \bar{v}^2 is therefore a decreasing function of time.

APPENDIX B: SECOND ORDER TRUNCATED SONINE EXPANSION

In this appendix, we calculate the dominant deviation of \tilde{f}_1 from the Gaussian shape, and the associated energy dissipation parameter α by setting $\tilde{f}_1(c) = \mathcal{M}(c) \{1 + a_2 S_2(c^2)\}$. The moments appearing in Eqs. (47) and (46) with $p=2$ are then computed as a function of a_2 . Upon writing

$$\alpha = 1 + \frac{2}{\mu+d} \left(1 - \frac{\langle c_1 \rangle}{\langle c_{12} \rangle} \right) = \frac{\langle c_{12} c_1^2 \rangle}{\langle c_{12} \rangle \langle c_1^2 \rangle}, \quad (\text{B1})$$

the last equality provides an equation for a_2 , which is solved so that α is finally explicitly known as functions of input parameters μ and dimension d . As in the main text, the angular brackets denote averages with weight $\tilde{f}_1(c_1) \tilde{f}_1(c_2)$

$$\langle \dots \rangle = \int (\dots) \tilde{f}_1(c_1) \tilde{f}_1(c_2) d\mathbf{c}_1 d\mathbf{c}_2, \quad (\text{B2})$$

$$\begin{aligned} \langle \dots \rangle &= \int (\dots) \mathcal{M}(c_1) \mathcal{M}(c_2) \{1 + a_2 [S_2(c_1^2) + S_2(c_2^2)]\} \\ &\times d\mathbf{c}_1 d\mathbf{c}_2 + \mathcal{O}(a_2^2). \end{aligned} \quad (\text{B3})$$

In the following, nonlinear terms of order a_2^2 will be neglected. In the spirit of Ref. [25], it is convenient to introduce center-of-mass and relative velocities $\mathbf{c}_1 = \mathbf{C} + \mathbf{c}_{12}/2$; $\mathbf{c}_2 = \mathbf{C} - \mathbf{c}_{12}/2$ and to define the generic moments

$$M_{np} = \langle c_{12}^n C^p \rangle, \quad (\text{B4})$$

$$\begin{aligned} M_{np} &= \int d\mathbf{c}_{12} d\mathbf{C} c_{12}^n C^p \left(\frac{d}{2\pi} \right)^d \\ &\times e^{-dc_{12}^2/4 - dC^2} \left\{ 1 + a_2 \left[\frac{d^2}{8} (c_1^4 + c_2^4) \right. \right. \\ &\left. \left. - \frac{d(d+2)}{4} (c_1^2 + c_2^2) + \frac{d(d+2)}{4} \right] \right\}. \end{aligned} \quad (\text{B5})$$

From $c_1^4 + c_2^4 = 2C^4 + 2(\mathbf{C} \cdot \mathbf{c}_{12})^2 + c_{12}^4/8 + C^2 c_{12}^2$, the term $(\mathbf{C} \cdot \mathbf{c}_{12})^2$ appearing under the integral sign in Eq. (B5) becomes $C^2 c_{12}^2/d$ for symmetry reasons, and making use of $c_1^2 + c_2^2 = 2C^2 + c_{12}^2/2$, the variables \mathbf{c}_{12} and \mathbf{C} decouple in Eq. (B5). The resulting integrals yield

$$\begin{aligned} \frac{M_{np}}{M_{np}^0} &= \frac{\langle c_{12}^n C^p \rangle}{\langle c_{12}^n C^p \rangle_0} = 1 + \frac{a_2}{16d} \{d(n^2 + p^2) - 2d(n+p) \\ &+ 2np(d+2)\} + \mathcal{O}(a_2^2). \end{aligned} \quad (\text{B6})$$

In this equation, the subscript 0 refers to averages with Gaussian measure (formally $a_2 = 0$):

$$\langle c_{12}^n C^p \rangle_0 = (\sqrt{d})^{-n-p} 2^n \frac{\Gamma\left(\frac{d+n}{2}\right) \Gamma\left(\frac{d+p}{2}\right)}{\Gamma^2(d/2)}, \quad (\text{B7})$$

where Γ is the Euler function. The moments $\langle c_{12} \rangle$ and $\langle c_{12} c_1^2 \rangle = \langle c_{12} (c_1^2 + c_2^2) \rangle / 2 = \langle c_{12}^3 \rangle / 4 + \langle c_{12} C^2 \rangle$ appearing in Eq. (B1) are then known:

$$\frac{\langle c_{12} \rangle}{\langle c_{12} \rangle_0} = 1 - \frac{1}{16} a_2 + \mathcal{O}(a_2^2), \quad (\text{B8})$$

$$\frac{\langle c_{12} c_1^2 \rangle}{\langle c_{12} \rangle_0} = 1 + \frac{1}{2d} + \frac{a_2}{32} \left(6 + \frac{11}{d} \right) + \mathcal{O}(a_2^2) \quad (\text{B9})$$

$$\frac{\langle c_{12} c_1^2 \rangle}{\langle c_{12} \rangle \langle c_1^2 \rangle} = 1 + \frac{1}{2d} + \frac{a_2}{8} \left(2 + \frac{3}{d} \right) + \mathcal{O}(a_2^2). \quad (\text{B10})$$

For an elastic hard sphere fluid at equilibrium (with thus $a_2 = 0$), this last quantity equals $1 + 1/(2d)$ and represents the ratio of the mean kinetic energy of colliding particles (averaged over successive collision events) to the mean kinetic energy of the population. As expected, this ratio exceeds 1, since typical colliding partners are ‘‘hotter’’ than the mean background. This quantity is easily measured in molecular dynamics or Monte Carlo simulations (see, e.g., Fig. 8). We also note that the ratio (B8) has been computed in Ref. [14] at the same level of approximation in the context of rapid granular flows, with the same result: van Noije and Ernst also reported non-Gaussian corrections to the cooling rate γ of an inelastic hard sphere fluid [14],

$$\frac{\gamma}{\gamma_0} = 1 + \frac{3}{16} a_2 + \mathcal{O}(a_2^2), \quad \forall d, \quad (\text{B11})$$

where γ_0 denotes the cooling rate evaluated assuming Maxwellian velocity distributions. In terms of the moments M_{np} introduced in Eq. (B4), it can be shown that $\gamma/\gamma_0 = M_{30}/M_{30}^0$, and it is then easily checked that expression (B6) reduces to Eq. (B11) for $n=3$ and $p=0$, for arbitrary dimensionality.

The remaining unknown quantity is $\langle c_1 \rangle$, which may be calculated following similar lines as above:

$$\frac{\langle c_1^n \rangle}{\langle c_1^n \rangle_0} = 1 + \frac{a_2}{8} n(n-2) + \mathcal{O}(a_2^2), \quad (\text{B12})$$

$$\langle c_1^n \rangle_0 = \left(\frac{2}{d}\right)^{n/2} \frac{\Gamma\left(\frac{d+n}{2}\right)}{\Gamma\left(\frac{d}{2}\right)}, \quad (\text{B13})$$

from which we extract $\langle c_1 \rangle = \langle c \rangle$. As expected, the a_2 correction in Eq. (B13) vanishes for $n=0$ and $n=2$, which follows, respectively, from the normalization constraint and the definition (26) of \mathbf{c} implying $\langle c^2 \rangle = 1$. Gathering results, we obtain Eqs. (58) and (59) from Eq. (B1).

-
- [1] Y. Elskens and H.L. Frisch, *Phys. Rev. A* **31**, 3812 (1985).
 [2] J. Piasecki, *Phys. Rev. E* **51**, 5535 (1995).
 [3] M. Droz, P.A. Rey, L. Frachebourg, and J. Piasecki, *Phys. Rev. Lett.* **75**, 160 (1995).
 [4] E. Ben-Naim, S. Redner, and F. Leyvraz, *Phys. Rev. Lett.* **70**, 1890 (1993).
 [5] E. Ben-Naim, P.L. Krapivsky, F. Leyvraz, and S. Redner, *J. Phys. Chem.* **98**, 7284 (1994).
 [6] P.A. Rey, M. Droz, and J. Piasecki, *Phys. Rev. E* **57**, 138 (1998).
 [7] Y. Kafri, *J. Phys. A* **33**, 2365 (1999).
 [8] R.A. Blythe, M.R. Evans, and Y. Kafri, *Phys. Rev. Lett.* **85**, 3750 (2000).
 [9] P.L. Krapivsky and C. Sire, *Phys. Rev. Lett.* **86**, 2494 (2001).
 [10] E. Trizac, *Phys. Rev. Lett.* **88**, 160601 (2002).
 [11] D. Ruelle, *Statistical Mechanics, Rigorous Results* (Benjamin, New York, 1969).
 [12] E. Trizac and J.-P. Hansen, *Phys. Rev. Lett.* **74**, 4114 (1995).
 [13] P. Résibois and M. de Leener, *Classical Kinetic Theory of Fluids* (Wiley, New York, 1977).
 [14] T.P.C. van Noije and M.H. Ernst, *Granular Matter* **1**, 57 (1998).
 [15] A. Barrat, T. Biben, Z. Rácz, E. Trizac, and F. van Wijland, *J. Phys. A* **35**, 463 (2002).
 [16] L. Landau and E. Lifshitz, *Physical Kinetics* (Pergamon Press, New York, 1981).
 [17] J.M. Montanero and A. Santos, *Granular Matter* **2**, 53 (2000).
 [18] N.V. Brilliantov and T. Poschel, *Phys. Rev. E* **61**, 2809 (2000).
 [19] E. Ben-Naim (private communication).
 [20] G. Bird, *Molecular Gas Dynamics* (Oxford University Press, New York, 1976); *Molecular Gas Dynamics and the Direct Simulation of Gas Flows* (Clarendon Press, Oxford, 1994).
 [21] J.M. Montanero, V. Garzó, A. Santos, and J.J. Brey, *J. Fluid Mech.* **389**, 391 (1999).
 [22] A. Frezzotti, *Physica A* **278**, 161 (2000).
 [23] M.P. Allen and D.J. Tildesley, *Computer Simulations of Liquids* (Clarendon Press, Oxford, 1987).
 [24] B. Chopard, A. Masselot, and M. Droz, *Phys. Rev. Lett.* **81**, 1845 (1998).
 [25] I. Pagonabarraga, E. Trizac, T.P.C. van Noije, and M.H. Ernst, *Phys. Rev. E* **65**, 011303 (2002).

Chapitre B

Gaz granulaires : des petites échelles vers les grandes

Randomly driven granular fluids: Large-scale structure

T. P. C. van Noije and M. H. Ernst

Instituut voor Theoretische Fysica, Universiteit Utrecht, Postbus 80006, 3508 TA Utrecht, The Netherlands

E. Trizac* and I. Pagonabarraga

FOM Institute for Atomic and Molecular Physics, Kruislaan 407, 1098 SJ Amsterdam, The Netherlands

(Received 20 October 1998)

The nonequilibrium steady state of a granular fluid, driven by a random external force, is demonstrated to exhibit long-range correlations, which behave as $\sim 1/r$ in three and $\sim \ln(L/r)$ in two dimensions. We calculate the corresponding structure factors over the whole range of wave numbers, and find good agreement with two-dimensional molecular dynamics simulations. It is also shown by means of a mode coupling calculation, how the mean field values for the steady-state temperature and collision frequency, as obtained from the Enskog-Boltzmann equation, are renormalized by long wavelength hydrodynamic fluctuations.

[S1063-651X(99)03804-0]

PACS number(s): 81.05.Rm, 05.20.Dd, 05.40.-a

I. INTRODUCTION

Systems of granular particles, like grains of sand or more ideally glass, plastic, or metal beads, exhibit different flow regimes [1], depending on the external forcing. A systematic experimental study of the rapid or collisional flow regime as compared to the quasistatic, slow, or frictional regime was first performed by Bagnold [2] using an annular shear cell. Later, a similar but more refined characterization was made in Ref. [3]. The possibility of coexistence of different flow regimes was observed in an experimental study of flows down an inclined chute [4].

In several more recent experimental studies of the *rapid granular flow* regime, more microscopic properties have been measured. In Ref. [5] the fluidization behavior of a vertically vibrated two-dimensional model granular material has been investigated using high-speed photography. Patterns at the surface of a vertically vibrated granular layer, analogous to Faraday waves in molecular fluids, have been observed in Ref. [6] and stimulated the interest of many theorists [7]. An understanding of these patterns through a derivation of, e.g., an amplitude equation [8] from the hydrodynamic description of the system, is still lacking, however. In Ref. [9] the effect of inelastic collisions on the formation of clusters is investigated in a system of particles rolling on a smooth surface and driven by a moving wall. Finally, Ref. [10] studies the steady state of a vertically shaken granular monolayer, and discusses clustering, inelastic collapse, and long-range order.

Even rapid flows of *model* granular materials are poorly understood in general, since complicating effects, such as gravity and interactions with boundaries, have to be taken into account. If the model granular material consists of spherical grains with a smooth surface, collisions between particles can be characterized only by their coefficient of

restitution α or their inelasticity $\epsilon = 1 - \alpha^2$. We assume this coefficient of restitution to be a constant, independent of the relative velocity between the colliding particles, and refer to the model as the inelastic hard-sphere (IHS) model. Dissipative collisions complicate the dynamics in a nontrivial way: they may cause the system to become unstable, and give rise, for instance, to clustering; they create several new intrinsic length scales that might interfere for small inelasticity with the system size L , and for large inelasticity with the mean free path l_0 .

By driving an IHS fluid by boundaries or external fields it can reach a steady or oscillatory state. Due to the existence of these new “cooling” lengths, this state is frequently inhomogeneous, where the spatial gradients become larger at higher inelasticity. Only for small inelasticity, the mean-free path is well separated from the scale on which the macroscopic fields vary, and a hydrodynamic description [11] through Navier-Stokes or Burnett equations is expected to hold. In fact, one of the primary goals in the study of rapid granular flows at *larger* inelasticities is to find the proper reduced set of macroscopic fields and the correct form of the relevant macroscopic continuum equations. The conceptual basis for the validity of the Navier-Stokes and Burnett equations of fluid dynamics in rapid granular flows breaks down due to the lack of scale separation. Therefore, we restrict ourselves mostly to small inelasticities, and explore the region of validity of the standard fluid dynamic description.

In the present paper we investigate the properties of an IHS fluid that is heated uniformly so that it reaches a spatially homogeneous steady state. This way of forcing, where a random external force accelerates a particle, was proposed by Williams and MacKintosh [12] for inelastic particles moving on a line. Peng and Ohta [13] performed simulations on a 2D version of this model. In two dimensions the model may be considered to describe the dynamics of light disks moving on an air table, a system that has been investigated experimentally in Ref. [14]. In three dimensions it can be extended to include gravitational and drag forces, making it to some extent relevant for gas-fluidized beds [15] when hydrodynamic interactions are unimportant. A similar IHS

*Present address: Laboratoire de Physique Théorique et Hautes Energies, Bâtiment 211, Université Paris-Sud, 91405 Orsay Cedex, France.

model with random external accelerations has been used by Bizon and Swinney [16] in their computer simulations to test continuum theories for vertically vibrated layers of granular material.

In the present paper we will describe the randomly driven IHS fluid in two and three dimensions, and characterize its nonequilibrium steady state (NESS). The single-particle velocity distribution function in the NESS has been calculated in Ref. [17] from the Enskog-Boltzmann equation and was shown to be well approximated by a Maxwellian, except for an overpopulated tail $\sim \exp(-Ac^{3/2})$, where c is the velocity scaled by the thermal velocity and $A \sim 1/\sqrt{\epsilon}$. Computer simulations of the one-dimensional system of Ref. [12] showed the existence of long-range spatial correlations in the steady state, which were addressed theoretically in Ref. [18]. Here we will give quantitative predictions for long-range correlations [19] in the two- and three-dimensional NESS. Moreover, we extend the mode coupling theory of Brito and Ernst [20] to analyze how long wavelength fluctuations in the NESS renormalize the mean-field predictions of kinetic theory, and use this theory to calculate the renormalized temperature and collision frequency in the NESS.

To obtain an adequate description of the structures in steady granular flows, one does not only need the equations of fluid dynamics for the average macroscopic behavior, but also the spatial correlation functions $G_{ab}(\mathbf{r})$, and their Fourier transforms, the structure factors $S_{ab}(\mathbf{k})$. Let $\delta a(\mathbf{r}, t) = a(\mathbf{r}, t) - \langle a(\mathbf{r}, t) \rangle$ with $(a = n, T, u_\alpha)$ be the fluctuations of the slowly varying fields $a(\mathbf{r}, t)$, i.e., the local density $n(\mathbf{r}, t)$, local temperature $T(\mathbf{r}, t)$, and local flow velocity $u_\alpha(\mathbf{r}, t)$ ($\alpha = x, y, \dots$), around their average values $\langle a(\mathbf{r}, t) \rangle$. Then the objects of interest are the correlation functions in the NESS, which are given by the limit,

$$G_{ab}(\mathbf{r}) = \lim_{t \rightarrow \infty} \frac{1}{V} \int d\mathbf{r}' \langle \delta a(\mathbf{r} + \mathbf{r}', t) \delta b(\mathbf{r}', t) \rangle, \quad (1)$$

$$S_{ab}(\mathbf{k}) = \lim_{t \rightarrow \infty} V^{-1} \langle \delta a(\mathbf{k}, t) \delta b(-\mathbf{k}, t) \rangle.$$

Here $\langle \dots \rangle$ is an average over some initial distribution, $\delta a(\mathbf{k}, t)$ is the spatial Fourier transform of $\delta a(\mathbf{r}, t)$, and $S_{ab}(\mathbf{k})$ is that of $G_{ab}(\mathbf{r})$. Moreover, we consider the unequal-time correlation functions in the NESS, defined as

$$F_{ab}(\mathbf{k}, t) = \lim_{t' \rightarrow \infty} V^{-1} \langle \delta a(\mathbf{k}, t' + t) \delta b(-\mathbf{k}, t') \rangle, \quad (2)$$

where $F_{nn}(\mathbf{k}, t)$ is the *intermediate scattering function* [21]. The *dynamic structure factor* is then

$$S_{nn}(\mathbf{k}, \Omega) = \text{Re} \tilde{F}_{nn}(\mathbf{k}, z = i\Omega + 0), \quad (3)$$

where $\tilde{F}_{ab}(\mathbf{k}, z)$ is the Laplace transform of $F_{ab}(\mathbf{k}, t)$.

The paper is organized as follows. In Sec. II we show how the macroscopic equations for granular flow are modified to account for the external driving/heating by the random accelerations. Section III characterizes the noise of external and internal fluctuations, and the structure factors and spatial correlation functions are calculated in Secs. IV and V. The latter section also presents the mode coupling calculations for the temperature and the collision frequency in the

NESS. Computational details of our molecular dynamics (MD) simulations are described in Sec. VI, and Sec. VII compares our predictions with simulations. Some general comments and conclusions are presented in Sec. VIII.

II. MACROSCOPIC EQUATIONS

Consider a system of inelastic disks or spheres (IHS) ($d = 2, 3$), driven by a heat source, which is described as a random acceleration $\hat{\xi}_i$,

$$\frac{d\mathbf{v}_i}{dt} = \frac{\mathbf{F}_i}{m} + \hat{\xi}_i(t). \quad (4)$$

Here \mathbf{F}_i is the systematic force on particle $i = (1, 2, \dots, N)$ due to inelastic collisions. If the time constant of the heat source is much smaller than the mean free time t_0 between collisions, then $\hat{\xi}_i(t)$ can be considered as Gaussian white noise with zero mean and correlation,

$$\overline{\hat{\xi}_{i\alpha}(t) \hat{\xi}_{j\beta}(t')} = \xi_0^2 \delta_{ij} \delta_{\alpha\beta} \delta(t - t'), \quad (5)$$

where $\alpha, \beta = \{x, y, \dots\}$ denote Cartesian components of vectors or tensors. The overline indicates an average over the noise source. It is understood that the ensemble average in Eqs. (1) and (2), denoted by the angular brackets, also includes this noise average. To guarantee conservation of total momentum, the random force has to obey the constraint $\sum_i \hat{\xi}_i(t) = \mathbf{0}$. In thermodynamically large systems this constraint gives a correction to Eq. (5) of $\mathcal{O}(1/N)$, which can be neglected.

The uniformly heated fluid is described by the standard macroscopic equations of fluid dynamics, where the temperature equation is supplemented with an additional source term $m\xi_0^2$, and a sink term Γ to account, respectively, for the heating and the energy loss through inelastic collisions:

$$\partial_t n + \nabla \cdot (n\mathbf{u}) = 0,$$

$$\partial_t \mathbf{u} + \mathbf{u} \cdot \nabla \mathbf{u} = -\frac{1}{\rho} \nabla \cdot \mathbf{\Pi}, \quad (6)$$

$$\partial_t T + \mathbf{u} \cdot \nabla T = -\frac{2}{dn} (\nabla \cdot \mathbf{J} + \mathbf{\Pi} : \nabla \mathbf{u}) - \Gamma + m\xi_0^2,$$

where $\rho = mn$, \mathbf{u} is the flow velocity, and $\frac{1}{2} dnT$ is the kinetic-energy density in the local rest frame of the IHS fluid. The pressure tensor $\mathbf{\Pi}_{\alpha\beta} = p\delta_{\alpha\beta} + \delta\mathbf{\Pi}_{\alpha\beta}$ contains the local pressure p and the dissipative momentum flux $\delta\mathbf{\Pi}_{\alpha\beta}$, which is proportional to $\nabla_\alpha u_\beta$ and contains the kinematic and longitudinal viscosities ν and ν_l , defined below Eq. (A1) of Appendix A. The constitutive relation for the heat flux, $\mathbf{J} = -\kappa \nabla T$, defines the heat conductivity κ . For *small* inelasticity the transport coefficients ν , ν_l , and κ are assumed to be given by the Enskog theory for a dense gas of elastic hard spheres (EHS) [22].

To lowest order in the spatial inhomogeneities, the sink term, representing the energy loss through inelastic collisions, is given by [23]

$$\Gamma = 2\gamma_0 \omega T. \quad (7)$$

It is proportional to the granular temperature, to the average Enskog collision frequency [$\omega \sim \sqrt{T}$, explicitly given in Eq. (A2) of Appendix A], and to the coefficient of inelasticity $\epsilon = 1 - \alpha^2 \equiv 2d\gamma_0$, where α is the coefficient of normal restitution. To explain the term $m\xi_0^2$ in Eqs. (6), we calculate the energy gain of a single particle due to the random force in a small time δt . This is done by formally integrating Eq. (4) and averaging over the noise source, i.e.,

$$\frac{1}{2}m[\overline{v_i^2(t+\delta t)} - \overline{v_i^2(t)}] = \frac{d}{2}m\xi_0^2 \delta t, \quad (8)$$

where Eq. (5) has been used. Note that we have defined the granular temperature as twice the average random kinetic energy per translational degree of freedom, so that the Boltzmann constant k_B does not appear in its definition.

The above equations provide a consistent description for the heated IHS fluid at small inelasticity. The energy is not conserved in inelastic collisions, and consequently, the temperature is *not* a hydrodynamic mode, but a kinetic mode with a relaxation rate $\propto \gamma_0\omega$. Nevertheless, at small inelasticities ($\gamma_0 \ll 1$), it is consistent to include temperature among the slowly changing macroscopic variables, which describe the dynamics of the system on time scales t large compared to the mean free time $t_0 = 1/\omega$, and on spatial scales λ large compared to the mean free path, $l_0 = v_0 t_0$, where $v_0 = \sqrt{2T/m}$ is the thermal velocity.

At large inelasticities, where $\epsilon \sim \mathcal{O}(1)$, we expect that the temperature is a *fast* kinetic mode, that decays on the time scale t_0 , and cannot be included among the slow macroscopic variables. In that case, the IHS fluid becomes *athermal*, and the slow macroscopic fields only involve the density and flow field, as is the case in lattice gas cellular automata without energy conservation [24,25]. However, the proper constitutive relations for the IHS fluid at large inelasticities are not known.

Let us consider the decay of temperature in more detail. For a homogeneous state, the fluid dynamic equations (6) will have as a solution $n(\mathbf{r},t) = n$, $\mathbf{u}(\mathbf{r},t) = \mathbf{0}$, and $T(\mathbf{r},t) = T(t)$, the latter satisfying

$$\partial_t T(t) = -\Gamma + m\xi_0^2. \quad (9)$$

For long times the system approaches a steady state with a constant temperature, determined by $m\xi_0^2 = 2\gamma_0\omega T$. As $\omega \sim \sqrt{T}$, we obtain the mean-field prediction [Eq. (A2)], as deduced from the Enskog theory,

$$T_E \equiv m \left(\frac{\xi_0^2 \sqrt{\pi}}{2\gamma_0 \Omega_d \chi n \sigma^{d-1}} \right)^{2/3}. \quad (10)$$

Further symbols are defined below [Eqs. (A1)] in the Appendix. To obtain the final approach to the NESS, we linearize Eq. (9) around T_E in Eq. (10). This yields an exponential approach, i.e.,

$$\delta T(t) \equiv T(t) - T_E = \delta T(0) \exp[-3\gamma_0\omega t]. \quad (11)$$

In fact, $3\gamma_0\omega$ can be identified as the decay rate $z_H(0)$ of the long wavelength components of the temperature fluctuations, as derived in Sec. IV below Eqs. (25). The exact time depen-

dent solution of Eq. (9) can be obtained implicitly (t as a function of temperature), and reads

$$f\left(\sqrt{\frac{T(t)}{T_E}}\right) - f\left(\sqrt{\frac{T_0}{T_E}}\right) = -\frac{3}{2} \frac{m\xi_0^2}{T_E} t, \quad (12)$$

where

$$f(x) = \ln|x-1| - \frac{1}{2} \ln(x^2+x+1) + \sqrt{3} \arctan\left(\frac{2x+1}{\sqrt{3}}\right). \quad (13)$$

and T_0 is the temperature at $t=0$.

III. NOISE CHARACTERISTICS IN THE NESS

The goal of this paper is to analyze the effects of spatial fluctuations $\delta a(\mathbf{r},t)$ with ($a = n, T, u_\alpha$) around the NESS on hydrodynamic space and time scales. As we are dealing with fluctuations, we linearize the nonlinear equations (6) around the NESS, with the result (A1) of Appendix A. Moreover, to extend the average equations to fluctuating equations, valid on mesoscopic spatial and temporal scales, we need to calculate the *external noise* terms $\hat{\xi}^{\text{ex}}(\mathbf{r},t)$ and $\hat{\theta}^{\text{ex}}(\mathbf{r},t)$ that contribute to $\partial_t \mathbf{u}$ and $\partial_t T$ in Eqs. (A1). These terms originate from the random acceleration $\hat{\xi}_i(t)$, which enters in the microscopic equations of motion (4). By starting from the microscopic expressions for the momentum and energy density, one finds that the noise sources are given by the *long* wavelength components of

$$\hat{\xi}^{\text{ex}}(\mathbf{r},t) = \frac{1}{n} \sum_i \hat{\xi}_i(t) \delta(\mathbf{r} - \mathbf{r}_i(t)), \quad (14)$$

$$\hat{\theta}^{\text{ex}}(\mathbf{r},t) = \frac{2m}{dn} \sum_i \mathbf{v}_i(t) \cdot \hat{\xi}_i(t) \delta(\mathbf{r} - \mathbf{r}_i(t)).$$

These fields are again Gaussian white noise with zero mean and correlations

$$\overline{\hat{\xi}_\alpha^{\text{ex}}(\mathbf{r},t) \hat{\xi}_\beta^{\text{ex}}(\mathbf{r}',t')} = \frac{1}{n} \xi_0^2 \delta_{\alpha\beta} \delta(\mathbf{r} - \mathbf{r}') \delta(t - t'), \quad (15)$$

$$\overline{\hat{\theta}^{\text{ex}}(\mathbf{r},t) \hat{\theta}^{\text{ex}}(\mathbf{r}',t')} = \frac{4mT}{dn} \xi_0^2 \delta(\mathbf{r} - \mathbf{r}') \delta(t - t'),$$

as follows from Eq. (5).

Next, we argue on the basis of the hydrodynamic equations (6) that there exists, close to the NESS, a range of hydrodynamic wave numbers $k \gg k^*$, the so-called *elastic regime*, where the dynamics of the fluctuations is the same as in a fluid of elastic hard spheres or disks, and is driven by *internal noise* that will be studied next. The validity of the hydrodynamic equations (6) and Eqs. (A1) is restricted to wave numbers $k \ll 2\pi/l_0$ (to guarantee *separation* of kinetic and hydrodynamic scales), and to $k \ll 2\pi/\sigma$, where σ is the disk or sphere diameter (to guarantee that the Euler equations involve strictly *local* hydrodynamics). So, for the existence of an elastic regime in the IHS hydrodynamics, the following constraints must be satisfied:

$$k^* \ll k \ll \min\left\{\frac{2\pi}{l_0}, \frac{2\pi}{\sigma}\right\}. \quad (16)$$

Moreover, following McNamara [26] we can distinguish a *dissipative regime*, $kl_0 \ll \epsilon$ [typically $kl_0 \ll \mathcal{O}(\epsilon^2)$], and a *standard regime*, $kl_0 \gg \epsilon$ [typically, $kl_0 \gg \mathcal{O}(\sqrt{\epsilon})$], separated by a *crossover regime*, around $kl_0 \sim \mathcal{O}(\epsilon)$. In the dissipative regime, dissipation dominates compression effects and sound propagation, which are $\mathcal{O}(kl_0)$, as well as heat conduction, which is $\mathcal{O}(k^2 l_0^2)$. In the standard regime, dissipation effects are of the same order as heat conduction. As a consequence, the hydrodynamic modes and their propagation velocities are those of a fluid of *elastic* particles, while the corresponding damping rates of heat and sound modes still depend on the inelasticity. Only in the *elastic regime*, $kl_0 \gg k^* l_0 \sim \mathcal{O}(\sqrt{\epsilon})$; also, these damping coefficients attain their elastic values. The above argument applies for small enough $\epsilon = 1 - \alpha^2 = 2d\gamma_0$, where the inequalities (16) are obeyed, and an elastic regime exists and is well separated from the dissipative regime.

In the *elastic regime* the equations for the macroscopic deviations from the NESS are the same as those for a fluid of *elastic* hard spheres, deviating from *thermal* equilibrium. To describe fluctuating mesoscopic hydrodynamics on these length scales, one can add *internal* noise $\hat{\xi}^{\text{in}}(\mathbf{r}, t)$ and $\hat{\theta}^{\text{in}}(\mathbf{r}, t)$, describing the rapid microscopic degrees of freedom. The noise strength of the internal fluctuations can be obtained from the fluctuation-dissipation theorem [27,23] for the EHS fluid, and is given in Fourier representation by

$$\begin{aligned} V^{-1} \overline{\hat{\xi}_\alpha^{\text{in}}(\mathbf{k}, t) \hat{\xi}_\beta^{\text{in}}(-\mathbf{k}, t')} \\ = \frac{2T}{\rho} k^2 [v(\delta_{\alpha\beta} - \hat{k}_\alpha \hat{k}_\beta) + v_l \hat{k}_\alpha \hat{k}_\beta] \delta(t-t'), \\ V^{-1} \overline{\hat{\theta}^{\text{in}}(\mathbf{k}, t) \hat{\theta}^{\text{in}}(-\mathbf{k}, t')} = \frac{8\kappa T^2}{d^2 n^2} k^2 \delta(t-t'), \end{aligned} \quad (17)$$

where ν , ν_l , and κ are the transport coefficients for the EHS fluid, and \hat{k}_α is a component of the unit vector $\hat{\mathbf{k}} = \mathbf{k}/k$. The *effective* noise in the heated IHS fluid may, therefore, be described by the sum of external and internal noise, $\hat{\xi}(\mathbf{k}, t) = \hat{\xi}^{\text{ex}}(\mathbf{k}, t) + \hat{\xi}^{\text{in}}(\mathbf{k}, t)$, with a similar expression for $\hat{\theta}(\mathbf{k}, t)$. The noise characteristics of $\hat{\xi}(\mathbf{k}, t)$ and $\hat{\theta}(\mathbf{k}, t)$ *interpolate* between two limiting behaviors and the corresponding noise strengths are given by the sum of Eqs. (15) and (17).

Having specified the characteristics of the noise sources in the macroscopic equations, we conclude this section by summarizing the Langevin-type equations that describe the dynamics of the slow fluctuations. To do so, it is convenient to introduce the Fourier modes $\delta \mathbf{a}(\mathbf{k}, t) \exp[i\mathbf{k} \cdot \mathbf{r}]$ of the linearized hydrodynamic equations (A1). The mesoscopic equations, valid on hydrodynamic space and time scales, i.e., $t \gg t_0$ and $kl_0 \ll 1$, then take the form

$$\partial_t \delta \mathbf{a}(\mathbf{k}, t) = \mathbf{M}(\mathbf{k}) \delta \mathbf{a}(\mathbf{k}, t) + \hat{\mathbf{f}}(\mathbf{k}, t), \quad (18)$$

where the components of the vector \mathbf{a} are labeled with $a = \{n, T, l, \perp\}$. Here $a = l$ refers to the longitudinal velocity

component $u_l(\mathbf{k}, t) = \hat{\mathbf{k}} \cdot \mathbf{u}(\mathbf{k}, t)$, and $a = \perp$ refers to $(d-1)$ transverse components of $\mathbf{u}(\mathbf{k}, t)$. The matrix M_{ab} with $a, b = \{n, T, l, \perp\}$ is given explicitly in Eq. (A3), and $\hat{f}_a(\mathbf{k}, t)$ is Gaussian white noise with *nonvanishing* components for $a = T, l, \perp$ and correlation function

$$V^{-1} \overline{\hat{f}_a(\mathbf{k}, t) \hat{f}_b(-\mathbf{k}, t')} = C_{ab}(k) \delta(t-t'). \quad (19)$$

The noise strength $C_{ab}(k) = \delta_{ab} C_{ab}(k)$ is obtained by taking the Fourier transform of Eqs. (15) together with Eqs. (17), and is only nonvanishing for the following diagonal elements:

$$\begin{aligned} C_{TT}(k) &= \frac{4mT\xi_0^2}{dn} + \frac{8\kappa T^2 k^2}{d^2 n^2} = \frac{4T\Gamma}{dn} + \frac{8\kappa T^2 k^2}{d^2 n^2}, \\ C_{ll}(k) &= \frac{\xi_0^2}{n} + \frac{2\nu_l T k^2}{\rho} = \frac{\Gamma}{\rho} + \frac{2\nu_l T k^2}{\rho}, \\ C_{\perp\perp}(k) &= \frac{\xi_0^2}{n} + \frac{2\nu T k^2}{\rho} = \frac{\Gamma}{\rho} + \frac{2\nu T k^2}{\rho}, \end{aligned} \quad (20)$$

where the NESS condition of Eq. (9), i.e., $\Gamma = 2\gamma_0 \omega T = m\xi_0^2$, has been used.

IV. STRUCTURE FACTORS

The equal-time structure factors, introduced in Eqs. (1), obey the equations of motion,

$$\partial_t S_{ab}(\mathbf{k}) = \sum_c \{M_{ac}(\mathbf{k}) S_{cb}(\mathbf{k}) + M_{bc}(-\mathbf{k}) S_{ac}(\mathbf{k})\} + C_{ab}(k), \quad (21)$$

which follows by formally integrating Eq. (18) and using Eq. (19). The left-hand side of Eq. (21) vanishes since the structure factors do not depend on time in the NESS. The resulting equation can be solved by spectral analysis, or numerically. The spectral analysis is summarized in Appendix A, where $w_{\lambda a}$ and $v_{\lambda a}$ are, respectively, the a th component of the right and left eigenvectors of the hydrodynamic matrix \mathbf{M} , and $z_\lambda(k)$ is the corresponding eigenvalue.

Taking then the scalar product of Eq. (21) on both sides with left eigenvectors (A5) of the Appendix, yields

$$\begin{aligned} \sum_{ab} \langle v_{\lambda a}(\mathbf{k}) | S_{ab}(\mathbf{k}) | v_{\mu b}(-\mathbf{k}) \rangle \\ = - \sum_{ab} \frac{\langle v_{\lambda a}(\mathbf{k}) | C_{ab}(k) | v_{\mu b}(-\mathbf{k}) \rangle}{z_\lambda(k) + z_\mu(k)}. \end{aligned} \quad (22)$$

Using the completeness relation (A6) and the fact that off diagonal elements of C_{ab} in Eqs. (20) vanish, we obtain

$$S_{ab}(\mathbf{k}) = - \sum_{\lambda\mu c} \frac{w_{\lambda a}(\mathbf{k}) v_{\lambda c}(\mathbf{k}) C_{cc}(k) v_{\mu c}(-\mathbf{k}) w_{\mu b}(-\mathbf{k})}{z_\lambda(k) + z_\mu(k)}, \quad (23)$$

which is the final result for the static structure factors. The time correlation function (2) in the NESS reduces in a similar manner to

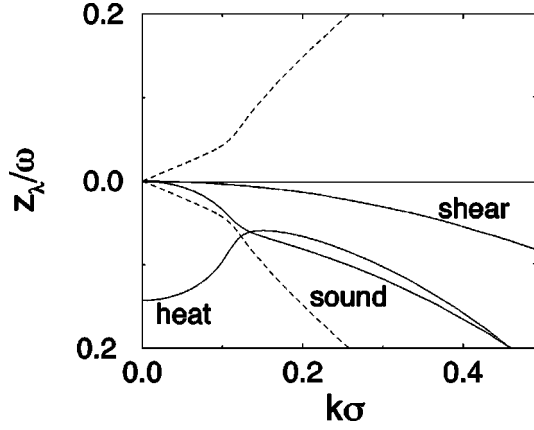


FIG. 1. Dispersion relations $z_\lambda(k)/\omega$ versus $k\sigma$ for $\phi=0.4$, $\alpha=0.9$; the solid lines refer to the real parts for $\lambda=\perp, \pm$, and H , respectively. Dashed lines represent the imaginary parts of the sound-mode relaxation rates ($\lambda=\pm$). Here, $l_0/\sigma \approx 0.34$, $\gamma_0\sigma/l_0 \approx 0.14$, and $\sqrt{\gamma_0\sigma/l_0} \approx 0.64$.

$$F_{ab}(\mathbf{k}, t) = \sum_{\lambda c} \exp[z_\lambda(\mathbf{k})t] w_{\lambda a}(\mathbf{k}) v_{\lambda c}(\mathbf{k}) S_{cb}(\mathbf{k}). \quad (24)$$

The above result corresponds to the Landau-Placzek theory [21] for hydrodynamic correlations in the NESS.

To obtain more explicit results we need the explicit forms of eigenvalues and eigenvectors, which have only been calculated for small k . The eigenvalue equation can be solved numerically for any given wave number, and the results are illustrated in Fig. 1 for the two-dimensional case. Transport coefficients, equation of state $p(n, T)$, and pair-correlation function at contact are obtained from Enskog's theory for *elastic* hard spheres or disks. The generic features of the spectrum in Fig. 1 are the same as McNamara's case " $\alpha = \beta = 0$," illustrated in Fig. 6(a) of his study [26] on hydrodynamics of granular materials, which corresponds to a temperature- and density-independent heat source. However, neither the equation of state, nor the transport coefficients, used in Ref. [26], correspond to the heated fluid of inelastic hard spheres, used in the present simulations. In the hydrodynamic regime ($kl_0 \leq 1$), all eigenvalues are found to be *negative* for nonvanishing wave numbers (see Appendix A). So, all modes are linearly *stable*.

With the help of MATHEMATICA, the structure factors in the steady state have been calculated numerically from Eq. (21) with $\partial_t S_{ab}(\mathbf{k}) = 0$ for a given wave number. The resulting structure factors are shown by solid lines in Fig. 2, and will be tested against MD simulations in Sec. VII.

Next, we present analytic results for the dissipative regime ($kl_0 \ll \gamma_0$). The eigenvalues on the largest spatial scales can be determined as an expansion in powers of k at a fixed value of γ_0 , with the results

$$\begin{aligned} z_\perp(k) &= -\nu k^2, \\ z_\pm(k) &= \mp ikv_D - D_S k^2, \\ z_H(k) &= -3\gamma_0\omega + D_H k^2. \end{aligned} \quad (25)$$

In later applications, the explicit form of the eigenvectors of $\mathbf{M}(\mathbf{k})$ is needed to lowest order in \mathbf{k} . They read

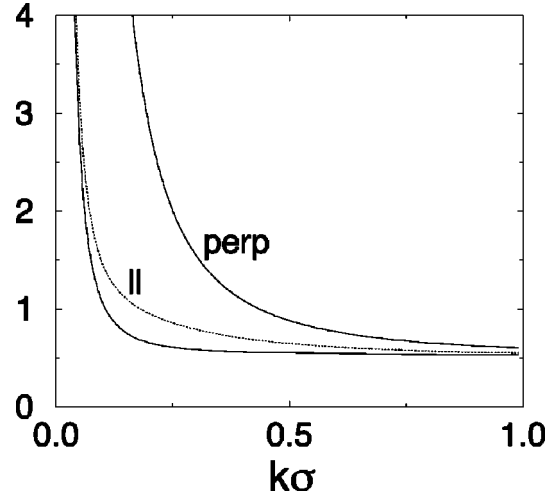


FIG. 2. Structure factors, $S_\perp(k)$ and $S_\parallel(k)$ in units $T_0\sigma^2/m$, as obtained from the full theory (solid lines) with external *and* internal noise. The dotted line represents $S_\parallel^{\text{without}}(k)$ without internal noise with the plateau value added (see discussion at the end of Sec. VII). The parameters are $\alpha=0.92$, $\phi=0.63$, and $T_E=0.41T_0$. Figure 6 shows that the S_\parallel simulation data agree much better with the solid line than with the dotted line.

$$\mathbf{w}_\perp(\mathbf{k}) = (0, 0, 0, 1), \quad \mathbf{v}_\perp(\mathbf{k}) = (0, 0, 0, 1),$$

$$\mathbf{w}_\pm(\mathbf{k}) = \frac{1}{\sqrt{2}} [1, -g(n)T/3n, \pm v_D/n, 0], \quad (26)$$

$$\mathbf{v}_\pm(\mathbf{k}) = \frac{1}{\sqrt{2}} (1, 0, \pm n/v_D, 0),$$

$$\mathbf{w}_H(\mathbf{k}) = (0, 1, 0, 0), \quad \mathbf{v}_H(\mathbf{k}) = (g(n)T/3n, 1, 0, 0).$$

The coefficients $g(n)$, v_D , and D_λ with $\lambda = \{\perp, H, \pm\}$ are calculated in the Appendix. In the dissipative regime there are two propagating sound modes ($\lambda = \pm$) with a propagation speed v_D and a damping constant D_S . There is a *kinetic* heat mode ($\lambda = H$), with a long wavelength relaxation rate $z_H(0) = -3\gamma_0\omega$, in agreement with Eq. (11). Therefore, on the largest spatial scales, the temperature deviations have decayed to zero, and temperature gradients do not exist; there is no heat conduction. In addition, there are $(d-1)$ transverse velocity or shear modes ($\lambda = \perp$), which are purely diffusive. The corresponding diffusivity, $D_\perp = \nu$, has the same form as for EHS. In Eqs. (A7)–(A10), the coefficients are expressed explicitly in terms of thermodynamic quantities and transport coefficients.

In the standard regime, $kl_0 \gg \gamma_0$ (and γ_0 small), the eigenvalues for shear and sound modes are to leading nonvanishing order the same as for the EHS fluid, where the sound waves propagate with the *adiabatic* sound speed v_S of the elastic fluid, which is larger than the propagation speed v_D in Eq. (A7). The damping of the sound and heat modes, on the other hand, are larger than in the elastic fluid due to the inelastic collisions. In the elastic regime, defined in Sec. III, where $kl_0 \gg \sqrt{\gamma_0}$, all transport coefficients are equal to their EHS values.

In summary, the eigenvalue spectrum $z_\lambda(k)$ for the uniformly heated IHS fluid is quite different from that of the freely evolving IHS fluid, linearized around the homogeneous cooling state [26]. In the *free* case, all shear modes ($\lambda = \perp$) and the heat mode ($\lambda = H$) are unstable in the dissipative regime (small k), and propagating modes do not exist for $kl_0 \ll \gamma_0$. Moreover, there exist in this regime a stable diffusive density mode and a kinetic temperature mode, which combine into two propagating modes for $kl_0 \sim \mathcal{O}(\gamma_0)$, where crossover occurs from the dissipative to the standard regime. In the *heated* case, however, all modes are linearly stable, and the sound modes remain propagating in the dissipative regime down to $k=0$.

V. EFFECTS OF LONG-RANGE CORRELATIONS

In this section we study static and dynamic structure factors and corresponding correlation functions at the largest spatial scales. Moreover, we show by means of a mode coupling calculation, how average properties, which were calculated in Sec. II on the basis of a mean-field theory (i.e., the Enskog-Boltzmann equation), are renormalized by spatial fluctuations.

The static structure factors have been calculated in Eq. (23). In the *dissipative regime* ($kl_0 \lesssim \gamma_0$), the relevant eigenvalues (25) and eigenmodes (26) are discussed below [Eq. (26)]. The dominant singularity at small wave number of the structure factors $S_{ab}(k) \sim \mathcal{O}(1/k^2)$ in Eq. (23) originates from pairs of transverse modes, where $2z_\perp(k) = -2\nu k^2$, and from antiparallel sound modes, where $z_+(k) + z_-(k) = -2D_S k^2$. We start with the transverse structure factor, where only the shear modes in Eqs. (26) contribute, and deduce from the equations above,

$$S_\perp(k) \equiv S_{\perp\perp}(k) \approx \frac{\Gamma}{2\rho\nu k^2}, \quad (27)$$

where the relation (20) has been used for $kl_0 \ll \gamma_0$. The structure factors $S_{ab}(k)$ for $a, b \neq \perp$ derive their dominant small- k behavior from two antiparallel sound modes and we obtain with the help of Eqs. (23), (25), (26), and (20) at small k ,

$$S_\parallel(k) \equiv S_{\parallel\parallel}(k) \approx \frac{\Gamma}{4\rho D_S k^2}, \quad (28)$$

where the sound damping constant in the dissipative regime D_S has been calculated in Eq. (A9). It depends on the inelasticity. The contribution of the internal noise is subdominant in this regime. In a similar manner, we find

$$S_{ab}(k) \approx B_{ab} S_{\parallel\parallel}(k) \quad (k \rightarrow 0), \quad (29)$$

where all nonvanishing coefficients labeled (ab) = (ll, nn, TT, nT) are listed in Table I. The remaining structure factors are of $\mathcal{O}(1)$ as $k \rightarrow 0$.

Next, we consider the spatial correlation functions $G_{ab}(r)$, which are the inverse Fourier transforms of $S_{ab}(k)$. The small- k behavior of $S_{ab}(k)$, obtained above, enables us to calculate the large- r behavior of the spatial correlation

TABLE I. Coefficients B_{ab} in Eq. (29).

ab	B_{ab}
ll	1
nn	n^2/v_D^2
TT	$g^2(n)T^2/9v_D^2$
nT	$-g(n)nT/3v_D^2$

functions. The calculations are given in Appendix B. One finds for the leading large- r behavior in *three-dimensional* systems,

$$G_\parallel(r) \approx \left(\frac{\Gamma}{8\pi\rho\nu} \right) \frac{1}{r}, \quad (30)$$

$$G_\perp(r) \approx \frac{\Gamma}{16\pi\rho} \left(\frac{1}{\nu} + \frac{1}{2D_S} \right) \frac{1}{r},$$

and in *two-dimensional* systems,

$$G_\parallel(r) \approx G_\perp(r) \approx \frac{\Gamma}{8\pi\rho} \left(\frac{1}{\nu} + \frac{1}{2D_S} \right) \ln\left(\frac{L}{r}\right), \quad (31)$$

valid for $r \ll L$, where L is the linear dimension of the system. The subleading large- r corrections to Eq. (31) are constant terms, independent of r . In the calculations given in Appendix B, these constants depend on a cutoff wave vector $k_{\min} = 2\pi/L$, used to evaluate the divergent \mathbf{k} integrals occurring in the Fourier inversion of $S_{ab}(k)$. To calculate their precise values, the subleading small- k corrections to Eqs. (27) and (28) are required.

The long wavelength behavior of the time-dependent correlation function $F_{ab}(k, t)$ in Eq. (24) can be evaluated in a similar manner. We quote the result in terms of the Laplace transform $\tilde{F}_{ab}(k, z)$, from which the dynamic structure factor (3) follows. In the *dissipative regime* ($kl_0 \ll \gamma_0$), we find to leading order for small wave numbers,

$$\tilde{F}_{\perp\perp}(k, z) \approx \frac{S_{\perp\perp}(k)}{z + \nu k^2}, \quad (32)$$

$$\tilde{F}_{\parallel\parallel}(k, z) \approx \frac{1}{2} \sum_{\lambda=\pm} \frac{S_{\parallel\parallel}(k)}{z + i\lambda k v_D + D_S k^2}.$$

In a similar manner we obtain

$$\tilde{F}_{ab}(k, z) \approx B_{ab} \tilde{F}_{\parallel\parallel}(k, z), \quad (33)$$

where all nonvanishing coefficients B_{ab} are listed in Table I. The dynamic structure factor (3) then becomes

$$S_{nn}(k, \Omega) \approx \frac{1}{2} \sum_{\lambda=\pm} \frac{D_S k^2 S_{nn}(k)}{(\Omega + \lambda k v_D)^2 + D_S^2 k^4}. \quad (34)$$

It contains only Brillouin peaks, coming from the sound modes. There is no central Rayleigh peak, because the heat mode is not a slow, but a fast kinetic mode in this regime. In the elastic regime, $S_{nn}(k, \Omega)$ has the standard Rayleigh and Brillouin lines of the EHS fluid.

The existence of long-range spatial correlations shows that the NESS is quite different from a thermal equilibrium state [19]. In fact, the spatial fluctuations also modify (renormalize) the mean-field predictions for the averages and the particle distribution functions. In Appendix C a mode coupling calculation is presented to estimate the renormalization effects on the average energy per particle $E = (1/N)\sum_i \langle \frac{1}{2} m v_i^2 \rangle$ and average collision frequency ω in the NESS, and we recall their mean-field values, i.e., $E_E = \frac{1}{2} d T_E$ and ω_E given by Eq. (A2), i.e., $\omega_E \propto n \chi(n) \sqrt{T_E}$, where T_E is given in Eq. (10).

As it turns out, the fluctuation contributions, δE and $\delta \omega$, are finite and well-behaved in *three* dimensions, but logarithmically divergent in the system size L in *two* dimensions, so that $d=2$ is the upper critical dimension. The mode coupling calculations of Appendix C yield then in two dimensions, for large L ,

$$\begin{aligned} T_{\text{NESS}} &\approx T_E + \frac{C_E}{4\pi} \ln\left(\frac{\gamma_0 L}{l_0}\right), \\ \omega_{\text{NESS}} &\approx \omega_E + \frac{C_\omega}{4\pi} \ln\left(\frac{\gamma_0 L}{l_0}\right), \end{aligned} \quad (35)$$

where C_E and C_ω are calculated in Appendix C. The argument of the logarithm $\gamma_0 L/l_0$ is an estimate for the ratio of the values for the right ($k \sim \gamma_0/l_0$) and left ($k_{\min} = 2\pi/L$) boundaries of the dissipative k range, where the small- k behavior in Eqs. (27) to (29) is valid. The logarithmic correction becomes only appreciable for large systems with a size L , much larger than the so-called homogeneous cooling length $l_T = l_0/\gamma_0$, which diverges in the elastic limit. Then the renormalization corrections for small inelasticity vanish as $\delta T \sim \epsilon \ln(\epsilon L/l_0)$ and $\delta \omega \sim \epsilon^2 \ln(\epsilon L/l_0)$. Here, we have used the relations $C_E \sim \epsilon$ and $C_\omega \sim \epsilon^2$ for $\epsilon \rightarrow 0$, as can be deduced from the results in Appendix C. A similar mode coupling theory has been recently used in Ref. [20] for freely evolving granular fluids to calculate the long-time decay of the energy, which deviates from Haff's cooling law due to inhomogeneities in the hydrodynamic fields, and good agreement between theory and simulations was found.

Before concluding this section, we compare the theoretical predictions for the structure factors, with and without internal noise in Eqs. (20) and (21), as shown in Fig. 2. Inspection of Eqs. (27) and (28) shows that only the external noise determines their dominant small- k behavior. The question then arises, what are the effects of internal noise, and is it meaningful to include it in the theoretical description? The answer is affirmative, as we will show below. The steady state solution of Eq. (21) *without internal noise* clearly behaves at small wave numbers as k^{-2} , but the k -independent plateau values, shown by the full theory (solid lines in Fig. 2), are missing. These plateau values represent a very short-distance correlation $\sim \delta(\mathbf{r})$. Calculation of the plateau value for $S_{\alpha\beta}(\mathbf{k})$ yields $(1/n^2 V) \langle \sum_i v_{i\alpha} v_{i\beta} \rangle = (T/\rho) \delta_{\alpha\beta}$, i.e., the self-correlation term ($i=j$) in the definition (1) of $S_{\alpha\beta}(\mathbf{k})$, or more explicitly in Eq. (40) below. Then, addition of this plateau value to the numerical solution of Eq. (21) *without internal noise* yields the structure factors $S_{\alpha\beta}^{\text{without}}(\mathbf{k})$, shown as dotted lines in Fig. 2. For the transverse velocity structure

factor, the dotted line coincides with the solid line in Fig. 2, as can be shown analytically from Eqs. (20) and (21). Only the structure factor for the longitudinal flow field, $S_{\parallel}^{\text{without}}(k)$ differs appreciably from $S_{\parallel}(k)$ in the relevant intermediate regime, $0.2 \leq k\sigma \leq 0.5$.

In Sec. VII the simulation results will be compared with the theoretical predictions with and without internal noise. As it turns out, the comparison shows convincingly that the theory with/without internal noise agrees/disagrees with the simulations.

VI. COMPUTATIONAL DETAILS

In the two subsequent sections we describe molecular dynamics simulations performed to verify our theoretical predictions. In this section we present the computational details, before testing our theoretical results against simulations in the next section.

The model studied here has been extensively used in computer simulations for the freely evolving case (no forcing) [28–30,23], as well as for the randomly accelerated case in one [12] and two dimensions [13]. We consider a system of N inelastic hard disks having diameter σ in a two-dimensional square cell of length L , with periodic boundary conditions. The disks interact via inelastic collisions with coefficient of normal restitution α . For a colliding pair (i, j) of particles having equal masses, the postcollision velocities are:

$$\begin{aligned} \mathbf{v}_i^* &= \mathbf{v}_i - \frac{1}{2}(1+\alpha)(\mathbf{v}_{ij} \cdot \hat{\boldsymbol{\sigma}})\hat{\boldsymbol{\sigma}}, \\ \mathbf{v}_j^* &= \mathbf{v}_j + \frac{1}{2}(1+\alpha)(\mathbf{v}_{ij} \cdot \hat{\boldsymbol{\sigma}})\hat{\boldsymbol{\sigma}}, \end{aligned} \quad (36)$$

where $\mathbf{v}_{ij} = \mathbf{v}_i - \mathbf{v}_j$, the asterisk denotes velocities after collision, and $\hat{\boldsymbol{\sigma}}$ is a unit vector along the line connecting the centers of particle j and particle i .

The energy loss in consecutive collisions, which is proportional to $\epsilon = 1 - \alpha^2$, is compensated by a periodic (in time) and instantaneous perturbation of all velocities by a random amount. After every time step Δt , the velocity of each particle is modified according to

$$\mathbf{v}_i \rightarrow \mathbf{v}_i + \boldsymbol{\varphi}_i, \quad 1 \leq i \leq N, \quad (37)$$

where the components of the vectors $\boldsymbol{\varphi}_i$ are taken from a random distribution of zero mean and variance φ_0 (in practice, a Gaussian or a flat function of finite support). The time step Δt of this ‘‘heating’’ or ‘‘kicking’’ is chosen much smaller than the mean time between successive collisions of a tagged particle (typically a factor 10^4 smaller), so that the system under scrutiny reduces to that described in Sec. II. The opposite limit, where Δt is much bigger or comparable to the mean-free path, was considered in Ref. [31] (in the presence of an additional external damping or drag force), and in that limit, clustering was observed. The relation between φ_0 and ξ_0 , the variance of the noise term in Eq. (4), can be deduced from the energy fed into the system by the kicks. This yields straightforwardly,

$$\xi_0^2 = \frac{\varphi_0^2}{\Delta t}. \quad (38)$$

Between the heating events, the motion of the disks is free, which enables us to implement an event-driven molecular dynamics scheme with a linked-list method [32]. The CPU time, however, scales like N^2 because the lists in all cells need to be updated after each heating event.

Four parameters determine the state of the system: the inelasticity $\epsilon = 1 - \alpha^2$, the packing fraction $\phi = \pi N \sigma^2 / (4L^2)$, the reduced lower wave number cutoff $k_{\min} \sigma = 2\pi \sigma / L$, and the heating rate ξ_0^2 . The values of N investigated in this article vary between 10^3 and 10^4 , and we shall restrict our attention to high packing fractions for which the use of linked lists implies the most significant reduction of computer time. We consider the cases of moderate inelasticities ($0.6 < \alpha < 1$) and complete inelasticity ($\alpha = 0$). For the latter case, inelastic collapse occurs, i.e., the collision frequency involving only a small number of correlated particles diverges, as observed first by McNamara and Young [29] in freely evolving fluids of inelastic hard disks. Also in our system, for high enough inelasticity, the heating seems never sufficient to prevent the inelastic collapse. For $\alpha < 0.5$, the inelastic collapse has been avoided by introducing a slight modification of collision rule (36), as proposed in [30]: in each collision, the velocities are first computed according to the standard procedure $(\mathbf{v}_1, \mathbf{v}_2) \rightarrow (\mathbf{v}_1^*, \mathbf{v}_2^*)$; the relative velocity \mathbf{v}_{12}^* is then rotated by a random angle smaller than a maximum value Θ (typically less than a few degrees), keeping the center-of-mass velocity fixed. Note that this modified collision rule does not change the total energy loss of the colliding pair, and does not introduce any spurious drag or forcing on the particles.

The structure factors in the NESS have been computed for wave vectors compatible with the periodic boundary conditions, i.e., of the form $(2\pi/L)(n_x, n_y)$. We have obtained the density-density structure factors,

$$\begin{aligned} S_{nn}(\mathbf{k}) &= \frac{1}{V} \left\langle \left| \sum_{i,j} \exp(-i\mathbf{k} \cdot \mathbf{r}_{ij}) \right|^2 \right\rangle \\ &= \frac{1}{V} \left\langle \left| \sum_i \exp(-i\mathbf{k} \cdot \mathbf{r}_i) \right|^2 \right\rangle, \end{aligned} \quad (39)$$

and the velocity-velocity structure factor, defined as

$$n^2 S_{\alpha\beta}(\mathbf{k}) = \frac{1}{V} \left\langle \sum_{i,j} v_{i\alpha} v_{j\beta} \exp(-i\mathbf{k} \cdot \mathbf{r}_{ij}) \right\rangle. \quad (40)$$

Here, the averages are taken in the spatially uniform NESS. The fluctuation δg_α in the momentum density, $\delta g_\alpha(\mathbf{k}) = \sum_i m v_{i\alpha} \exp(-i\mathbf{k} \cdot \mathbf{r}_i)$, and those in the flow field are related as $\delta g_\alpha = \rho \delta u_\alpha$, where ρ is the average mass density in the steady state. The second rank tensor $S_{\alpha\beta}(\mathbf{k})$ is isotropic and can be split into a longitudinal and transverse part,

$$S_{\alpha\beta}(\mathbf{k}) = \hat{k}_\alpha \hat{k}_\beta S_{\parallel}(k) + (\delta_{\alpha\beta} - \hat{k}_\alpha \hat{k}_\beta) S_{\perp}(k), \quad (41)$$

where $\hat{k} = \mathbf{k}/k$. From Eq. (39), it appears that the knowledge of S_{nn} requires the computation of an $\mathcal{O}(N)$ quantity. We can rewrite the velocity-velocity structure factor so that its computation also increases linearly with the number of particles. For example, for the longitudinal part of $S_{\alpha\beta}(\mathbf{k})$ in Eq. (41) we have,

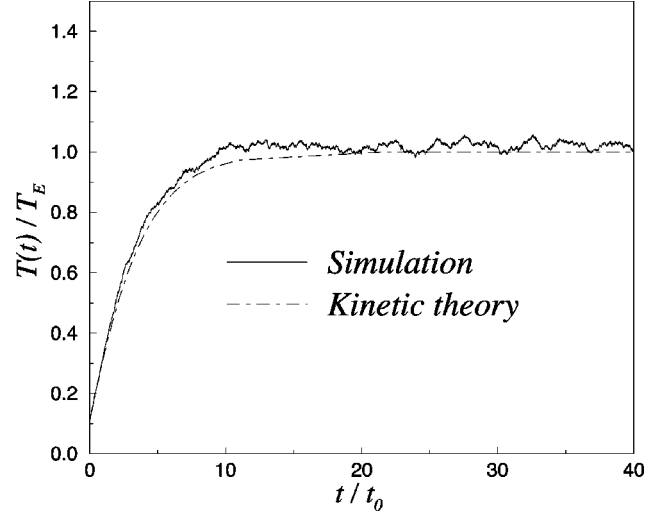


FIG. 3. Granular temperature as a function of time for $\alpha = 0.92, \phi = 0.078$ ($l_0/\sigma \approx 3.5$), and $N = 1600$ particles. The simulation result is compared to the analytical expression (12) (dashed curve). The initial condition corresponds to a fluidlike configuration of elastic hard disks. Here $\Delta t = 3.8 \times 10^{-3} (m\sigma^2/T_0)^{1/2} \approx 1.5 \times 10^{-3} t_0$ and $\varphi_0 = 5.77 \times 10^{-2} (T_0/m)^{1/2}$. T_E is the temperature expected on the basis of the Enskog theory [see Eq. (10)]. For the above parameters, there are on average 3.7 collisions per time interval Δt in the NESS, and $T_E/T_0 = 9.3$.

$$n^2 S_{\parallel}(k) = \frac{1}{V} \left\langle \left| \sum_i (\mathbf{v}_i \cdot \hat{\mathbf{k}}) \exp(-i\mathbf{k} \cdot \mathbf{r}_i) \right|^2 \right\rangle. \quad (42)$$

In practice, the different $S_{aa}(k)$ have been computed for every \mathbf{k} lying in the disk $|\mathbf{k}| < k_{\max} = 6\pi/\sigma$, then averaged over shells of thickness $k_{\min} = 2\pi/L$, to achieve better accuracy. Moreover, the statistics in the NESS has been increased by averaging over time. Note that the above procedure, which gives insight into the microscopic to large scale structure of the system, does not require the knowledge of the hydrodynamic (coarse-grained) density and velocity fields.

VII. SIMULATION RESULTS

A. Approach and characterization of the NESS

Before addressing the question of the large scale structure of the inelastic fluid, we investigate the validity of the macroscopic description given in Secs. II and V. The former section gives the mean-field results for the steady-state temperature T_E in Eq. (10) and collision frequency ω_E in Eq. (A2), based on the Enskog-Boltzmann equation. The latter section and Appendix C show how the long-range spatial fluctuations renormalize these mean-field values and lead to estimates in Eqs. (35) for the corrections $\delta T = T - T_E$ and $\delta \omega = \omega - \omega_E$, using a mode coupling calculation.

When the system is initially prepared in a configuration having a temperature T_0 different from the steady-state temperature T_E , the time dependence predicted by the mean-field result (12) is in good agreement with the numerical data. This is shown in Fig. 3 for a system with small inelasticity. When the initial temperature T_0 is much larger than T_E , the heating at short times is dominated by the inelastic dissipation, and Eq. (12) becomes Haff's homogeneous cool-

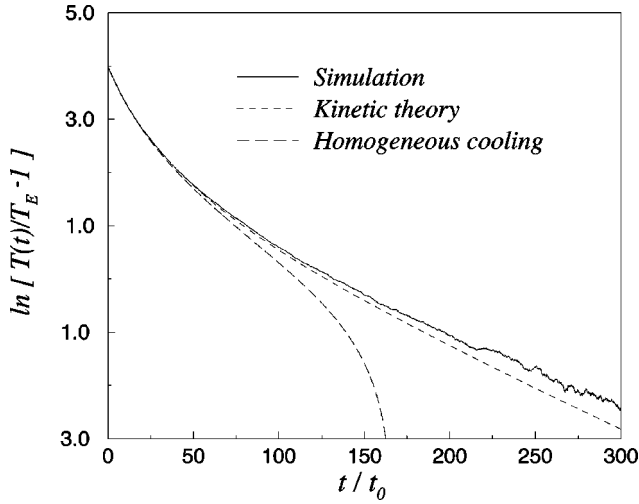


FIG. 4. Time dependence of the granular temperature obtained in the simulation for the two-dimensional system of Fig. 3, with $\Delta t = 3.8 \times 10^{-2} (m\sigma^2/T_0)^{1/2}$, $\varphi_0 = 1.7 \times 10^{-3} (T_0/m)^{1/2}$. Comparison is made with Haff's law (43) for homogeneous cooling (dashed curve), and with the full solution of Eq. (12) (long-dashed curve). Here, $T_E/T_0 = 0.018$.

ing law for a freely evolving system,

$$\frac{T(t)}{T_0} = \frac{1}{(1 + \gamma_0 t/t_0)^2}, \quad (43)$$

where $t_0 = 1/\omega_E(T_0)$ is the mean-free time in the initial state. This can be seen from the asymptotic expansion of the function f defined in Eq. (13),

$$f(x) \simeq \sqrt{3} \frac{\pi}{2} - \frac{3}{x} \quad \text{for } x \rightarrow \infty. \quad (44)$$

These analytic results for short times are confirmed by MD simulations, as shown in Fig. 4. Moreover, for initial temperatures $T_0 \ll T_E$, Eq. (12) predicts at short times a linear increase of T , as in a heated fluid of elastic hard spheres. Our simulations confirm this behavior.

Figure 5 shows that the measured kinetic energy per particle T is larger than the temperature T_E predicted on the basis of mean-field theory. This effect is noticeable albeit small in the results reported in Figs. 3 and 4, which correspond to the nearly elastic limit. For the densities studied here, we observe (see Fig. 5) that the correction δT is positive and decreases with decreasing inelasticity. The positive excess in temperature is already present for small inelasticity (see, e.g., Fig. 4), and vanishes as $\epsilon \rightarrow 0$. Note that the above results are at variance with those reported by Peng and Ohta [13], who find that T/T_E does not depend on α . The measured collision frequency ω is also larger than the Enskog estimate ω_E , as shown in Fig. 5. The excess $\delta\omega$ increases with increasing inelasticity.

We first observe that the simulation data in Fig. 5, where both $\omega > \omega_E$ and $T > T_E$, cannot be explained consistently as a possible over or underestimation of the IHS pair correlation function χ_{IHS} at contact by its value for elastic disks. On the basis of Eqs. (10) and (A2), we note that an overestimation of χ_{IHS} would increase the collision frequency (A2), and

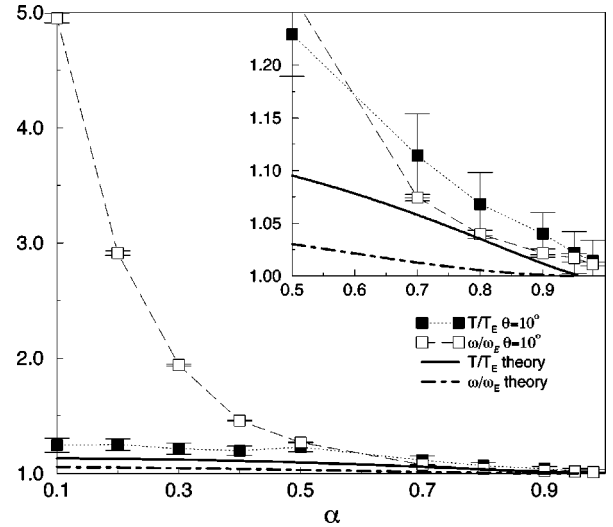


FIG. 5. Measured excess temperature $\delta T = T - T_E$ and collision frequency $\delta\omega = \omega - \omega_E$ versus coefficient of restitution α , for $L = 60\sigma$, $N = 917$ ($\phi = 0.2$, $l_0 = 1.1\sigma$), and a maximal random rotation angle $\Theta = 10^\circ$, together with the predictions of the mode coupling theory, Eq. (35).

decrease the temperature (10). These trends are at variance with the observations. The discrepancy between the measured and predicted temperatures and collision frequencies is more likely due to large scale fluctuations, at least for not too large inelasticities ($\alpha \gtrsim 0.6$). These long-range spatial fluctuations renormalize the mean-field Enskog values for the temperature T_E and collision frequency ω_E by amounts δT and $\delta\omega$. The theoretical estimates (35), based on mode coupling arguments, show the correct trends for the dependence of these corrections on the inelasticity, i.e., $\delta T \sim \epsilon$ and $\delta\omega \sim \epsilon^2$ as $\epsilon \rightarrow 0$, and give a rough estimate of the magnitude of these terms as illustrated in the inset of Fig. 5. We also point out that the system size considered in Fig. 5 is much too small for the asymptotic theory (35) to be applicable. For instance, at $\alpha = 0.8$, we deduce from the data ($l_0 = 1.1\sigma$, $L = 60\sigma$) in the caption of Fig. 5 that $\gamma_0 L/l_0 \approx 4.9$. Consequently, the leading asymptotic term $\ln(\gamma_0 L/l_0) \approx 1.6$ does not dominate the full mode coupling contribution (C2) in Appendix C, where subleading terms of $\mathcal{O}(1)$ have been neglected. The corresponding ratios $\gamma_0 L/l_0$ for Figs. 6 ($\alpha = 0.92$), 8 ($\alpha = 0.6$), and 11 ($\alpha = 0$) are, respectively, 46, 127, and 297. This predicts for the systems in Figs. 6, 8, and 11, respectively, $T_{\text{NESS}}/T_E \approx 1.07$, 1.41, and 1.77, whereas the simulations yield for the observed values $T/T_E \approx 1.05$, 1.45, and 1.5, which agrees quite well. The good agreement at $\alpha = 0$ is unexpected, as the theory is constructed under conditions that apply at small inelasticity. However, the renormalized values for the collision frequency, as predicted by the mode coupling theory, are much too small. We find in the above Figs. 6, 8, and 11, respectively, for the theoretical values $\omega_{\text{NESS}}/\omega_E \approx 1.003$, 1.06, and 1.12, whereas the simulations yield $\omega/\omega_E \approx 1.05$, 1.36, and 22.9.

For large inelasticity ($\alpha < 0.5$), the temperature T and collision frequency ω depend on the maximum angle Θ of the random rotations, used to avoid the collapse singularity, as explained in Sec. VI. In fact, ω diverges at $\Theta = 0$ (inelastic collapse), in agreement with the observations of Peng and

TABLE II. Collision frequency (normalized by the Enskog value) as a function of Θ , for a totally inelastic system ($\alpha=0$) with $N=1600$ particles, and packing fraction $\phi=0.07$.

Θ	1.5°	3.5°	5°	45°	90°
ω/ω_E	8.2	7.4	7	4.3	4.3

Ohta [13]. Intuitively, one expects that a *larger* randomization of the postcollision velocities (larger Θ) more effectively destroys the correlations leading to inelastic collapse, and consequently *decreases* the deviations in T and ω from the mean field and the mode coupling predictions. This does happen indeed for both temperature and collision frequency, as can be seen from Table II.

B. Fluctuations in the NESS

In this section we analyze the effects of inelasticity on the large distance behavior of the fluid. We have computed the structure factors in the spatially homogeneous NESS of the inelastic hard disk fluid as explained in the previous section, and have focused either on values of α close to the elastic limit, where the theoretical description is supposed to apply, or on values close to 0, in order to test how large deviations from the theory might be. Local mean-field values, like T_E and ω_E , reach their steady-state values rapidly. However, the time scale needed for the structure factors $S_{ab}(\mathbf{k})$ and the contributions of spatial fluctuations, δT and $\delta\omega$, to reach their steady-state values are diffusive, and increase as $k_{\min}^{-2} \sim L^2$ with system size. We have checked in the simulations

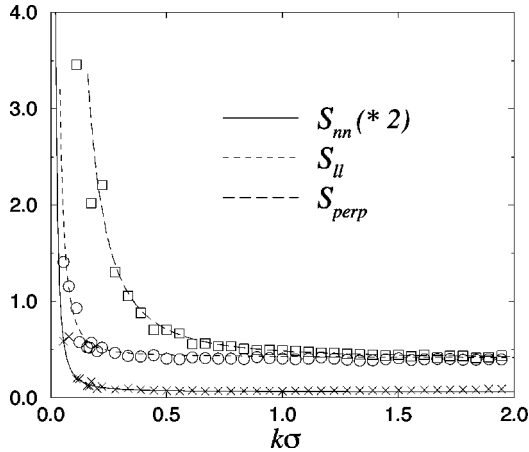


FIG. 6. Structure factors S_{\perp} and S_{\parallel} (in units $T_0\sigma^2/m$) and S_{nn} (in units $1/\sigma^2$) versus wave vector for $\alpha=0.92$, $\phi=0.63$ ($l_0/\sigma \approx 0.095$), and $N=10201$. The noise strength is chosen such that $T_E=0.41T_0$. The simulation data (symbols) have been averaged over 10^2 successive configurations, separated by a time interval of 20 collisions per particle. S_{\parallel} and $S_{perp} \equiv S_{\perp}$ are, respectively, the parallel and perpendicular parts of the velocity-velocity structure factor, defined by Eq. (40). Comparison is made with the theoretical expressions (full, dashed, and long-dashed curves) deduced from Eq. (23) (compare also Fig. 2). There is a dissipative regime for $k\sigma \lesssim \gamma_0\sigma/l_0 \approx 0.40$, and an elastic regime for $k\sigma \gtrsim \sqrt{\gamma_0}\sigma/l_0 \approx 2.1$. Here, $T/T_E \approx \omega/\omega_E \approx 1.05$, whereas the mode coupling approach of Sec. V predicts $T_{NESS}/T_E \approx 1.07$ and $\omega_{NESS}/\omega_E \approx 1.003$.

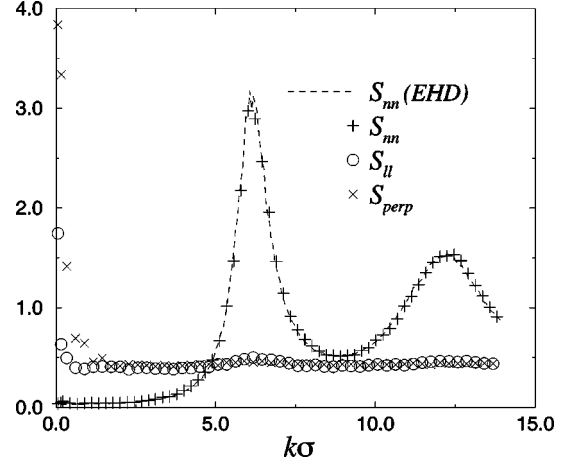


FIG. 7. Same as Fig. 6, with k beyond the dissipative regime. The dashed curve corresponds to the density-density structure factor of an elastic hard disk system of the same size and packing fraction (dashed curve). All results are deduced from MD simulations.

that the large scale behavior of the structure factors was properly equilibrated before accumulating the data used to compute the averages.

First of all, we have tested the isotropy of tensor (40) by checking that the average,

$$\left\langle \sum_{i,j} (\mathbf{v}_i \cdot \hat{\mathbf{k}})(\mathbf{v}_j \cdot \hat{\mathbf{k}}_{\perp}) \exp(i\mathbf{k} \cdot \mathbf{r}_{ij}) \right\rangle, \quad \text{with } \hat{\mathbf{k}} \cdot \hat{\mathbf{k}}_{\perp} = 0, \quad (45)$$

vanishes for \mathbf{k} values compatible with the periodic boundary conditions.

In Fig. 6 we show the density-density structure factor and the relevant components of the velocity-velocity structure factors. For *elastic* hard disks the plateau values of $S_{aa}(k)$ around $k\sigma \approx 2$ extend all the way down to $k=0$. The excess correlations in the dissipative regime ($k \lesssim \gamma_0/l_0$), which for $S_{\perp}(k)$ extend up to $k \approx \sqrt{\gamma_0}/l_0$, are characteristic of the randomly driven inelastic fluid. Figure 6 shows that for small inelasticities the agreement between simulations and theory is quite reasonable. The structure factors diverge at small scales like k^{-2} , in agreement with the theoretical predictions (27)–(29). The packing fraction has been chosen fairly high ($\phi=0.63$) but lower than the two-dimensional random close packing of monodisperse disks $\phi_{RCP} \approx 0.82$ [33], and inside the *liquid* region of the phase diagram for elastic hard disks. In addition to the gain in computer time, such a packing fraction leads to a mean-free-path l_0 smaller than the particle diameter σ (e.g., $l_0 \approx 0.095\sigma$ for $\phi=0.63$). Therefore, the hydrodynamic regime will hold up to typical particle diameters, enlarging the range of wave vectors where comparison between simulations and theoretical predictions is feasible. Moreover, for dense systems, a marked density structure is to be expected at the molecular scale, especially at wavelengths close to σ ($k\sigma \approx 2\pi$). Figure 7 shows that for α close to 1, this structure is indistinguishable from the structure for elastic hard disks. Note that $S_{\parallel}(k)$ and $S_{\perp}(k)$, although quite structureless for $k\sigma > 1$, show a weak and broad peak correlated with the maximum of $S_{nn}(k)$. This feature is more pronounced as the inelasticity increases, as shown in Figs. 10

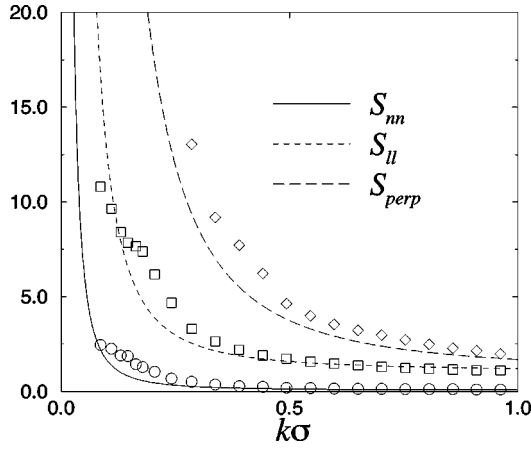


FIG. 8. Structure factors for $\alpha=0.6$, $\phi=0.55$ ($l_0/\sigma \approx 0.15$), $N=10201$, and $T_E=1.0T_0$. The lines are the corresponding theoretical predictions. The measured temperature $T/T_E \approx 1.45$ and our mode coupling theory gives $T_{\text{NESS}}/T_E \approx 1.41$. Units as in Fig. 6.

and 13. As the molecular structure of the fluid has not been taken into account in the long wavelength hydrodynamic approach of Sec. IV, the present theory cannot explain the structure in Figs. 10 and 13, and the structure factors predicted by the theory reach a plateau in the elastic regime ($kl_0 \gtrsim \sqrt{\gamma_0}$), given by

$$\begin{aligned} S_{nn}(k) &\rightarrow n^2 T \chi_T, \\ S_{\alpha\beta}(\mathbf{k}) &\rightarrow \frac{T}{\rho} \delta_{\alpha\beta}, \end{aligned} \quad (46)$$

where $\chi_T = (\partial n / \partial p)_T / n$ is the isothermal compressibility of the elastic hard disk fluid. For α close to 1, the above limiting behavior is observed numerically for S_{ll} or S_{\perp} , and for S_{nn} , only in the limit of small packing fraction, where the molecular structure disappears.

When the inelasticity is increased, the structure factors exhibit the same k^{-2} behavior at large scale, but the theoretical expressions are less accurate (see Fig. 8). However, the theoretical curves are based on the Enskog estimate T_E for

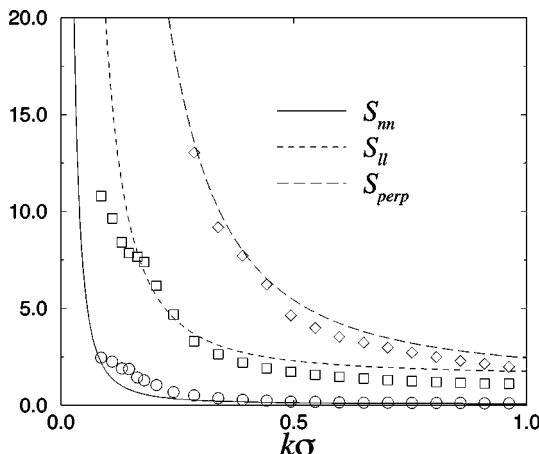


FIG. 9. Same as Fig. 8 where for the theoretical expressions (lines), the temperature has been set to the measured kinetic energy per particle, $T \approx 1.45T_E$.

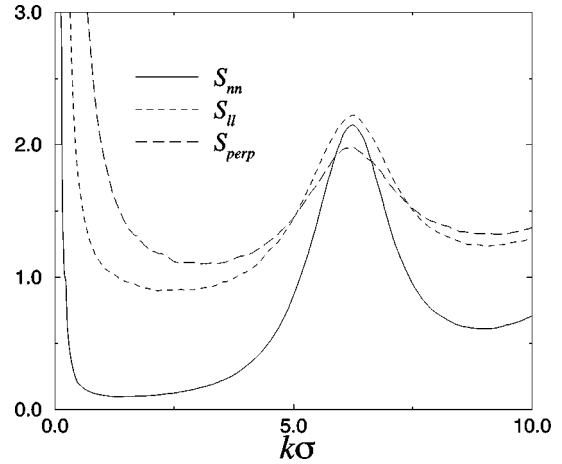


FIG. 10. Same as Fig. 8 beyond the dissipative regime. The theoretical structure factors are not displayed.

the granular temperature T , whereas for the system corresponding to Fig. 8, $T \approx 1.45T_E$. Our mode coupling theory predicts here $T_{\text{NESS}} \approx 1.41T_E$. Figure 9 displays the comparison between theory and simulation when the measured granular temperature is taken as an input for the hydrodynamic description. It appears that the large scale correlations (for which the present theory has been constructed) are well described by the theory, as long as the temperature is corrected from the mean-field Enskog prediction (10) to the measured value T . In the case of S_{\perp} , the amplitude only depends on the shear viscosity. The good agreement of the amplitude when the temperature is rescaled, while keeping for the shear viscosity the elastic hard disk value, suggests that the dependence of the shear viscosity on the inelasticity could be attributed only to the change in temperature. At the molecular scale, $S_{ll}(k)$ and $S_{\perp}(k)$ appear to be correlated to the density-density structure factor (see Fig. 10), in marked contrast to the elastic situation, where a plateau value would be reached. Such an effect is beyond the scope of our hydrodynamic approach, and is currently under investigation.

Surprisingly, in the case of complete inelasticity ($\alpha = 0$), the theoretical structure factors give a reasonable pic-

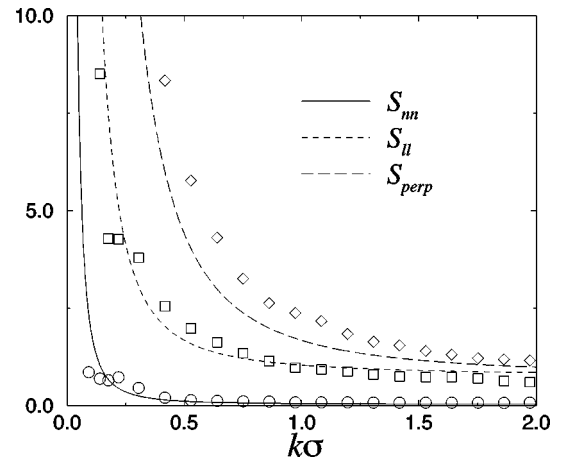


FIG. 11. Structure factors for $\alpha=0$, $\phi=0.63$, $N=10201$, and $T_E=0.76T_0$. Comparison is made with the hydrodynamic theory (lines). Here, $T/T_E \approx 1.5$, whereas mode coupling gives $T_{\text{NESS}}/T_E \approx 1.77$. Units as in Fig. 6.

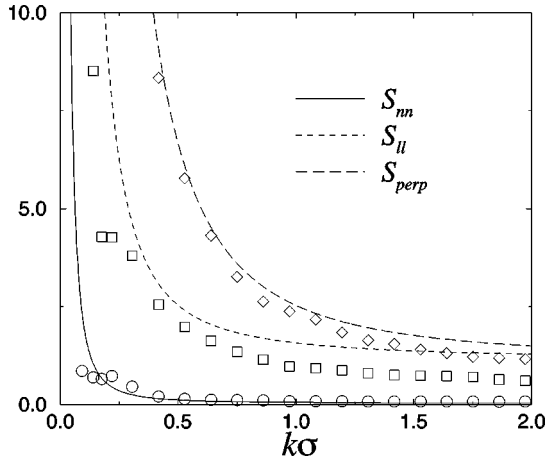


FIG. 12. Same as Fig. 11, where the simulation data (symbols) are compared to the theoretical predictions (lines) for which the temperature has been set to the measured kinetic energy per particle, $T \approx 1.5T_E$.

ture of the large wavelengths correlations in the fluid [especially for the longitudinal velocity component $S_{\parallel}(k)$, as shown in Fig. 11]. When the theoretical structure factors are deduced from the measured granular temperature $T \approx 1.5T_E$ and not from T_E (our mode coupling theory predicts $T_{\text{NESS}} \approx 1.77T_E$), the agreement for $S_{\perp}(k)$ improves, but the mismatch for $S_{\parallel}(k)$ increases (see Fig. 12). At small scales, the density correlations differ significantly from the elastic ones (Fig. 13) and the velocity structure factors exhibit the oscillatory behavior already present in Fig. 10, with peak positions locked in on the peaks in $S_{nn}(k)$. As can be expected from Figs. 11 and 12, the large scale correlations are compatible with the expected k^{-2} law (see Fig. 14) unlike the results of Peng and Ohta who report a $k^{-1.4}$ asymptotic behavior for $\alpha=0$. However, a log-log plot such as Fig. 14 does not allow an accurate evaluation of the scaling exponents. The k^{-2} law is better inferred from the direct comparison with theory (Figs. 6,9,12).

Before concluding this section we compare the structure factors for the longitudinal flow fields, obtained from MD

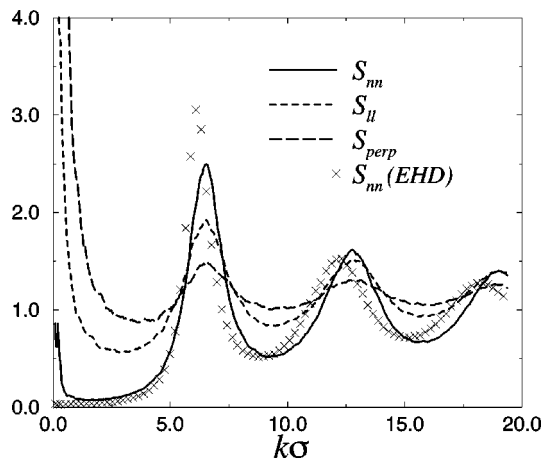


FIG. 13. Structure factors up to the molecular scale, for the same parameters as in Fig. 11. S_{nn} for elastic hard disks and the same packing fraction has also been plotted (crosses). Units as in Fig. 6.

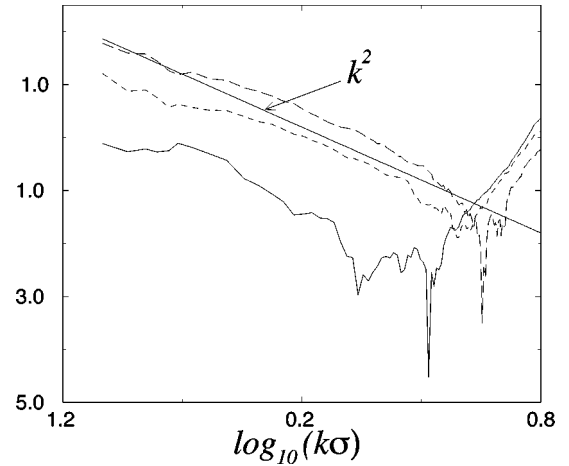


FIG. 14. $\log_{10}|S - S_{\min}|$ versus $\log_{10}(k\sigma)$, for the same parameters as in Fig. 11. Here S_{\min} denotes the lowest value of structure factor S . The full, dashed, and long-dashed curves refer to S_{nn} , S_{\parallel} , and S_{\perp} , respectively. Units as in Fig. 6.

simulations with two different theoretical predictions in Fig. 2, obtained by including or excluding internal noise. First, observe that all parameters in Fig. 2 and Fig. 6 are identical, as well as units on both axes. The simulation results for $S_{\parallel}(k)$ in Fig. 6 are in excellent agreement with the theoretical prediction (dashed line), which corresponds to the solid line in Fig. 2 (internal plus external noise). The dotted line (without internal noise) for $S_{\parallel}^{\text{without}}(k)$ in Fig. 2 disagrees with the simulations in the relevant interval $0.2 \leq k\sigma \leq 0.5$.

Hence, inclusion of internal noise extends the validity of the asymptotic theory to intermediate wave numbers.

VIII. CONCLUSION

We have presented a theory for the large scale dynamics of a granular fluid that is driven into a nonequilibrium steady state by a random external force. Our description combines the macroscopic equations of motion for the hydrodynamic fields, accounting for energy dissipation through inelastic collisions and uniform heating, together with the fluctuating forces. The long-range character of the spatial correlation functions is determined by the small wave number divergence $\sim k^{-2}$ of the corresponding structure factors. This k^{-2} behavior is typical for systems that combine conserving deterministic dynamics (conservation of particle number and momentum in collisions) with nonconserving noise [34], thus violating the fluctuation-dissipation condition, and is generic for rapid granular flows that are driven by external noise. We also draw attention to the analogy of our equations of motion for the fluctuating fields to the Edwards-Wilkinson model [35] that was proposed for growth of a granular surface. In that case the dynamic variable is a scalar field, namely, the height of the surface that obeys a similar equation of motion as any of the $(d-1)$ components of the transverse velocity field, $u_{\perp\alpha}(\mathbf{k}, t)$, in our case. The only difference is that in the Edwards-Wilkinson model there is only nonconserving noise, whereas in our case both nonconserving (external) and conserving (internal) noise are present.

We have tested our predictions for the structure factors against molecular dynamics simulations and have demon-

strated that there is quantitative agreement over the whole wave-number range, if internal fluctuations are taken into account. In our two-dimensional simulations we have found deviations in the steady-state temperature and collision frequency that grow with the inelasticity and the system size. For not too large inelasticities ($\alpha \geq 0.6$), we have explained these deviations in terms of mode coupling effects of the long-range fluctuations.

The phenomenological mode coupling theory, proposed in [20] and extended here to the driven IHS fluid, starts from the same basic ingredients as in the case of elastic fluids [36], where that theory was used to calculate the long-time tails of the velocity autocorrelation function and other current-current time correlation functions. For the elastic case the mode coupling theory can be derived from the *ring kinetic theory* in the low-density limit [37], which accounts for dynamic correlations built up by sequences of correlated binary collisions, leading to nonlocal effects in space and time. Such collision sequences correct the mean-field-type Boltzmann or Enskog kinetic equations for the errors induced by the breakdown of the molecular chaos assumption. The ring kinetic theory for rapid granular flows of IHS has been developed in Ref. [38], but has not yet been used to derive the present phenomenological mode coupling theory from the more fundamental kinetic theory, valid in the low-density limit.

In detailed balance models, such as elastic hard spheres, dynamic correlations created by correlated collision sequences lead to long-time tails, which imply that transport coefficients in two dimensions diverge as $\ln L$ for large systems [36,37].

Nondetailed balance models, such as IHS fluids, generically exhibit long-range spatial correlations [19]. In randomly driven IHS fluids, as studied in this paper, these correlations between densities and flow fields at distant points in the fluid behave as $1/r$ in 3D and $\ln r$ in 2D, and already modify (renormalize) the mean-field Enskog-Boltzmann values for steady-state properties, such as the temperature and collision frequency. In 2D systems these renormalization corrections, δT and $\delta \omega$, exhibit the $\ln L$ divergence, which in the case of detailed balance models appears only in the transport coefficients [19].

At larger inelasticity ($\alpha \leq 0.6$), molecular chaos is also violated due to the presence of short-range velocity-velocity correlations (see Fig. 13), which are beyond our mode coupling theory. A detailed investigation of the small scale structure, which for large inelasticity clearly deviates from an equilibrium structure, will be reported in a subsequent publication. It is surprising that our description, which is based on the Enskog theory and neglects any dependence of transport coefficients on inelasticity, even at $\alpha=0$ predicts the long-range structure reasonably well, provided that the temperature is not taken as the mean-field Enskog value, but set equal to the value measured in the simulations.

ACKNOWLEDGMENTS

The authors acknowledge useful discussions with D. Frenkel and I. Goldhirsch. E.T. and I.P. thank D. Frenkel and B. Mulder for the hospitality of their groups at AMOLF. T.v.N. and I.P. acknowledge support of the foundation

“Fundamenteel Onderzoek der Materie (FOM),” which is financially supported by the Dutch National Science Foundation (NWO).

APPENDIX A

In this appendix we derive expressions for the transport coefficients that govern the decay of fluctuations in the steady state. Linearization of the macroscopic equations (6) around the NESS, defined in Eqs. (9) and (10), gives the deterministic part of the following set of equations:

$$\begin{aligned} \partial_t \delta n &= -n \nabla \cdot \mathbf{u}, \\ \partial_t \mathbf{u} &= -\frac{1}{\rho} \nabla p + \nu \nabla^2 \mathbf{u} + (\nu_l - \nu) \nabla \nabla \cdot \mathbf{u} + \hat{\xi}, \\ \partial_t \delta T &= \frac{2\kappa}{dn} \nabla^2 \delta T - \frac{2p}{dn} \nabla \cdot \mathbf{u} - \delta \Gamma + \hat{\theta}. \end{aligned} \quad (\text{A1})$$

The noise terms $\hat{\xi}(\mathbf{r}, t)$ and $\hat{\theta}(\mathbf{r}, t)$ have been discussed in Sec. III. The pressure p is assumed to be that of EHS, $p = nT(1 + \Omega_d \chi n \sigma^d / 2d)$, where $\Omega_d = 2\pi^{d/2} / \Gamma(d/2)$ is the d -dimensional solid angle, and $\chi(n)$ is the equilibrium value of the pair-correlation function of EHS of diameter σ and mass m at contact. The kinematic and longitudinal viscosities ν and ν_l , as well as the heat conductivity κ , are also assumed to be approximately equal to the corresponding quantities for EHS, as calculated from the Enskog theory [22], where $\rho\nu = \eta$ and $\rho\nu_l = 2\eta(d-1)/d + \zeta$ are expressed in shear viscosity η and bulk viscosity ζ . The collisional energy loss in Eq. (7), $\Gamma = 2\gamma_0 \omega T$, is proportional to the collision frequency

$$\omega = \Omega_d \chi n \sigma^{d-1} \sqrt{\frac{T}{\pi m}}, \quad (\text{A2})$$

as obtained from the Enskog theory. In two dimensions we use the Verlet-Levesque approximation $\chi = (1 - 7\phi/16)/(1 - \phi)^2$.

By taking spatial Fourier transforms $\delta a(\mathbf{k}, t) = \int d\mathbf{r} \delta a(\mathbf{r}, t) \exp(-i\mathbf{k} \cdot \mathbf{r})$ in Eqs. (A1), one obtains the mesoscopic equation (18) with the hydrodynamic matrix

$\mathbf{M}(\mathbf{k})$

$$= - \begin{pmatrix} 0 & 0 & ikn & 0 \\ \gamma_0 \omega g(n) T / n & 3\gamma_0 \omega + D_T k^2 & ik2p/dn & 0 \\ ikv_T^2/n & ikp/\rho T & \nu_l k^2 & 0 \\ 0 & 0 & 0 & \nu k^2 \end{pmatrix}. \quad (\text{A3})$$

It contains the coefficients

$$\begin{aligned} g(n) &= 2 \left(1 + \frac{n}{\chi} \frac{d\chi}{dn} \right), \\ v_T^2 &= \left(\frac{\partial p}{\partial \rho} \right)_T, \end{aligned} \quad (\text{A4})$$

$$D_T = \frac{2\kappa}{dn}.$$

In the body of the paper we need the eigenvalues $z_\lambda(\mathbf{k})$ of the asymmetric matrix $M_{ab}(\mathbf{k})$, and its right and left eigenvectors, which are obtained from

$$\begin{aligned} \mathbf{M}(\mathbf{k})\mathbf{w}_\lambda(\mathbf{k}) &= z_\lambda(\mathbf{k})\mathbf{w}_\lambda(\mathbf{k}), \\ \mathbf{M}^T(\mathbf{k})\mathbf{v}_\lambda(\mathbf{k}) &= z_\lambda(\mathbf{k})\mathbf{v}_\lambda(\mathbf{k}), \end{aligned} \quad (\text{A5})$$

where \mathbf{M}^T is the transpose of \mathbf{M} . Here $\lambda = \pm$ labels the sound modes, $\lambda = H$ labels the heat mode, and $\lambda = \perp$ labels $(d-1)$ degenerate shear or transverse velocity modes. The eigenvectors form a complete biorthonormal basis, i.e.,

$$\begin{aligned} \sum_a v_{\lambda a}(\mathbf{k}) w_{\mu a}(\mathbf{k}) &\equiv \langle \mathbf{v}_\lambda | \mathbf{w}_\mu \rangle = \delta_{\lambda\mu}, \\ \sum_\lambda |\mathbf{w}_\lambda(\mathbf{k})\rangle \langle \mathbf{v}_\lambda(\mathbf{k})| &= \mathbf{I}. \end{aligned} \quad (\text{A6})$$

Moreover, the eigenvalue equation, $\det[z(k)\mathbf{I} - \mathbf{M}(\mathbf{k})] = 0$, is an *even* function of \mathbf{k} . Consequently, $\mathbf{M}(\mathbf{k})$ and $\mathbf{M}(-\mathbf{k})$ have the same eigenvalues, which are either real or form a complex conjugate pair. So we choose $z_\lambda(\mathbf{k}) = z_\lambda(-\mathbf{k}) = z_\lambda(k)$. The corresponding eigenvectors of $\mathbf{M}(-\mathbf{k})$ in case of the sound modes are obtained from the transformation $\{\mathbf{w}_+(-\mathbf{k}), \mathbf{v}_+(-\mathbf{k})\} \leftrightarrow \{\mathbf{w}_-(\mathbf{k}), \mathbf{v}_-(\mathbf{k})\}$. All other eigenvectors are invariant under the transformation $\mathbf{k} \rightarrow -\mathbf{k}$.

By setting $z(k) = 0$ in the eigenvalue equation, one can verify that there are no zero crossings at any finite wave number. So, all eigenvalues have a definite (here *negative*) sign. Consequently, all modes of the heated IHS fluid are linearly stable. There is *no* clustering instability [23,28] and *no* instability in the flow field [23], as in the freely evolving IHS fluid.

In the *dissipative regime* ($kl_0 \ll \gamma_0$), the eigenvalue equation is solved by an expansion in powers of k , and one finds to dominant orders the eigenvalues in the form (25) and eigenvectors in the form (26). The eigenmodes to dominant nonvanishing order in k are listed in Eq. (26). There are $(d-1)$ transverse velocity or shear modes ($\lambda = \perp$), which are purely diffusive with a diffusivity $D_\perp = \nu$; there are two propagating modes ($\lambda = \pm$) with a speed of propagation v_D , and sound damping constant D_S , and a *kinetic* heat mode ($\lambda = H$) with a nonvanishing $z_H(0)$.

For later reference we also express these coefficients in thermodynamic quantities and transport coefficients. The speed of sound v_D in the *dissipative regime* ($kl_0 \ll \gamma_0$) is

$$v_D^2 = \left(\frac{\partial p}{\partial \rho} \right)_T - \frac{2p}{3\rho} \left(1 + \frac{n}{\chi} \frac{d\chi}{dn} \right). \quad (\text{A7})$$

It satisfies the inequality $v_D < v_S$, where v_S is the adiabatic speed of sound in the *standard regime* ($\gamma_0 \ll kl_0 < 1$),

$$v_S^2 = v_T^2 + \left(\frac{2p}{dn} \right) \left(\frac{p}{\rho T} \right) = \left(\frac{\partial p}{\partial \rho} \right)_S. \quad (\text{A8})$$

The damping constant of the sound modes is

$$D_S = \frac{1}{2} v_l + \frac{p}{9\gamma_0\omega\rho} \left(1 + \frac{n}{\chi} \frac{d\chi}{dn} + \frac{3p}{dnT} \right), \quad (\text{A9})$$

and the dispersion relation for the kinetic heat mode contains the positive constant

$$D_H = -\frac{2\kappa}{dn} + \frac{2p}{9\gamma_0\omega\rho} \left(1 + \frac{n}{\chi} \frac{d\chi}{dn} + \frac{3p}{dnT} \right). \quad (\text{A10})$$

The ratios v_D^2/T , v_S^2/T , D_S/\sqrt{T} , and D_H/\sqrt{T} are independent of temperature.

APPENDIX B

In this appendix we calculate the tails of the spatial correlation functions $G_{ab}(\mathbf{r})$, which is done by Fourier inversion of $S_{ab}(\mathbf{k})$. Consider first the tensor fields $G_{\alpha\beta}(\mathbf{r})$ and $S_{\alpha\beta}(\mathbf{k})$ in Eq. (1) with $\delta a_\alpha(\mathbf{r}, t) = u_\alpha(\mathbf{r}, t)$ ($\alpha, \beta = x, y, \dots$) being the components of the flow field. Both tensor fields are isotropic and can be split into longitudinal and transverse components, i.e.,

$$\begin{aligned} G_{\alpha\beta}(\mathbf{r}) &= \hat{r}_\alpha \hat{r}_\beta G_{\parallel}(r) + (\delta_{\alpha\beta} - \hat{r}_\alpha \hat{r}_\beta) G_{\perp}(r) \\ &= \int \frac{d\mathbf{k}}{(2\pi)^d} \exp(i\mathbf{k} \cdot \mathbf{r}) [\hat{k}_\alpha \hat{k}_\beta S_{\parallel}(k) \\ &\quad + (\delta_{\alpha\beta} - \hat{k}_\alpha \hat{k}_\beta) S_{\perp}(k)], \end{aligned} \quad (\text{B1})$$

where the small- k behavior of $S_{\perp}(k)$ and $S_{\parallel}(k)$ is given in Eqs. (27) and (28). By contracting the second line above with $\hat{r}_\alpha \hat{r}_\beta$, we obtain

$$\begin{aligned} G_{\parallel}(r) &= \int \frac{d\mathbf{k}}{(2\pi)^d} \exp(i\mathbf{k} \cdot \mathbf{r}) [(\hat{\mathbf{k}} \cdot \hat{\mathbf{r}})^2 S_{\parallel}(k) \\ &\quad + [1 - (\hat{\mathbf{k}} \cdot \hat{\mathbf{r}})^2] S_{\perp}(k)]. \end{aligned} \quad (\text{B2})$$

Contraction of the second line of Eq. (B1) with $(\delta_{\alpha\beta} - \hat{k}_\alpha \hat{k}_\beta)$ yields in a similar manner an expression for $G_{\perp}(r)$.

In *three* dimensions the \mathbf{k} integral can be performed explicitly and yields

$$\int \frac{d\mathbf{k}}{(2\pi)^3} \frac{\exp(i\mathbf{k} \cdot \mathbf{r})}{k^2} = \frac{1}{4\pi r}, \quad (\text{B3})$$

$$\int \frac{d\mathbf{k}}{(2\pi)^3} \frac{\exp(i\mathbf{k} \cdot \mathbf{r})}{k^2} (\hat{\mathbf{k}} \cdot \hat{\mathbf{r}})^2 = 0.$$

The resulting large- r behavior of $G_{\alpha\beta}(\mathbf{r})$ is given in Eqs. (30).

In *two* dimensions the integral in Eq. (B2) over the azimuthal angle yields for large r ,

$$\begin{aligned} \int \frac{d\mathbf{k}}{(2\pi)^2} \frac{\exp(i\mathbf{k} \cdot \mathbf{r})}{k^2} &= \frac{1}{2\pi} \int_{k_{\min}}^{\infty} \frac{dk}{k} J_0(kr) \\ &\simeq \frac{1}{2\pi} \ln \left(\frac{L}{r} \right) + \mathcal{O}(1), \end{aligned}$$

$$\begin{aligned} & \int \frac{d\mathbf{k}}{(2\pi)^2} \frac{\exp(i\mathbf{k}\cdot\mathbf{r})}{k^2} [1 - (\hat{\mathbf{k}}\cdot\hat{\mathbf{r}})^2] \\ &= \frac{1}{2\pi r} \int_{k_{\min}}^{\infty} \frac{dk}{k^2} J_1(kr) \approx \frac{1}{4\pi} \ln\left(\frac{L}{r}\right) + \mathcal{O}(1). \end{aligned} \quad (\text{B4})$$

In two dimensions the \mathbf{k} integral diverges for $k \rightarrow 0$. It should, in fact, be restricted to $k \geq k_{\min} = 2\pi/L$, which is the smallest allowed wave number when periodic boundary conditions are imposed. To obtain the last equalities one needs the small- z behavior of the Bessel functions $J_\nu(z) \approx (z/2)^\nu / \Gamma(\nu + 1)$ [39]. Combining these results with Eq. (B2) yields for large r ,

$$G_{\parallel}(r) \approx G_{\perp}(r) \approx \frac{\Gamma}{8\pi\rho} \left(\frac{1}{\nu} + \frac{1}{2D_S} \right) \ln\left(\frac{L}{r}\right). \quad (\text{B5})$$

The remaining spatial correlation functions $G_{ab}(r)$ involving $a, b = \{n, T\}$, are scalar fields. Their large- r behavior is given by

$$\begin{aligned} G_{ab}(r) &= \int \frac{d\mathbf{k}}{(2\pi)^d} \exp(i\mathbf{k}\cdot\mathbf{r}) S_{ab}(k) \\ &= \frac{\Gamma B_{ab}}{8\pi\rho D_S} \begin{cases} \ln(L/r) & (d=2) \\ 1/2r & (d=3), \end{cases} \end{aligned} \quad (\text{B6})$$

where $B_{ab}(k)$ is given in Table I. The subleading corrections of $\mathcal{O}(r^0)$ depend on the cutoff k_{\min} . To evaluate these terms requires the subleading small- k behavior of $S_{ab}(k)$ in Eqs. (27) to (29).

APPENDIX C

In this appendix we present a mode coupling calculation to estimate the contributions of the long wavelength fluctuations in the NESS to some quantity h . Examples are the particle distribution functions, the energy per particle E , and the collision frequency ω . The fluctuations are correlated over large distances, as a consequence of sequences over dynamically correlated collisions, the so-called ring collisions [40], as shown in Sec. V by explicit calculation of their spatial tails.

To calculate their contributions to average quantities like h , one may solve the ring kinetic equations [38], or estimate these quantities from a more phenomenological mode coupling approach, as developed in Ref. [36]. The basic assumption made there is that the state of the system rapidly decays to a state of local equilibrium, described by the fluctuating hydrodynamic fields $\mathbf{a}(\mathbf{r}, t) = \{n(\mathbf{r}, t), u_\alpha(\mathbf{r}, t), T(\mathbf{r}, t)\}$.

For the quantity under consideration this can be implemented by representing $h = (1/V) \int d\mathbf{r} h(\mathbf{r})$, and approximating $h(\mathbf{r})$ by its value in local equilibrium, i.e.,

$$h_{\text{NESS}} = \frac{1}{V} \int d\mathbf{r} \langle h_l(\mathbf{a}(\mathbf{r})) \rangle, \quad (\text{C1})$$

where the average is taken over the fluctuating hydrodynamic fields $\mathbf{a}(\mathbf{r})$ in the NESS. To carry out the average over

the fluctuations, we expand $h_l(\mathbf{a})$ in powers of the fluctuations $\delta a = a - \langle a \rangle$ around the NESS, yielding

$$\begin{aligned} h_{\text{NESS}} &\approx h_l(\langle \mathbf{a} \rangle) + \frac{1}{2V} \int d\mathbf{r} \langle \delta a(\mathbf{r}) \delta b(\mathbf{r}) \rangle A_{ab} \\ &= h_l(\langle \mathbf{a} \rangle) + \frac{1}{2} \int \frac{d\mathbf{k}}{(2\pi)^d} S_{ab}(k) A_{ab}, \end{aligned} \quad (\text{C2})$$

where summation convention for repeated indices has been used. Here A_{ab} is the matrix of second derivatives $\partial^2 h_l(\mathbf{a}) / \partial \mathbf{a} \partial \mathbf{a}$ at $\mathbf{a} = \langle \mathbf{a} \rangle$. The asterisk indicates that \mathbf{k} integrals are restricted to the long wavelength range, $k < \gamma_0/l_0$, the so-called dissipative range, discussed below (16). In this range the structure factors have the form $S_{ab}(k) \approx E_{ab}/k^2$ on account of Eqs. (27) to (29).

For dimensionality $d \geq 3$ the fluctuation contribution $\delta h = h_{\text{NESS}} - h_l(\langle \mathbf{a} \rangle)$ is convergent at small k , and gives only small well-behaved corrections to $h_l(\langle \mathbf{a} \rangle)$. However, for $d = 2$, the \mathbf{k} integral diverges logarithmically at small k (where $k \geq 2\pi/L$), and the excess δh is given by

$$\delta h \approx \frac{A_{ab} E_{ab}}{4\pi} \int_{2\pi/L}^{\gamma_0/l_0} \frac{dk}{k} \approx \frac{A_{ab} E_{ab}}{4\pi} \ln\left(\frac{\gamma_0 L}{l_0}\right). \quad (\text{C3})$$

Consequently, the fluctuation contribution δh in 2D systems is a singular function of the system size L that diverges in the thermodynamic limit.

We first apply the above results to the energy per particle, $E = (1/N) \int d\mathbf{r} e_l(\mathbf{a}(\mathbf{r}))$, where $e_l(\mathbf{a}) = \frac{1}{2} \rho u^2 + (d/2) n T$ is the energy density in local equilibrium. From $e_l(\mathbf{a})$, the expansion coefficients corresponding to $h_l(\langle \mathbf{a} \rangle)$ and A_{ab} in Eq. (C2) can be calculated, to yield in $d = 2$:

$$\delta E \approx \frac{1}{2n} \int \frac{d\mathbf{k}}{(2\pi)^2} [\rho S_{\perp}(k) + \rho S_{ll}(k) + 2S_{nT}(k)]. \quad (\text{C4})$$

Inserting Eq. (27) to (29) then yields

$$\delta E \approx \frac{\gamma_0 \omega_E T_E}{4\pi n} \left[\frac{1}{\nu} + \frac{1}{2D_S} \left(1 + \frac{2B_{nT}}{\rho} \right) \right] \ln\left(\frac{\gamma_0 L}{l_0}\right), \quad (\text{C5})$$

where the coefficient B_{nT} is listed in Table I.

For the collision frequency the analog of Eq. (C1) is $\omega = (1/N) \int d\mathbf{r} \langle n(\mathbf{r}) \omega_l(\mathbf{a}(\mathbf{r})) \rangle$ with $\omega_l(\mathbf{a}) \propto n \chi(n) \sqrt{T}$ given in Eq. (A2). This gives in two dimensions:

$$\begin{aligned} \delta \omega &\approx \frac{1}{2n} \int \frac{d\mathbf{k}}{(2\pi)^2} [S_{nn}(k) A_{nn} + 2S_{nT}(k) A_{nT} + S_{TT}(k) A_{TT}] \\ &\approx \frac{\gamma_0 \omega_E T_E}{8\pi n \rho D_S} [B_{nn} A_{nn} + 2B_{nT} A_{nT} + B_{TT} A_{TT}] \ln\left(\frac{\gamma_0 L}{l_0}\right), \end{aligned} \quad (\text{C6})$$

where the coefficients B_{ab} are given in Table I, and $A_{nn} = \partial^2(n\omega) / \partial n^2$, $A_{nT} = \partial^2(n\omega) / \partial n \partial T$, and $A_{TT} = \partial^2(n\omega) / \partial T^2$ at $\mathbf{a} = \langle \mathbf{a} \rangle$.

The same method can be used to calculate other averages, as well as particle distribution functions. For instance, for the single-particle distribution function, the starting point would be

$$f_{\text{NESS}}(\mathbf{v}) = (1/V) \int d\mathbf{r} \langle f_i(\mathbf{v} | \mathbf{a}(\mathbf{r})) \rangle, \quad (\text{C7})$$

and the above procedure can be applied at once.

-
- [1] H. M. Jaeger, S. R. Nagel, and R. P. Behringer, *Rev. Mod. Phys.* **68**, 1259 (1996).
- [2] R. A. Bagnold, *Proc. R. Soc. London, Ser. A* **225**, 49 (1954).
- [3] S. B. Savage and M. Sayed, *J. Fluid Mech.* **142**, 391 (1984).
- [4] P. C. Johnson, P. Nott, and R. Jackson, *J. Fluid Mech.* **210**, 501 (1990).
- [5] S. Warr, J. M. Huntley, and G. T. H. Jacques, *Phys. Rev. E* **52**, 5583 (1995).
- [6] F. Melo, P. B. Umbanhowar, and H. L. Swinney, *Phys. Rev. Lett.* **75**, 3838 (1995).
- [7] L. S. Tsimring and I. S. Aranson, *Phys. Rev. Lett.* **79**, 213 (1997); D. H. Rothman, *Phys. Rev. E* **57**, R1239 (1998); S. C. Venkataramani and E. Ott, *Phys. Rev. Lett.* **80**, 3495 (1998).
- [8] M. Cross and P. C. Hohenberg, *Rev. Mod. Phys.* **65**, 851 (1993).
- [9] A. Kudrolli, M. Wolpert, and J. P. Gollub, *Phys. Rev. Lett.* **78**, 1383 (1997).
- [10] J. S. Olafsen and J. S. Urbach, *Phys. Rev. Lett.* **81**, 4369 (1998).
- [11] J. T. Jenkins and M. W. Richman, *Arch. Ration. Mech. Anal.* **87**, 355 (1985); J. J. Brey, J. W. Dufty, and A. Santos, *J. Stat. Phys.* **87**, 1051 (1997); N. Sela and I. Goldhirsch, *J. Fluid Mech.* **361**, 41 (1998).
- [12] D. R. Williams and F. C. MacKintosh, *Phys. Rev. E* **54**, R9 (1996).
- [13] G. Peng and T. Ohta, *Phys. Rev. E* **58**, 4737 (1998).
- [14] L. Oger, C. Annic, D. Bideau, R. Dai, and S. B. Savage, *J. Stat. Phys.* **82**, 1047 (1996).
- [15] R. Jackson, in *Fluidization*, edited by J. F. Davidson, R. Clift, and D. Harrison (Academic Press, London, 1985).
- [16] C. Bizon and H. L. Swinney (private communication).
- [17] T. P. C. van Noije and M. H. Ernst, *Granular Matter* **1**, 57 (1998).
- [18] M. R. Swift, M. Boamfa, S. J. Cornell, and A. Maritan, *Phys. Rev. Lett.* **80**, 4410 (1998).
- [19] J. R. Dorfman, T. R. Kirkpatrick, and J. Sengers, *Annu. Rev. Phys. Chem.* **45**, 213 (1994).
- [20] R. Brito and M. H. Ernst, *Europhys. Lett.* **43**, 497 (1998).
- [21] J. P. Hansen and I. R. McDonald, *Theory of Simple Liquids* (Academic Press, London, 1986).
- [22] S. Chapman and T. G. Cowling, *The Mathematical Theory of Non-uniform Gases* (Cambridge University Press, Cambridge, 1970).
- [23] T. P. C. van Noije, M. H. Ernst, R. Brito, and J. A. G. Orza, *Phys. Rev. Lett.* **79**, 411 (1997); T. P. C. van Noije, R. Brito, and M. H. Ernst, *Phys. Rev. E* **57**, R4891 (1998).
- [24] U. Frisch, B. Hasslacher, and Y. Pomeau, *Phys. Rev. Lett.* **56**, 1505 (1986).
- [25] D. H. Rothman and S. Zaleski, *Rev. Mod. Phys.* **66**, 1417 (1994).
- [26] S. McNamara, *Phys. Fluids A* **5**, 3056 (1993).
- [27] L. Landau and E. M. Lifshitz, *Fluid Mechanics* (Pergamon Press, New York, 1959), Chap. 17.
- [28] I. Goldhirsch and G. Zanetti, *Phys. Rev. Lett.* **70**, 1619 (1993).
- [29] S. McNamara and W. R. Young, *Phys. Fluids A* **4**, 496 (1992); *Phys. Rev. E* **50**, R28 (1994); **53**, 5089 (1996).
- [30] P. Deltour and J.-L. Barrat, *J. Phys. I* **7**, 137 (1997).
- [31] A. Puglisi, V. Loreto, U. Marini Bettolo Marconi, A. Petri, and A. Vulpiani, *Phys. Rev. Lett.* **81**, 3848 (1998).
- [32] M. P. Allen and D. J. Tildesley, *Computer Simulations of Liquids* (Clarendon Press, Oxford, 1987).
- [33] S. Jasty, M. Al-Naghy, and M. de Llano, *Phys. Rev. A* **35**, 1376 (1987).
- [34] G. Grinstein, D.-H. Lee, and S. Sachdev, *Phys. Rev. Lett.* **64**, 1927 (1990).
- [35] S. F. Edwards and D. R. Wilkinson, *Proc. R. Soc. London, Ser. A* **381**, 17 (1982).
- [36] M. H. Ernst, E. H. Hauge, and J. M. J. van Leeuwen, *Phys. Rev. Lett.* **25**, 1245 (1970); *Phys. Rev. A* **4**, 2055 (1971).
- [37] J. R. Dorfman and E. G. D. Cohen, *Phys. Rev. Lett.* **25**, 1257 (1970); M. H. Ernst and J. R. Dorfman, *Physica (Amsterdam)* **61**, 157 (1972).
- [38] T. P. C. van Noije, M. H. Ernst, and R. Brito, *Physica A* **251**, 266 (1998).
- [39] I. S. Gradshteyn and I. M. Ryzhik, *Table of Integrals, Series, and Products* (Academic Press, New York, 1965).
- [40] J. R. Dorfman and H. van Beijeren, in *Statistical Mechanics, Part B: Time-Dependent Processes*, edited by B. J. Berne (Plenum Press, New York, 1977), Chap. 3.

Randomly driven granular fluids: Collisional statistics and short scale structure

I. Pagonabarraga

Departament de Física Fonamental, Universitat de Barcelona, Av. Diagonal 647, 08028-Barcelona, Spain

E. Trizac

Laboratoire de Physique Théorique, Bâtiment 210, Université Paris-Sud, 91405 Orsay Cedex, France*

T. P. C. van Noije and M. H. Ernst

Instituut voor Theoretische Fysica, Universiteit Utrecht, Postbus 80006, 3508 TA Utrecht, The Netherlands

(Received 26 July 2001; published 14 December 2001)

We present a molecular-dynamics and kinetic theory study of granular material, modeled by inelastic hard disks, fluidized by a random driving force. The focus is on collisional averages and short-distance correlations in the nonequilibrium steady state, in order to analyze in a quantitative manner the breakdown of molecular chaos, i.e., factorization of the two-particle distribution function, $f^{(2)}(x_1, x_2) \approx \chi f^{(1)}(x_1) f^{(1)}(x_2)$ in a product of single-particle ones, where $x_i = \{\mathbf{r}_i, \mathbf{v}_i\}$ with $i = 1, 2$ and χ represents the position correlation. We have found that molecular chaos is only violated in a small region of the two-particle phase space $\{x_1, x_2\}$, where there is a predominance of grazing collisions. The size of this singular region grows with increasing inelasticity. The existence of particle- and noise-induced recollisions magnifies the departure from mean-field behavior. The implications of this breakdown in several physical quantities are explored.

DOI: 10.1103/PhysRevE.65.011303

PACS number(s): 45.70.-n, 51.10.+y

I. INTRODUCTION

The interesting phenomena observed in recent experiments with mono- and multi-layers of granular material on vibrating plates [1–4] show the need to develop kinetic theories for rapid granular flows with mechanisms for energy input, different from those in shear flows or flows through vertical pipes. In the present paper, the fluidization is driven by a random external force, which gives frequent kicks to each particle in between collisions. Such a driving mechanism has recently been studied by many authors [5–11]. The basic physical interest is the understanding of the nonequilibrium stationary states (NESS) that exist in the presence of this random force. The advantage of this fluidization mechanism, besides its potential physical realizations, lies in the fact that the NESS is linearly stable against spatial inhomogeneities.

In Ref. [10], to which we will refer to as paper I, we have studied the large-scale structure and presented a hydrodynamic description of randomly driven granular fluids, modeled as systems of smooth inelastic hard spheres (IHS). The IHS model accounts for two essential features of granular matter: hard-core exclusion and dissipative collisions [12]. The dynamics is described by a constant coefficient α of normal restitution. In collisions, a fraction of the relative kinetic energy is lost, which is proportional to the inelasticity $\epsilon = 1 - \alpha^2$. The stochastic external force compensates this energy loss, and drives the IHS fluid into a NESS. This stationary state, though homogeneous and stable against spatial fluctuations on large space and time scales (at least for weakly inelastic spheres), was shown to exhibit long-range spatial correlations in density, velocity, and granular tem-

perature fields that extend much beyond the mean free path. In fact, the corresponding structure functions $S(k)$ diverge as $1/k^2$ as the wave-number $k \rightarrow 0$, a behavior caused by the random external force, which does not conserve momentum whereas the collisions between particles do. These long-range correlations are of algebraic form, $\sim 1/r^{d-2}$, which corresponds to $\ln r$ in two dimensions ($d=2$). The existence of such extremely long-range spatial correlations is one example of the many nontrivial properties of nonequilibrium stationary states in general [13,14].

Differences in the stationary states between fluids with dissipative and conservative interactions also manifest themselves in the kinetic properties of the fluid, such as the velocity distribution function, which deviates from a Maxwellian, in particular, in the high-energy tail of the distribution. In Ref. [9], the existence of an overpopulated high-energy tail $\hat{f} \sim \exp[-Cv^{3/2}]$, where C is a constant that depends on the inelasticity, has been obtained from kinetic theory. A similar behavior has been observed experimentally at high-vibrational accelerations [3,4]. This observation indicates that certain features of the experiment might be reproduced by modeling the input of energy into the horizontal motion of the beads by a random external force, although other energy injection mechanisms that could be relevant to recover the large-velocity tail have been put forward [15]. In similar experiments [2], with a vertically vibrating plate covered with a monolayer of steel balls with a packing fraction around 50%, the velocity distribution of the horizontal velocities has been measured, and again, overpopulated non-Gaussian high-energy tails have been observed. In the present paper, we will investigate the kinetic properties and short-scale correlations that characterize the stationary state. More specifically, we will compare molecular-dynamics (MD) simulations of inelastically colliding disks with analytic predictions based on the assumption of molecular chaos.

*Unité Mixte de Recherche UMR 8627 du CNRS.

The Boltzmann equation for dilute gases of particles that interact via short-ranged repulsive interactions is based on the assumption of *molecular chaos*, also called the Stosszahlansatz or mean-field approximation. It assumes that the velocities of colliding particles just before collisions are uncorrelated, i.e., their pair-distribution function factorizes, $\hat{f}^{(2)}(x_1, x_2, t) = \hat{f}(x_1, t)\hat{f}(x_2, t)$, where $x_i = \{\mathbf{r}_i, \mathbf{v}_i\}$ denotes the position and velocity of particle i . Enskog's extension of the Boltzmann equation to a dense system of hard spheres [16], referred to as Enskog-Boltzmann equation, is also based on the fundamental assumption of the absence of velocity correlations. Here, the assumption of molecular chaos postulates that $\hat{f}^{(2)}(x_1, x_2, t) = \chi \hat{f}(x_1, t)\hat{f}(x_2, t)$ for approaching particles ($\mathbf{v}_{12} \cdot \mathbf{r}_{12} < 0$) just before collision ($r_{12} = \sigma + 0$), where χ is assumed to be the radial pair-distribution function at contact $g(r_{12} = \sigma + 0)$ in local equilibrium. It implies the *additional* assumption that spatial correlations between colliding particles just before collision are independent of their velocities, i.e., the absence of position-velocity correlations. The Enskog χ factor enhances the collision frequency at higher densities. For dilute gases, the assumption of molecular chaos seems to be justified. Recently, Lutsko [17] and Soto and Marechal [18] derived for a freely evolving inelastic hard disk fluid a relation between pre- and post-collision radial distribution function at contact, as a function of the angle, $\theta = \cos^{-1}(\hat{\mathbf{v}}_{12} \cdot \hat{\mathbf{r}}_{12})$, between the relative velocity \mathbf{v}_{12} of the colliding particles, and their relative position at contact \mathbf{r}_{12} , and they confirmed their results by MD simulations. Their observations made it clear that further arguments are needed to clarify the meaning of the χ factor in Enskog's formulation of the molecular chaos assumption. This will be done in Sec. II A.

The breakdown of molecular chaos at higher densities in classical fluids with conservative forces has been extensively investigated in the 1960s and 1970s [19]. This breakdown is caused by sequences of correlated binary collisions, the so-called ring collisions [20]. They lead to long-time tails in velocity and stress autocorrelation functions [21,22], and to long-range spatial correlations in NESS [13]. The quantitative effects of velocity correlations on transport coefficients at liquid densities are also significant. For instance, molecular-dynamics simulations on elastic hard-sphere systems at liquid densities [23] have shown that the long-time tails increase the measured self-diffusion coefficient D typically by 15 to 20 % with respect to the prediction of the Enskog theory $D_E = D_B/\chi$, where D_B is the Boltzmann value of the self-diffusion coefficient.

A well-known example of short-scale structure in granular fluids are the position-velocity correlations leading to the phenomenon of inelastic collapse [24,25], which is a *divergence* of the collision frequency ω in a finite time. The collapse singularity implies that an infinite number of collisions occurs within a finite-time interval in a subset of (nearly) touching particles, ordered in linear arrays. The phenomenon is, however, an artifact of the assumption that the coefficient of restitution α is independent of the impact velocities, whereas on physical grounds $\alpha(v_{12}) \rightarrow 1$ (elastic limit), as the relative velocity v_{12} vanishes. Molecular-dynamics simu-

lations have shown that the assumption of molecular chaos is also violated in undriven granular fluids in their late stages of evolution, the so-called nonlinear clustering regime. For instance, the measured distribution of impact parameters is not uniform, as expected on the basis of molecular chaos, but biased toward grazing collisions [26–28].

As shown below, in the driven IHS fluid there is an important additional reason for the breakdown of molecular chaos, namely, the strong increase in collision frequency at small relative velocities between two isolated particles, caused by the so-called noise-induced re-collisions. This correction to the collision frequency, that is important at all densities, is also neglected in the molecular chaos assumption.

The main goal of this paper is to quantify, analyze, and interpret the effects of the breakdown of molecular chaos in the NESS of inelastic hard spheres that are subject to a random external force between collisions. We will focus in particular on velocity-velocity correlations and position-velocity correlations between particles almost in contact, i.e., the short-scale structure.

Section II presents the analytic results, based on the Enskog-Boltzmann equation, which has been modified to account for the external energy input. In Sec. III, we present molecular-dynamics results for several quantities that characterize the collision processes and related short-scale structure of the NESS, and make a comparison with predictions based on molecular chaos.

II. KINETIC THEORY FOR THE NESS

A. Molecular chaos and Enskog approximation

The Enskog-Boltzmann equation for the single-particle distribution $\hat{f}(\mathbf{v}_1, t)$ in a spatially homogeneous randomly driven fluid of inelastic hard spheres of diameter σ reads in $d=2$ or 3 dimensions [9]

$$\begin{aligned} \partial_t \hat{f}(\mathbf{v}_1, t) = & n \chi \sigma^{d-1} \int d\mathbf{v}_2 \int d\hat{\boldsymbol{\sigma}} \Theta(\mathbf{v}_{12} \cdot \hat{\boldsymbol{\sigma}}) (\mathbf{v}_{12} \cdot \hat{\boldsymbol{\sigma}}) \\ & \times \left\{ \frac{1}{\alpha^2} \hat{f}(\mathbf{v}_1^{**}, t) \hat{f}(\mathbf{v}_2^{**}, t) - \hat{f}(\mathbf{v}_1, t) \hat{f}(\mathbf{v}_2, t) \right\} \\ & + \frac{\xi_0^2}{2} \left(\frac{\partial}{\partial \mathbf{v}_1} \right)^2 \hat{f}(\mathbf{v}_1, t), \end{aligned} \quad (1)$$

where $\mathbf{v}_{12} = \mathbf{v}_1 - \mathbf{v}_2$ and n the number density. The Heaviside function $\Theta(x)$ restricts the $\hat{\boldsymbol{\sigma}}$ integration to the hemisphere $\mathbf{v}_{12} \cdot \hat{\boldsymbol{\sigma}} > 0$, where $\hat{\boldsymbol{\sigma}}$ is the unit vector along the line of centers of the colliding spheres at contact, pointing from particle 2 to 1. In the sequel $\hat{\mathbf{a}} = \mathbf{a}/|\mathbf{a}|$ denotes a unit vector. The gain term of the collision integral describes the *restituting* collisions that convert the precollision velocities ($\mathbf{v}_1^{**}, \mathbf{v}_2^{**}$) into ($\mathbf{v}_1, \mathbf{v}_2$), while the loss term describes the *direct* collisions, and contains the precollision velocities ($\mathbf{v}_1, \mathbf{v}_2$) leading to postcollision velocities ($\mathbf{v}_1^*, \mathbf{v}_2^*$). The postcollision and restituting velocities have been defined in [29]. The χ factor will be discussed below.

As derived in [9], the Fokker-Planck term accounts for the external energy input, and describes diffusion in velocity space with a diffusivity proportional to the rate of energy input ξ_0^2 per unit mass. Here, ξ_0 is the strength of the random driving force, which is assumed to be Gaussian white noise [9,10].

Before studying the short-scale structure, we consider the single-particle distribution function $\hat{f}(\mathbf{v})$ in the NESS. The stationary solution of Eq. (1) is determined by the balance $m\xi_0^2 = \Gamma$, of external heating $m\xi_0^2$, and internal loss of energy due to collisions, Γ . It is characterized by a time-independent temperature $T = \langle mv^2/d \rangle$ defined as the average kinetic energy per particle, and discussed in paper I. As mentioned in the introduction, this stationary solution exhibits an overpopulated high-energy tail $\hat{f} \sim \exp[-Cv^{3/2}]$. The structure of the tail distribution is determined by collisions of very energetic particles with “thermal” particles, and may be obtained by neglecting the gain term in the Boltzmann equation [9].

In Ref. [9], $\hat{f}(\mathbf{v})$ has been calculated by solving the Enskog-Boltzmann Eq. (1) by an expansion in Sonine polynomials. To formulate this result, it is convenient to introduce a rescaled distribution function $f(\mathbf{c})$, defined by $\hat{f}(\mathbf{v}) \equiv [1/v_0^d]f(\mathbf{c})$ with $\mathbf{c} \equiv \mathbf{v}/v_0$, where $v_0 \equiv \sqrt{2T/m}$ is the thermal velocity and d the dimensionality. This gives

$$f(\mathbf{c}) = \varphi(c) \left\{ 1 + a_2 \left[\frac{1}{2}c^4 - \frac{1}{2}(d+2)c^2 + \frac{1}{8}d(d+2) \right] + \dots \right\}, \quad (2)$$

where the Maxwellian $\varphi(c) \equiv \pi^{-d/2} \exp(-c^2)$. Note that a_2 is proportional to the fourth cumulant of the scaling form $f(\mathbf{c})$, i.e.,

$$a_2 = \frac{4}{d(d+2)} \left[\langle c^4 \rangle - \frac{1}{4}d(d+2) \right] = \frac{4}{3} [\langle c_x^4 \rangle - 3\langle c_x^2 \rangle^2], \quad (3)$$

and vanishes in the elastic limit. An explicit calculation to linear order in a_2 gives [9]

$$a_2 = \frac{16(1-\alpha)(1-2\alpha^2)}{73+56d-24\alpha d-105\alpha+30(1-\alpha)\alpha^2}. \quad (4)$$

In the next section, this prediction will be tested against molecular-dynamics simulations.

Consider first the exact expression for the mean collision frequency in the homogeneous NESS, defined as

$$\omega = n\sigma^{d-1} \int d\mathbf{v}_1 \int d\mathbf{v}_2 \int d\hat{\boldsymbol{\sigma}} \Theta \times (-\mathbf{v}_{12} \cdot \hat{\boldsymbol{\sigma}}) |\mathbf{v}_{12} \cdot \hat{\boldsymbol{\sigma}}| \hat{f}^{(2)}(\mathbf{v}_1, \mathbf{v}_2, \boldsymbol{\sigma}), \quad (5)$$

where $\hat{f}^{(2)}(\mathbf{v}_1, \mathbf{v}_2, \boldsymbol{\sigma})$ is the *dynamic* or *constrained* pair-distribution function with velocities aiming to collide, just *before* contact with $\mathbf{r}_{12} = \boldsymbol{\sigma}$. *Molecular chaos*, also referred to as mean-field theory, requires the complete factorization of the dynamic precollisional pair function,

$$\hat{f}^{(2)}(\mathbf{v}_1, \mathbf{v}_2, \boldsymbol{\sigma}) = \chi \hat{f}(\mathbf{v}_1) \hat{f}(\mathbf{v}_2). \quad (6)$$

What is the meaning of the χ factor, used in formulating the *molecular chaos* hypothesis? This hypothesis for *dilute gases* concerns the absence of correlations in *precollision* velocities, and in *precollision* positions ($\chi = 1$). In *dense fluids* on the other hand, the precollision position correlation χ is different from 1, but the precollision velocity-velocity and position-velocity correlations are still assumed to be absent.

In the literature, it is common to take χ equal to the radial distribution function at contact in *local equilibrium*, i.e., $\chi = \chi_E \equiv g_{\text{eq}}(r \rightarrow \sigma + 0)$, which mainly accounts for precollision hard-core exclusion effects. For hard disks and hard spheres, the latter function is approximately given by the Verlet-Levesque (2D) and Carnahan-Starling (3D) approximations [31],

$$\chi_E(\phi) = \left(1 - \frac{7}{16}\phi \right) / (1 - \phi)^2 \quad (2D),$$

$$\chi_E(\phi) = (2 - \phi)/2(1 - \phi)^3 \quad (3D), \quad (7)$$

where the packing fraction in d dimensions is defined as $\phi = n(\sigma/2)^d \Omega_d/d$, and $\Omega_d = 2\pi^{d/2}/\Gamma(d/2)$ is the surface area of a d -dimensional unit sphere. In this paper, we refer to the molecular chaos approximation with $\chi = \chi_E$, as the *Enskog approximation*.

In principle, different options are open for the χ factor. As $\hat{f}^{(2)}$ is the dynamic precollision pair-distribution function at contact, an alternative choice for the χ in the factorized form could be the dynamic precollision radial distribution function at contact, defined as an average over the precollision hemisphere,

$$\chi^{(-)} \equiv [2/\Omega_d] \int d\mathbf{v}_1 \int d\mathbf{v}_2 \int d\hat{\boldsymbol{\sigma}} \Theta(-\mathbf{v}_{12} \cdot \hat{\boldsymbol{\sigma}}) \hat{f}^{(2)}(\mathbf{v}_1, \mathbf{v}_2, \boldsymbol{\sigma}). \quad (8)$$

Another option could be the unconstrained radial distribution, $g(r)$, in the NESS, extrapolated to contact ($r \rightarrow \sigma$). This function is further discussed in Sec. II D.

For the randomly heated fluid under study here, the dynamics is not purely hard-sphere like. The random force acting on the particles may be expected to contribute to the value of the pair-distribution function at contact. This effect will be addressed in the subsequent sections.

Equation (5) with $\hat{f}(\mathbf{v})$ replaced by the Maxwellian, yields for the collision frequency in the molecular chaos approximation $\omega_{\text{mc}}(T) = \chi \omega_0(T)$, and more specifically, in the Enskog approximation,

$$\omega_E(T) = \chi_E \omega_0(T). \quad (9)$$

Here, the Boltzmann collision frequency for dilute gases is given by

$$\omega_0(T) = \Omega_d n \sigma^{d-1} \sqrt{T/\pi m}, \quad (10)$$

and the small correction of $\mathcal{O}(a_2)$ appearing in Eq. (2) has been neglected.

Spatial correlation functions in nonequilibrium stationary states are quite different from local equilibrium ones, and show long-range correlations due to correlated sequences of ring collisions, also referred to as mode-coupling effects [13]. In paper I, we have shown the existence of very long-range correlations $\sim 1/r^{d-2}$ in the randomly driven IHS fluid. The short-range correlations in the NESS may, in principle, be obtained from the ring kinetic equation for IHS (see Ref. [29]). However, systematic methods to evaluate collisional integrals and pair-correlation functions at short distances using this ring kinetic theory have not yet been developed. In the section on simulation results, we return to the

effects of ring collisions, and present arguments why their contributions are expected to be more important here than for elastic hard spheres.

B. Collisional averages

In hard-sphere systems, there are many properties that involve the pair-distribution function of particles just before collision. To study these, it is convenient to introduce the collisional average $\langle \dots \rangle_{\text{coll}}$ for a quantity A in the NESS, defined as

$$\langle A(\mathbf{v}_1, \mathbf{v}_2, \boldsymbol{\sigma}) \rangle_{\text{coll}} = \frac{\int d\mathbf{v}_1 \int d\mathbf{v}_2 \int d\hat{\boldsymbol{\sigma}} \Theta(-\mathbf{v}_{12} \cdot \hat{\boldsymbol{\sigma}}) |\mathbf{v}_{12} \cdot \hat{\boldsymbol{\sigma}}| A(\mathbf{v}_1, \mathbf{v}_2, \boldsymbol{\sigma}) \hat{f}^{(2)}(\mathbf{v}_1, \mathbf{v}_2, \boldsymbol{\sigma})}{\int d\mathbf{v}_1 \int d\mathbf{v}_2 \int d\hat{\boldsymbol{\sigma}} \Theta(-\mathbf{v}_{12} \cdot \hat{\boldsymbol{\sigma}}) |\mathbf{v}_{12} \cdot \hat{\boldsymbol{\sigma}}| \hat{f}^{(2)}(\mathbf{v}_1, \mathbf{v}_2, \boldsymbol{\sigma})}. \quad (11)$$

In the sequel, it is more convenient to work with a rescaled pair-distribution function $\hat{f}^{(2)}(\mathbf{v}_1, \mathbf{v}_2, \mathbf{r}_{12}) = [1/v_0^{2d}] f^{(2)}(\mathbf{c}_1, \mathbf{c}_2, \mathbf{r}_{12})$. To express the collisional averages (11) in rescaled variables, one replaces $\hat{f}^{(2)}$ by $f^{(2)}$, \mathbf{v}_i by \mathbf{c}_i , \mathbf{v}_{12} by $\mathbf{g} = \mathbf{c}_1 - \mathbf{c}_2$, and $A(\mathbf{v}_1, \mathbf{v}_2, \boldsymbol{\sigma})$ by $A(v_0 \mathbf{c}_1, v_0 \mathbf{c}_2, \boldsymbol{\sigma})$.

These objects may be conveniently computed in event-driven molecular-dynamics algorithms for hard-sphere systems [30]. Collisional averages are defined for particles that are about to collide (i.e., $|r_{12}| = \sigma + 0$), and may be calculated from kinetic theory using the molecular chaos assumption, possibly supplemented with the Enskog approximation at higher densities.

Collisional averages of great importance are the collisional energy loss per unit time $(d/2)n\Gamma$, and the excess hydrostatic pressure $p - nT$, resulting from collisional transfer of momentum. With a minor generalization to d dimensions, we obtain from Ref. [32] the exact expression for the pressure in the NESS

$$\begin{aligned} \frac{p(T)}{nT} - 1 &= \left(\frac{1+\alpha}{2d} \right) n \sigma^d \int d\mathbf{c}_1 \int d\mathbf{c}_2 \int d\hat{\boldsymbol{\sigma}} \\ &\times \Theta(-\mathbf{g} \cdot \hat{\boldsymbol{\sigma}}) |\mathbf{g} \cdot \hat{\boldsymbol{\sigma}}|^2 f^{(2)}(\mathbf{c}_1, \mathbf{c}_2, \boldsymbol{\sigma}) \\ &= \left(\frac{1+\alpha}{2d} \right) \frac{\sigma \omega}{v_0} \langle |\mathbf{g} \cdot \hat{\boldsymbol{\sigma}}| \rangle_{\text{coll}}. \end{aligned} \quad (12)$$

The second equality is obtained by introducing the collisional average (11) and expressing its denominator in terms of the collision frequency given by Eq. (5). In fact, inserting Eq. (6) into the first line of Eq. (12) allows one to carry out the $\hat{\boldsymbol{\sigma}}$ integration, and the right-hand side becomes proportional to the rescaled velocity average $\int d\mathbf{c}_1 \int d\mathbf{c}_2 g^2 f(\mathbf{c}_1) f(\mathbf{c}_2) = 2$ without any further assumption about neglecting the term proportional to a_2 in Eq. (2). This argument is special for the pressure, as other moments

involve the knowledge of the complete $f(c)$. Indeed, the generic collisional average becomes $\langle |\mathbf{g} \cdot \hat{\boldsymbol{\sigma}}|^m \rangle_{\text{coll}} = 2^{m/2} \Gamma[(1/2)m + 1]$, independent of dimensionality, assuming molecular chaos (6) and replacing $f(c)$ by the Maxwellian $\varphi(c)$ (the contributions coming from a_2 are quite small and may be neglected; they have been computed in [9]). Finally, the pressure may be expressed as

$$\frac{p_{\text{mc}}(T)}{nT} - 1 = 2^{d-2} (1+\alpha) \chi \phi. \quad (13)$$

Different choices for χ yield different approximations. For instance, with $\chi = \chi_E$, we obtain the Enskog approximation $p_E(T)$ for the pressure of IHS.

In the elastic limit $p_E(T)$ at $\alpha = 1$ gives the standard equation of state for elastic hard disks or spheres. Notice that the pressure for IHS is only defined *kinetically* as the momentum flux, which leads to Eq. (12). A statistical mechanical derivation of the equation of state from the partition function or free energy for the IHS fluid does not exist.

In a similar manner, we obtain the exact expression for the collisional damping rate

$$\begin{aligned} \Gamma(T) &= \left(\frac{1-\alpha^2}{2d} \right) n \sigma^{d-1} v_0 T \int d\mathbf{c}_1 \int d\mathbf{c}_2 \int d\hat{\boldsymbol{\sigma}} \\ &\times \Theta(-\mathbf{g} \cdot \hat{\boldsymbol{\sigma}}) |\mathbf{g} \cdot \hat{\boldsymbol{\sigma}}|^3 f^{(2)}(\mathbf{c}_1, \mathbf{c}_2, \boldsymbol{\sigma}) \\ &= \gamma_0 \omega T \langle |\mathbf{g} \cdot \hat{\boldsymbol{\sigma}}|^2 \rangle_{\text{coll}} = m \xi_0^2, \end{aligned} \quad (14)$$

where $\gamma_0 = (1-\alpha^2)/2d$ is the dimensionless damping constant introduced in Refs. [9,10]. The last equality (14) expresses the balance between the energy input due to the white noise, and the collisional loss of energy in the NESS, and determines the temperature T in the NESS. By special-

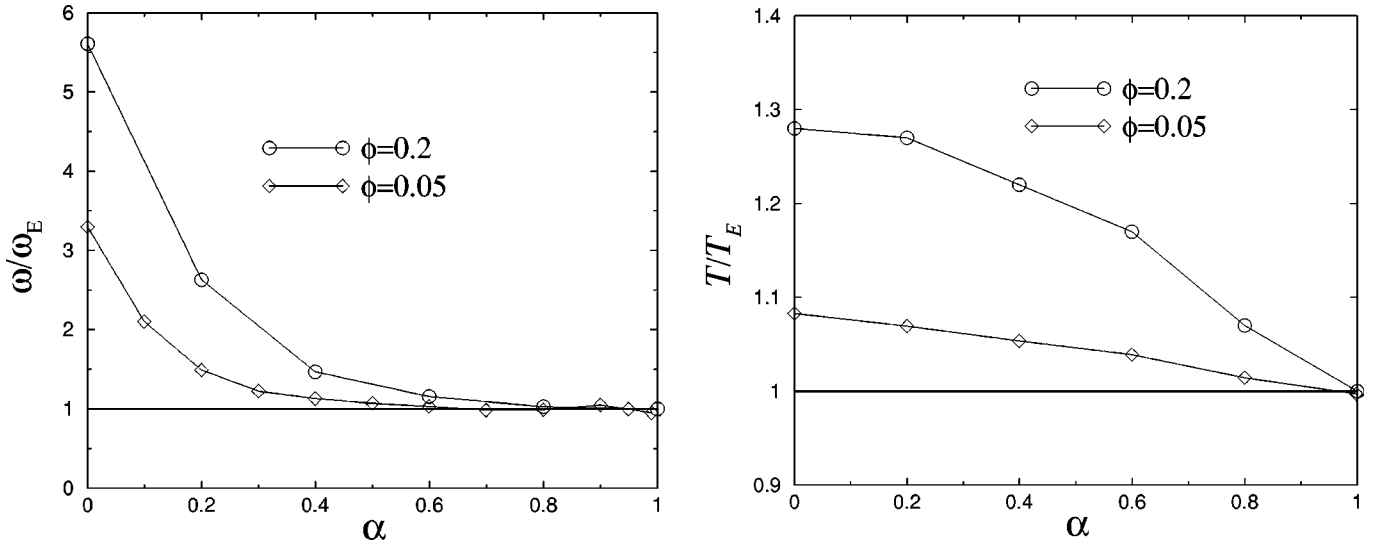


FIG. 1. Kinetic temperature T/T_E and collision frequency ω/ω_E where T_E and ω_E are defined in Eqs. (17) and (19), for a packing fractions $\phi=0.05$ and $\phi=0.2$.

izing this equation to the Enskog mean-field approximation, $f^{(2)} = \chi_E f f$, where $\langle |\mathbf{g} \cdot \hat{\boldsymbol{\sigma}}|^2 \rangle_{\text{coll}} = 2$, we obtain the approximate result

$$\Gamma_E(T) = 2\gamma_0\omega_E(T)T \quad (15)$$

and similar relations for different choices of χ . It is convenient to define a *reference* temperature T_E through the relation

$$\Gamma_E(T_E) = m\xi_0^2, \quad (16)$$

or more explicitly

$$T_E = m \left(\frac{\xi_0^2 \sqrt{\pi}}{2\gamma_0 \Omega_d \chi_E n \sigma^{d-1}} \right)^{2/3}. \quad (17)$$

Moreover, the definition of T_E combined with the NESS condition $\Gamma(T) = m\xi_0^2$ implies the relation $\Gamma(T) = \Gamma_E(T_E)$, and consequently,

$$\frac{\Gamma(T)}{\Gamma_E(T)} = \frac{\Gamma_E(T_E)}{\Gamma_E(T)} = \left(\frac{T_E}{T} \right)^{3/2}. \quad (18)$$

In the sequel, we will also use a reference frequency ω_E without any argument to denote

$$\omega_E \equiv \omega_E(T_E) = \chi_E \Omega_d n \sigma^{d-1} \sqrt{T_E / \pi m}. \quad (19)$$

Although we will discuss the simulation results in detail in the next section, it is of interest already at this point to note that for these systems, as shown in Fig. 1, the ratio of the kinetic temperature and the reference temperature, T/T_E , is only somewhat larger than one for all α , that it approaches one in the elastic limit ($\alpha \rightarrow 1$), and that it monotonically increases with decreasing α (see Fig. 1). The same figure shows that the ratio, ω/ω_E also approaches one for $\alpha \rightarrow 1$, with a steep increase to a value 5.6 as $\alpha \rightarrow 0$. Further discus-

sion of these points is postponed until Sec. III. If the Enskog factorization $\hat{f}^{(2)} = \chi_E \hat{f} \hat{f}$ would be exact, then $T = T_E$ and $\omega = \omega_E$.

A third quantity of interest, the precollisional $\chi^{(-)}$ factor, defined in Eq. (8), may also be expressed as a collisional average using Eq. (11),

$$\chi^{(-)} = (2\omega/\Omega_d n \sigma^{d-1} v_0) \langle |\mathbf{g} \cdot \hat{\boldsymbol{\sigma}}|^{-1} \rangle_{\text{coll}}. \quad (20)$$

Before closing this section, a *caveat* about internal consistency is appropriate. To obtain consistent theoretical predictions for the pressure p or dissipation rate Γ , it is paramount that both factors ω and $\langle |\mathbf{g} \cdot \boldsymbol{\sigma}|^m \rangle_{\text{coll}}$ be calculated using identical approximations for $f^{(2)}$. For instance, the mean-field or molecular chaos approximation for the dissipation rate, $\Gamma_E(T) = 2\gamma_0\omega T$,—an expression commonly used in granular hydrodynamic equations—should necessarily be combined with $\omega_E(T)$ in Eq. (9). Any improved theoretical calculation for ω without a concomitant correction to the mean-field result for $\langle |\mathbf{g} \cdot \boldsymbol{\sigma}|^m \rangle_{\text{coll}}$ is *inconsistent*.

C. Velocity distributions

We study a variety of collisional averages and corresponding probability distributions. By choosing $A(\mathbf{c}_1, \mathbf{c}_2, \boldsymbol{\sigma}) = \delta(|\mathbf{g}| - g)$ we obtain the probability $P_r(g)$ that two colliding particles have a relative speed $|\mathbf{c}_{12}| = g$. From here on, we only quote results for two dimensions. *Analytic* calculations are based on the molecular chaos assumption (6) in combination with Eq. (2). Inspection of Eq. (11) shows that under this assumption, the collisional averages are independent of the χ factor. Straightforward algebra gives for the constrained g distribution,

$$\begin{aligned} P_r(g) &= \langle \delta(|\mathbf{c}_{12}| - g) \rangle_{\text{coll}} \\ &= \sqrt{\frac{2}{\pi}} g^2 e^{-1/2 g^2} \left\{ 1 + \frac{1}{16} a_2 (g^4 - 8g^2 + 9) \right\}. \end{aligned} \quad (21)$$

Similarly, we obtain the probability distribution for the center of mass velocity $\mathbf{G} \equiv 1/2(\mathbf{c}_1 + \mathbf{c}_2)$,

$$P_{\text{CM}}(G) = \langle \delta(|\mathbf{C}| - G) \rangle_{\text{coll}} = 4Ge^{-2G^2} \{1 + a_2(G^4 - G^2)\}. \quad (22)$$

It equals the unconstrained equilibrium distribution function apart from a small term of $\mathcal{O}(a_2)$. Furthermore, the probability that the precollision speed $|\mathbf{c}_i|$ of one of the colliding particles ($i=1,2$) has a value v is

$$P(v) = \langle \delta(|\mathbf{c}_1| - v) \rangle_{\text{coll}} = \sqrt{2}ve^{-3v^2/2} \left\{ (1+v^2)I_0\left(\frac{1}{2}v^2\right) + v^2I_1\left(\frac{1}{2}v^2\right) \right\}, \quad (23)$$

whereas the unconstrained distribution is $\sim v \exp(-v^2)$. In evaluating this collisional average, we neglect the a_2 contribution, and carry out the constrained $\hat{\sigma}$ integration. To calculate the remaining integral $\int d\mathbf{c}_2 c_{12} \varphi(c_2)$, we change integration variables to \mathbf{g} expressed in polar coordinates $\{g, \phi\}$, and use the relation $\int_0^\pi d\phi \exp(-2c_{1g} \cos \phi) = \pi I_0(2c_{1g})$. The subsequent g integration follows from (6.618.4) in Ref. [33]. Using the asymptotic expressions $I_0(x) \sim I_1(x) \sim \exp(x)/\sqrt{2\pi x}$ for the modified Bessel functions of the zeroth and first order, we obtain the high-energy behavior $P(v) \sim 2\sqrt{2/\pi}v^2 \exp(-v^2)$.

In a similar manner, we obtain the following velocity moments and correlations, using the molecular chaos assumption:

$$\langle g^2 \rangle_{\text{coll}} = 3 \left\{ 1 + \frac{1}{4}a_2 \right\}, \quad \langle G^2 \rangle_{\text{coll}} = \frac{1}{2} \left\{ 1 + \frac{1}{2}a_2 \right\},$$

$$\langle g^{*2} \rangle_{\text{coll}} = \langle g^2 \rangle_{\text{coll}} - (1 - \alpha^2) \left\{ 1 + \frac{1}{4}a_2 \right\},$$

$$\langle c_1^2 \rangle_{\text{coll}} = \langle G^2 \rangle_{\text{coll}} + \frac{1}{4} \langle g^2 \rangle_{\text{coll}} = \frac{5}{4} \left\{ 1 + \frac{7}{20}a_2 \right\},$$

$$\langle \mathbf{c}_1 \cdot \mathbf{c}_2 \rangle_{\text{coll}} = \langle G^2 \rangle_{\text{coll}} - \frac{1}{4} \langle g^2 \rangle_{\text{coll}} = -\frac{1}{4} \left\{ 1 - \frac{1}{4}a_2 \right\},$$

$$\langle \mathbf{c}_1^* \cdot \mathbf{c}_2^* \rangle_{\text{coll}} = \langle \mathbf{c}_1 \cdot \mathbf{c}_2 \rangle_{\text{coll}} + \frac{1}{2}(1 - \alpha^2) \left\{ 1 + \frac{1}{4}a_2 \right\}. \quad (24)$$

Here, \mathbf{c}_i^* are the postcollision velocities, as defined in paper I. The sum of the third and fourth equality depends only on the center-of-mass velocity, i.e., $\langle G^2 \rangle_{\text{coll}}$. In the elastic limit $\alpha \rightarrow 1$, the average energy of a particle that is about to collide $\langle c^2 \rangle_{\text{coll}} = (5/4)\langle c^2 \rangle$, is above the mean energy per particle $\langle c^2 \rangle$, which equals unity.

In the molecular chaos approximation, an average such as $\langle (\mathbf{c}_1 \cdot \mathbf{c}_2)^m g^n \rangle_{\text{coll}}$ with $\{m, n\}$ integers, is in general nonvanishing, except in the special case $n = -1$. Then, $\langle (\mathbf{c}_1 \cdot \mathbf{c}_2)^m / g \rangle_{\text{coll}}$ reduces to an unconstrained average, proportional to $\langle (\mathbf{c}_1 \cdot \mathbf{c}_2)^m \rangle$, which vanishes for odd values of m . Additional information about the relative orientation of the incoming velocities may be obtained from the distribution of the angle ψ_{12} , defined by $\mathbf{c}_1 \cdot \mathbf{c}_2 = c_1 c_2 \cos \psi_{12}$. A numerical calculation (again neglecting a_2 corrections) gives $\langle \cos \psi_{12} \rangle_{\text{coll}} \approx -0.233$, which is close to the value -0.2 , estimated from $\langle \mathbf{c}_1 \cdot \mathbf{c}_2 \rangle_{\text{coll}} \approx \langle c_1^2 \rangle_{\text{coll}} \langle \cos \psi_{12} \rangle_{\text{coll}}$ using the above results.

A very sensitive probe for studying the violation of molecular chaos is the probability distribution $P(b)$ of impact parameters $b = |\hat{\mathbf{g}} \times \hat{\sigma}| = \sin \theta$, where $\theta = \cos^{-1}(\hat{\mathbf{g}} \cdot \hat{\sigma})$ is the angle of incidence. It is defined as the collisional average

$$P(b) = \langle \delta(b - |\hat{\mathbf{g}} \times \hat{\sigma}|) \rangle_{\text{coll}} = \frac{\int d\hat{\sigma} \int d\mathbf{c}_1 \int d\mathbf{c}_2 \delta(b - |\hat{\mathbf{g}} \times \hat{\sigma}|) |\mathbf{g} \cdot \hat{\sigma}| \Theta(-\hat{\mathbf{g}} \cdot \hat{\sigma}) f^{(2)}(\mathbf{c}_1, \mathbf{c}_2, \sigma)}{\int d\hat{\sigma} \int d\mathbf{c}_1 \int d\mathbf{c}_2 |\mathbf{g} \cdot \hat{\sigma}| \Theta(-\hat{\mathbf{g}} \cdot \hat{\sigma}) f^{(2)}(\mathbf{c}_1, \mathbf{c}_2, \sigma)}, \quad (25)$$

and $P(b)$ can be easily computed in a molecular-dynamics experiment. As long as molecular chaos holds, the distribution of b is independent of the functional form of f and we obtain straightforwardly

$$P(b) = \begin{cases} (d-1)b^{d-2} & \text{if } 0 < b < 1 \\ 0 & \text{otherwise,} \end{cases} \quad (26)$$

which reduces in two dimensions to the uniform distribution,

$$P(b) = \begin{cases} 1 & \text{if } 0 < b < 1 \\ 0 & \text{otherwise.} \end{cases} \quad (27)$$

In order to analyze molecular chaos breakdown in more detail, we have introduced a collection of moments M_{nm} and their dimensionless counterparts B_{nm} for $n, m = \{0, 1, 2, \dots\}$, (see definition below), to analyze in detail the possible breakdown of the molecular chaos factorization (6). These moments $M_{nm}(T)$ of the pair distribution at contact are defined as,

$$M_{nm}(T) \equiv \frac{2}{\Omega_d} \int d\mathbf{v}_1 d\mathbf{v}_2 \int d\hat{\sigma} \Theta \times (-\mathbf{v}_{12} \cdot \hat{\sigma}) \hat{f}^{(2)}(\mathbf{v}_1, \mathbf{v}_2, \sigma | T) v_{12}^n |\cos \theta|^m, \quad (28)$$

which are averages over the precollision hemisphere, where $\theta = \cos^{-1}(\hat{\mathbf{g}} \cdot \hat{\boldsymbol{\sigma}})$. Let $M_{nm}^E(T_E)$ denote the same quantity evaluated in Enskog's formulation of the *molecular chaos* approximation, and evaluated at the reference temperature T_E , i.e., evaluated with $\hat{f}^{(2)}(\mathbf{v}_1, \mathbf{v}_2, \boldsymbol{\sigma}|T)$ replaced by $\chi_E \hat{f}(\mathbf{v}_1|T_E) \hat{f}(\mathbf{v}_2|T_E)$, then the reduced moments are defined as

$$B_{nm}(T) = M_{nm}(T)/M_{nm}^E(T_E), \quad (29)$$

where $M_{nm}^E(T_E)$ is evaluated in Eq. (A2). It is proportional to v_E^n , where $v_E = \sqrt{2T_E/m}$. We prefer to normalize the reduced moments by $M_{nm}^E(T_E)$, because its analytic form is given explicitly. One could also normalize by $M_{nm}^E(T) = (T_E/T)^{n/2} M_{nm}^E(T_E)$. The disadvantage of $M_{nm}^E(T)$ is that the computation requires the simulated values of the kinetic temperature T . The collisional averages $\langle v_{12}^n |\cos \theta|^m \rangle_{\text{coll}}$ expressed in terms of these new moments give

$$\langle v_{12}^n |\cos \theta|^m \rangle_{\text{coll}} = \frac{M_{n+1, m+1}(T)}{M_{11}(T)}. \quad (30)$$

We first observe that the average collision frequency ω , defined in Eq. (5), is proportional to $M_{11}(T)$, so that

$$B_{11}(T) = \frac{M_{11}(T)}{M_{11}^E(T_E)} = \frac{\omega}{\omega_E} \quad (31)$$

with ω_E defined in Eq. (19). This implies that the reduced moments $B_{nm}(T)$ may all be expressed in collisional averages, i.e.,

$$B_{nm}(T) = \frac{\omega}{\omega_E} \frac{\langle v_{12}^{n-1} |\cos \theta|^{m-1} \rangle_{\text{coll}}}{\langle v_{12}^{n-1} |\cos \theta|^{m-1} \rangle_{\text{coll}}^E}. \quad (32)$$

The average $\langle \dots \rangle_{\text{coll}}^E$ is defined through Eq. (30) with $M_{nm}(T)$ replaced by $M_{nm}^E(T_E)$, and calculated in Eq. (A2). It represents the collisional average, evaluated with the Enskog factorization $f^{(2)} = \chi_E f$ and also taken at the reference temperature T_E . Note that the equality (32) consists of two factors, ω and $\langle \dots \rangle_{\text{coll}}$, which are measured separately in event driven MD simulations.

We also observe that the equality $\Gamma(T) = \Gamma_E(T_E)$, explained above Eq. (18), implies that

$$B_{33}(T) = \frac{M_{33}(T)}{M_{33}^E(T_E)} = \frac{\Gamma(T)}{\Gamma_E(T_E)} = 1. \quad (33)$$

Furthermore, we have for the excess pressure $p^{\text{ex}}(T) \equiv p(T) - nT$,

$$B_{22}(T) = \frac{p^{\text{ex}}(T)/nT}{p_E^{\text{ex}}(T_E)/nT_E} = \frac{\omega}{\omega_E} \times \frac{\langle |v_{12} \cos \theta| \rangle_{\text{coll}}}{\langle |v_{12} \cos \theta| \rangle_{\text{coll}}^E} \quad (34)$$

and for the dynamic pair correlation at contact $\chi^{(-)}$,

$$B_{00}(T) = \frac{\chi^{(-)}}{\chi_E} = \frac{\langle |v_{12} \cos \theta|^{-1} \rangle_{\text{coll}}}{\langle |v_{12} \cos \theta|^{-1} \rangle_{\text{coll}}^E}. \quad (35)$$

In the Appendix, we present a more complete set of relations for the B_{nm} .

In the next section MD simulations will show that the predicted deviation from a Maxwellian [see Eq. (2)] in the (unconstrained) velocity distribution of a single particle may be observed for small inelasticities. However, *larger* deviations are found between the observed constrained probability distributions and averages, and the corresponding kinetic theory predictions given by Eq. (24), based on molecular chaos. Consequently, the small corrections resulting from a_2 in Eq. (2) may be neglected in most cases.

D. Radial distributions

The static or unconstrained radial distribution function in the spatially homogeneous IHS fluid is defined as

$$g(r) = \int \frac{d\hat{\boldsymbol{\sigma}}}{\Omega_d} \int d\mathbf{c}_1 d\mathbf{c}_2 f^{(2)}(\mathbf{c}_1, \mathbf{c}_2, r \hat{\boldsymbol{\sigma}}). \quad (36)$$

It may be averaged over all directions of \mathbf{r} because of statistical isotropy. The unconstrained radial distribution function at contact is defined as the extrapolation, $Y = g(r \rightarrow \sigma + 0)$. By splitting the $\hat{\boldsymbol{\sigma}}$ integration into a precollision ($\hat{\mathbf{g}} \cdot \hat{\boldsymbol{\sigma}} < 0$) and postcollision hemisphere ($\hat{\mathbf{g}} \cdot \hat{\boldsymbol{\sigma}} > 0$), we obtain Y as sum of two terms,

$$Y = \frac{1}{2} (Y^{(-)} + Y^{(+)}). \quad (37)$$

The definitions of $Y^{(-)}, Y^{(+)}$ follow from Eq. (36) by adding, respectively, factors $\Theta(-\hat{\mathbf{g}} \cdot \hat{\boldsymbol{\sigma}})$ and $\Theta(\hat{\mathbf{g}} \cdot \hat{\boldsymbol{\sigma}})$ under the integral sign in Eq. (36). The dummy integration variables in $Y^{(+)}$ represent the postcollision velocities, $(\mathbf{c}_1^*, \mathbf{c}_2^*)$, corresponding to the precollision ones, $(\mathbf{c}_1, \mathbf{c}_2)$.

On the other hand, we have the dynamic precollision correlation $\chi^{(-)}$, defined in Eq. (8), and a similar postcollision one, $\chi^{(+)}$, defined by replacing $\Theta(-\hat{\mathbf{g}} \cdot \hat{\boldsymbol{\sigma}})$ in Eq. (8) by $\Theta(\hat{\mathbf{g}} \cdot \hat{\boldsymbol{\sigma}})$. They are related by continuity of flux. Because the incident flux of $(\mathbf{c}_1 \mathbf{c}_2)$ pairs just before collision is equal to the scattered flux of $(\mathbf{c}_1^* \mathbf{c}_2^*)$ pairs just after collision, we have inside dynamic averages the equality

$$\begin{aligned} \Theta(-g_n) |g_n| f^{(2)}(\mathbf{c}_1 \mathbf{c}_2, \boldsymbol{\sigma}) d\mathbf{c}_1 d\mathbf{c}_2 d\hat{\boldsymbol{\sigma}} \\ = \Theta(g_n^*) |g_n^*| f^{(2)}(\mathbf{c}_1^* \mathbf{c}_2^*, \boldsymbol{\sigma}) d\mathbf{c}_1^* d\mathbf{c}_2^* d\hat{\boldsymbol{\sigma}}, \end{aligned} \quad (38)$$

where $g_n = \mathbf{g} \cdot \hat{\boldsymbol{\sigma}} = g \cos \theta$. The reflection law $g_n^* = \alpha |g_n|$, for inelastic collisions in combination with the continuity of the flux and Eq. (8) yields at once,

$$\chi^{(+)} = (1/\alpha) \chi^{(-)}. \quad (39)$$

In principle, Eqs. (37) and (20) provide two alternative routes to compute the precollisional pair correlation at con-

tact: the first one, denoted by $Y^{(-)}$, may be implemented numerically as a static or unconstrained average, namely, by extrapolation to contact of the pair-correlation function for pairs aiming to collide. The second one, denoted by $\chi^{(-)}$, may be computed as a dynamic collisional average, calculated from $f^{(2)}(\mathbf{c}_1, \mathbf{c}_2, \boldsymbol{\sigma})$ at contact. It is important to stress that the dynamic $\chi^{(-)}$ is calculated as a time average over the *subset of colliding pairs at contact*, and the static $Y^{(-)}$ as a time average over *all pairs*, satisfying the relation, $\mathbf{g} \cdot \hat{\boldsymbol{\sigma}} < 0$ and extrapolated to $r \rightarrow \sigma + 0$, i.e., calculated from $f^{(2)}(\mathbf{c}_1, \mathbf{c}_2, \mathbf{r})$, where the limit is taken after all integrations have been performed. This may lead to different results, because the integrand contains the function $f^{(2)}$ that turns out to be singular near $r = \sigma$ and \mathbf{v}_{12} small (see discussion in Sec. III C).

Physically, it is also clear why the averages in the NESS need not be the same. For instance, the relation (38) may not hold for the limiting ($r \rightarrow \sigma$) values, $Y^{(-)}$ and $Y^{(+)}$, because non-mean-field effects (in particular, the “rotation-induced” recollisions discussed at the start of Sec. III, or noise-induced recollisions, see below) may result in differences between the two methods to evaluate $\chi^{(-)}$ and $Y^{(-)}$. The reason is that the validity of Eq. (38), expressing flux continuity for the limiting values ($r \rightarrow \sigma + 0$), is questionable in the presence of the external random force. When the kicking frequency is much larger than the collision frequency (situation considered here), a pair of particles may indeed be put in contact under the action of the random force only. We will investigate possible numerical differences between $\chi^{(-)}$ and $Y^{(-)}$ in the next section on MD simulations.

In paper I, we have studied the long-range spatial correlation functions $G_{ab}(r)$ of the density field $n(\mathbf{r}, t)$ and the flow field $\mathbf{u}(\mathbf{r}, t)$ in the NESS. These functions are closely related to Eq. (36), i.e.,

$$\begin{aligned} G_{nn}(r) &= \frac{1}{n^2} \left\langle \sum_i \delta(\mathbf{r}_i - \mathbf{r}) \left[\sum_j \delta(\mathbf{r}_j) - n \right] \right\rangle \\ &= \frac{1}{n} \delta(\mathbf{r}) + (g(r) - 1) \end{aligned} \quad (40)$$

and, in the notation of paper I,

$$\begin{aligned} G_{\mathbf{u}\mathbf{u}}(r) &= \frac{1}{n^2} \left\langle \sum_{i,j} \mathbf{v}_i \cdot \mathbf{v}_j \delta(\mathbf{r}_i - \mathbf{r}) \delta(\mathbf{r}_j) \right\rangle \\ &= G_{\parallel}(r) + (d-1)G_{\perp}(r) \\ &= \frac{d}{2} \frac{v_0^2}{n} \delta(\mathbf{r}) + v_0^2 g(r) \langle \mathbf{c}_1 \cdot \mathbf{c}_2 \rangle(r), \end{aligned} \quad (41)$$

where $\langle \dots \rangle$ is an average over the N -particle nonequilibrium steady state and the static velocity correlation, $\langle \mathbf{c}_1 \cdot \mathbf{c}_2 \rangle(r)$, is defined as

$$\langle \mathbf{c}_1 \cdot \mathbf{c}_2 \rangle(r) = \int \frac{d\hat{\boldsymbol{\sigma}}}{\Omega_d} \int d\mathbf{c}_1 d\mathbf{c}_2 f^{(2)}(\mathbf{c}_1, \mathbf{c}_2, r\hat{\boldsymbol{\sigma}}) (\mathbf{c}_1 \cdot \mathbf{c}_2) / g(r). \quad (42)$$

The correlation functions $G_{ab}(r)$ above are very long ranged, decaying similar to r^{2-d} for large distances. In the first part of this section, we have introduced the static correlations, Y , $Y^{(\pm)}$, and the dynamic ones, $\chi^{(\pm)}$. In Eq. (A8) and (A9) we have done the same for the dynamic counter parts $\langle \mathbf{c}_1 \cdot \mathbf{c}_2 \rangle_{\text{dyn}}$ and $\langle \mathbf{c}_1 \cdot \mathbf{c}_2 \rangle_{\text{dyn}}^{(-)}$ of the static correlation $\langle \mathbf{c}_1 \cdot \mathbf{c}_2 \rangle(r \rightarrow \sigma)$, introduced in Eq. (41).

In the next section, the short-range behavior of these functions will be studied by MD simulations.

III. SIMULATION RESULTS FOR THE NESS

To investigate the short-scale structure characterizing the NESS and the validity of molecular chaos, we will present in this section MD simulation results, and compare these with our theoretical predictions whenever possible. The details of the simulations of the randomly driven inelastic hard disk system have been reported elsewhere [10]. We will work in the limit in which the kicking frequency of the external random force is much larger than the collision frequency. This is the limit in which the Fokker-Planck term in Eq. (1) models the random energy input through the random kicks. The external random force will, in principle, have a quantitative influence on the short range structure of the fluid. There is only one important difference with respect to the simulations carried out in [10]. There, the random rotation proposed in [36] was implemented to avoid inelastic collapse at high inelasticities ($\alpha < 0.5$). This procedure amounts to rotating the relative velocity \mathbf{g} by a small random angle after each collision. Consider the completely inelastic situation $\alpha = 0$ for the sake of the argument. After each collision, the vector \mathbf{g} lies exactly at the border of the precollisional hemisphere ($\mathbf{g} \cdot \hat{\boldsymbol{\sigma}} = 0$), so that if the aforementioned random angle has equiprobable positive and negative values, the rotation procedure will lead to a recollision with probability 1/2. This leads to a spurious increase of the number of collisions by a factor $\sum_{n=0}^{\infty} 1/2^n = 2$ (the recollision may itself induce a recollision with probability 1/2 etc. so that the frequency of collision effectively doubles). When α is small but nonvanishing, this effect is still present but weaker. This is clearly an artificial violation of molecular chaos that has been discarded in the present paper: for $\alpha < 0.5$, we have also implemented the rotation procedure, but if a small rotation leads to a recollision, a new angle is drawn until the pair separates. In this way, we reduce an important source of correlations (the effect is dramatic on all the low-order moments B_{nm} , not only on the collision frequency; in particular, the moments with $n \leq 1$ that correspond to collisional averages of negative powers of g , are strongly biased toward bigger values if the “rotation-induced recollisions” are present). After applying this rule, we are then left only with correlations induced by the hard sphere dynamics plus the ones induced by the noise itself (see below).

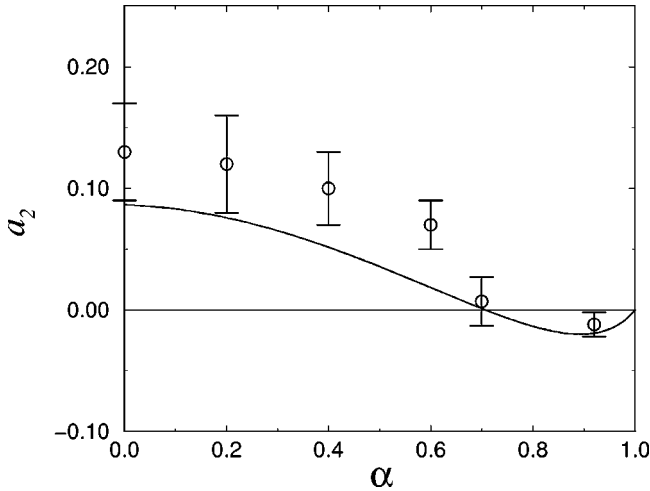


FIG. 2. Fourth cumulant as a function of the coefficient of restitution. Comparison is made between the two-dimensional version of Eq. (4) and MD results (circles) obtained for a system of 10 201 inelastic disks, measured at several densities (see Sec. III A).

A. Cumulants

First, we focus on the single-particle velocity distribution function f averaged over all particles, which deviates from a Maxwellian distribution due to the inelasticity of the collisions. In the previous section, we presented predictions for these deviations, assuming molecular chaos. The resulting expression given by Eq. (4) for the fourth cumulant a_2 of the distribution as well as the prediction for its overpopulated tail are in perfect agreement with three-dimensional (3D) direct simulation monte carlo (DSMC) results over the whole region of inelasticities [34]. As DSMC itself invokes molecular chaos, this observation merely justifies the approximations made in the analytic calculation. Information about the validity of molecular chaos may only be obtained from a comparison with molecular-dynamics simulations, and Fig. 2 shows this comparison for the fourth cumulant a_2 as a function of the coefficient of restitution α in 2D. The simulation results are in agreement with Eq. (4) for small inelasticity, but start to deviate significantly from the theoretical prediction at $\alpha = 0.6$. These deviations, together with the perfect agreement between the theoretical prediction and DSMC results, provide direct evidence for the breakdown of molecular chaos for $\alpha \leq 0.6$. The theoretical result (4) is independent of the density. As a_2 represents only a small correction in Eq. (2), one needs a large number of collisions and a large number of particles to reach sufficient statistical accuracy. So, high densities, for which one may use linked lists [30], are well suited. The data in Fig. 2 are typically obtained at high-packing fractions ($\phi = 0.63$ at $\alpha = 0.92$ and 0.7 , and $\phi = 0.55$ at $\alpha = 0.6$) and $N = 10\,201$ particles. At low densities and weaker inelasticities ($\alpha \geq 0.6$) we are unable to collect enough statistics to measure the small correction, represented by a_2 . Simulations at higher inelasticities did not show any density dependence of a_2 in the range $0.2 \leq \phi \leq 0.6$, suggesting that the cumulant expression (3), obtained from the Enskog-Boltzmann equation also applies at liquid

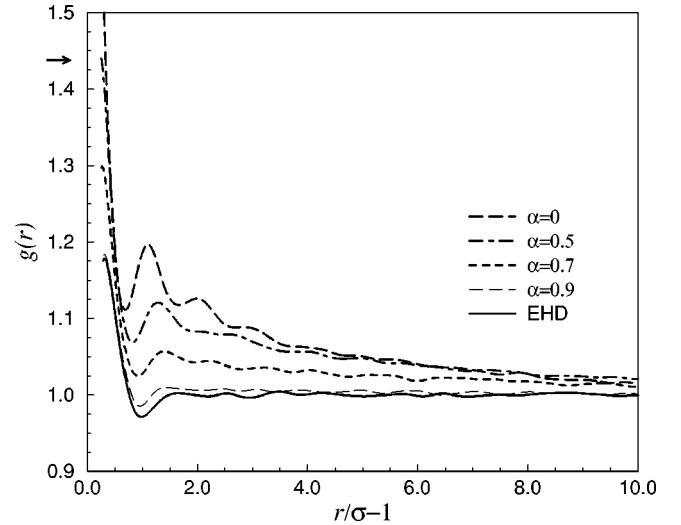


FIG. 3. Pair-distribution functions $g(r)$ versus distance between the particles at a packing fraction $\phi = 0.2$. The arrow indicates the value at contact for an elastic hard disc (EHD) fluid (from Verlet and Levesque [31]).

densities. Similar results as those displayed in Fig. 2 have been observed for the 3D version of the present model [11].

B. Radial distribution function

Next, we present results for the static or unconstrained radial distribution function $g(r)$, and in particular, its extrapolated values at contact $Y, Y^{(-)}, Y^{(+)}$. Here, $g(r)$ is essentially the density-density correlation function, whose long range behavior was studied in Ref. [10].

Figure 3 shows the measured values of $g(r)$ for short distances and packing fraction $\phi = 0.2$, at different inelasticities. At small inelasticities ($\alpha \approx 0.9$), $g(r)$ resembles the radial distribution function for elastic hard disks (EHD). At higher inelasticities, deviations start to appear: the first and second maximum in the measured $g(r)$ are enhanced with respect to their EHD values at the same density. Moreover, the functional shape also deviates from the corresponding pair distribution of EHD at an appropriately chosen *higher* density; e.g., if this density is chosen such that the value of the second maximum of the pair distribution of EHD coincides with the simulation result for IHD, the observed value at contact would still be underestimated by the EHD pair distribution.

It seems worthwhile to compare these results with existing experiments on granular fluids in which the pair distribution $g(r)$ has been measured. In the experiment of Ref. [2] on a vertically vibrated thin granular layer, $g(r)$ has been measured at $\phi = 0.46$. In the fluidized (“gaslike”) phase, it follows the equilibrium result for elastic hard disks almost identically. This result may be compared to our simulations for a randomly driven fluid of inelastic disks at $\alpha = 0.9$, corresponding to the value for stainless steel balls used in the experiment. It would be of interest to measure experimentally how $g(r)$ in the fluidized phase depends on the inelasticity, and see if a behavior similar to that of Fig. 3 is observed. It is also interesting to note that the pair-correlation

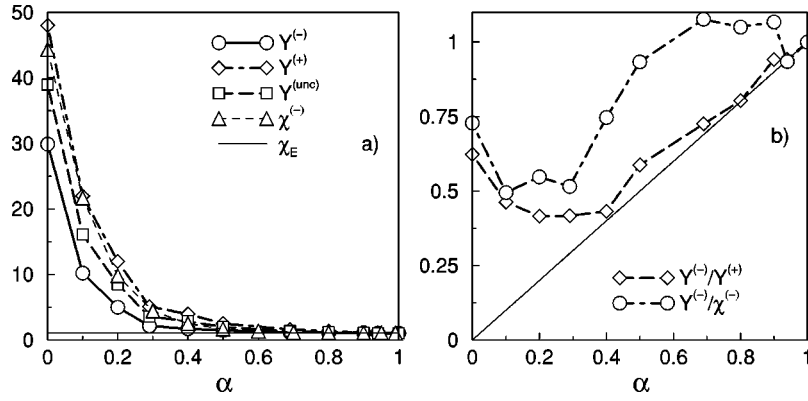


FIG. 4. (a) Static or unconstrained pair-distribution functions at contact $Y, Y^{(-)}, Y^{(+)}$, as extrapolated from the corresponding pair-distribution function $g(r \rightarrow \sigma)$ at $\phi = 0.05$, compared with the dynamic correlation $\chi^{(-)}$ at contact. The straight line corresponds to the EHD prediction ($\chi_E = 1.084$). (b) Ratio of dynamic to static correlation $\chi^{(-)}/Y^{(-)}$, to be compared with 1, and the static ratio $Y^{(-)}/Y^{(+)}$, to be compared with the dynamic ratio $\chi^{(-)}/\chi^{(+)} = \alpha$.

function $g(r)$ in a non-Brownian suspension of spherical particles, fluidized between two vertical parallel plates, shows an enhanced value at contact as well [35].

In Fig. 4(a), we show the value at contact, Y , obtained by extrapolation from $g(r)$ at $\phi = 0.05$, together with the extrapolated values for approaching and receding pairs, $Y^{(-)}$ and $Y^{(+)}$, respectively. For $\alpha \geq 0.8$, no significant deviations are found from the Verlet-Levesque value $\chi_E = 1.084$ for elastic hard disks at the same density. More surprising is the value of $g(r = \sigma)$ at large inelasticities, reaching a value around 40 for $\alpha \rightarrow 0$. This property, combined with the observation that the first and second maximum in $g(r)$ are shifted to smaller r values, and are larger (up to 20% at small α) than the corresponding hard disks values, may be interpreted as a tendency to cluster, i.e., to stay in continuously rearranging configurations with large-density inhomogeneities. We return to this point in Sec. III G.

Figure 4 also shows the dynamic correlation, $\chi^{(-)} = \chi_E B_{00}$, measured as a collisional average. Figure 4(b) compares the static ratio $Y^{(-)}/Y^{(+)}$ with the dynamic one, $\chi^{(-)}/\chi^{(+)} = \alpha$, and also shows the ratio $Y^{(-)}/\chi^{(-)}$. The plots clearly show that the dynamic and static correlations $\chi^{(\pm)}$ and $Y^{(\pm)}$ are different. For $\alpha \leq 0.5$, the differences are large, and for $\alpha \geq 0.6$, both functions are about equal. For the case of a freely evolving IHS fluid, Soto and Maréchal [18] have recently observed a similar behavior, and explained it in terms of the effect of the increase of grazing collisions on the effective $\chi^{(-)}$. In the randomly driven IHD fluid the same effects are present. All correlations, $\chi^{(-)}, Y^{(\pm)}$ are large, especially at small α . This is caused by the divergence of $f^{(2)}(\mathbf{c}_1, \mathbf{c}_1, \boldsymbol{\sigma})$ at small g and small $\cos \theta$, which corresponds to grazing collisions and will be further discussed in the next section. As a result of noise-induced recollisions, collisions with small g and small $\cos \theta$ are oversampled; consequently, a dynamical average involving negative powers of $g \cos \theta$ such as $\chi^{(-)}$ is expected to be larger than its static counterpart $Y^{(-)}$. This feature may be observed in Fig. 4(b). Moreover, in the absence of recollisions, we would expect $Y^{(-)} = \alpha Y^{(+)}$ as a result of plain hard-sphere dynamics. However, in the heated system, the flux continuity, as expressed in Eq.

(38), is no longer satisfied for the extrapolated Y 's; some pairs are put in precollision configuration under the action of the random force, which leads to $Y^{(-)} > \alpha Y^{(+)}$. The breakdown of $Y^{(-)} = \alpha Y^{(+)}$ signals the inelasticity beyond which noise-induced correlations become relevant. It is furthermore possible to consider situations where the recollisions dominate the dynamics, e.g., at small α by allowing rotation-induced recollisions. In this extreme limit, we expect $Y^{(-)} \approx Y^{(+)}$, the pairs being put in pre- or post-collision configuration essentially at random. In the same limit, the population of colliding pairs with small g and small $\cos \theta$ is enhanced, leading to a more pronounced discrepancy between dynamic and static averages [i.e., a much smaller ratio $Y^{(-)}/\chi^{(-)}$ than observed in Fig. 4(b)].

C. Equation of state. Molecular chaos breakdown

To what extent does the extrapolated static radial distribution function, $Y = g(r \rightarrow \sigma)$ describe the nontrivial dependence in the NESS of collision frequency in Eq. (5), collisional damping in Eq. (14) and pressure in Eq. (12) on the inelasticity? If molecular chaos holds, the latter quantities depend, according to Eqs. (6), (13), (9), and (15), on the precollisional pair function at contact, $\chi^{(-)}$, where the particles are aiming to collide. This function differs from the extrapolated static $Y^{(-)}$ at high inelasticities (see Fig. 4). Consider first the collision frequency in the molecular chaos approximation, $\omega_{mc} = \chi \omega_0(T)$ above Eq. (9), with $\chi = \chi^{(-)}$ the dynamic correlation, i.e.,

$$\frac{\omega_{mc}(T)}{\omega_E} = \frac{\chi^{(-)} v_0}{\chi_E v_E} = B_{00} \sqrt{\frac{T}{T_E}}, \quad (43)$$

where we have used Eqs. (9) and (35). This is an extremely poor approximation, as can be seen from Fig. 1, which shows that the measured value ω/ω_E approaches 5.6 as $\alpha \rightarrow 0$, whereas B_{00} is essentially divergent. Next, we replace $\chi^{(-)}$ in Eq. (43) by its static counterpart $Y^{(-)}$, shown in Fig. 4. This yields $\omega_{stat}(T)/\omega_E = Y^{(-)} v_0 / \chi^{(-)} v_E$. Its limiting value for $\alpha \rightarrow 0$ is about a factor three too large when compared to

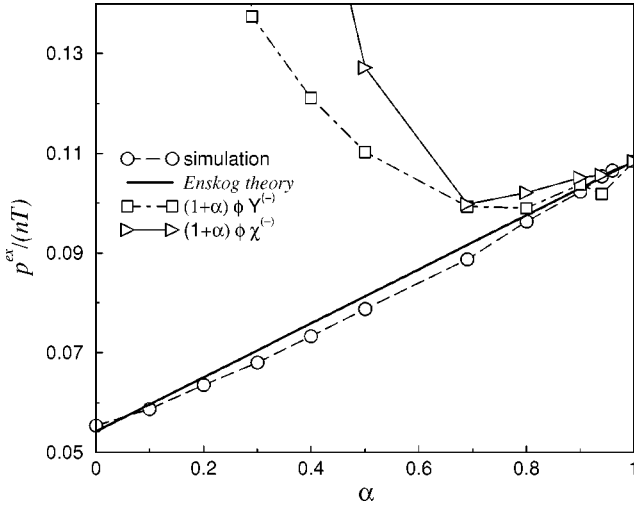


FIG. 5. Pressure versus coefficient of restitution at a packing fraction $\phi=0.05$. The simulation results (direct or through B_{22}) are compared with molecular chaos prediction (13), where χ is either the static $Y^{(-)}$ in Eq. (37), or the dynamic $\chi^{(-)}$ in Eq. (8), or the Enskog approximation χ_E in Eq. (7), corresponding to $B_{22}=1$.

ω/ω_E . We conclude that all mean-field approximations for the collision frequency, including the Enskog approximation $\omega_E(T)/\omega_E = \sqrt{T/T_E}$, break down for $\alpha < 0.6$.

Figure 5 shows the pressure of the IHD fluid, compared with the molecular chaos prediction given by Eq. (13), taking for χ either the Enskog approximation χ_E in Eq. (7), or the simulated $Y^{(-)}$, or $\chi^{(-)}$. The Enskog approximation, accounting for the short-range geometric exclusion effects in the precollision state, gives a reasonable description of $p(T)$ for all α , while both the static $Y^{(-)}$ and the dynamic $\chi^{(-)}$ give an extremely poor description except for $\alpha > 0.8$.

Consistent with this conclusion is the good estimate for the temperature T_E in the NESS, obtained by balancing the energy dissipation rate $\Gamma_E(T_E)$ in Eq. (16) with the energy input from the random force, as shown in Fig. 1. Moreover, the collisional energy loss $\Gamma(T)/\Gamma_E(T) = (T_E/T)^{3/2}$ in Eq. (18), is in agreement with MD simulations over the whole α interval within 30%. All other mean-field approximations with ω_E replaced by $\omega_{mc}(T)$ or $\omega_{stat}(T)$ give very poor results for $\Gamma(T) = m\xi_0^2$.

How can these paradoxical results be reconciled? Let us compare the individual definitions of $\chi^{(-)}$, ω , p , and Γ , which all contain factors $|\mathbf{g} \cdot \boldsymbol{\sigma}|^n f^{(2)}(\mathbf{c}_1, \mathbf{c}_2, \boldsymbol{\sigma})$ with $n=0,1,2,3$. To find a possible explanation of these paradoxical results, we test the following scenario: *the molecular chaos assumption (6) only breaks down at very small relative velocities \mathbf{g} , and more precisely, at very small $g_n = \mathbf{g} \cdot \hat{\boldsymbol{\sigma}} = g \cos \theta$, which is the component of \mathbf{g} , parallel to the line of centers of the colliding particles* (physical arguments for this scenario will be offered in Sec. III F where we discuss the noise-induced recollisions). On the basis of this scenario, the singularity in $f^{(2)}$ at small \mathbf{g} makes the dynamic correlation $\chi^{(-)} = B_{00}\chi_E$ (shown in Fig. 6) very much larger than χ_E , essentially divergent as $\alpha \rightarrow 0$. In calculating the collisional frequency from Eq. (5), the extra factor g_n in the integrand

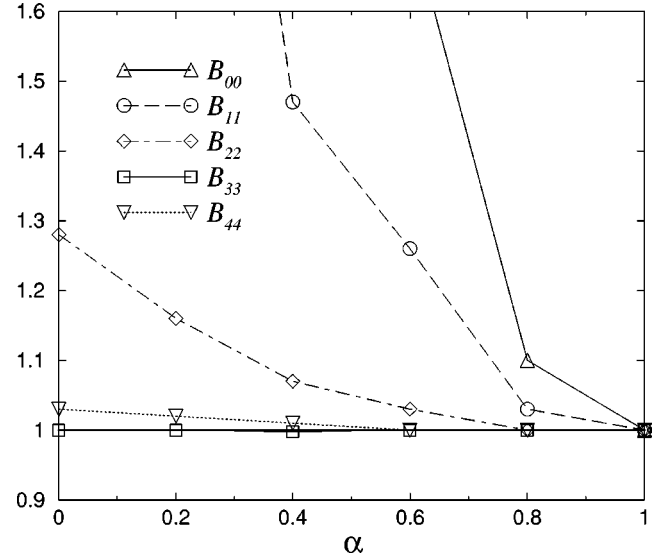


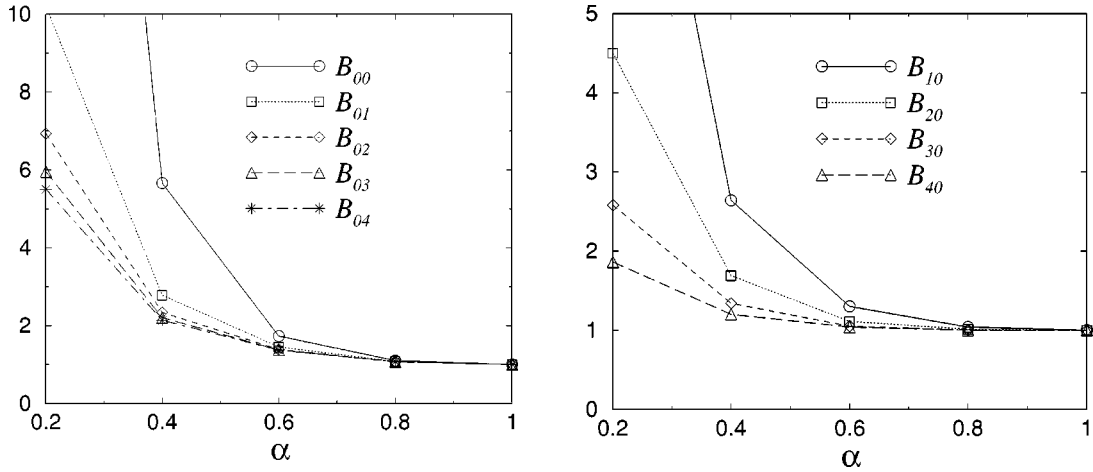
FIG. 6. Reduced moments B_{nm} for $n=1,2,3$ as a function of the restitution coefficient at $\phi=0.2$ and $N=5041$. A similar behavior is observed at lower densities.

makes the small g_n singularity integrable, giving a *finite* correction to the Enskog collision frequency, also for $\alpha \rightarrow 0$ (see Fig. 1). The contributions of the small g_n -singularity in $p(T)$ and $\Gamma(T)$ are essentially suppressed by extra factors of $|\mathbf{g} \cdot \hat{\boldsymbol{\sigma}}|^n$.

This possibility has been analyzed systematically by measuring the behavior of the moments $B_{nm}(T)$, which are useful tools to investigate the breakdown of the molecular chaos assumption. We have made n and/or m small in order to analyze the nature of the singularities in $f^{(2)}$ near small relative velocities and near grazing collisions, as displayed in Fig. 7. All deviations of these quantities from unity give a quantitative measure for the violation of the molecular chaos assumption. In the elastic limit, we have carefully checked for a large number of cases that the reduced moments $B_{nm}(T)$, and one can clearly see how the deviations from the elastic limit rapidly decrease as n increases to $n=3$, after which they start to increase slowly. For larger n -values, the moments are reasonably close to unity, but statistical inaccuracy precludes any definite conclusion about the large n behavior.

Further evidence for the above scenario is shown in Fig. 7, where we display two sequences of moments B_{nm} . To draw some further conclusions from Figs. 6 and 7, we note that the integrands in B_{nn} , B_{0n} , and B_{n0} , as defined in Eq. (28), contain apart from $f^{(2)}$, respectively, the factors $g^n |\cos \theta|^n$, $|\cos \theta|^n$, g^n . The reduced moments B_{01} and B_{10} contain again very large contributions from the divergence of $f^{(2)}$ near vanishing $g_n = g \cos \theta$. Figure 7 suggests that the presence of equal powers of g and $\cos \theta$ in B_{nn} simultaneously suppresses the large contributions from the singularities at $g=0$ and $\cos \theta=0$.

We conclude that the numerical results, displayed in Figs. 6 and 7, give support to the previous scenario, showing that molecular chaos breaks down only in a very small portion of


 FIG. 7. Reduced moments B_{0m} and B_{n0} as a function of α at $\phi=0.2$ and $N=5041$.

the phase space, around $g_n = \mathbf{g} \cdot \hat{\boldsymbol{\sigma}} = g \cos \theta = 0$. The size of this “pocket” in phase space increases as α decreases. Therefore, only those collisional quantities that contain low powers of g and $\cos \theta$ (such as $\chi^{(-)}$ and ω) will be very sensitive to this breakdown as the inelasticity increases, while physical quantities involving higher powers of g and $\cos \theta$, such as the temperature, pressure, or energy dissipation will be well approximated by their molecular chaos counterparts.

D. Velocity correlations at contact

In the previous section, we have considered the pair-distribution function $f^{(2)}(\mathbf{c}_1, \mathbf{c}_2, \boldsymbol{\sigma})$ in the precollision state, and have examined how molecular chaos is broken down, and which physical quantities are most sensitive to it. Now we will analyze the effect of the breakdown of molecular chaos on collisional statistics.

We show in Fig. 8 different velocity collisional averages at $\phi=0.05$. In the simulations, these quantities are obtained by averaging over successive collision events in the steady state. We first observe that the simulation results in Fig. 8 approach for $\alpha \rightarrow 1$ the analytic results for elastic spheres, calculated in Eq. (24). At small inelasticities, the simulation data follow the trends of the theoretical prediction with systematic deviations depending on the quantity considered. For instance, the behavior of the center-of-mass motion $\langle G^2 \rangle_{\text{coll}}$ is close to the analytical prediction of Eq. (24) in the whole range of α values. This indicates that the center of mass velocity \mathbf{G} is not correlated with the relative velocity \mathbf{g} . Consequently, $f^{(2)}(\mathbf{c}_1, \mathbf{c}_2, \boldsymbol{\sigma})$ in the collisional average (11) factorizes, and we may expect the contributions in numerator and denominator in Eq. (11) coming from \mathbf{G} integrations to cancel. Consistent with this behavior, we observe that the two curves in Fig. 8, $\langle c_1^2 \rangle_{\text{coll}}$ (labeled by circles) and $\langle \mathbf{c}_1 \cdot \mathbf{c}_2 \rangle_{\text{coll}}$ (labeled by squares), are symmetric around 1/2. In Eqs. (A4) and (A5) of the Appendix, these quantities have been expressed in reduced moments

$$\langle \mathbf{c}_1 \cdot \mathbf{c}_2 \rangle_{\text{coll}} = \frac{1}{2} - \frac{3}{4} \frac{b_{31}}{b_{11}},$$

$$\langle c_1^2 \rangle_{\text{coll}} = \frac{1}{2} + \frac{3}{4} \frac{b_{31}}{b_{11}}, \quad (44)$$

where

$$b_{nm} = \frac{M_{nm}(T)}{M_{nm}^E(T)} = \left(\frac{T_E}{T} \right)^{n/2} B_{nm}. \quad (45)$$

The reduced moments have been measured independently (see Figs. 6 and 7), and used to calculate the expressions (44) and (45). The results have been plotted in Fig. 8 as dashed and dashed-dotted lines, which agree very well with the direct measurements of these quantities as collisional averages, shown in Fig. 8, respectively, as squares and circles. In deriving Eq. (44) and (45), we have again used that the velocity

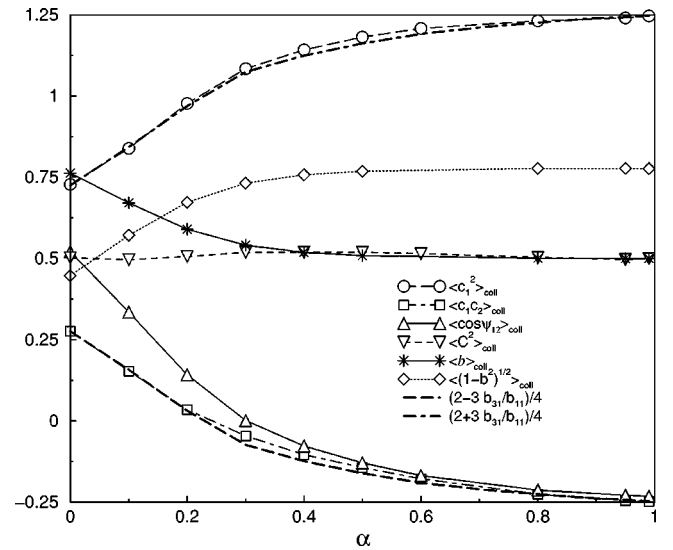


FIG. 8. Values of different collisional averages obtained in MD simulations, as a function of α at $\phi=0.05$ (see Sec. II B for definitions). For $\alpha < 0.5$, the random rotation introduced to avoid inelastic collapse has a maximum deviation angle of 2.5° . The symbols b_{nm} are defined in Eq. (45).

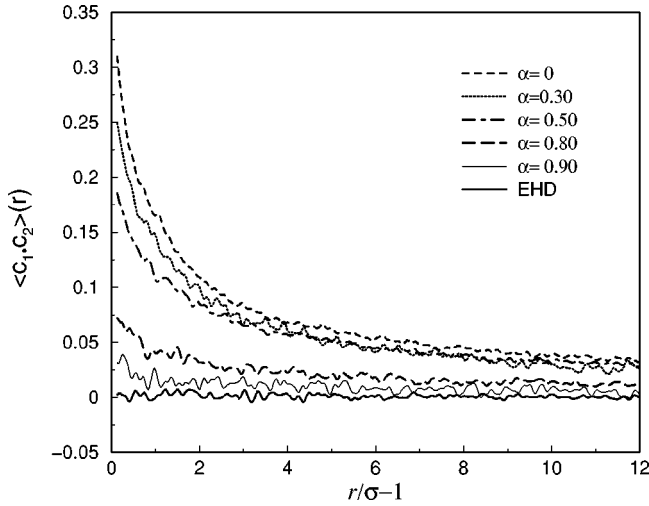


FIG. 9. Distribution of $\langle \mathbf{c}_1 \cdot \mathbf{c}_2 \rangle(r)$ as a function of the distance between the particles at $\phi = 0.05$.

variables \mathbf{G} and \mathbf{g} are statistically uncorrelated. The present results strongly support this assumption.

The correlation $\langle \hat{\mathbf{c}}_1 \cdot \hat{\mathbf{c}}_2 \rangle_{\text{coll}} = \langle \cos \psi_{12} \rangle_{\text{coll}}$, also plotted in Fig. 8, cannot be expressed in B moments. However, the approximate relation already employed to show that $\langle \cos \psi_{12} \rangle_{\text{coll}} \approx \langle \mathbf{c}_1 \cdot \mathbf{c}_2 \rangle_{\text{coll}} / \langle c^2 \rangle_{\text{coll}}$ in Sec. II C, holds for the simulation data over the whole range of inelasticities. As the system becomes more inelastic, the typical “temperature” of colliding particles (defined as the collisional average $\langle c^2 \rangle_{\text{coll}}$) decreases and even becomes lower than the unconstrained average $\langle c^2 \rangle$ that defines the temperature. On the other hand, as already noted below (24), $\langle c^2 \rangle_{\text{coll}} = 5/4 > 1$ in the elastic limit. This decrease of $\langle c^2 \rangle_{\text{coll}}$ is directly related to the increase of the small g portion of phase space where molecular chaos is violated. At small α , most of the collisions occur between particles with small and even vanishing relative velocities. An extreme example is the inelastic collapse, mentioned in the Introduction.

The correlation function $\langle \mathbf{c}_1 \cdot \mathbf{c}_2 / g \rangle_{\text{coll}}$ for the freely evolving IHD fluid has been simulated by Soto and Marechal, and was shown to be small, but nonvanishing [18].

We have also investigated $r-v$ correlations by measuring the expectation value of $\langle \mathbf{c}_1 \cdot \mathbf{c}_2 \rangle(r)$ for two particles separated by a distance r , as defined in Eq. (42). The results are shown in Figs. 9 and 10. The plot shows an intermediate range of r values with an exponentially decaying correlation. It is again of interest to compare the extrapolation of the static correlation $\langle \mathbf{c}_1 \cdot \mathbf{c}_2 \rangle(r \rightarrow \sigma)$ with its dynamic counterpart $\langle \mathbf{c}_1 \cdot \mathbf{c}_2 \rangle_{\text{dyn}}$ calculated at collision. The results, derived in Eqs. (A8) and (A9) of the Appendix, read for hard disks

$$\langle \mathbf{c}_1 \cdot \mathbf{c}_2 \rangle_{\text{dyn}} = \frac{1}{2} \left(1 - \frac{b_{20}}{b_{00}} \right) + \frac{1 - \alpha}{4} \frac{b_{22}}{b_{00}}. \quad (46)$$

The first term on the right-hand side (RHS) represents the precollision part,

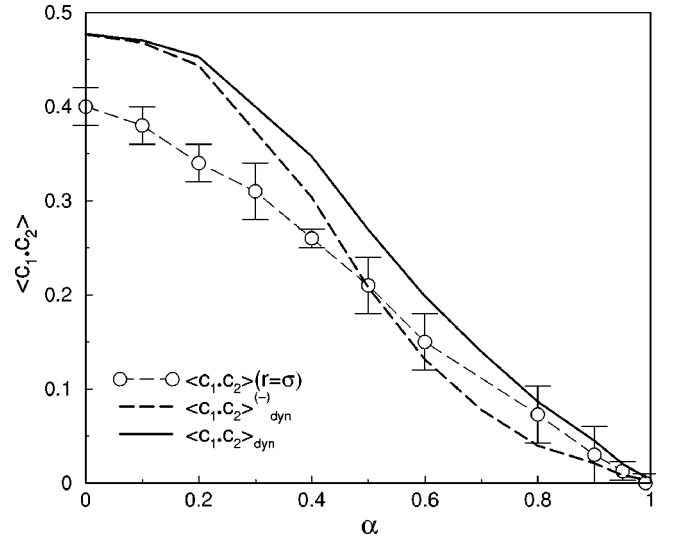


FIG. 10. Mean-velocity-velocity correlation function at contact, as extrapolated from $\langle \mathbf{c}_1 \cdot \mathbf{c}_2 \rangle(r)$ (previous figure), compared with the dynamic analogs $\langle \mathbf{c}_1 \cdot \mathbf{c}_2 \rangle_{\text{dyn}}$ and $\langle \mathbf{c}_1 \cdot \mathbf{c}_2 \rangle_{\text{dyn}}^{(-)}$, defined in Eq. (A8) and (A9).

$$\langle \mathbf{c}_1 \cdot \mathbf{c}_2 \rangle_{\text{dyn}}^{(-)} = \frac{1}{2} \left(1 - \frac{b_{20}}{b_{00}} \right). \quad (47)$$

Figure 10 compares the extrapolation $\langle \mathbf{c}_1 \cdot \mathbf{c}_2 \rangle(r \rightarrow \sigma)$ (circles) of the static correlation with its dynamic analogs (46) and (47). The numerical data for both correlations agree well for $\alpha \geq 0.8$, but for $\alpha \leq 0.5$, the dynamic correlation (solid line) is substantially larger than the static one. This is consistent with the difference between $\chi^{(-)}$ and $Y^{(-)}$ observed in Fig. 4. For comparison, the dynamic precollision correlation (dashed line) is also shown. It should be noted that the divergence of $f^{(2)}$ at small g and small $\cos \theta$ implies in particular that $B_{00} \gg B_{20} > B_{22}$, so that Eq. (46) predicts that the dynamic correlation at contact $\langle \mathbf{c}_1 \cdot \mathbf{c}_2 \rangle_{\text{dyn}}$ should increase at $\alpha \rightarrow 0$ and saturate close to $1/2$. By the same arguments, its precollision part in Eq. (47) approaches the same limit. This can be observed in Fig. 10.

The velocity correlation $\langle \mathbf{c}_1 \cdot \mathbf{c}_2 \rangle_{\text{coll}}$ in Eq. (44) involves the reduced moments b_{31} and b_{11} . Consistent with the scenario, developed in Sec. III C, the divergence of $f^{(2)}(\mathbf{c}_1, \mathbf{c}_2, \boldsymbol{\sigma})$ near $g = 0$ and $\cos \theta = 0$ is largely suppressed in these higher moments, which remain finite for $\alpha \rightarrow 0$, where $b_{11} \approx 4b_{31}$. Consequently, $\langle \mathbf{c}_1 \cdot \mathbf{c}_2 \rangle_{\text{coll}}$ does not approach the value $1/2$ as $\alpha \rightarrow 0$, but a value close to 0.3 , as can be deduced from Fig. 8.

E. Grazing collisions

The data in Fig. 8 for $\langle \mathbf{c}_1 \cdot \mathbf{c}_2 \rangle_{\text{coll}}$, $\langle \cos \psi_{12} \rangle_{\text{coll}}$, $\langle \sqrt{1 - b^2} \rangle_{\text{coll}}$, and $\langle b \rangle_{\text{coll}}$ clearly illustrate that the violation of molecular chaos strongly increases with increasing inelasticity. Consider first the average

$$\langle b \rangle_{\text{coll}} = \int_0^1 db b P(b). \quad (48)$$

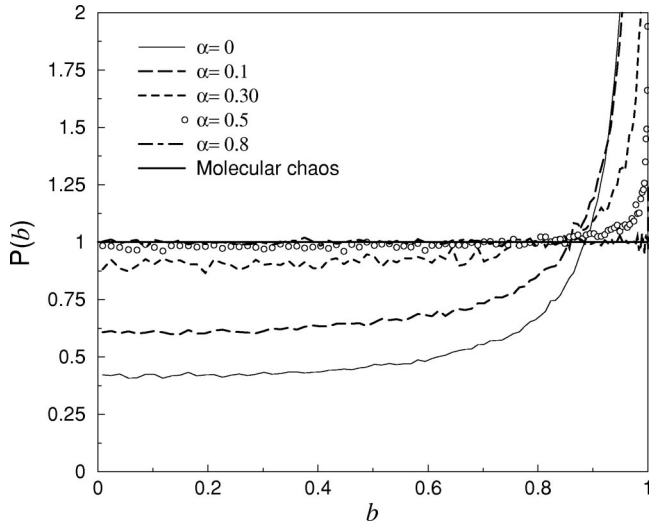


FIG. 11. Distribution of the impact parameter b for different α values for $\phi=0.05$.

This average remains at a plateau value $1/2$ for $\alpha \geq 0.5$, which is determined by the uniform distribution $P(b)$ corresponding to molecular chaos in two dimensions. Recall that the value $1/2$ holds regardless of the functional form of the velocity distribution function f . It is thus a good probe for molecular chaos breakdown. Moreover, from its trend we can also estimate the way in which such a breakdown takes place. Specifically, as the inelasticity increases the average value increases by about 50%, which indicates a strong bias toward grazing collisions. To illustrate this, we model the normalized distribution of impact parameters as a uniform background and a “half” delta peak at $b=1$, i.e., $P(b) = 1 - p + 2p\delta(1-b)$, where p is the fraction of grazing collisions. This yields the average $\langle b \rangle_{\text{coll}} = 1/2(1+p)$, which implies, according to Fig. 8, that at $\alpha=0.0, 0.1$, and 0.3 , respectively, a fraction of 50, 35, and 5 % is grazing at $\phi=0.05$. This qualitative picture is supported in a more quantitative manner in Fig. 11, which shows the measured $P(b)$, which is strongly peaked near grazing collisions ($b=1$). At small inelasticity, all impact parameters are equally probable as expected on the basis of molecular chaos, and consistent with Fig. 8. Only for $\alpha \leq 0.5$ deviations become significant: upon decreasing the coefficient of restitution, collisions with a larger impact parameter occur more frequently, implying an increase of the frequency of grazing collisions. The behavior of $P(b)$ is then fully consistent with the divergence of $f^{(2)}$ at small $\cos \theta$, discussed in Sec. III C.

To avoid inelastic collapse for $\alpha \leq 0.5$, the postcollision velocities of colliding pairs are rotated over a small random angle as described in Refs. [36,10], with the important restriction mentioned at the beginning of Sec. III. Alternative algorithms to avoid inelastic collapse are described in Ref. [37]. For $\alpha > 0.5$, no such rotation was applied. To check if the deviations of the impact parameter for $\alpha \leq 0.5$ are due to this applied rotation, we have also performed simulations where even for $\alpha > 0.5$ a random rotation was applied. Regardless of the applied random rotation, we found $\langle b \rangle_{\text{coll}}$ close to $1/2$ for $\alpha \geq 0.5$. Both Figs. 8 and 11 show that for

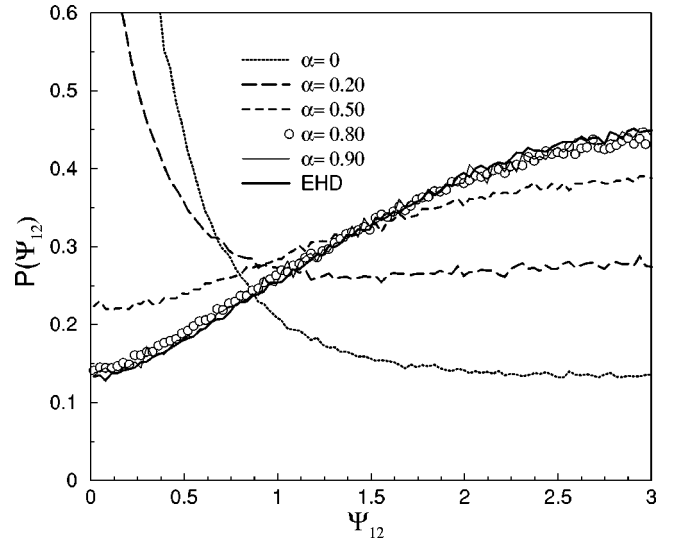


FIG. 12. Distribution of the relative orientation of the velocities at collision ($\cos \psi_{12} \equiv \hat{\mathbf{c}}_1 \cdot \hat{\mathbf{c}}_2$) at a packing fraction of 5%.

$\alpha \leq 0.5$ molecular chaos is strongly violated, and that the violation is weaker in the small inelasticity regime. The average $\langle \sqrt{1-b^2} \rangle_{\text{coll}}$ supports the same conclusions.

The data for $\langle \mathbf{c}_1 \cdot \mathbf{c}_2 \rangle_{\text{coll}}$ and $\langle \cos \psi_{12} \rangle_{\text{coll}}$ in Fig. 8 are consistent with the predominance of grazing collisions at large inelasticities. They show the average relative angle between the velocities of the incoming particles, which has a strong α dependence and no plateau value near the elastic limit. Near $\alpha=1$, the particles are on average on approaching trajectories with $\langle \cos \psi_{12} \rangle_{\text{coll}} \approx -0.25$ and $\langle \psi_{12} \rangle_{\text{coll}} \approx 105^\circ$. As α decreases, $\langle \cos \psi_{12} \rangle_{\text{coll}}$ increases linearly to a value 0.50, while $\langle \psi_{12} \rangle_{\text{coll}}$ approaches 60° , at $\alpha=0$. This corresponds to collisions of more or less parallel-moving pairs of particles, where faster particles overtake slower ones.

Figures 12 and 13 show the distribution of relative orientations of incoming velocities. The distribution of angles between the incoming particles (ψ_{12}) shows moderate devia-

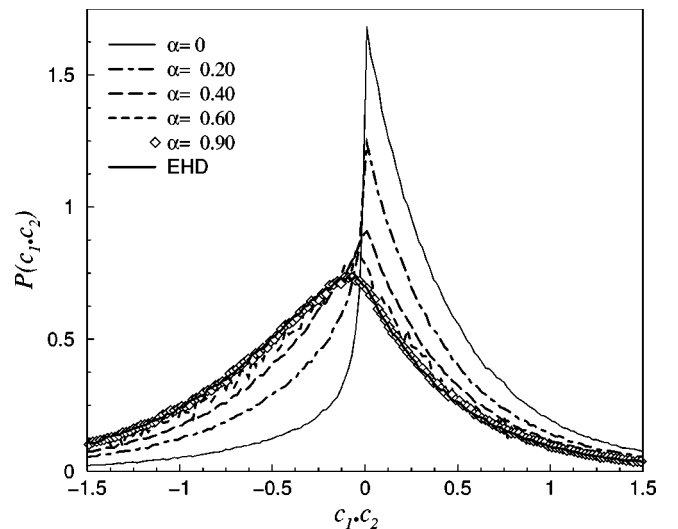


FIG. 13. Distribution of relative velocities $\mathbf{c}_1 \cdot \mathbf{c}_2$ of colliding inelastic disks at $\phi=0.05$.

TABLE I. Frequency of recollision events as a function of the inelasticity (see text for the definition of \mathcal{R}_0 and \mathcal{R}_1). The packing fraction is $\phi=0.2$ and the system contains $N=5000$ disks.

α	\mathcal{R}_0	\mathcal{R}_1
0	52%	18%
0.4	14%	15%
0.6	4%	15%
0.95	0.15%	7%
1.0	0%	6.7%

tions from what is expected for an elastic system in the range $0.5 \leq \alpha < 1$. As an analytic expression for elastic disks is not available, deviations are compared with the simulation results for elastic hard disks (in the absence of a random external force). At $\alpha=0.5$, the frequency of collisions of parallel-moving particles is strongly increased, a trend that is enhanced upon increasing the inelasticity. Finally, the probability distribution $P(\mathbf{c}_1 \cdot \mathbf{c}_2)$ is shown in Fig. 13. When the inelasticity increases, this distribution becomes more peaked around the origin, as the colliding particles on average move more slowly relative to each other. In the mean time, the typical angle ψ_{12} decreases, which causes this peak to shift to positive values.

F. Particle- and noise-induced recollisions

The mechanism for the breakdown of molecular chaos in classical fluids with conservative interactions are sequences of correlated ring collisions, as discussed in the introduction. The most simple ring collisions are the recollisions (1-2) (1-3) (1-2) and cyclic collisions (1-2)(2-3)(3-1) or permutations thereof [20].

There is strong evidence that the effects of ring collisions are considerably enhanced in fluids with dissipative interactions, such as granular flows, where *relative* kinetic energy is lost in binary collisions. As a result, the postcollision velocities $\{\mathbf{v}_1^*, \mathbf{v}_2^*\}$ will be on average more parallel than the pre-collision ones $\{\mathbf{v}_1, \mathbf{v}_2\}$ [24], i.e., the trajectories are less diverging than in the elastic case, and there is a much larger $\{\mathbf{r}_3, \mathbf{v}_3\}$ phase space, in which particle three will knock, say, particle one back to recollide with particle two.

This increase of phase space is confirmed by gathering recollision statistics. We have counted the fraction of recollisions as a function of α , as shown in Table I. The column labeled \mathcal{R}_1 (recollisions between two partners mediated by a third particle) shows that at a packing fraction $\phi=0.2$ in the elastic case ($\alpha=1$) only a fraction of 6.7% of all collisions is a recollision. This frequency gradually increases to about 15% at $\alpha=0.4$.

In the randomly driven IHS fluid, there is the additional effect of noise-induced recollisions that do not require the intervention of other particles. This type of recollision (denoted \mathcal{R}_0) occurs with high probability when the relative velocity after collision is so small that it may be simply reversed by a random kick. At $\alpha=0.6$, the frequency of noise-induced recollisions is about 4%, and it increases to 52% at $\alpha=0$ (see column \mathcal{R}_0 in Table I). The effect is of

importance at *all* densities, because it does not require the mediation of a third particle. Indeed, at a low-packing fraction of 1% and in the completely inelastic case $\alpha=0$, the frequency of \mathcal{R}_0 -like events is still 34%, while \mathcal{R}_1 -like events have dropped to 5%. Moreover, we have verified that inclusion of rotation-induced recollisions modifies most of the collisional quantities we have analyzed, increasing their deviations with respect to the molecular chaos prediction.

At present, more quantitative theories or estimates of the effect of both types of recollisions and other ring collisions on the short-range behavior of the pair-distribution function $f^{(2)}(x_1, x_2)$ are lacking. A natural way to incorporate the noise-induced recollisions into a kinetic theory description would be to include them into an effective two-particle scattering operator, which transforms an asymptotic precollision state of two independent particles into an asymptotic post-collision state, without involving intermediate two-particle scattering states, as in the present case. This may lead to an instantaneous Boltzmann collision term (without memory effects), provided the mean free time and the time between random kicks are very well-separated (dilute gases). Such a description would suppress the recollisions of type \mathcal{R}_0 , and make the violation of molecular chaos less severe, say comparable to the freely evolving IHD fluid.

G. Cold dense inhomogeneities

In Ref. [10], we have shown by analyzing the Fourier modes of the granular hydrodynamic equations, which are valid for small inelasticities (say $\alpha > 0.7$), that the NESS in a randomly driven IHS fluid is linearly stable against spatial inhomogeneities. Consequently, when observed over sufficiently long times, the NESS should be spatially homogeneous. However, it was also shown that the NESS exhibits strong fluctuations, resulting in long-range spatial correlations in density, flow field, and granular temperature. The observation of density inhomogeneities for large inelasticities has already been reported by Peng and Ohta [8]. These density inhomogeneities, as shown by the snapshot of the density in Fig. 14, are not quasistatic, as in the freely evolving case [38,36,39,24], but seem to behave as dynamic assemblies of particles that dissolve and reassemble again. Also, for a uniform shear flow, dynamical density inhomogeneities have been reported [40]. The existence of density inhomogeneities was already suggested by the static pair-distribution functions $g(r)$, which showed an enhancement of the first few maxima as compared to their elastic values (see Fig. 3).

In Fig. 8, we show that the mean energy $\langle c_1^2 \rangle_{\text{coll}}$, of particles aiming to collide, is above the mean, $\langle c^2 \rangle = 1$, for small inelasticity. It decreases from its elastic value $5\langle c^2 \rangle/4$ with decreasing α , then crosses the mean value $\langle c^2 \rangle = 1$ at $\alpha \approx 0.2$, and further decreases to approximately $0.7\langle c^2 \rangle$ at $\alpha=0$.

It is interesting to observe that in the strong dissipation range, the mean kinetic energy or granular temperature of particles that are about to collide is *lower* than the average temperature. We combine this observation with Figs. 3(a) and 3(b) of Peng and Ohta [8], which show that essentially

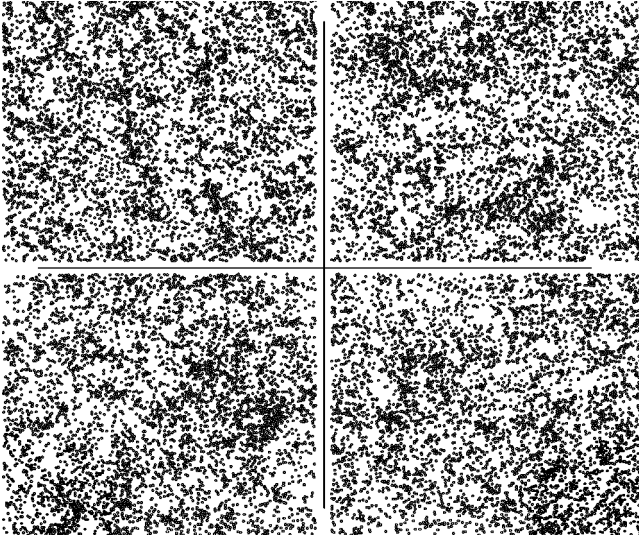


FIG. 14. To illustrate the slow reorganization of density inhomogeneities, four consecutive snapshots of the system are shown at $\alpha=0.1$, $\phi=0.2$, and $N=5000$ (the full simulation box is displayed). The time interval between two consecutive snapshots corresponds to 50 collisions per particle.

all collisions occur inside “cold” regions of high densities. This last observation applies even more so to undriven IHS fluids [38,41]. We expect that, also in the randomly driven IHS fluid, the majority of collisions takes place inside cold high-density regions.

If the predominance of *cold* particles in strongly inelastic collisions, $\langle c^2 \rangle_{\text{coll}} < \langle c^2 \rangle$ is indeed a signal for the appearance of density inhomogeneities, then Fig. 8 suggests that at

a packing fraction $\phi=0.05$ density inhomogeneities may occur for $\alpha \leq 0.2$. This is indeed confirmed by the snapshots in Figs. 14. In Fig. 15, we illustrate the existence of cold inhomogeneous dense regions for $\alpha=0.2$ and $\phi=0.2$. The particles with a less (more) than median kinetic energy are shown on the left (right). The formation of inhomogeneities is more clear for the colder particles. The temporal evolution of these regions show that they dissolve after some time, while inhomogeneous regions appear. The formation of “living” inhomogeneous regions may be understood using the hydrodynamic picture put forward in [10], where it was shown that the structure factor behaves as $S(\mathbf{k}) \sim k^{-2}$, implying density correlations *increasing* with distance as $\ln(r)$ in two dimensions. These long range spatial correlations induce a slowing down of the dynamics, as in critical phenomena. This, in turn, implies the slow decay of density perturbations, which could lead to visible density inhomogeneities as the kicking frequency is reduced (in this respect, see Refs. [6]). We may also expect that upon decreasing the forcing frequency, the dynamics should be closer to its “free cooling” counterpart so that well-defined clusters are then likely to appear.

More details about the predominance of cold particles, among those involved in collisions, may be seen in Fig. 16, which shows the constrained probability distribution $P(c)$, defined in Sec. II C and obtained from MD-simulations at different inelasticities. For $\alpha \leq 0.5$, the distribution has significantly shifted to smaller impact velocities. For the completely inelastic case, collision events involving “immobile” particles are more than twice as frequent as for the elastic case. The second moment of the distribution displayed in Fig. 16 decreases when increasing the inelasticity. In fact, all

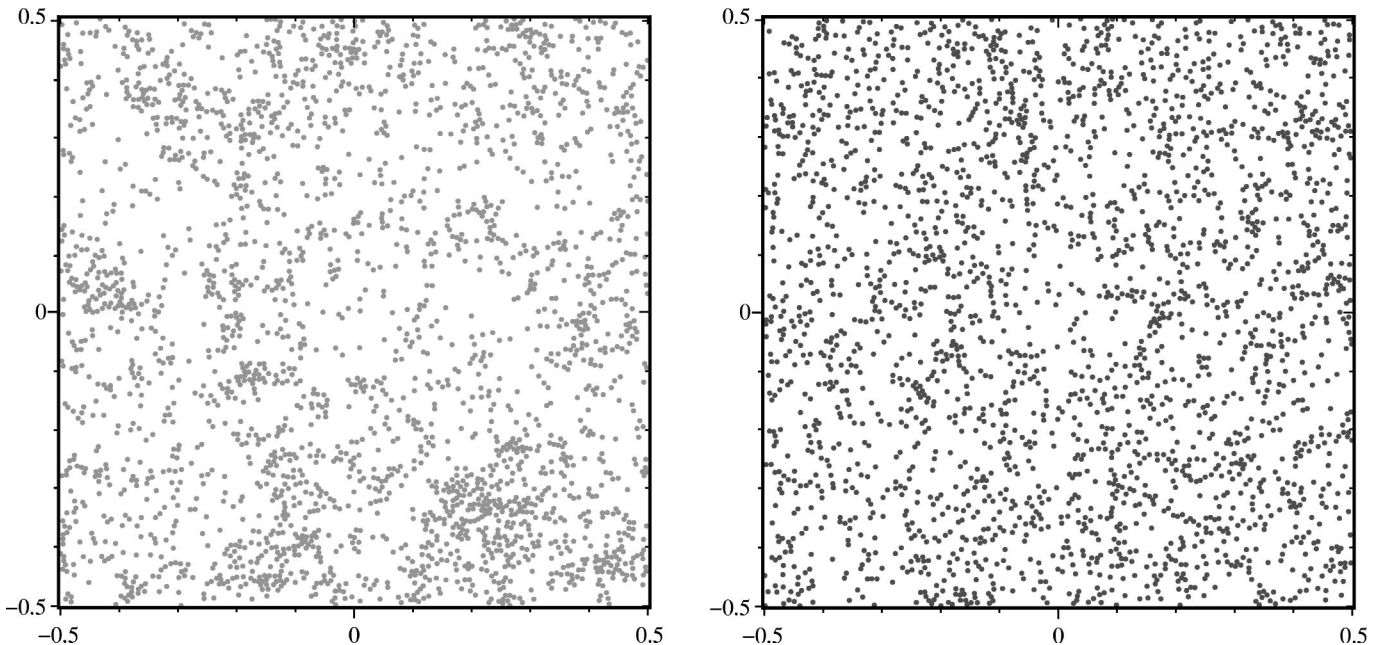


FIG. 15. Snapshot of a typical instantaneous configuration of the system at $\alpha=0.2$, $\phi=0.2$, and $N=5000$. To illustrate the existence of cold dense inhomogeneities, on the left (right) the particles with a less (more) than median kinetic-energy \mathcal{E}^* are shown at real scale (i.e., the cutoff \mathcal{E}^* is chosen such that there are exactly half of the particles on each graph). Lengths on the x and y axes are expressed in units of the simulation box length.

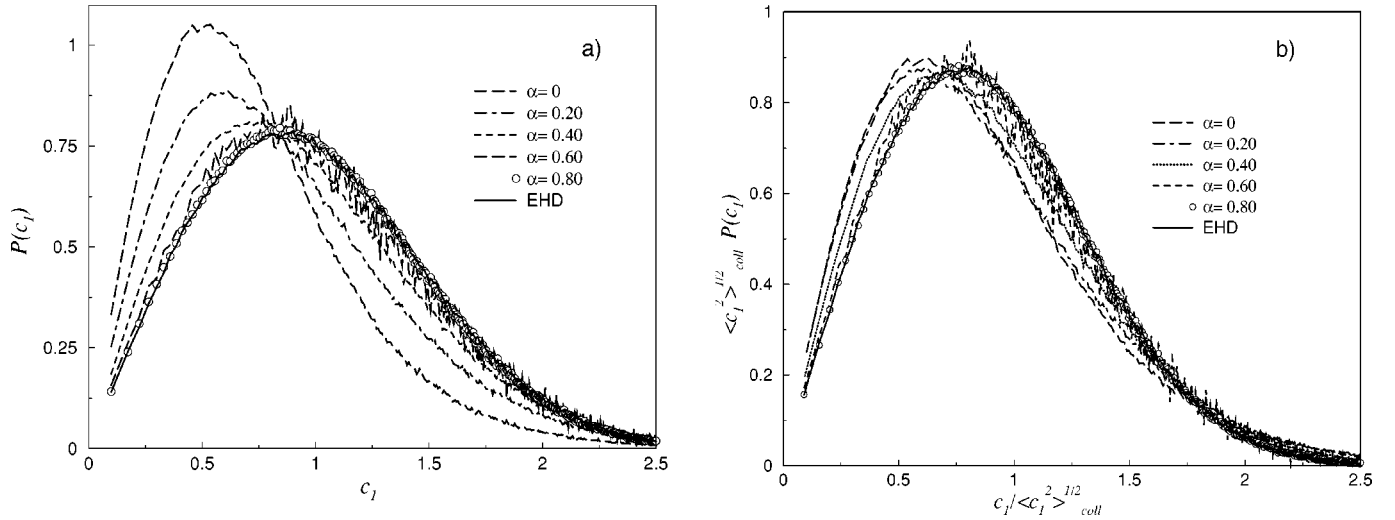


FIG. 16. Velocity distribution of the colliding particles at $\phi=0.05$ and $N=5041$: (a) Original distribution; (b) scaled velocity distributions as a function of the rescaled velocity $c/\sqrt{T(\alpha)}$ for different values of α .

functional forms with simulation data at different α can essentially be collapsed onto a single universal curve (the elastic one) by plotting $\sqrt{T(\alpha)}P(c|\alpha)$ as a function of $c/\sqrt{T(\alpha)}$, where $T(\alpha)=\langle c^2 \rangle_{coll}$ is the mean temperature of a particle at collision. The collapse plot is shown in Fig. 16(b). This data collapse confirms the concept of cold dense regions dominating the energy dissipation. This could point to a possibly relevant two fluid picture of a “hot” dilute background gas coexisting with continuously rearranging configurations of “cold” dense regions.

IV. CONCLUSION

We have performed extensive MD simulations to study the kinetic properties and short-range correlations in the non-equilibrium steady state of a randomly driven fluid of inelastic hard disks, as a model for fluidized granular material. The MD results have been compared with kinetic theory predictions derived from the Enskog-Boltzmann equation, properly modified with a Fokker-Planck diffusion term $\xi_0^2(\partial/\partial\mathbf{v})^2$ to account for the applied random driving force [9].

It appears that the kinetic theory predictions, based on molecular chaos, are essentially in agreement with the MD results for small inelasticities ($\alpha \geq 0.5$) at $\phi=0.05$. For larger inelasticities, the deviations from the molecular chaos predictions start to become manifest: the radial distribution function at contact differs strongly from its local equilibrium form; there is a predominance of grazing collisions. When increasing ϕ , the effects of the inelastic collisions become relevant at smaller inelasticities; e.g., at $\phi=0.2$ and $\phi=0.5$, we observe already significant deviations for $\alpha \leq 0.7$.

To avoid inelastic collapse of the system at low α , we have implemented a modified rotation procedure (see the beginning of Sec. III). In its original version, this procedure induces dramatic violations of molecular chaos. It could then be argued that the important deviations of low-order-reduced moments B_{nm} are also spurious consequences of the above rotation procedure. However, we checked that circumventing the collapse by applying elastic collisions when the relative

velocity of a pair is below a certain cutoff [37], also induces very important violations of molecular chaos (quantified by B_{00} for instance), unless the cutoff is chosen unphysically high.

Sequences of ring collision processes, which lead to the breakdown of molecular chaos in classical fluids with conservative interactions, are strongly enhanced in fluids with dissipative interactions, such as rapid granular flows. We have analyzed how molecular chaos is broken, i.e., essentially only through pairs of colliding particles at very small relative velocities. This means that molecular chaos is violated only in a small portion of phase space, implying that only certain physical properties will be sensitive to this violation. This explains why quantities such as the collision frequency, or the pair-distribution function at contact are very sensitive to the inelasticity parameters, while others such as the pressure or the energy dissipation rate are well approximated by their Enskog prediction. Disentangling the effects of hard disk and noise-induced correlations remains an interesting point to explore. The studies performed in a freely evolving IHS fluid also shows the predominance of grazing collisions at long times. The fact that we have observed an analogous behavior for this homogeneous steady state indicates that the mechanism of breakdown of molecular chaos in granular fluids through grazing collisions is generic for this type of fluids.

The extra feature of noise-induced recollisions, which do not require mediation of a third particle, will further enhance the violation of the molecular chaos assumption. A natural way to develop a kinetic theory for randomly driven fluids, thereby presumably restoring the validity of the molecular chaos assumption in the dilute gas case, could be to include the noise-induced recollisions in an effective two-particle scattering operator. It would be of interest to study its properties, either analytically or by simulating a two-particle inelastic collision in the presence of external noise. An additional theoretical complication here is the validity of the Boltzmann Eq. (1) with Fokker-Planck diffusion term due to the fact that there are two limits involved when dealing with

hard spheres in combination with external white noise. The actual properties of the effective collision operator depend on the order in which both limits are taken. In the simulations, one always takes the hard sphere limit first, while the white noise is approximated by discrete kicks that are applied to the particles at discrete times.

In Ref. [10], we have calculated the equal-time spatial correlations of the fluctuations in the hydrodynamic densities in the NESS. Here, we have focused on the dynamic properties of these enhanced fluctuations, in particular of the dynamic inhomogeneities observed in the density field. The collisional velocity moments, introduced in Sec. II and measured in MD simulations, reveal that the dense regions consist mostly of particles colder than average. This is clearly shown in the velocity distribution $P(v|\alpha)$ of particles that are about to collide.

The MD simulations have been carried out in the limit in which the time interval between the external random kicks is much shorter than the *mean* free time between collisions. In this limit, regions with density larger than average are not seen to survive for a long time. Rather, they form, dissolve, and reappear elsewhere. The spatial correlations analyzed in [10] show long-range correlations, which imply also a slowdown in the temporal decay of density perturbations. Therefore, we expect that the decrease of the kicking frequency will be accompanied by the appearance of apparent clusters. This fact, together with the shape modification of the velocity distribution $P(v|\alpha)$ (see Fig. 16) suggests the picture of a two-fluid model, in which a “hotter” more dilute background gas coexists with continuously rearranging configurations of “cold” dense clusters. This point remains open for subsequent investigation; for example, it would be interesting to analyze separately the collisional statistics in the dense and dilute regions to assess the role of density fluctuations.

ACKNOWLEDGMENTS

E.T. and I.P. thank D. Frenkel and B. Mulder for the hospitality of their groups at AMOLF. I.P. thanks M.E. Cates for his hospitality in the University of Edinburgh, where part of this work was done. We acknowledge stimulating discussions with H.J. Herrmann, S. Luding, R. Soto, M. Mareschal, and J. Piasecki. T.v.N. and I.P. acknowledge support of the foundation “Fundamenteel Onderzoek der Materie (FOM),” which is financially supported by the Dutch National Science Foundation (NWO).

APPENDIX: REDUCED MOMENTS $B_{nm}(T)$

In the body of the paper, we have considered the collisional averages $\langle g^n | \cos \theta^m \rangle_{\text{coll}}$ and the moments $M_{n,m}(T)$ and $B_{n,m}(T)$. We first list the Enskog values of these quantities, which have been calculated from its definitions, given below Eq. (28): i.e.,

$$M_{nm}^E(T_E) = v_E^n \chi_E 2^{n/2} \frac{\Gamma((d+n)/2)\Gamma((m+1)/2)}{\sqrt{\pi}\Gamma((d+m)/2)}, \quad (\text{A1})$$

$$\langle g^n | \cos \theta^m \rangle_{\text{coll}}^E = 2^{n/2} \frac{\Gamma((d+n+1)/2)\Gamma((m+2)/2)}{\Gamma((d+m+1)/2)}. \quad (\text{A2})$$

Many physical quantities of interest may be expressed in terms of reduced moments B_{nm} , as already illustrated in Sec. II C for $\chi^{(-)}$, ω , p , and Γ . Analogous relations hold for the velocity moments $\langle g^n \rangle_{\text{coll}}$, which are proportional to $M_{n+1,1}$. This yields

$$B_{n+1,1} = \frac{\omega}{\omega_E} \times \frac{\langle v_{12}^n \rangle_{\text{coll}}}{\langle v_{12}^n \rangle_{\text{coll}}^E} = \frac{\omega}{\omega_E} \times \frac{\langle g^n \rangle_{\text{coll}}}{\langle g^n \rangle_{\text{coll}}^E} \left(\frac{T}{T_E} \right)^{n/2}, \quad (\text{A3})$$

where the denominator has been calculated in Eq. (A2).

Velocity correlations between nearby particles may also be expressed in the reduced moments $B_{nm}(T)$. First, consider the constrained averages $\langle \mathbf{c}_1 \cdot \mathbf{c}_2 \rangle_{\text{coll}}$, defined in Eq. (24). They contain $\langle G^2 \rangle_{\text{coll}}$, which equals $d/4$ from the MD simulations, in agreement with Eq. (24) (see Fig. 8 of Sec. III). The center of mass velocity \mathbf{G} is consequently uncorrelated with the relative velocity, and independent of the inelasticity. Substitution of $\langle G^2 \rangle_{\text{coll}} = d/4$ in Eq. (24) yields

$$\langle \mathbf{c}_1 \cdot \mathbf{c}_2 \rangle_{\text{coll}} = \frac{d}{4} - \frac{1}{4} \langle g^2 \rangle_{\text{coll}} = \frac{d}{4} - \frac{d+1}{4} \left(\frac{T_E}{T} \right) \frac{B_{31}}{B_{11}}, \quad (\text{A4})$$

$$\langle c_1^2 \rangle_{\text{coll}} = \frac{d}{4} + \frac{1}{4} \langle g^2 \rangle_{\text{coll}} = \frac{d}{4} + \frac{d+1}{4} \left(\frac{T_E}{T} \right) \frac{B_{31}}{B_{11}}. \quad (\text{A5})$$

Similarly we find

$$\begin{aligned} \langle \mathbf{c}_1 \cdot \mathbf{c}_2 / g \rangle_{\text{coll}} &= \langle G^2 / g \rangle_{\text{coll}} - \frac{1}{4} \langle g \rangle_{\text{coll}} \\ &= \frac{d}{4\sqrt{2}} \frac{\Gamma(d/2)}{\Gamma((d+1)/2)} \sqrt{\frac{T}{T_E}} \\ &\quad \times \frac{B_{01}}{B_{11}} \left\{ 1 - \left(\frac{T_E}{T} \right) \frac{B_{21}}{B_{01}} \right\} \end{aligned} \quad (\text{A6})$$

and

$$\begin{aligned} \langle \mathbf{c}_1 \cdot \mathbf{c}_2 / |g \cos \theta| \rangle_{\text{coll}} &= \langle G^2 / |g \cos \theta| \rangle_{\text{coll}} - \frac{1}{4} \langle g / |\cos \theta| \rangle_{\text{coll}} \\ &= \frac{d}{4} \sqrt{\frac{\pi}{2}} \sqrt{\frac{T}{T_E}} \times \frac{B_{00}}{B_{11}} \left\{ 1 - \left(\frac{T_E}{T} \right) \frac{B_{21}}{B_{01}} \right\}. \end{aligned} \quad (\text{A7})$$

Note that the last two averages are vanishing in the elastic case.

In the body of the paper we have considered the extrapolation of the static correlation $\langle \mathbf{c}_1 \cdot \mathbf{c}_2 \rangle(r \rightarrow \sigma)$. Here, we calculate its dynamic analog $\langle \mathbf{c}_1 \cdot \mathbf{c}_2 \rangle_{\text{dyn}}$, obtained by interchanging limits and replacing $f^{(2)}(\mathbf{c}_1, \mathbf{c}_2, r)$ under the integral sign in Eq. (41) by its value at contact, $f^{(2)}(\mathbf{c}_1, \mathbf{c}_2, \sigma)$. We proceed in the same fashion as in Eqs. (36)–(39), and

split the numerator in Eq. (42) in a pre- and postcollision part, as done in Sec. II D. One finds after a lengthy calculation,

$$\langle \mathbf{c}_1 \cdot \mathbf{c}_2 \rangle_{\text{dyn}} = \frac{d}{4} \left\{ 1 - \left(\frac{T_E}{T} \right) \frac{B_{20}}{B_{00}} \right\} + \frac{1 - \alpha}{4} \left(\frac{T_E}{T} \right) \frac{B_{22}}{B_{00}}. \quad (\text{A8})$$

Here, the first term on the RHS is its precollision part, i.e.,

$$\begin{aligned} \langle \mathbf{c}_1 \cdot \mathbf{c}_2 \rangle_{\text{dyn}}^{(-)} &= \langle \mathbf{c}_1 \cdot \mathbf{c}_2 | g \cos \theta |^{-1} \rangle_{\text{coll}} / \langle | g \cos \theta |^{-1} \rangle_{\text{coll}} \\ &= \frac{d}{4} \left\{ 1 - \left(\frac{T_E}{T} \right) \frac{B_{20}}{B_{00}} \right\}. \end{aligned} \quad (\text{A9})$$

In Sec. III, these quantities are compared with MD simulations.

-
- [1] F. Melo, P.B. Umbanhowar, and H.L. Swinney, *Phys. Rev. Lett.* **75**, 3838 (1995); P.B. Umbanhowar, F. Melo, and H.L. Swinney, *Nature (London)* **382**, 793 (1996); C. Bizon and H.L. Swinney, in *Models and Kinetic Methods for Non-equilibrium Many Body Systems*, Vol. 371 of NATO Advanced Studies Series, edited by J. Karkheck (Kluwer, Dordrecht, 2000).
- [2] J.S. Olafsen and J.S. Urbach, *Phys. Rev. Lett.* **81**, 4369 (1998); J.S. Urbach, in *Granular Gases*, Lecture Notes in Physics Vol. 564, edited by T. Pöschel and S. Luding (Springer Verlag, Berlin, 2001).
- [3] W. Losert, D.G.W. Cooper, J. Delour, A. Kudrolli, and J.P. Gollub, *Chaos* **9**, 682 (1999).
- [4] F. Rouyer and N. Menon, *Phys. Rev. Lett.* **85**, 3676 (2000).
- [5] D.R.M. Williams and F.C. MacKintosh, *Phys. Rev. E* **54**, R9 (1996).
- [6] A. Puglisi, V. Loreto, U.M.B. Marconi, A. Petri, and A. Vulpiani, *Phys. Rev. Lett.* **81**, 3848 (1998); *Phys. Rev. E* **59**, 5582 (1999).
- [7] R. Caferio, S. Luding, and H.J. Herrmann, *Phys. Rev. Lett.* **84**, 6014 (2000).
- [8] G. Peng and T. Ohta, *Phys. Rev. E* **58**, 4737 (1998).
- [9] T.P.C. van Noije and M.H. Ernst, *Granular Matter* **1**, 57 (1998).
- [10] T.P.C. van Noije, M.H. Ernst, E. Trizac, and I. Pagonabarraga, *Phys. Rev. E* **59**, 4326 (1999).
- [11] S.J. Moon, M.D. Shattuck, and J.B. Swift, *Phys. Rev. E* **64**, 031303 (2001).
- [12] P.K. Haff, *J. Fluid Mech.* **134**, 401 (1983).
- [13] J.R. Dorfman, T.R. Kirkpatrick, and J.V. Sengers, *Annu. Rev. Phys. Chem.* **45**, 213 (1994).
- [14] G. Grinstein, D.-H. Lee, and S. Sachdev, *Phys. Rev. Lett.* **64**, 1927 (1990).
- [15] A. Barrat, E. Trizac, and J.N. Fuchs, *Eur. Phys. J. E* **5**, 161 (2001).
- [16] S. Chapman and T.G. Cowling, *The Mathematical Theory of Non-uniform Gases* (Cambridge University Press, Cambridge, 1970).
- [17] J.F. Lutsko, *Phys. Rev. Lett.* **86**, 3344 (2001).
- [18] R. Soto and M. Maréchal, *Phys. Rev. E* **63**, 041303 (2001).
- [19] B.J. Alder and T.E. Wainwright, *Phys. Rev. Lett.* **18**, 988 (1967); *Phys. Rev. A* **1**, 18 (1970); B.J. Alder and W.E. Alley, *Phys. Today* **37**, 56 (1984); E.G.D. Cohen, *ibid.* **37**, 64 (1984); *Am. J. Phys.* **61**, 524 (1993).
- [20] J.R. Dorfman and H. van Beijeren, *The Kinetic Theory of Gases*, in *Statistical Mechanics, Part B: Time-Dependent Processes*, edited by B. J. Berne (Plenum Press, New York, 1977), Chap. 3.
- [21] J.R. Dorfman and E.G.D. Cohen, *Phys. Rev. Lett.* **25**, 1257 (1970).
- [22] M.H. Ernst, E.H. Hauge, and J.M.J. van Leeuwen, *Phys. Rev. Lett.* **25**, 1254 (1970).
- [23] J.-P. Hansen and I.R. McDonald, *Theory of Simple Liquids* (Academic Press, London, 1986).
- [24] S. McNamara and W.R. Young, *Phys. Rev. E* **50**, R28 (1994); **53**, 5089 (1996).
- [25] E. Trizac and A. Barrat, *Eur. Phys. J. E* **3**, 291 (2000).
- [26] M. Müller and H. J. Herrmann, in *Physics of Dry Granular Media*, edited by H. J. Herrmann, J.-P. Hovi, and S. Luding (Kluwer Academic Publishers, Dordrecht, 1998).
- [27] S. Luding, *Z. Angew. Math. Mech.* **80**, S9 (2000).
- [28] I. Goldhirsch, M.L. Tan, and G. Zanetti, *J. Sci. Comput.* **8**, 1 (1993).
- [29] T.P.C. van Noije, M.H. Ernst, and R. Brito, *Physica A* **251**, 266 (1998).
- [30] M.P. Allen and D.J. Tildesley, *Computer Simulation of Liquids* (Clarendon Press, Oxford, 1987).
- [31] L. Verlet and D. Levesque, *Mol. Phys.* **46**, 969 (1982); N.F. Carnahan and K.E. Starling, *J. Chem. Phys.* **51**, 635 (1969).
- [32] J.J. Brey, J.W. Dufty, and A. Santos, *J. Stat. Phys.* **87**, 1051 (1997).
- [33] I.S. Gradshteyn and I.M. Ryzhik, *Table of Integrals, Series, and Products* (Academic Press, New York, 1965).
- [34] J.M. Montanero and A. Santos, *Granular Matter* **2**, 53 (2000).
- [35] F. Rouyer, J. Martin, and D. Salin, *Phys. Rev. Lett.* **83**, 1058 (1999).
- [36] P. Deltour and J.-L. Barrat, *J. Phys. I* **7**, 137 (1997).
- [37] S. Luding and S. McNamara, *Granular Matter* **1**, 113 (1998).
- [38] I. Goldhirsch and G. Zanetti, *Phys. Rev. Lett.* **70**, 1619 (1993).
- [39] T.P.C. van Noije, M.H. Ernst, R. Brito, and J.A.G. Orza, *Phys. Rev. Lett.* **79**, 411 (1997).
- [40] M.L. Tan and I. Goldhirsch, *Phys. Fluids* **9**, 856 (1997).
- [41] S. Luding and H.J. Herrmann, *Chaos* **9**, 673 (1999).

On the velocity distributions of the one-dimensional inelastic gas

A Barrat¹, T Biben², Z Rácz^{1,3}, E Trizac¹ and F van Wijland¹

¹ Laboratoire de Physique Théorique, Université de Paris-Sud, 91405 Orsay Cedex, France

² Laboratoire de Spectrométrie Physique, Bâtiment 45, Avenue de la Physique, Domaine Universitaire, BP 87, 38402 Saint Martin d'Heres, France

³ Institute for Theoretical Physics, Eötvös University, Pázmány sétány 1/a, 1117 Budapest, Hungary

Received 23 October 2001

Published 11 January 2002

Online at stacks.iop.org/JPhysA/35/463

Abstract

We consider the single-particle velocity distribution of a one-dimensional fluid of inelastic particles. Both the freely evolving (cooling) system and the non-equilibrium stationary state obtained in the presence of random forcing are investigated, and special emphasis is paid to the small inelasticity limit. The results are obtained from analytical arguments applied to the Boltzmann equation along with three complementary numerical techniques (molecular dynamics, direct Monte Carlo simulation methods and iterative solutions of integro-differential kinetic equations). For the freely cooling fluid, we investigate in detail the scaling properties of the bimodal velocity distribution emerging close to elasticity and calculate the scaling function associated with the distribution function. In the heated steady state, we find that, depending on the inelasticity, the distribution function may display two different stretched exponential tails at large velocities. The inelasticity dependence of the crossover velocity is determined, and it is found that the extremely high-velocity tail may not be observable at 'experimentally relevant' inelasticities.

PACS numbers: 05.70.Ln, 02.70.Ns, 02.70.Uu, 05.10.Ln

1. Introduction

1.1. Motivation

In the widely studied context of non-equilibrium stationary states, granular gases stand out as an interesting model system, accessible to and the subject of many experimental and analytic investigations. Their theoretical description and understanding is one of the present important issues of the development of the out-of-equilibrium statistical mechanics.

The main difference between molecular gases and granular gases stems from the fact that at each collision between, e.g., steel or glass beads (in experiments), or idealized smooth hard spheres (in analytical and numerical investigations), a fraction of the relative kinetic energy is lost [1]. This inelasticity is responsible for many interesting phenomena, such as the appearance of spatial heterogeneities, non-Gaussian velocity distributions, etc. Theoretically, two opposite situations have been extensively studied in the context of smooth inelastic hard spheres we shall consider here, namely, the free cooling case where no forcing mechanism compensates the energy loss due to dissipative collisions (see, e.g., the review [2] and references therein), and the uniformly heated system where an external random force acts as a heating process on the grains, allowing a non-equilibrium stationary state to be reached [3–5].

In this paper, we will study the above two situations (i.e. with or without energy input), and concentrate on a one-dimensional granular fluid. For the homogeneously heated gas (section 2), the focus will be on the high-energy tail of the velocity distribution $P(v)$. Whereas the velocities up to the thermal scale obey a Maxwell–Boltzmann-like distribution, we will show by combining kinetic theory arguments and numerical simulations (both molecular dynamics (MD) and Monte Carlo) that in the limit of vanishing inelasticity, $P(v)$ displays an $\exp(-v^3)$ large v behaviour. At finite inelasticity, this tail is asymptotically dominated by the $\exp(-v^{3/2})$ law already predicted in [4]. These predictions will also be confirmed by the results of a high-precision iterative solution of the non-linear Boltzmann equation. On the other hand, without energy injection (section 3), we will similarly concentrate on the limit of small inelasticity (that appears quite singular, unlike in the heated case), and shed some light on the importance of spatial heterogeneities and velocity correlations: detailed scaling properties of the solutions of the homogeneous Boltzmann equation will be obtained analytically and checked numerically. Further confrontation against molecular dynamics simulations will show that the velocity distributions of the Boltzmann homogeneous cooling state share some common features with those obtained by integrating the exact equations of motion.

1.2. The model

We shall consider a one-dimensional gas of equal mass particles of length σ and density n , evolving on a line of length $L = N/n$ with periodic boundary conditions. These particles undergo binary collisions with conservation of momentum but loss of a fraction (α^2) of the kinetic energy in the centre-of-mass frame: consequently, if v_1 and v_2 (respectively v'_1 and v'_2) are the velocities of the two particles involved before (respectively after) the collision, then

$$v'_1 + v'_2 = v_1 + v_2 \quad (1)$$

$$v'_1 - v'_2 = -\alpha(v_1 - v_2) \quad (2)$$

where $0 \leq \alpha \leq 1$ is the restitution coefficient. We also introduce the inelasticity parameter $\varepsilon = 1 - \alpha$ ($\varepsilon = 0$ for elastic collisions).

We will focus on the behaviour of the velocity distribution $P(v, t)$ in the following two cases:

- Without energy injected, the above collision rules define a system where energy dissipation through collisions is not balanced and the typical velocities of particles progressively decrease. This free cooling regime has been widely studied [6–19] and in particular in dimension 1 by molecular dynamics studies [6, 7, 9, 19]. Slight modifications of the collision rule allow us to bypass the inelastic collapse [20] and observe an asymptotic scaling regime for $P(v, t)$ [19].

- A steady state can be reached if the loss of energy through collisions is balanced by an injection that can be achieved through a random force $\eta(t)$ acting on each particle,

$$\frac{dv}{dt} = F + \eta(t) \quad \langle \eta(t)\eta(t') \rangle = 2D\delta(t-t') \quad (3)$$

where D is the amplitude of the injected power and F the systematic force due to inelastic collisions. Velocities consequently execute a random walk between the collisions, and in the collisionless case $P(v, t)$ obeys a diffusion equation with a ‘diffusion’ coefficient D . This model was first introduced and discussed by Williams and MacKintosh [3] in dimension 1, and studied in higher dimensions [5]; variants have also been proposed [21, 22].

We define the granular temperature as the average kinetic energy of the system:

$$T(t) = \int dv v^2 P(v, t). \quad (4)$$

The function $T(t)$ decreases for the freely cooling system, but it eventually fluctuates around a steady-state value in the heated case.

1.3. Investigation methods

Our study relies on the following three complementary approaches:

- Molecular dynamics (MD) simulations [23] integrate the exact equations of motion in a finite box: we consider N hard rods of length σ , on a line of linear size L , with periodic boundary conditions and random initial velocities, and we use an event-driven algorithm to study their dynamics.
- The Boltzmann equation describes the evolution of the one-particle distribution function $P(v, t)$, upon the molecular chaos factorization hypothesis [24]. This equation is therefore a mean-field approximation of the problem, in which density becomes irrelevant. It can be solved numerically by the direct simulation Monte Carlo (DSMC) method [25], or in certain cases, with an even better precision, by an iterative method similar to that used in [26].
- In the elastic limit $\alpha \rightarrow 1$, an analytical scaling approach can be used to study the Boltzmann equation. It is important to note that, in the particular case of one-dimensional hard spheres, the elastic case $\varepsilon = 0$ is quite peculiar. Indeed, for $\varepsilon = 0$, the collisions only exchange the velocities of the particles: this system is therefore unable to thermalize and is equivalent to one with transparent particles where $P(v, t)$ is frozen in time.

2. Steady state of the heated fluid

The exact solution of the problem of a $d = 1$ inelastic gas appears inaccessible, which prompted us to carry out MD simulations to calculate $P(v, t)$. In order to see whether a mean-field-type approach can give a reasonable description of the inelastic gas, we reconsider the kinetic theory of the process. We solve the appropriate Boltzmann equation by simulations in the general α case, and derive exact results in the $\varepsilon \rightarrow 0$ limit.

Since the gas systematically reaches a stationary state with a temperature T that depends on the inelasticity (see below), it is useful to introduce the rescaled velocity

$$c = \frac{v}{\sqrt{T}} \quad (5)$$

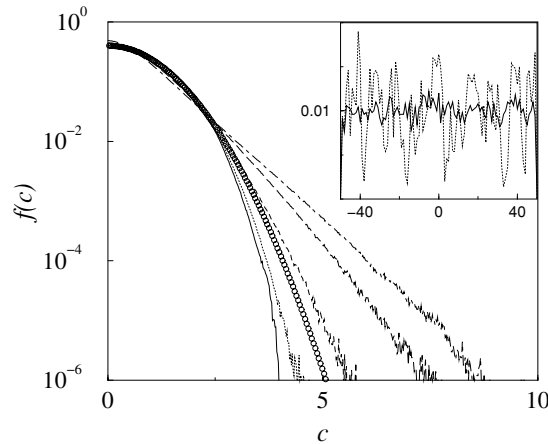


Figure 1. Velocity distributions for MD simulations with 5000 particles, density $n\sigma = 0.5$, for restitution coefficients 0.6, 0.9, 0.95, 0.99 and 0.999 (from top to bottom). The symbols show the Gaussian distribution. The inset shows a typical snapshot of the space density fluctuations for 0.99 (continuous line) and 0.6 (dotted line).

and the corresponding distribution function

$$f(c) = \sqrt{T(t)}P(v, t). \quad (6)$$

In order to compare the velocity distributions at various inelasticities, numerical data for the *rescaled velocity* distributions will always be displayed in the figures.

2.1. General α case

2.1.1. Molecular dynamics simulations. The molecular dynamics simulations are carried out with $N = 5000$ hard rods, using an event-driven algorithm, and submitting the rods to random kicks at a frequency that remains much higher than the collision frequency, in order to simulate the noise of equation (3). Note that, since the Langevin equation considered in [21] is different from ours⁴, comparing the two approaches is not possible without further investigations on either side.

Starting from an initial distribution of velocities, a steady state is reached after a transient, and velocity distributions can be measured. Figure 1 displays such distributions for inelasticity ranging from $\alpha = 0.6$ to 0.999. Strong non-Gaussian behaviour is observed, with over- or under-populated high-energy tails depending on α . Moreover, the inset shows that the system remains quite homogeneous at low inelasticity, while strong density fluctuations develop at larger inelasticity. The value of the density n of the system seems to have no influence on the shape of the velocity distributions, and density fluctuations seem to increase roughly proportional to $1/(n\sigma)$ (at constant α). Detailed investigations of the spatial correlations are left for future studies.

2.1.2. Kinetic theory. Assuming that the density of the particles is low and neglecting both velocity and spatial correlations of colliding partners, the Boltzmann equation for the spatially

⁴ It contains a friction term in velocity space whose amplitude is linked to the force amplitude, whereas detailed balance is not satisfied by our model, where the forcing is independent of the state of the system. We did not consider the friction term in order to study a model (leading to a steady state) with a minimal number of parameters.

averaged velocity distribution function $P(v, t)$ can be written as [7, 15]

$$\begin{aligned} \partial_t P - D \partial_v^2 P = & -n \int_{-\infty}^{\infty} dv' |v - v'| P(v) P(v') \\ & + \frac{4n}{(1 + \alpha)^2} \int_{-\infty}^{\infty} dv' |v - v'| P(v') P\left(\frac{2v - (1 - \alpha)v'}{1 + \alpha}\right). \end{aligned} \quad (7)$$

The right-hand side of equation (7) contains the collision terms corresponding to the ‘dissipative’ rules (2), while the Fokker–Planck term $D \partial_v^2 P$ on the left-hand side takes into account the energy injected by the random forces (3).

The system described by equation (7) is expected to relax to a steady state since the power input is independent of the velocities while the loss of energy is roughly proportional to the energy itself. This expectation can be made more quantitative by deducing the equation for the temperature ($T = \langle v^2 \rangle$) of the system

$$\frac{d\langle v^2 \rangle}{dt} = 2D - \frac{n}{4}(1 - \alpha^2)\langle |v - v'|^3 \rangle \quad (8)$$

where $\langle \cdot \cdot \rangle$ denotes averaging with $P(v, t)$ and $|v - v'|$ represents the relative velocity of two randomly chosen particles. There is a stationary solution to this equation that has a simple physical meaning. Namely, the rate of input of energy ($\sim D$) is equal to the rate of loss of kinetic energy in the centre-of-mass frame $\sim (1 - \alpha^2) \langle |v - v'|^2 \rangle$ (with the extra factor $n|v - v'|$ coming from the collision rate). One may also estimate the characteristic time of reaching the steady state. Indeed, the quantities $T^{3/2} = \langle v^2 \rangle^{3/2}$ and $\langle |v|^3 \rangle$ are expected to have the same leading large-time ($t \rightarrow \infty$) dependence, and thus, up to an unknown numerical constant \mathcal{C} , equation (8) can be written as

$$\frac{dT}{dt} = 2D - \mathcal{C} n(1 - \alpha^2) T^{3/2}. \quad (9)$$

The typical relaxation time is then $\tau_{\text{relax}} \sim [D/(n(1 - \alpha^2))]^{2/3}$. In the small inelasticity limit ($\varepsilon \rightarrow 0$), this relaxation time diverges as $\tau_{\text{relax}} \sim \varepsilon^{-2/3}$. We have indeed observed such a behaviour of the approach to the steady state in both MD and DSMC simulations.

Many pieces of information on the stationary distribution function have been obtained in [4]; in particular, the deviations from a Gaussian $\Phi(c) = e^{-c^2/2}/\sqrt{2\pi}$ have been investigated by the Sonine expansion [27]

$$f(c) = \Phi(c) \left(1 + \sum_{p=1}^{\infty} a_p S_p(c^2) \right) \quad (10)$$

where S_p are polynomials orthogonal with the Gaussian weight Φ . The coefficients a_p are then obtained from the moments of f . From the definition of temperature, a_1 vanishes and the first correction a_2 , which is related to the kurtosis of the velocity distribution, has been computed in any dimension neglecting non-linear contributions of $\mathcal{O}(a_2^2)$; in dimension 1, it has the expression

$$a_2 \equiv 4 \left(\frac{\langle v^4 \rangle}{3\langle v^2 \rangle^2} - 1 \right) = \frac{16(1 - 2\alpha^2)}{129 + 30\alpha^2}. \quad (11)$$

We note a peculiarity of dimension 1: a_2 does not vanish as $\alpha \rightarrow 1$, unlike in space dimensions $d > 1$ in which $\lim_{\alpha \rightarrow 1} a_2 = 0$. This is a hint that the quasi-elastic limit is more singular in $d = 1$ than in higher dimensions.

Besides, it was shown in [4] how to determine the high-energy tail of the velocity distribution. We briefly recall the argument. The ε -dependent gain term in the collision

integral appearing in the Boltzmann equation (7) is *a priori* neglected. In the large velocity limit the resulting equation for the steady-state distribution $P_s(v)$ reads

$$D \frac{d^2 P_s}{dv^2} = -n|v|P_s(v) \quad (12)$$

which yields a high-energy tail of the form $\exp(-\frac{2}{3}\sqrt{n/D}|v|^{3/2})$. Then one verifies that the gain term is indeed negligible (as would be the case for any solution decaying faster than exponentially). The 3/2 exponent is independent of the space dimension; therefore the behaviour of the large- c tail is singular for $\varepsilon \rightarrow 0$, with an exponent jumping abruptly from 3/2 for $\varepsilon > 0$ to 2 for $\varepsilon = 0$ (for dimensions larger than 1, the elastic system equilibrates and thus f is a Gaussian).

2.1.3. Numerical solution of the homogeneous Boltzmann equation. We have obtained numerically the exact solution of the Boltzmann equation, i.e. the velocity distributions, in the homogeneous situation, for various values of the restitution coefficient. Two methods have been used: the well known DSMC method and another powerful iterative method, recently introduced by Biben *et al* [26]. Let us recall the idea of this method.

The stationary velocity distribution can be obtained numerically through a direct iteration of equation (7). From an initial guess for the velocity distribution $P(v)$ (a step function for example), the time evolution can be computed from equation (7) until the steady state is reached. Taking advantage of the $v \rightarrow -v$ symmetry of the velocity distribution, we only need to know the values of P for positive velocities. $P(v)$ is then discretized from $v = 0$ to $v = (N_v - 1)dv$, where typically $N_v = 1000$ and $dv = 0.01\sqrt{D\sqrt{\pi}/(n(1-\alpha^2))}$. The right-hand side of equation (7) can be estimated using the Simpson integration, combined with a quadratic interpolation method to estimate the values of

$$P\left(\frac{2v - (1-\alpha)v'}{1+\alpha}\right)$$

whose argument does not necessarily coincide with the velocity discretization. An implicit method is used to solve the diffusion equation: if P_i^{t+dt} denotes the new estimate of $P(i dv)$ at time $t + dt$, the left-hand side of equation (7) can be written in the time-velocity discretized space:

$$\frac{dP}{dt} - D\partial_v^2 P \rightarrow \frac{P_i^{t+dt} - P_i^t}{dt} - D \frac{P_{i+1}^{t+dt} - 2P_i^{t+dt} + P_{i-1}^{t+dt}}{dv^2}$$

which leads to the following equation for P_i^{t+dt} :

$$\left(1 + 2D \frac{dt}{dv^2}\right) P_i^{t+dt} - D \frac{dt}{dv^2} (P_{i+1}^{t+dt} + P_{i-1}^{t+dt}) = P_i^t + dt \{\text{RHS of (7) at site } i \text{ and time } t\}. \quad (13)$$

We recognize a band tridiagonal matrix on the left-hand side which can easily be inverted numerically to provide the new value of the velocity distribution at time $t + dt$. Normalization of the velocity distribution is enforced at each time step.

Figure 2 shows a perfect agreement between the two methods, the iterative method allowing much higher precision to be reached (see the y -scale). The obtained distributions show strong deviations from the Gaussian, just as in the MD case. However, the distributions obtained by MD and DSMC agree only in the $\alpha \rightarrow 1$ limit, as was expected because of the spatial inhomogeneities appearing in the MD simulations.

The measure of the fourth cumulant a_2 (the first correction to the Gaussian) shows excellent agreement between the DSMC data and the kinetic theory predictions from equation (11),

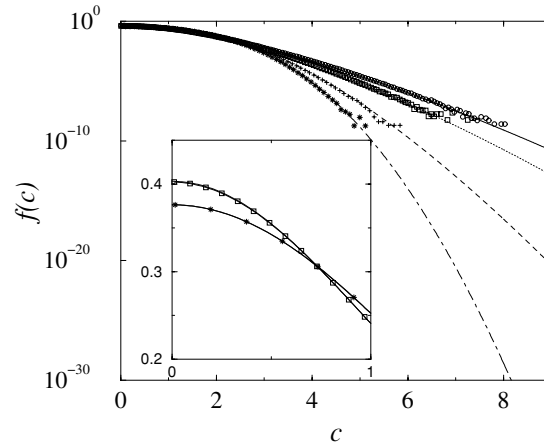


Figure 2. Velocity distributions obtained by DSMC with 25 000 particles (symbols) or by the iteration method (lines), in a log-linear scale, for restitution coefficients 0.1, 0.6, 0.9 and 0.99 (from top to bottom). Inset: same distributions on a linear scale, for restitutions 0.6 (stars) and 0.99 (squares).

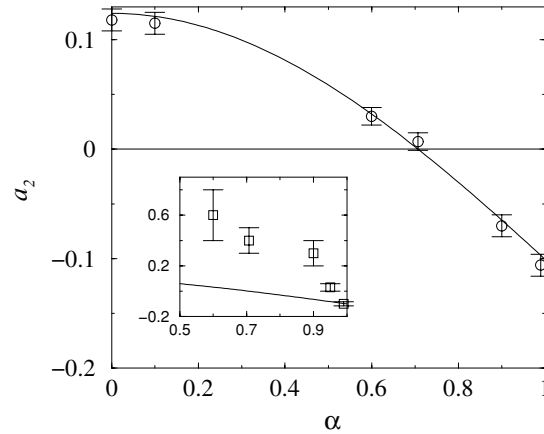


Figure 3. Values of the second Sonine coefficient a_2 , obtained by measuring the fourth cumulant of $f(c)$ in DSMC simulations (circles), together with the kinetic theory prediction equation (11) (line). Inset: MD values for a_2 (squares) and kinetic theory prediction (line).

over the whole range of inelasticities (see figure 3). In the limit $\alpha \rightarrow 1$, a_2 obtained in MD coincides with the prediction of equation (11), namely, $a_2 \rightarrow -16/159$. Moreover, the full velocity distribution function coincides with that obtained in DSMC (see figure 5 below). However, as α decreases, the MD results significantly deviate from their molecular chaos counterparts (see the inset to figure 3)

Moreover, plotting the velocity distribution versus either $c^{3/2}$ or c^3 , as in figure 4, shows that the high-energy tail obtained by the DSMC method has a shape going from the predicted $\exp(-Ac^{3/2})$ at large inelasticity to an $\exp(-Ac^3)$ behaviour at low inelasticity. For intermediate values of α , a fit to a form $\exp(-Ac^B)$ would lead to intermediate values of B . Since the *real* high-energy limit *has to* follow an $\exp(-Ac^{3/2})$ law [4], this shows that

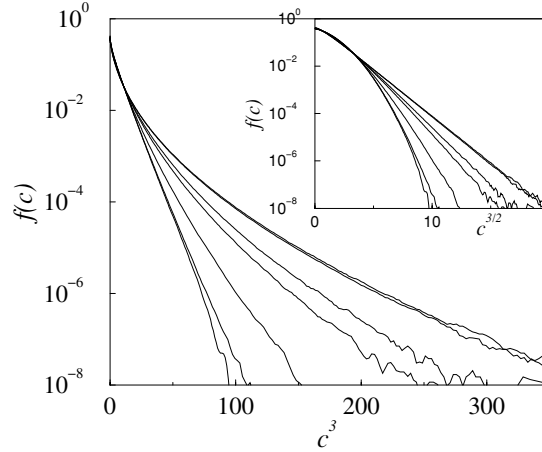


Figure 4. Velocity distributions, obtained by DSMC with 25 000 particles, versus c^3 and in the inset versus $c^{3/2}$, for restitution coefficients 0, 0.1, 0.6, 0.707, 0.9, 0.99 and 0.999 (from top to bottom): at low restitution coefficient, $f(c)$ shows an $\exp(-Ac^{3/2})$ behaviour, and an $\exp(-Ac^3)$ behaviour as α goes to 1.

for low ε , this limit is far beyond the reach of usual numerical methods, and emphasizes the fact that the range over which the large- c limit is valid depends on the inelasticity. This is an important point since experiments have a limited precision, and the distribution function will have a practically vanishing weight long *before* this range is reached. In the next subsection we will see that the investigation of the $\alpha \rightarrow 1$ limit and the use of the iterative method allow us to understand the $\exp(-Ac^3)$ form obtained for α close to 1.

2.2. Small inelasticity limit

For small values of $\varepsilon \equiv 1 - \alpha$, the Boltzmann equation takes the form

$$\begin{aligned} \partial_t P(v, t) = D \partial_v^2 P(v, t) + n\varepsilon \int_{-\infty}^{\infty} dw |v - w| P(w, t) \\ \times \left[P(v, t) + \frac{1}{2}(v - w) \partial_v P(v, t) \right] + \mathcal{O}(\varepsilon^2). \end{aligned} \quad (14)$$

The $\varepsilon \rightarrow 0$ limit can now be taken by introducing a scaled velocity $x = (n\varepsilon/D)^{1/3}v$. Using x , the Boltzmann equation yields an equation for the scaled distribution function $\phi(x) = (n\varepsilon/D)^{1/3}P_s(v)$ (where $P_s(v)$ is the stationary distribution $\lim_{t \rightarrow \infty} P(v, t)$):

$$\frac{d^2 \phi}{dx^2} + \int_{-\infty}^{\infty} dy |x - y| \phi(y) \left[\phi(x) + \frac{1}{2}(x - y) \frac{d\phi}{dx} \right] = 0 \quad (15)$$

and we can integrate this equation twice to obtain

$$\phi(x) = C \exp \left\{ -\frac{1}{6} \int_{-\infty}^{\infty} dy |y - x|^3 \phi(y) \right\}. \quad (16)$$

Here C is a constant determined from the normalization condition $\int dx \phi(x) = 1$. We have used the above equation to implement an iterative scheme to find numerically the corresponding

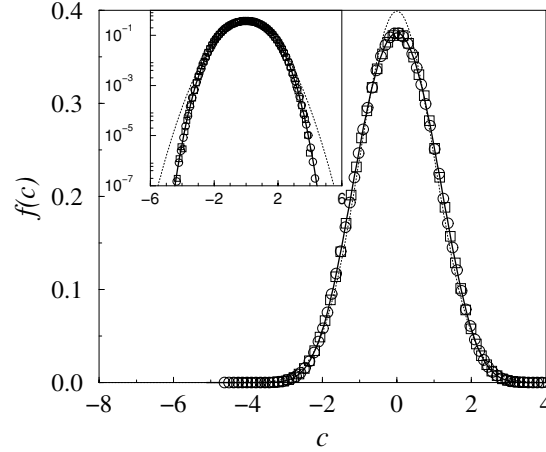


Figure 5. Symbols: velocity distributions obtained numerically at $\alpha = 0.999$ by MD and DSMC simulations; the solid line is the numerical solution $\phi(x)$ of equation (16), corresponding to the $\alpha \rightarrow 1$ limit, and here rescaled in order to have the same variance as the simulation data ($\langle c^2 \rangle = 1$). A perfect agreement between the three sets of data is observed. The dotted line is the Gaussian distribution.

velocity distribution. Moreover, as already pointed out in [13], one can easily see that the large $|x|$ limit is given by

$$\phi(x) = C e^{-\frac{1}{6}|x|^3} \quad (17)$$

while at small x , the function can be approximated by a Gaussian

$$\phi(x) = \tilde{C} e^{-\frac{1}{2}\lambda x^2} \quad (18)$$

with $\lambda = \int dx |x| \phi(x) \approx 0.785$ determined from the numerical solution of equation (16) and $\tilde{C} = C \exp(-\int dx |x|^3 \phi(x)/6)$. The full numerical solution (displayed in figure 5) can also be investigated for locating the place where the crossover between the Gaussian and the $\exp(-|x|^3/6)$ type behaviour takes place. We find that the crossover range deduced from comparing the asymptotics (17) and (18), $x_{\text{cr}} = 3\lambda \simeq 2.36$, is actually in agreement with numerical observations of the full function. Thus returning to non-scaled velocities, we can see that the crossover velocity $v_{\text{cr}}^{(1)}$ diverges in the $\varepsilon \rightarrow 0$ limit as

$$v_{\text{cr}}^{(1)} \approx \left(\frac{D}{n\varepsilon} \right)^{1/3}. \quad (19)$$

The important consequence of this result is that, for small dissipation, the $\exp(-Av^3)$ regime is reached for larger and larger velocities.

At large but finite velocities, an effective exponent can be defined by

$$n = \frac{d}{d \ln v} \ln \left\{ -\ln \left[\frac{P(v)}{P(0)} \right] \right\} \quad (20)$$

corresponding to an apparent $\exp(-Av^n)$ behaviour. The values of n for various inelasticities, obtained with the iterative method, are displayed in figure 6, together with the $\alpha \rightarrow 1$ limit. The effective exponent, starting from 2 at small velocities, increases and reaches a maximum at velocities that scale as $\varepsilon^{-1/3}$ for small ε (as $v_{\text{cr}}^{(1)}$). The height of the maximum, $n_{\text{cr}}^{(1)}$, scales as $3 - n_{\text{cr}}^{(1)} \sim \varepsilon^{1/3}$.

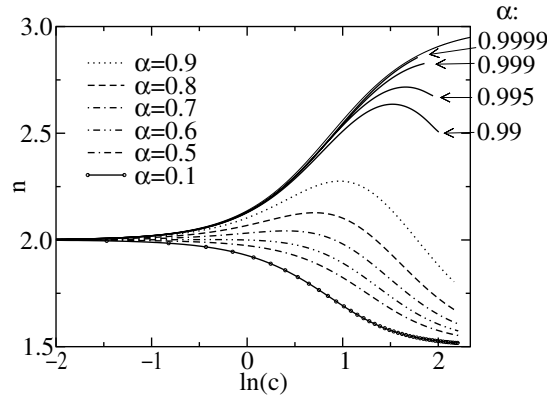


Figure 6. Effective exponent defined by equation (20) for the solution of the Boltzmann equation obtained by the iterative method and for the numerical solution of the $\alpha \rightarrow 1$ limit (upper curve, obtained from the iterative resolution of equation (16)).

One should note that the above scaling analysis explores only the $v \sim \varepsilon^{-1/3}$ range of the velocity space. As already mentioned, for any fixed ε , the large v limit of the distribution function is a stretched exponential

$$P_s(v) \sim \exp\left\{-\frac{2}{3}\left(\frac{n}{D}\right)^{1/2}|v|^{3/2}\right\} \quad (21)$$

which is indeed observed numerically at relatively low values of α (see figure 4). Comparing the arguments of the exponents in (17) and (21), one finds a crossover scale diverging as

$$v_{\text{cr}}^{(2)} \approx \left(\frac{D}{n\varepsilon^2}\right)^{1/3}. \quad (22)$$

The effective exponent displayed in figure 6 indeed decreases at velocities larger than $v_{\text{cr}}^{(1)}$. For large inelasticities, the $n \rightarrow 3/2$ limit of large velocities is observed; however, since $v_{\text{cr}}^{(2)} \approx v_{\text{cr}}^{(1)}/\varepsilon^{1/3}$, it becomes impossible to observe the asymptotics (21) for small inelasticities, even for almost realistic values of α , e.g. 0.95 (in experiments, $\alpha \sim 0.8$ – 0.9).

It has to be emphasized that this kind of behaviour is also observed in higher dimensions (for example, simulations of a two-dimensional heated granular gas with $\alpha = 0.8$ yield an almost Gaussian velocity distribution, even if the predicted high-energy behaviour is $\exp(-v^{3/2})$); it is therefore to be kept in mind for the comparisons of models with experiments in which the available precision often does not allow the predicted tails to be reached.

Finally, as already mentioned, it can be seen in figure 5 that, for $\varepsilon \rightarrow 0$, there is an excellent agreement between the single particle velocity distribution obtained in MD simulations (including both the space and velocity correlations) and that derived either from the asymptotic ($\varepsilon \rightarrow 0$) distribution function $\phi(x)$ or from the Monte Carlo simulation of the Boltzmann equation.

3. Freely cooling system

3.1. General considerations

In the freely cooling system, no energy is injected and the temperature is monotonically decreasing with time. The first investigations of the one-dimensional freely evolving gas were

undertaken in [6–9]; it was shown by molecular dynamics simulations that, depending on the values of the number of particles and the restitution coefficient, different instabilities could occur: e.g. at fixed number of particles N , if α is lower than a threshold, strong clustering occurs and leads to an inelastic collapse [6]. At larger α , the instability develops more slowly, and the inelastic collapse is avoided. The temperature then decays according to the rate equation $dT/dt \propto -T^{3/2}$, i.e. $T(t) \sim t^{-2}$ [28], however derived for a homogeneous system, whereas strong heterogeneities develop in both velocity and space coordinates; a wavy, oscillatory in time, perturbation appears in a ‘phase-space’ plot (velocity versus position) [7, 8] with a tendency to form a bimodal velocity distribution.

The choice of a suitable quasi-elastic limit (where $\varepsilon \rightarrow 0$ and $N \propto 1/\varepsilon$ to avoid the inelastic collapse) leads to a simplified Boltzmann equation [7, 9–11], which can be understood using arguments from kinetic theory and hydrodynamics. This equation can be considered as formally exact as it has also been derived in [12] from the exact BBGKY-like hierarchy governing the evolution of the distribution [24]. In this quasi-elastic limit, the velocity was observed to develop a two-hump structure reminiscent of the bimodal velocity distribution observed in molecular dynamics [7, 9]. Moreover, exact results were derived in the context of the above-mentioned limit, where it was shown in particular that to leading order in ε , the velocity distribution consists of two symmetric Dirac peaks [12].

Extensive MD simulations were carried out in [19], using large sizes and probing large times, starting from a homogeneous situation with an initial given velocity distribution. As long as the system is homogeneous, the temperature decays according to $T(t) \sim t^{-2}$ [28]. As time evolves, space clustering of particles occurs and a $t^{-2/3}$ decay is obtained [19]. Since the number of particles is large, inelastic collapse should then occur; this catastrophic event is avoided by imposing that the collisions between particles with relative velocity smaller than a given threshold are elastic (they can equally be chosen to be sticky), and it was checked that the results do not depend on the chosen threshold. In this respect, the authors of [19] showed that the one-dimensional inelastic fluid belongs to the ‘universality class’ of the sticky gas, and advocated a mapping to the Burgers equation to describe the appearing heterogeneities. Moreover, at large times the rescaled velocity distribution $f(c)$ was found stationary and very close to a Gaussian up to the available accuracy (see also figure 7), even if the mapping to the Burgers equation predicts an $\exp(-Ac^3)$ high-energy tail. In fact, the bimodal structure of $f(c)$ reported in [7, 9] can also be observed in this case during the transient homogeneous behaviour, during which spatial heterogeneities and correlations build up, as shown in [29]; moreover, it can be clearly seen only by a convenient choice of the initial velocity distribution. The importance of spatial heterogeneities and correlations is emphasized in figure 7, where the rescaled velocity distribution obtained following the prescription put forward by Ben-Naim *et al* [19] (that is essentially Gaussian) is compared to that obtained from the homogeneous Boltzmann equation⁵. The two-hump structure displayed by the latter appears for $\alpha > 0.8$ and becomes more and more pronounced as α increases. In the next subsection, we will investigate in detail this structure in the $\varepsilon \rightarrow 0$ limit.

3.2. Small inelasticity limit

We have performed MD simulations using the two possibilities to avoid inelastic collapse mentioned in section 3.1.

- In figure 8, the top panel displays the results obtained for $\varepsilon = 5 \times 10^{-4}$ at various stages of the evolution: at first the system remains homogeneous but the tendency to form a

⁵ As expected, the temperature obeys the scaling law $T \propto t^{-2}$ in DSMC.

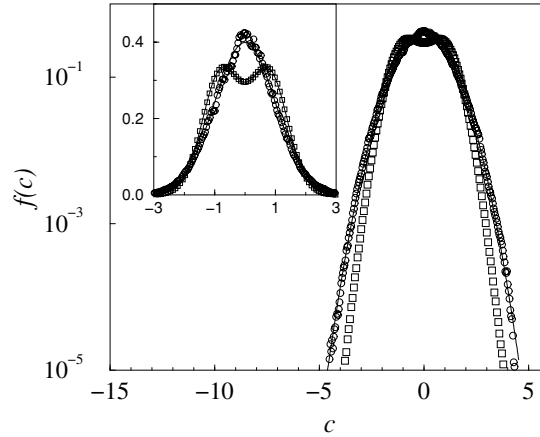


Figure 7. Rescaled velocity distributions at large times (in the scaling regime) at $\alpha = 0.85$ obtained by MD with $N = 25\,000$ (circles) and DSMC (squares) simulations. The solid line is the Gaussian distribution. In MD simulations, the inelastic collapse has been regularized by considering the same modified collision rule as in [19].

bimodal velocity distribution is rapidly obtained. The large time situation consists of two well defined clusters evolving with opposite velocities and yielding a sharply peaked bimodal velocity distribution (figure 8, bottom panel). In this case, the overall kinetic energy decay $E(t) \sim t^{-2}$ consists in a series of plateau since most of the dissipation occurs when the two clusters collide [7].

- On the other hand, with the regularization proposed in [19], the duration of the transient behaviour increases with α , but the large time behaviour of the velocity distribution is always Gaussian.

It is striking to note that the above two procedures (small number of particles or elastic collisions at small enough velocities) lead to drastically different behaviour for the decay of the temperature, the spatial heterogeneities and the velocity distributions. Moreover it is remarkable that the homogeneous solution of the Boltzmann equation captures the bimodality of $f(c)$ (see figure 8, bottom panel) associated with a strongly heterogeneous system. In order to gain an insight into the approach to the limit $\varepsilon \rightarrow 0$, we devote the remainder of this paper to the analysis of the scaling properties of the homogeneous non-linear Boltzmann equation. We expect that for low enough inelasticity, $f(c)$ tends towards two delta peaks at $c = \pm 1$, as predicted in [12]. Performing DSMC simulations for smaller and smaller inelasticities allow this regime to be approached, and figure 9 shows how the peaks become narrower as α increases.

As the system cools, the velocity distribution $P(v, t)$ evolves into the Dirac distribution $\delta(v)$. The above numerical results indicate that this distribution actually consists of two peaks located symmetrically around the velocity origin, at positions decaying as $\pm(\varepsilon t)^{-1}$. Moreover, it appears that the results displayed in figure 9 for the rescaled velocity c hide a self-similar structure, with the width of the peaks scaling as $\varepsilon^{1/3}$, as evidenced in figure 10 where the distributions corresponding to different inelasticities collapse onto a master curve. The characteristic features of this master curve are investigated below and to this end, we return to the ε expansion of the Boltzmann equation (14), omitting the Fokker–Planck term $D\partial_v^2 P$, since the fluid evolves freely in the present situation.

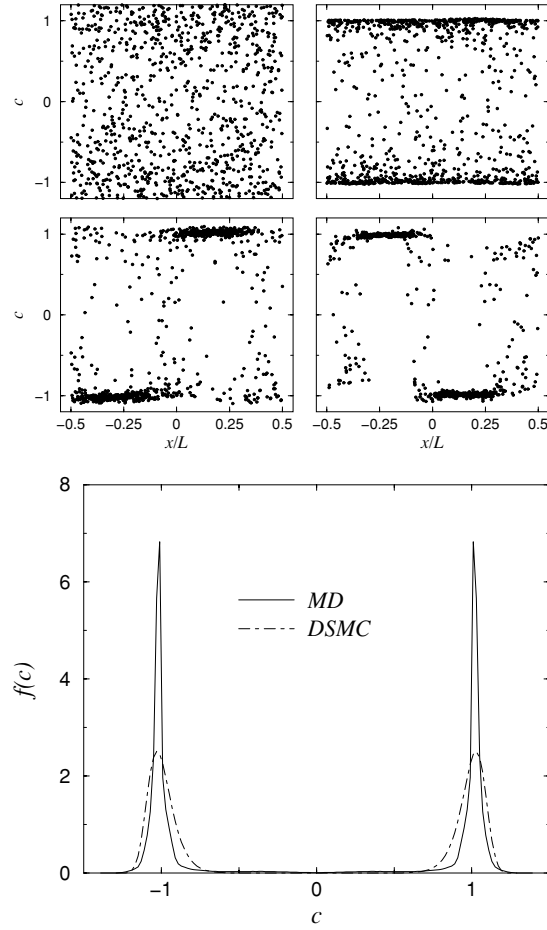


Figure 8. Top: velocity–density scatter plots obtained in MD simulations with $N = 1000$ and $\alpha = 0.9995$. Each dot marks the location of a particle in the x - c plane, where x denotes the position in the simulation box and c denotes the velocity rescaled by the thermal velocity. Starting from an initial Gaussian distribution of velocities and random initial positions, the four snapshots correspond, from left to right and top to bottom, to four instantaneous configurations observed after respectively 4×10^3 , 2×10^4 , 4×10^4 and 6×10^4 collisions per particle. Bottom: velocity statistics obtained in MD by averaging in the late time regime for the same initial situation and parameters as above, compared to its ‘mean-field’ counterpart provided by DSMC simulations at the same inelasticity ($\alpha = 0.9995$).

From the evolution of temperature ($T \propto \varepsilon^{-2}t^{-2}$), it appears that a convenient scaling variable is $x \equiv n\varepsilon t v$ with a corresponding probability distribution function Φ related to $P(v, t)$ through $P(v, t) = n\varepsilon t \Phi(n\varepsilon t v)$. To leading order in ε , the Boltzmann equation is then brought into the simple form

$$\frac{d(x\Phi)}{dx} = \int dy |x - y| \Phi(y) \left[\Phi(x) + \frac{1}{2}(x - y) \frac{d\Phi}{dx} \right] \quad (23)$$

the solution of which reads [12]

$$\Phi(x) = \frac{1}{2}[\delta(x - 1) + \delta(x + 1)]. \quad (24)$$

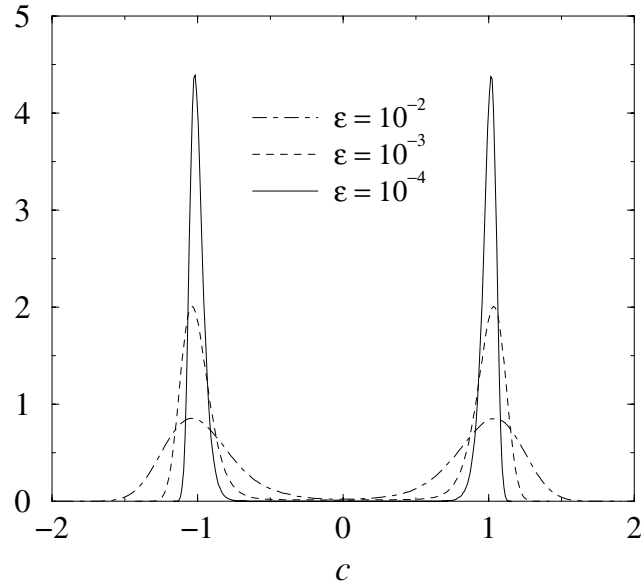


Figure 9. Rescaled velocity distributions at $\alpha = 1 - \varepsilon$ with $\varepsilon = 10^{-2}$, 10^{-3} and 10^{-4} obtained by DSMC simulations.

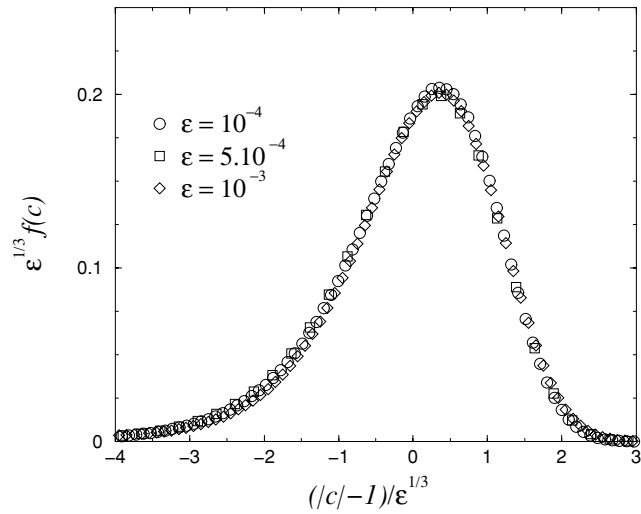


Figure 10. Self-similarity of the rescaled distribution functions for small inelasticities.

Looking for the self-similar structure of the peaks shown in figures 9 and 10 requires pushing the ε -expansion one order further compared to equation (23),

$$\frac{d(x\Phi)}{dx} = \int dx' |x - x'| \Phi(x') \left[\frac{1}{(1 - \varepsilon/2)^2} \Phi\left(x + \frac{\varepsilon}{2 - \varepsilon}(x - x')\right) - \Phi(x) \right] \quad (25)$$

and considering solutions for Φ of the form

$$\Phi(x) = \varepsilon^{-\nu} \left[\frac{1}{2} \psi \left(\frac{1+b(\varepsilon)x}{\varepsilon^\nu} \right) + \frac{1}{2} \psi \left(\frac{1-b(\varepsilon)x}{\varepsilon^\nu} \right) \right]. \quad (26)$$

In equation (25), the positive function ψ has the interpretation of the (ε -rescaled) velocity distribution of left (or right) movers, and $b(\varepsilon) = b_0 + \varepsilon^\nu b_1 + \varepsilon^{2\nu} b_2$. Substituting the scaling assumption for Φ into (25) and performing the change of variables $x = -1 + \varepsilon^\nu y$, we obtain a non-linear integro-differential equation for $\psi(y)$:

$$\begin{aligned} a(\varepsilon)[\varepsilon^{1-\nu}(y\psi)' - \varepsilon^{1-2\nu}\psi'] &= \frac{\varepsilon}{2} \int dy' |y - y'| \psi(y') \left(\psi(y) + \frac{1}{2}(y - y')\psi'(y) \right) \\ &+ \frac{\varepsilon^{-\nu}}{2} \int dy' |2 - \varepsilon^\nu(y + y')| \psi(y') \\ &\times \left[-\varepsilon^{1-\nu}\psi' + \frac{\varepsilon}{2}(y + y')\psi' + \varepsilon\psi + \frac{1}{2}\varepsilon^{2-2\nu}\psi'' \right] \end{aligned} \quad (27)$$

where terms of the form $\psi(-2\varepsilon^{-\nu} + y)$ have been neglected, anticipating that they will be exponentially small. Terms of order $\varepsilon^{2-2\nu}$ and $\varepsilon^{1+\nu}$ were equally neglected. Assuming again that ψ will have a sharp decay, we write that under the integrals $|2 - \varepsilon^\nu(y + y')| = 2 - \varepsilon^\nu(y + y')$. Identifying on both sides of equation (27) terms of order $\varepsilon^{1-2\nu}$ and $\varepsilon^{1-\nu}$ leads, respectively, to

$$b_0 = \int dy' \psi(y') \quad (28)$$

which is the normalization condition, and

$$\psi'(y) \left\{ b_1 + \int dy' y' \psi(y') \right\} = 0 \quad (29)$$

which relates b_1 to $\langle y \rangle$ (a constant function ψ cannot be a solution). We choose to impose $b_1 = -\langle y \rangle_\psi = 0$, where the notation $\langle \dots \rangle_\psi$ stands for an average with respect to weight function ψ . Then one notices that the expansion is consistent only with the condition that the $\varepsilon^{2-3\nu}$ term can be cancelled by terms of order ε , which imposes that

$$\nu = \frac{1}{3} \quad (30)$$

and we recover the exponent 1/3 that was needed to collapse the velocity distributions at several small inelasticities, as done empirically in figure 10. Finally we equate to zero the terms of order ε to obtain the following integro-differential equation:

$$\begin{aligned} b_2 \psi'(y) &= \int dy' \psi(y') \left[\frac{1}{2} \psi(y) (|y - y'| - (y + y')) \right. \\ &\left. + \frac{1}{4} \psi'(y) (|y - y'| (y - y') - (y + y')^2) + \frac{1}{2} \psi''(y) \right] \end{aligned} \quad (31)$$

which we integrate once, remembering that $b_0 = \langle 1 \rangle_\psi$,

$$b_0 \psi'(y) + 2b_2 \psi(y) + \frac{1}{2} \psi(y) \int dy' \psi(y') (|y - y'| (y - y') - (y + y')^2) = 0. \quad (32)$$

We know from the direct analysis of the $\varepsilon \rightarrow 0$ limit of the scaling function that $b_0 = 1$, which we use from here on. At this stage we note that integrating the above equation and using $\langle y \rangle_\psi = 0$ leads to

$$2b_2 = \langle y^2 \rangle_\psi. \quad (33)$$

Conversely, setting $b_2 = \frac{1}{2}\langle y^2 \rangle_\psi$ will automatically enforce $\langle y \rangle_\psi = 0$. We rewrite the equation for ψ in the form

$$\ln \psi(y) = \ln C - 2b_2 y + \frac{1}{6} \int dy' \psi(y') [|y - y'|^3 - (y + y')^3]. \quad (34)$$

We now investigate the asymptotics of ψ . The left tail of the distribution at large negative values of y reads

$$y \rightarrow -\infty \quad \psi(y) \simeq C \exp\left[\frac{1}{3}y^3 + o(1)\right]. \quad (35)$$

This sharp decay at $y \rightarrow -\infty$ *a posteriori* justifies the approximations made in the course of the calculation. Note that omitting the first line on the rhs of equation (27) leads to exactly the same behaviour of the tail of the distribution. This has a physical interpretation: collisions between particles heading in the same direction can be neglected at large velocities. Opposite-velocity collisions are responsible for the form of the tail at large velocities. $o(1)$ represents contributions going exponentially fast to 0.

The right tail $y \rightarrow +\infty$ decays exponentially fast as

$$\psi(y) \simeq C' \exp\{-2\langle y^2 \rangle_\psi y + o(1)\} \quad \text{with} \quad C' = C \exp\left\{-\frac{1}{3}\langle y^3 \rangle_\psi\right\} \quad (36)$$

which again justifies the assumptions made so far. $o(1)$ again represents contributions going exponentially fast to 0. For completeness we mention the $y \rightarrow 0$ behaviour of the scaling function:

$$\psi(y) = C'' \exp\left\{-\frac{y}{2}(3s^2 + |s|s)_\psi + y^2(|s|)_\psi + \mathcal{O}(y^3)\right\} \quad \text{with} \\ C'' = C \exp\left\{\frac{1}{6}(|y|^3 - y^3)_\psi\right\}. \quad (37)$$

As a side remark, the integro-differential equation for ψ can be cast in the form of an ordinary fourth-order differential equation

$$(\ln \psi)^{(iv)} = \psi. \quad (38)$$

Finally, we note that numerical iteration of the integro-differential equation (32) converges extremely rapidly. This allows us to determine the numerical constants C , $\langle y^2 \rangle_\psi$ and $\langle y^3 \rangle_\psi$ appearing in the asymptotics. The results obtained from this numerical scheme are compared with those of the DSMC method in figure 11, and show a quantitative agreement which improves as ε is lowered in DSMC, as expected (see the dotted line at $\varepsilon = 10^{-4}$, closer to the asymptotic scaling form for ψ than the dashed line corresponding to $\varepsilon = 10^{-3}$).

4. Conclusion

We have investigated the velocity statistics of one-dimensional granular fluids of inelastic particles with a particular emphasis on scaling properties in the elastic limit, both in the absence of an external forcing and in a system heated by random accelerations. For the heated system, we showed that the expected high-energy tail $\sim \exp(-Ac^{3/2})$ yields the correct asymptotic behaviour at finite inelasticity ε , but this asymptotics is masked by a tail $\sim \exp(-Bc^3)$ for $\varepsilon \rightarrow 0$, with the *rescaled* crossover velocity between the two regimes scaling as $\varepsilon^{-1/3}$. This shows that the limits of high velocity and low inelasticity do not commute: if $\varepsilon \rightarrow 0$ is taken *before* the high-energy limit, the distribution exhibits an asymptotic $\sim \exp(-Ac^3)$ large- c behaviour:

$$f(\varepsilon, c) \stackrel{c \rightarrow \infty}{\propto} \exp(-Ac^{3/2}) \quad \text{for any } \varepsilon \neq 0 \quad (39)$$

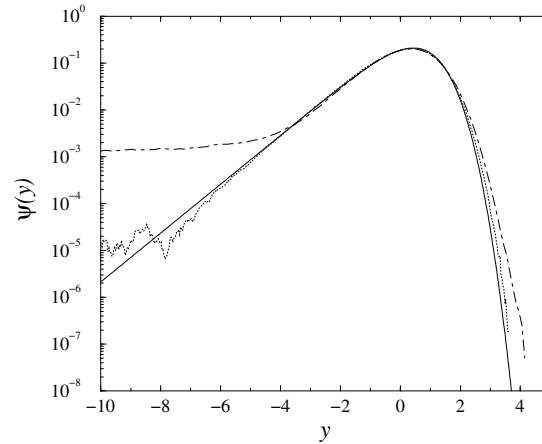


Figure 11. Comparison of the scaling function $\psi(y)$ (see text for definition) obtained within DSMC ($\varepsilon = 10^{-4}$, dotted line and $\varepsilon = 10^{-3}$, dashed line), with the solution of equation (32) corresponding to the quasi-elastic limit.

whereas

$$\lim_{\varepsilon \rightarrow 0} f(\varepsilon, c) \stackrel{c \rightarrow \infty}{\propto} \exp(-Ac^3). \quad (40)$$

Thanks to a high-precision iterative scheme allowing the homogeneous non-linear Boltzmann equation to be solved, we could obtain the velocity distribution over 30 orders of magnitude at arbitrary ε , and thus define the apparent exponent n of the stretched exponential law for large c [$f(c) \propto \exp(-Cc^n)$]. However, even with such precision, the crossover between the two behaviours (39) and (40) is difficult to investigate (see figure 6).

For the freely evolving 1D granular fluid, we have investigated in detail the structure and scaling properties of the two-hump velocity distribution exhibited by the solution of the homogeneous cooling state of the Boltzmann equation, both numerically and analytically. Such a bimodal distribution captures an essential feature of the velocity distributions obtained in molecular dynamics simulations for parameters hindering the inelastic collapse (i.e. extremely small ε or small systems). In this respect, a perturbative Sonine expansion in the spirit of that put forward in [4] fails at small ε , whereas such an expansion turned out to be remarkably accurate for the heated gas (see figure 3). In both cases it would predict a non-vanishing kurtosis correction a_2 for $\varepsilon \rightarrow 0$, which is a peculiarity of $d = 1$; as soon as $d > 1$, a_2 vanishes for small inelasticities, with or without forcing.

Given the striking features of the velocity distributions obtained in dimension 1, it would be of interest to perform the same analysis for realistic space dimensions $d > 1$, and to quantify more precisely space and velocity correlations [30], for both the heated and unforced systems, in order to understand in particular which of these features survive.

Acknowledgments

ZR has been partially supported by the Hungarian Academy of Sciences (grant no OTKA T029792).

References

- [1] Jaeger H M, Nagel S R and Behringer R P 1996 *Rev. Mod. Phys.* **68** 1259
- [2] Dufty J 2001 *Preprint* cond-mat/0108444
- [3] Williams D R M and MacKintosh F C 1996 *Phys. Rev. E* **54** R9
- [4] van Noije T P C and Ernst M 1998 *Gran. Matter* **1** 57
- [5] Peng G and Ohta T 1998 *Phys. Rev. E* **58** 4737
- van Noije T P C, Ernst M H, Trizac E and Pagonabarraga I 1999 *Phys. Rev. E* **59** 4326
- Henrique C, Batrouni G and Bideau D 2000 *Phys. Rev. E* **63** 011304
- Moon S J, Shattuck M D and Swift J B 2001 *Phys. Rev. E* **64** 031303
- Pagonabarraga I, Trizac E, van Noije T P C and Ernst M H 2001 *Phys. Rev. E*
(Pagonabarraga I, Trizac E, van Noije T P C and Ernst M H 2001 *Preprint* cond-mat/0107570)
- [6] McNamara S and Young W R 1992 *Phys. Fluids A* **4** 496
- [7] McNamara S and Young W R 1993 *Phys. Fluids A* **5** 34
- [8] Goldhirsch I and Zanetti G 1993 *Phys. Rev. Lett.* **70** 1619
- [9] Sela N and Goldhirsch I 1995 *Phys. Fluids* **7** 507
- [10] Du Y, Li H and Kadanoff L P 1995 *Phys. Rev. Lett.* **74** 1268
- [11] Ramirez R and Cordero P 1999 *Phys. Rev. E* **59** 656
- Ramirez R and Cordero P 2001 *Granular Gases* ed T Poschel and S Luding (New York: Springer)
- [12] Benedetto D, Caglioti E and Pulvirenti M 1997 *Math. Mod. Num. An.* **31** 615
- [13] Benedetto D, Caglioti E, Carrillo J A and Pulvirenti M 1998 *J. Stat. Phys.* **91** 979
- [14] Brey J J, Ruiz-Montero M J and Cubero D 1996 *Phys. Rev. E* **54** 3664
- [15] Esipov S E and Pöschel T 1997 *J. Stat. Phys.* **86** 1385
- [16] Brey J J, Cubero D and Ruiz-Montero M J 1999 *Phys. Rev. E* **59** 1256
- [17] Montanero J M and Santos A 2000 *Gran. Matter* **2** 53
- [18] Huthmann M, Orza J A G and Brito R 2000 *Gran. Matter* **2** 189
- [19] Ben-Naim E, Chen S Y, Doolen G D and Redner S 1999 *Phys. Rev. Lett.* **83** 4069
- [20] Bernu B and Mazighi R 1990 *J. Phys. A: Math. Gen.* **23** 5745
- [21] Puglisi A, Loreto V, Marconi U M and Vulpiani A 1999 *Phys. Rev. E* **59** 5582
- [22] Cafiero R, Luding S and Herrmann H J 2000 *Phys. Rev. Lett.* **84** 6014
- [23] Allen M P and Tildesley D J 1987 *Computer Simulations of Liquids* (Oxford: Clarendon)
- [24] Résibois P and de Leener M 1977 *Classical Kinetic Theory of Fluids* (New York: Wiley)
- [25] Bird G 1976 *Molecular Gas Dynamics* (New York: Oxford University Press)
- Bird G 1994 *Molecular Gas Dynamics and the Direct Simulation of Gas Flows* (Oxford: Clarendon)
- [26] Biben T, Martin Ph A and Piasecki J 2002 *Physica A*, submitted
- [27] Landau L and Lifshitz E 1981 *Physical Kinetics* (Oxford: Pergamon)
- [28] Haff P K 1983 *J. Fluid Mech.* **134** 401
- [29] Baldassarri A, Marini Bettolo Marconi U and Puglisi A 2001 *Preprint* cond-mat/0111066
- [30] Soto R and Maréchal M 2001 *Phys. Rev. E* **63** 041303

Chapitre C

Gaz granulaires : dynamique des systèmes vibrés

Molecular dynamics simulations of vibrated granular gases

Alain Barrat* and Emmanuel Trizac†

Laboratoire de Physique Théorique (UMR 8627 du CNRS), Bâtiment 210, Université de Paris–Sud, 91405 Orsay Cedex, France

(Received 10 July 2002; published 18 November 2002)

We present molecular dynamics simulations of monodisperse or bidisperse inelastic granular gases driven by vibrating walls, in two dimensions (without gravity). Because of the energy injection at the boundaries, a situation often met experimentally, density and temperature fields display heterogeneous profiles in the direction perpendicular to the walls. A general equation of state for an arbitrary mixture of fluidized inelastic hard spheres is derived and successfully tested against numerical data. Single-particle velocity distribution functions with non-Gaussian features are also obtained, and the influence of various parameters (inelasticity coefficients, density, etc.) are analyzed. The validity of a recently proposed random restitution coefficient model is assessed through the study of projected collisions onto the direction perpendicular to that of energy injection. For the binary mixture, the nonequipartition of translational kinetic energy is studied and compared both to experimental data and to the case of homogeneous energy injection (“stochastic thermostat”). The rescaled velocity distribution functions are found to be very similar for both species.

DOI: 10.1103/PhysRevE.66.051303

PACS number(s): 81.05.Rm, 45.70.Mg, 45.70.-n, 51.10.+y

I. INTRODUCTION

Due to the intrinsic dissipative character of interparticle collisions, an energy supply is requested to fluidize a granular gas. This is often achieved by a vibrating boundary, and the resulting vibrofluidized beds provide nontrivial realizations of nonequilibrium steady states. The understanding of such far from equilibrium systems requires a correct description of the energy exchange between the vibrating piston and the granular medium, as well as a macroscopic continuum theory to describe the evolution of the relevant coarse-grained fields [1–3] (density, temperature, etc.). In particular, the derivation of an accurate equation of state is a key step in the hydrodynamic approach.

A simple, fair, and much studied theoretical framework to capture the inelastic nature of grain-grain collisions in a rapid granular flow is provided by the inelastic hard sphere model [4,5]. In this paper, we present the results of extensive molecular dynamics (MD) simulations of inelastic hard spheres driven by an energy injection at the boundaries, for both a one-component fluid (monodisperse case) and a binary mixture (bidisperse situation). We analyze in detail the effects of several parameters that may be difficult to tune experimentally, with a particular emphasis on the profiles of the hydrodynamic fields.

This paper is organized as follows. In Sec. II, we present the model and derive an equation of state for an arbitrary mixture of inelastic hard spheres, going beyond the ideal gas contribution in view of performing accurate hydrodynamic tests. The equation of state obtained is a natural generalization of its standard counterpart for elastic hard spheres. The following two sections (Secs. III and IV) are then devoted to molecular dynamics simulations for one-component systems and for binary mixtures. In both cases, we restrict ourselves to two-dimensional simulations, both for simplicity and for

comparisons with two-dimensional (2D) experimental data [6–9]. As in the experiments, the energy loss due to inelastic collisions is compensated for by an energy injection by vibrating or thermal walls, which leads to heterogeneous density and temperature profiles. The various profiles and velocity distribution functions are studied and compared with experiments whenever possible. Moreover, projecting the dynamics onto the direction perpendicular to that of energy injection allows one to assess the validity of the random restitution coefficient model proposed in Refs. [10,11]. The influence of various parameters on the nonequipartition of energy in a binary mixture is studied in Sec. IV, and comparison with experimental data and with the case of homogeneous energy injection is performed. In this latter case, the velocity distribution functions are analyzed and shown to be very similar for the two species. Conclusions are finally presented in Sec. V.

II. THE MODEL—COMPUTATION OF AN EQUATION OF STATE

We consider a mixture of \mathcal{N}_s species of hard spheres in dimension d , with diameters σ_i and masses m_i , where $1 \leq i \leq \mathcal{N}_s$. A binary collision between grains of species i and j is momentum conserving and dissipates kinetic energy. In the simplest version of the model, the collision i - j is characterized by one inelasticity parameter: the coefficient of normal restitution α_{ij} . Accordingly, the precollisional velocities $(\mathbf{v}_i, \mathbf{v}_j)$ are transformed into the postcollisional couple $(\mathbf{v}'_i, \mathbf{v}'_j)$, such that

$$\mathbf{v}'_i = \mathbf{v}_i - \frac{m_j}{m_i + m_j} (1 + \alpha_{ij}) (\hat{\boldsymbol{\sigma}} \cdot \mathbf{v}_{ij}) \hat{\boldsymbol{\sigma}}, \quad (1)$$

$$\mathbf{v}'_j = \mathbf{v}_j + \frac{m_i}{m_i + m_j} (1 + \alpha_{ij}) (\hat{\boldsymbol{\sigma}} \cdot \mathbf{v}_{ij}) \hat{\boldsymbol{\sigma}}, \quad (2)$$

*Electronic address: Alain.Barrat@th.u-psud.fr

†Electronic address: Emmanuel.Trizac@th.u-psud.fr

where $\mathbf{v}_{ij} = \mathbf{v}_i - \mathbf{v}_j$ and $\hat{\boldsymbol{\sigma}}$ is the center-to-center unit vector from particle i to particle j . Note that $\alpha_{ij} = \alpha_{ji}$ to ensure the conservation of total linear momentum $m_i \mathbf{v}_i + m_j \mathbf{v}_j$.

We also considered an extension of the previous model allowing for rotations, introducing a coefficient of tangential restitution ($\alpha'_{ij} \in [-1; 1]$) [12], see Appendix A: the collision law for smooth spheres (1), (2) is then recovered for $\alpha'_{ij} = -1$, while complete reversal of the tangential component of the relative velocity is obtained for $\alpha'_{ij} = 1$. Values in between correspond to a decrease of the absolute value of the tangential relative velocity, with reversal for $\alpha'_{ij} > 0$ and without for $\alpha'_{ij} < 0$.

Irrespective of the value of the tangential restitution coefficient α' , the linear-momentum change for particle i in a collision i - j reads

$$\delta \mathbf{p}_i = -\delta \mathbf{p}_j = -\frac{m_i m_j}{m_i + m_j} (1 + \alpha_{ij}) (\hat{\boldsymbol{\sigma}} \cdot \mathbf{v}_{ij}) \hat{\boldsymbol{\sigma}}. \quad (3)$$

In Appendix B, we use this relation to compute an equation of state for the homogeneous isotropic mixture, invoking the virial theorem (the pressure is defined kinetically from the momentum transfer and does not follow from a statistical mechanics derivation). The total density is denoted by ρ and the partial densities by $\rho_i = x_i \rho$ (the number fractions x_i are such that $\sum_i x_i = 1$). The temperature of species i is T_i , defined from the mean kinetic energy of subpopulation i : $T_i = \langle m_i v_i^2 \rangle / d$. Only for an elastic system is the energy equipartition $T_i = T, \forall i$ recovered [6,13–23]. It is found in Appendix B that the pressure in dimension d reads

$$P = \sum_i \rho_i T_i + \rho \eta 2^{d-1} \sum_{i,j} x_i x_j \frac{m_j}{m_i + m_j} (1 + \alpha_{ij}) T_i \frac{\sigma_{ij}^d}{\langle \sigma^d \rangle} \chi_{ij}, \quad (4)$$

independent of α'_{ij} , where $\sigma_{ij} = (\sigma_i + \sigma_j)/2$, $\langle \sigma^d \rangle = \sum_i x_i \sigma_i^d$, η is the packing fraction (e.g. $\eta = \pi \rho \langle \sigma^3 \rangle / 6$ in

three dimensions), and the χ_{ij} are the pair correlation functions at contact. The latter (unknown) quantities may be approximated by their elastic counterparts (see Ref. [24] for a general procedure to infer reliable pair correlation functions in a multicomponent d -dimensional hard-sphere fluid from the equation of state of the monodisperse system). In the following analysis, it will turn sufficient to include only the low-density behavior, $\chi_{ij} = 1$, to improve upon the ideal equation of state $P = P^{\text{ideal}} = \sum_i \rho_i T_i$, that holds for $\rho \rightarrow 0$ only. We emphasize that no approximation has been made on the single-particle velocity distribution in the derivation of Eq. (4) (the key assumption is that the two-body distribution function factorizes at contact in a product of the single-particle distribution [25]).

It is instructive to check the validity of our equation of state by considering the elastic limit where $\alpha_{ij} = 1$ and $T_i = T$. A straightforward calculation (under the reasonable and often made assumption that $\chi_{ij} = \chi_{ji}$) shows that the mass ratio simplifies and expression (4) may be cast in the form

$$\frac{P}{\rho T} = 1 + \eta 2^{d-1} \sum_{i,j} x_i x_j \frac{\sigma_{ij}^d}{\langle \sigma^d \rangle} \chi_{ij}, \quad (5)$$

which is the correct result (see, e.g., Ref. [26]). In particular, for the single-species (monodisperse) problem, we recover the virial relation $P/(\rho T) = 1 + 2^{d-1} \eta \chi$. Note that Eq. (5) corresponds to the equation of state put forward in Ref. [27], which thus neglects the inelasticity of the collisions and the associated breakdown of kinetic energy equipartition. On the other hand, our approach fully incorporates these two features.

We finally generalize Eq. (4) to the situation of a continuous size distribution, with a probability density distribution $W(\sigma)$ (normalized to 1 so that $\langle \sigma^n \rangle = \int \sigma^n W$); the temperature is, in general, a continuous function $T(\sigma)$ of size and

$$\frac{P}{\rho} = \int W(\sigma) T(\sigma) d\sigma + \frac{\eta}{2} \int d\sigma d\sigma' W(\sigma) W(\sigma') \frac{m_{\sigma'}}{m_{\sigma} + m_{\sigma'}} (1 + \alpha_{\sigma\sigma'}) T(\sigma) \frac{(\sigma + \sigma')^d}{\langle \sigma^d \rangle} \chi_{\sigma\sigma'}. \quad (6)$$

In the following sections, the above equation of state will be used to test hydrodynamic predictions for a monodisperse system and for a binary mixture.

III. MOLECULAR DYNAMICS SIMULATIONS FOR THE ONE-COMPONENT SYSTEM

A. Introduction

We have implemented molecular dynamics simulations with an event-driven algorithm for N spherical particles in a two-dimensional $L \times L$ box. Periodic boundary conditions are enforced in the x direction, while the energy loss due to

collisions is compensated by an energy injection by two walls situated at $y=0$ and $y=L$ (we consider the amplitude of motion of the walls to be small so that their positions are considered as fixed [1], which avoids the complication of heat pulses propagating through the system [28]). We will refer to the y direction as the “vertical” one, although we are interested in regimes for which gravity can be neglected [7] (i.e., when the shaking is violent enough). The energy can be injected in two ways:

(1) By *thermal walls* that impose a given temperature of order T_0 [29]. When a particle collides with the wall, its new vertical (along y) velocity is extracted at random from the

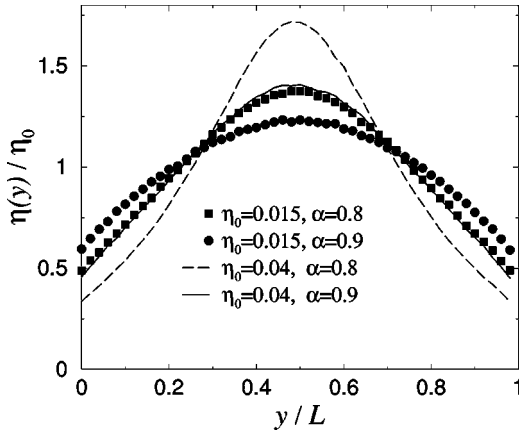


FIG. 1. Density profiles for two normal inelasticities and two densities. In all cases, the number of particles is $N=500$. The symbols correspond to the smallest density (the mean packing fraction averaged over the whole system is $\eta_0=0.015$) and the lines are for a higher density ($\eta_0=0.04$). The ratio $\eta(y)/\eta_0$ is also the ratio $\rho(y)/\rho_0$ of local density normalized by the mean one.

probability distribution function $v/\sqrt{T_0} \exp[-v^2/(2\sqrt{T_0})]$, whereas v_x is unaffected.

(2) By *vibrating walls*. For simplicity, we consider walls of infinite mass moving in a sawtooth manner; all particles colliding with a wall find it with the same velocity $v_0 > 0$ at $y=0$, $-v_0$ at $y=L$. The particle-wall collisions are considered elastic. A particle of velocity \mathbf{v} with $v_y < 0$ colliding with the bottom wall at $y=0$ (respectively, $v_y > 0$ at the upper wall) experiences its velocity change to \mathbf{v}' according to $v'_y = 2v_0 - v_y$ (respectively, $v'_y = -2v_0 - v_y$), whereas the x component is unaffected ($v'_x = v_x$).

In both cases, energy is injected in the vertical direction only, and transferred to the other degrees of freedom through interparticle collisions. The vibrating walls being the situation closer to the experimental one, most of our results will be presented in this case, and the effect of injection modes will be briefly discussed.

In this section, we consider the monodisperse case. All particles have the same mass $m (= 1)$, diameter σ , and restitution coefficients α and α^t . Most of the simulations are done with $N=500$ particles, and some with $N=1000$ particles (low enough to avoid clustering or inelastic collapse). For our two-dimensional system, the local packing fraction at height y , where the local density is $\rho(y)$, is defined as $\eta(y) = \pi\rho(y)\sigma^2/4$. The global (mean) packing fraction is denoted η_0 ; $\eta_0 = \int_0^L \eta(y) dy/L$.

Starting from a random configuration of the particles (with the constraint of no overlap), we let the system evolve until a steady state is reached. Data on density and temperature profiles as well as on velocity distributions are monitored as time averages; the various quantities are averaged along the x direction since the system remains homogeneous in this direction.

B. Density and temperature profiles

The first observations concern the density and temperature profiles: Figures 1 and 2 show that the density is lower

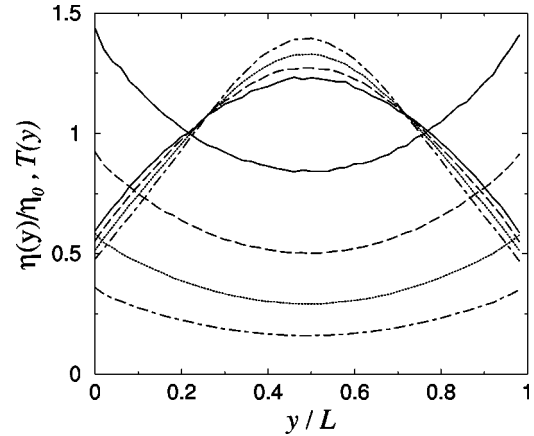


FIG. 2. Density profiles $\eta(y)/\eta_0$ (upward curves) and temperature profiles (downward curves) for a given normal restitution coefficient $\alpha=0.9$ and different tangential restitutions ($N=500$ particles, mean packing fraction $\eta_0=0.015$). The temperature is the total one (including horizontal and vertical degrees of freedom); it is expressed in arbitrary units but all curves correspond to the same velocity of the vibrating piston. From top to bottom for the temperature $T(y)$ and from bottom to top for the density, the curves correspond, respectively, to $\alpha^t = -1$, $\alpha^t = -0.8$, $\alpha^t = -0.5$, and $\alpha^t = 0.2$.

near the walls, where the temperature is higher as expected since energy is injected at the walls and dissipated in the bulk of the system [30]. The profiles are qualitatively similar for thermal or vibrating boundaries. Moreover, the whole temperature profile is proportional to the temperature T_0 imposed by a thermal wall or to the square of the velocity v_0 of the vibrating boundary, while a change in T_0 or v_0 does not change the density profile (not shown). As the mean density increases or α decreases, the profiles get more heterogeneous; as α^t is increased, more energy is transferred to rotational degrees of freedom, so that the temperature decreases, while the density profiles become slightly more peaked (Fig. 2).

Figure 3 clearly shows another feature resulting from the energy injection into the vertical direction: the temperature is anisotropic, i.e., $\langle v_x^2 \rangle \neq \langle v_y^2 \rangle$, with $T_y > T > T_x$. The anisotropy $A(y) = (T_y - T_x)/(2T)$ is larger at the boundaries, where energy is fed into the vertical direction, and reaches a plateau in the middle of the slab. The plateau value decreases for increasing number of particles or increasing densities (not shown), as in experiments [8]; the global anisotropy profile and the plateau values are comparable to experimental values [8].

C. Equation of state and hydrodynamics

The equation of state derived in Sec. II reduces, in the case of a two dimensional one-component homogeneous system, to the relation

$$P = \rho T [1 + (1 + \alpha)\eta\chi], \quad (7)$$

where χ , the pair correlation function at contact, depends on

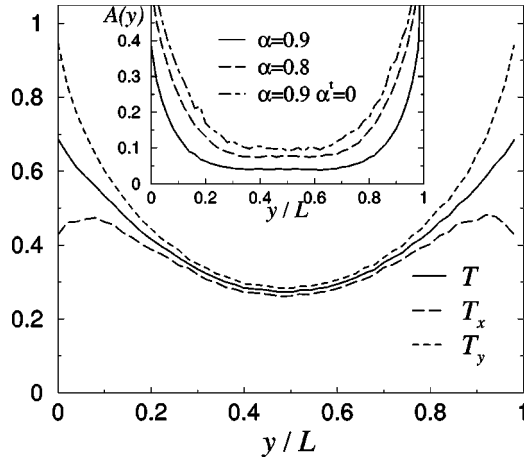


FIG. 3. Temperature profile for $\alpha=0.9$ and $\eta_0=4\%$. The horizontal temperature T_x , vertical temperature T_y , and the total temperature $T=(T_x+T_y)/2$ are shown. The inset shows the anisotropy factor $A=(T_y-T_x)/(2T)$ as a function of height.

the packing fraction η . We will use the form $\chi=(1-7\eta/16)/(1-\eta)^2$, which has been shown to be accurate for elastic hard-disk liquids [31].

The hydrodynamic equations (see Appendix C and Ref. [1]) lead to $\partial_y P=0$ in the absence of a flow field. We check in Fig. 4(a) the constancy of P with y by plotting the ideal gas contribution $\rho(y)T(y)$ (lines) and $P(y)$ given by Eq. (7) (i.e., ideal gas contribution plus Enskog correction). While, at small enough densities (not shown), $\rho(y)T(y)$ is constant in the bulk ($y \in [0.2L, 0.8L]$), the Enskog correction is necessary for the densities used in Fig. 4 (note that the density can be quite larger in the middle of the system than at the boundaries). We also note that the inelasticity term $(1+\alpha)$ is relevant, although small at the densities presented [the profiles of $\rho T(1+2\eta\chi)$, not shown, display a less uniform shape with y , the effect being stronger at larger densities]. In all cases, boundary layers ($y < 0.2L$ and $y > 0.8L$) are observed [1] in which the pressure decreases. This discrepancy can be related to the anisotropy described in the preceding section (pressure and temperature are most anisotropic near the walls).

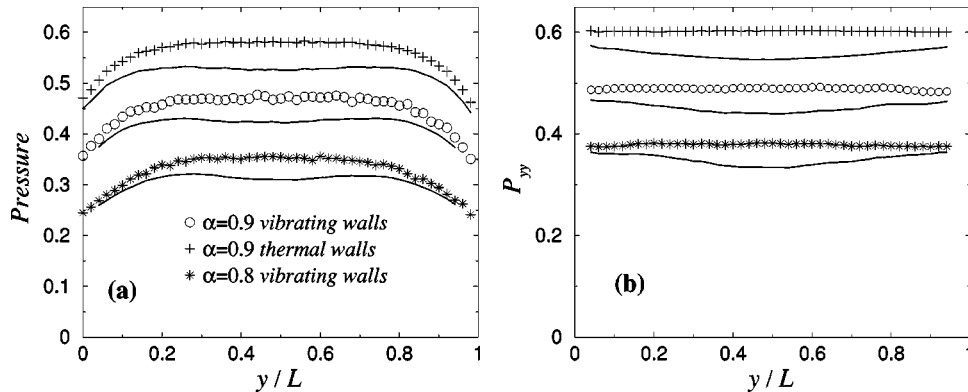


FIG. 4. Pressure given by the equation of state (7). (a) The symbols correspond to $P=\rho(y)T(y)[1+(1+\alpha)\eta(y)\chi(y)]$ (see text), where T is the total temperature. The lines immediately below a given set of symbols show the ideal gas contribution $\rho(y)T(y)$ only. For the three situations investigated, the mean density is the same ($\eta_0=0.04$). (b) Same figure with the vertical temperature T_y instead of T inserted in the equation of state, yielding therefore the yy component of the pressure tensor.

The comparison with hydrodynamics may be improved as follows. The pressure tensor \mathbf{P} is diagonal in the present no-flow situation, but has different xx and yy components, and the homogeneity along the x direction implies that the condition of vanishing flow field $\nabla \cdot \mathbf{P}=0$ reduces to $\partial_y P_{yy}=0$. We therefore check in Fig. 4(b) that the y - y component of the pressure tensor, given by the equation of state (7) with the total temperature $T=(T_x+T_y)/2$ replaced by its vertical component T_y , is uniform in the whole system. With Enskog correction, the corresponding profiles are remarkably flat. This result could be tested in experimental situations in which both T_x and T_y are measured. Such an analysis validates both the hydrodynamic picture and the equation of state proposed by automatically sampling several densities in a single run.

At low densities, assuming the ideal gas equation of state to hold, the hydrodynamic study of Ref. [1] (recalled in Appendix C), leads to the following analytical prediction for the temperature profile:

$$\frac{y}{L} = \frac{\xi + \sinh \xi \cosh(\xi_m - \xi)}{\xi_m + \sinh \xi_m},$$

$$\xi = \frac{\xi_m}{2} \pm \cosh^{-1} \left(\sqrt{\frac{T}{T_0}} \cosh \frac{\xi_m}{2} \right), \quad (8)$$

where T_0 is the temperature at the boundaries and ξ_m is proportional to the total number of particles. The corresponding fits of the temperature profiles are shown in Fig. 5; a good agreement is obtained, especially at lower densities as expected [since the ideal gas equation of state is a crucial ingredient in the derivation of Eq. (8)]. We use one fitting parameter ξ_m to obtain T/T_0 [32]. Figure 4 showed that consideration of the “vertical” pressure P_{yy} led to a better agreement with hydrodynamic predictions than the total $P_{xx}+P_{yy}$. A similar conclusion is incorrect for the temperature profiles: the transport equation for the temperature is scalar [see Eq. (C2)], and Eq. (8) holds for the total T , not for the vertical T_y .

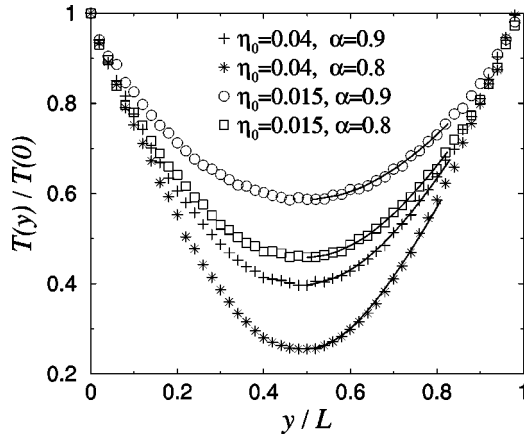


FIG. 5. Fits of the temperature profiles measured in MD with the analytical expression (8). The fits are shown with continuous curves while the symbols stand for the MD measures. For clarity, the fits are restricted to heights $L/2 \leq y \leq 0.8L$.

D. Velocity distributions

Because of the energy injection through the walls, the velocity distributions are anisotropic, and *a priori* depend on the distance to the walls. The vertical velocity distribution also depends on the nature of the walls as shown in Fig. 6. A smooth distribution is obtained in the vicinity of a thermal wall, while the incoming and outgoing particles yield two separated peaks for vibrating walls (see also Ref. [1]).

On the other hand, the *rescaled* horizontal velocity distribution $P(c_x)$ (with $c_x = v_x / \sqrt{T_x}$) is remarkably independent of the distance from the walls (outside the boundary layers), even if the temperature changes with y , at small enough densities (this result was also obtained in Ref. [29]). At larger densities, $P(c_x)$ becomes slightly dependent on y , as also seen in recent similar MD simulations [33]. Figure 7 shows clearly non-Gaussian features similar to the experimentally observed ones [7,13,34], with in particular overpopulated both small-velocity and high-velocity regions. A slight dependence on the parameters is obtained: $P(c_x)$ broadens if the inelasticity increases (i.e., if α decreases), if α' increases, or if η_0 or N increase. Experimentally, the dependence on density or material properties is weak and difficult to measure [7] but seems to exist, in particular as far as N is varied [9]. The angular velocity distributions, also displayed in Fig. 7, share a similar non-Gaussian character and the same de-

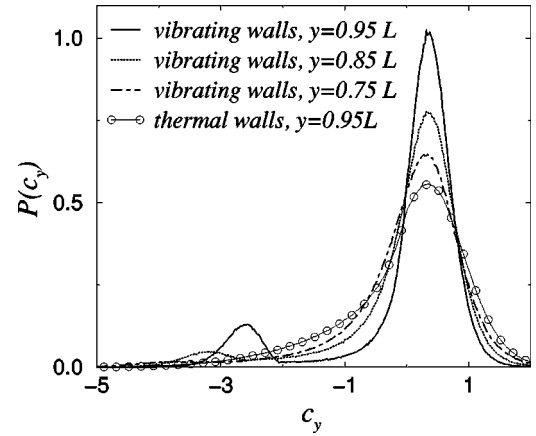


FIG. 6. Probability distribution function of the vertical velocity component $c_y = v_y / \sqrt{T_y}$ for different heights. By definition, $\langle c_y^2 \rangle = 1$, whatever the altitude y . Here, $\eta_0 = 0.04$, $N = 500$, $\alpha = 0.9$, and $\alpha' = 0$.

pendence with the parameters.

As density or inelasticity are further increased, clustering phenomena may occur, leading to heterogeneities along the x direction, with the coexistence of colder, denser regions with hotter, less dense ones. The average over the x direction then leads to artificially broad $P(c_x)$.

Finally, as a general rule, thermal walls lead to slightly broader velocity distributions than vibrating walls.

E. Effective restitution coefficients

We now turn to the study of the effective inelasticities introduced in the context of a random restitution coefficient (RRC) model [10,11]: even if the restitution coefficient α is constant, the energy is injected in the vertical direction and transferred to other degrees of freedom through collisions, so that the *effective* restitution coefficient for collisions projected onto the x direction,

$$\alpha_{1d} = \frac{v'_{12,x}}{v_{12,x}}, \quad (9)$$

may be either smaller or larger than 1 (see Ref. [3] for a related discussion).

Values of α_{1d} have been experimentally measured [9,11]

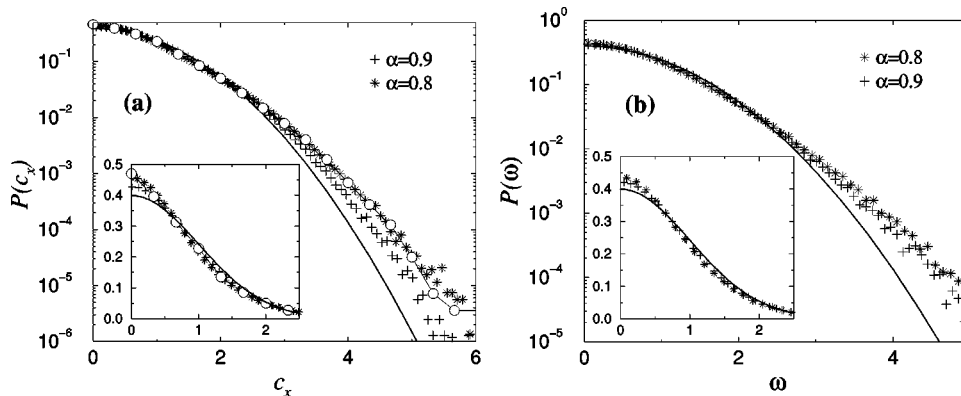


FIG. 7. (a) Probability distribution function of the rescaled horizontal velocity component $c_x = v_x / \sqrt{T_x}$, on a linear-log plot. Here $\eta_0 = 0.015$, $N = 500$, $\alpha = 0.9$ (pluses), 0.8 (stars), and $\alpha' = 0$. The solid line is the Gaussian with unit variance, the circles correspond to experimental data [7,9] for steel beads. (b) Probability distribution function of the angular velocities for the same parameters.

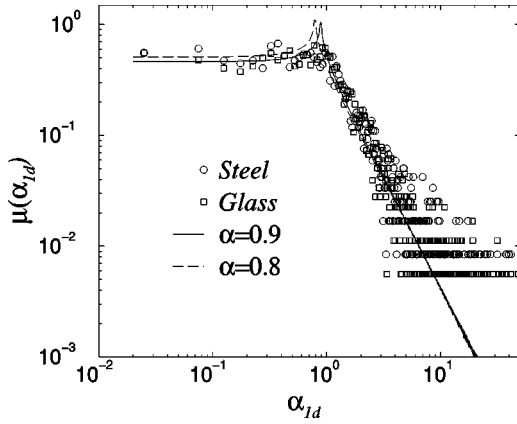


FIG. 8. Probability distribution function of effective one-dimensional restitution coefficients α_{1d} . The MD results are compared to the experimental measures of Feitosa and Menon [9] on steel and glass samples (for which the nominal restitution coefficient may be considered close to 0.9).

and shown to display a broad probability distribution $\mu(\alpha_{1d})$ very similar for various materials and densities. We have measured α_{1d} for many collisions and thus obtained its distribution, displayed in Fig. 8 together with experimental data for steel and glass beads. A remarkable agreement is found [35], with a broad range of possible values for α_{1d} . Our study shows, in particular, that $\mu(\alpha_{1d})$ displays a α_{1d}^{-2} tail for $\alpha_{1d} > 1$, irrespective of α , α' , and density.

The importance of the correlations between α_{1d} and the relative velocity $\mathbf{g} = \mathbf{v}_{12}/\sqrt{2T}$ of the colliding particles has been emphasized in Ref. [11] and is revealed by the computation of $\mu(\alpha_{1d}|g_x)$, the distribution of α_{1d} being conditioned by a given value of g_x ; although no precise experimental determination of the conditional $\mu(\alpha_{1d}|g_x)$ could be achieved in Ref. [11], strong evidences for a sharp cutoff $\propto 1/g_x$ at large values of α_{1d} were provided and the form $\mu(\alpha_{1d}|g_x) \propto \exp[-(\alpha_{1d}g_x)^2/R]$ at large α_{1d} has been proposed. The conditional $\mu(\alpha_{1d}|g_x)$ obtained in the present MD simulations confirm the above picture; they are displayed in Fig. 9 and show an $\exp[-(\alpha_{1d}g_x)^2/R]$ decrease for the case of vibrating walls (closer to the experimental situation), and a broader form $\exp[-(\alpha_{1d}g_x)/R']$ for thermal walls. Moreover, although $\mu(\alpha_{1d})$ is not sensitive to the various parameters, the cutoff R increases [i.e., leads to broader $\mu(\alpha_{1d}|g_x)$] if α decreases, and if α' or η_0 increases.

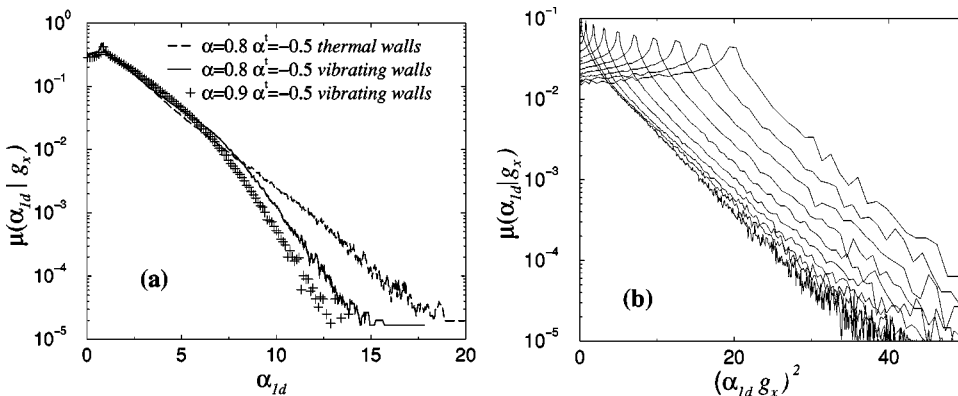


FIG. 9. (a) Conditional PDF of α_{1d} for a given value g_x of order unity. Note the different shapes for thermal and vibrating walls. (b) Same, but as a function of $(\alpha_{1d}g_x)^2$ (and $g_x = 0.2, 0.5, 1.0, 1.5, 2.0, 3.0, 4.0, 5.0$) for vibrated walls with $\alpha=0.9$, $\alpha'=0$, and $\eta_0=0.015$.

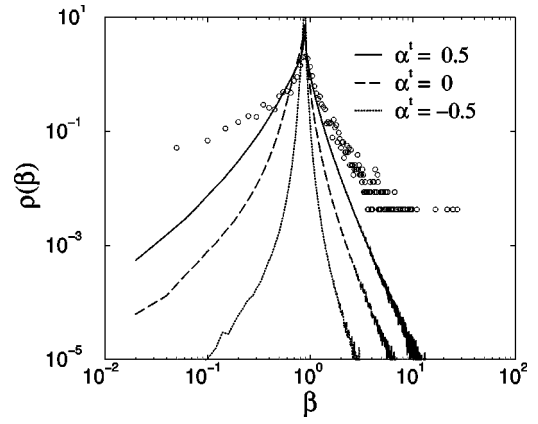


FIG. 10. Probability distribution function of energy restitution coefficients β . Various tangential restitution coefficients α' are considered for $\alpha=0.9$ and $\eta_0=1.5\%$. The circles represent the experimental data for steel grains [9].

Finally, the *energy* restitution coefficient

$$\beta = \frac{|\mathbf{v}'_{12}|}{|\mathbf{v}_{12}|} \quad (10)$$

may also be viewed as a random variable that can take values larger than unity due to energy transfers between rotational and translational degrees of freedom [9,11]. Figure 10 displays the probability distribution function (PDF) $\rho(\beta)$ obtained in the MD simulations for various values of α' , together with the experimental data of Refs. [9,11] for steel beads. $\rho(\beta)$ becomes wider as α' is increased, but the experimental distribution is broader, which may be traced back to the fact that in the experiments mentioned above, the beads can rotate in three dimensions, whereas our simulations are limited to 2D rotations.

The evolution with the parameters of the distributions μ , ρ , and of the velocity PDF $P(c_x)$ are clearly linked in our simulations: broader conditional $\mu(\alpha_{1d}|g_x)$ corresponds to broader velocity distributions; for instance, both broader μ and $P(c_x)$ are obtained if α decreases, or, at fixed parameters, if vibrating walls are replaced by thermal walls. This connection is in agreement with the phenomenology put forward in the context of the effective RRC model [10,11]. In the RRC approach, the d -dimensional system with energy injection along a preferential direction is replaced by a

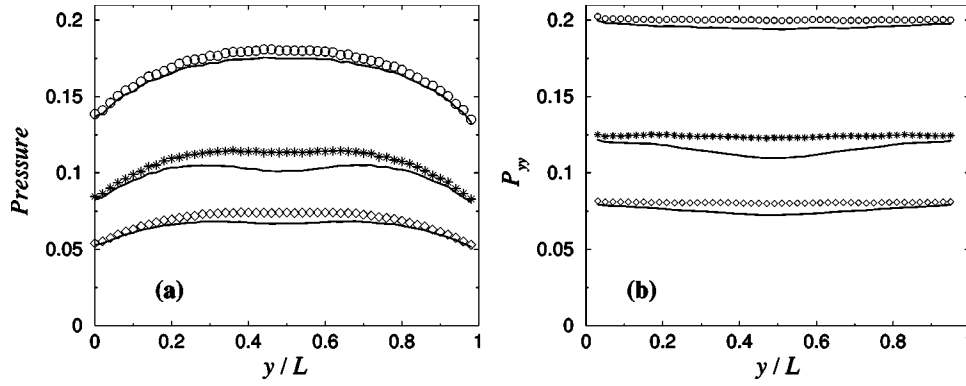


FIG. 11. (a) The symbols show the pressure calculated from the complete equation of state for a binary mixture (11) including Enskog correction, while the lines immediately below display the ideal gas contribution $\rho_1(y)T_1(y) + \rho_2(y)T_2(y)$ to the pressure. The three sets of curves correspond to: *upper set*, $\eta_0=0.015$, $\alpha_{11}=0.9$, $\alpha_{12}=0.8$, $\alpha_{22}=0.7$, $m_1=5m_2$; *middle set*, $\eta_0=0.04$, $\alpha_{11}=0.9$, $\alpha_{12}=0.8$, $\alpha_{22}=0.7$, $m_1=3m_2$; *lower set*, $\eta_0=0.04$, $\alpha_{11}=0.7$, $\alpha_{12}=0.8$, $\alpha_{22}=0.9$, $m_1=3m_2$. (b) Same curves, where the temperatures are the vertical ones ($T_{i,y}$) instead of the total $T_i=(T_{i,x}+T_{i,y})/2$, yielding therefore the yy component of the pressure tensor.

$(d-1)$ -dimensional projected *effective* system in which the restitution coefficient is a random variable [10] correlated with the relative velocities of the colliding particles [11]. In the present situation, $d=2$ and the effective model is one dimensional. Although the real projected collisions are not stochastic, one effectively injects at each collision a restitution coefficient randomly chosen from the distribution $\mu(\alpha_{1d}|g_x)$. Taking μ as an input for the model, close to the experimental data, one obtains velocity distributions as output, in good agreement with the experimental ones. The link between μ and $P(c_x)$ can be studied [11], and broader conditional distributions $\mu(\alpha_{1d}|g_x)$ yield broader $P(c_x)$ (at large c_x , compared to the Gaussian), as in our more realistic simulations.

IV. MOLECULAR DYNAMICS SIMULATIONS FOR THE BINARY MIXTURE

In this section, we investigate the properties of vibrated binary mixtures; such systems have recently attracted much attention, both on the experimental [6,13,14] and theoretical sides [15–23,36,37]. In particular, the breakdown of energy equipartition between the two constituents of the mixture has been thoroughly investigated.

The main difference with previous studies consists here in the realistic character of both MD simulations (as opposed to Monte Carlo methods) and the energy injection mechanism at the boundaries; the setup is the same as in the preceding section, with, however, two types of particles, with masses m_1 , m_2 , and sizes σ_1 , σ_2 . The three normal restitution coefficients (corresponding to the three possible types of collisions) are α_{11} , $\alpha_{12}=\alpha_{21}$, α_{22} . In the context of a forcing mechanism through a random external force [25,38], it has been shown that the influence of size ratio on the temperature ratio measuring the energy nonequipartition was rather weak [17] compared to that of inelasticity parameters or mass ratio. We shall consequently limit our study to identical sizes $\sigma_1=\sigma_2$ in two dimensions, which corresponds to the experimental situation we will refer to [6,9]. For simplicity, the tangential restitution coefficients α_{ij}^t are also taken equal.

As in the monodisperse case, we measure density and temperature profiles, velocity distributions, as well as the temperature ratios $\gamma(y)=T_2(y)/T_1(y)$, $\gamma_x(y)=T_{2,x}(y)/T_{1,x}(y)$, $\gamma_y(y)=T_{2,y}(y)/T_{1,y}(y)$. Some comparison with experimental data [6,9] will be proposed whenever possible.

A. Equation of state

We first test the equation of state (4) in Fig. 11. As in the monodisperse case, the Enskog correction is clearly relevant, even at low global densities, since the density profiles reach relatively high values for $y \approx L/2$. It is, however, sufficient to truncate the equation of state at second virial order, which amounts to taking the low-density limiting value $\chi_{ij}=1$ for the pair correlation functions at contact:

$$P \approx \rho_1 T_1 + \rho_2 T_2 + \frac{\pi \sigma^2}{2(m_1 + m_2)} [(1 + \alpha_{11}) \rho_1^2 m_2 T_1 + (1 + \alpha_{12}) \rho_1 \rho_2 (m_1 T_2 + m_2 T_1) + (1 + \alpha_{22}) \rho_2^2 m_1 T_2]. \quad (11)$$

Moreover, the boundary layer in which the anisotropy is strong is still apparent if the global temperatures T_1 and T_2 are used, while use of the vertical ones ($T_{1,y}$ and $T_{2,y}$), suggested by the anisotropy of temperatures and pressure as in the monodisperse case, leads to a uniform yy component of the pressure tensor in the whole system. The functional dependence of pressure upon densities is therefore accurately reproduced by the equation of state (11).

Although we have not extended the hydrodynamic approach of Brey *et al.* [1] to binary mixtures (it would be possible making use of the Navier-Stokes-like equations derived in Ref. [36] where only the overall temperature associated with both species serves as a hydrodynamic field, but where the transport coefficients explicitly depend on temperature ratio), we see in Fig. 12 that the temperature profiles can be fitted, at low density, by the form (8). We emphasize that there is no fundamental reason for the agreement. The quality of the fit is much better for the less massive particles

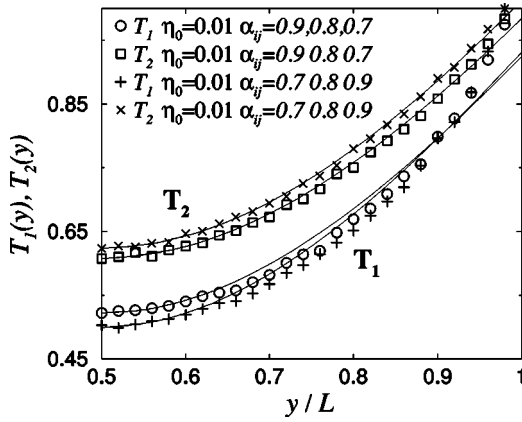


FIG. 12. Temperature profiles for an equimolar granular mixture, driven by vibrating walls. The symbols show the MD measures, and the lines are fits to the analytical expression derived for the single-component case. In all cases, the particle 1 (the heaviest) has mass $m_1=3m_2$; its temperature T_1 corresponds to the two lower sets.

whose density is more homogeneous across the system (see the following). For simplicity, we have used the shorthand notation $\alpha_{ij}=0.7;0.8;0.9$ for the situation where $\alpha_{11}=0.7$, $\alpha_{12}=0.8$, and $\alpha_{22}=0.9$.

B. Nonequpartition of translational kinetic energy

The density and temperature profiles are displayed for various values of the parameters in Figs. 13 and 14. The more massive particles (labeled 1), which display a more heterogeneous profile and are denser in the middle of the cell, have typically larger kinetic energies than the lighter ones; generically, $\gamma=T_2/T_1$ is smaller than 1, as in homogeneous mixtures [16,17]. The study of the y dependence of γ shows that γ increases from the boundaries to the center of the system, and is constant across a wide range of y even if T_1 and T_2 vary significantly. As also experimentally shown in Ref. [6], γ is very close to 1 if $m_1=m_2$, even if the

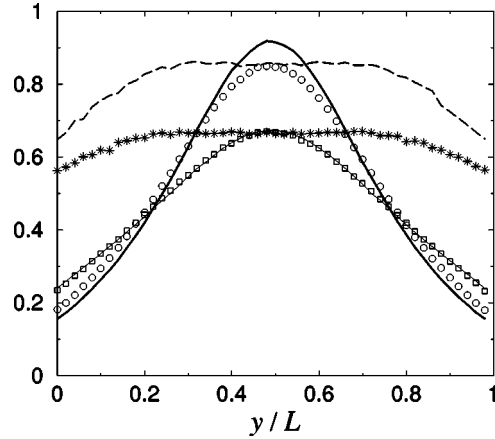


FIG. 14. Density profiles and temperature ratio profiles (binary mixture, vibrating walls). The lines correspond to $\alpha_{ij}=0.7;0.8;0.9$, whereas the symbols are associated with “reverse” inelasticities $\alpha_{ij}=0.9;0.8;0.7$. The other parameters are $\alpha^t=0$, $m_1=3m_2$, $\eta_{1,0}=\eta_{2,0}$, and $\eta_0=2\eta_{1,0}=0.015$. The upper flatter curves (dashed line and stars) show the temperature ratio. As in Fig. 13, the density of heavy particles ρ_1 (thick continuous curve and circles) is more peaked and denser in the middle of the cell than that of light grains (thin continuous curve and squares).

inelasticities of the particles are different. It decreases if the mass ratio increases (Fig. 13), but displays only a very weak (but strikingly similar to experimental data) sensitivity on the global density (Fig. 15) as well as on the relative densities of heavy and light particles; moreover, γ may increase or decrease as $\eta_{1,0}/\eta_{2,0}$ is increased (see Fig. 16), depending on the relative inelasticities.

The anisotropy in the temperatures yield an anisotropic γ ; we obtain, $\gamma_x > \gamma > \gamma_y$, as in experiments [9], also with different shapes. γ_x decreases from the walls to the center while γ and γ_y increase (Fig. 15). All these results are in very good agreement with the existing experimental results for two-dimensional vibrated mixtures [6,9]. We summarize in Tables I and II some of the effects reported here.

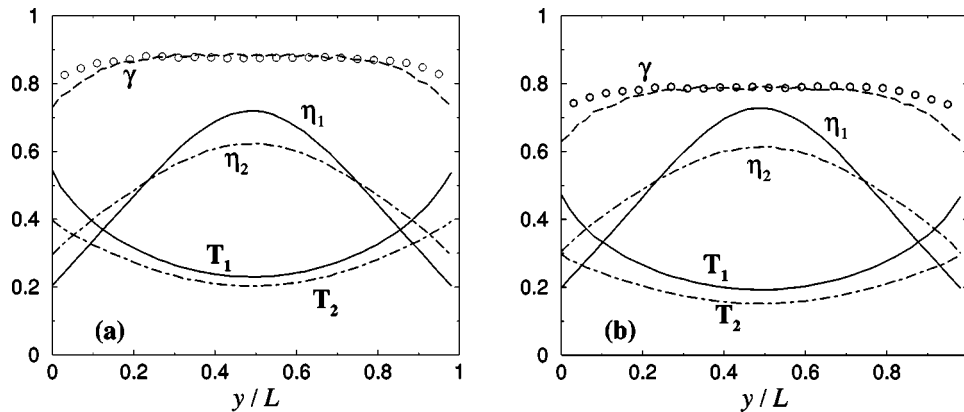


FIG. 13. (a) Vertical profiles for a binary mixture with $m_1=3m_2$, $\eta_0=0.015$, $\alpha_{ij}=0.85$, $N=500$, and equal mean densities $\eta_{1,0}=\eta_{2,0}$ (excitation by vibrating walls). From bottom to top: temperature profiles of both species, density profiles $\eta_2(y)/(2\eta_0)$ and $\eta_1(y)/(2\eta_0)$. Since $\sigma_1=\sigma_2$, the packing fraction η_i is proportional to the local density ρ_i of species i . The upper dashed curve shows the temperature ratio $\gamma=T_2/T_1$ as a function of height, and the circles show the same quantity for a nonequimolar mixture where $\eta_{1,0}=8\eta_{2,0}$. (b) Same with a higher mass ratio $m_1=5m_2$.

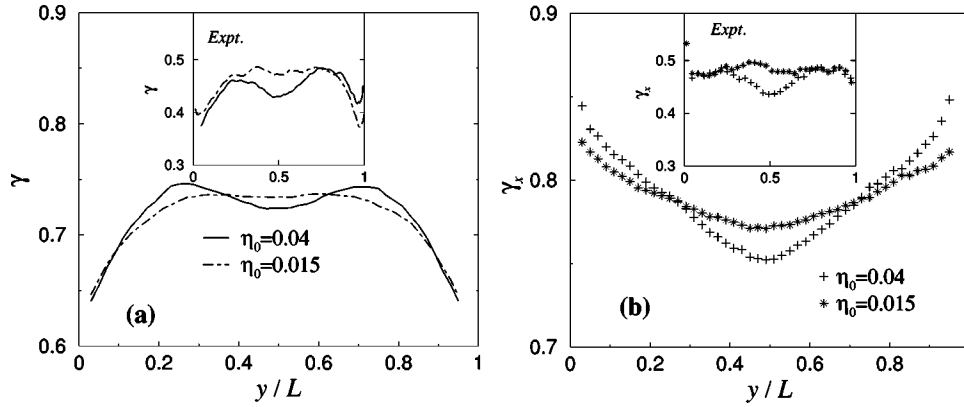


FIG. 15. Effect of density on the temperature ratio for $m_1 = 3m_2$, $\alpha_{ij} = 0.9; 0.8; 0.7$ (vibrating walls). (a) shows the total ratio T_2/T_1 and (b) shows the ratio of horizontal temperatures $T_{2,x}/T_{1,x}$. In both cases, the corresponding experimental measures are shown in the insets for a steel-glass mixture (at different densities, but with a density ratio of 2, close to that of the MD simulations $0.04/0.015 \approx 2.6$). The purpose is to show that the changes induced by density in MD are qualitatively the same as in the experiments.

When rotations are included (and thus $\alpha^t > -1$), γ decreases. Moreover, the ratio of rotational kinetic energies γ_r can then be measured. As shown in Tables I and II, γ_r takes values of the same order as γ . This quantity may also be computed from experimental data, although measures of rotational velocities are *a priori* more difficult than that of translational ones.

The measured values of γ are of the same order as the experimental data. We do not however try to obtain a precise numerical agreement for the following reasons:

(i) In the experiments of Ref. [6], the beads can rotate in three dimensions, whereas the simulated spheres rotate in two dimensions only. Since α^t has a strong effect on γ , we suspect that this difference between experiments and simulations may affect γ . Moreover, the experimental value of α^t is not known, and the precise validity of the inelastic hard-sphere model with a tangential restitution coefficient should be assessed

(ii) Different energy injection mechanisms (thermal vs vibrating walls, homogeneous driving vs injection at the

boundaries) lead to different values of γ . Even if the energy injection by vibrating walls is reasonably realistic, such a sensitivity of γ renders its precise numerical prediction elusive.

Nonetheless, the *qualitative* very good agreement, even for subtle effects (see, e.g., Fig. 15), between numerics and experiment, and the possibility to change the various parameters in the simulations allow us to make some predictions on the effect of various parameters. For example, increasing the mass ratio should yield smaller values of γ (Fig. 13). Moreover, Fig. 14 makes it clear that the value of γ , at given mass ratio, is smaller for inelasticities $\alpha_{ij} = 0.9; 0.8; 0.7$ than with “reverse” inelasticities $\alpha_{ij} = 0.7; 0.8; 0.9$. This effect was already noted in Ref. [17] and has the following intuitive interpretation: when the more massive particles are more inelastic, they lose more energy, their temperature decreases, which results in a higher γ . We therefore predict that in the context of the experiments reported in Ref. [6], a mixture of steel and aluminum ($\alpha_{steel} \approx 0.9, \alpha_{al} \approx 0.83, m_{steel} \approx 3m_{al}$) should yield a smaller value of γ than the brass-glass mixture ($\alpha_{brass} \approx 0.8, \alpha_{glass} \approx 0.9, m_{brass} \approx 3m_{glass}$) for which the measured γ is close to 0.6–0.7. The dependence of γ upon number fraction $x_i = \rho_i/\rho$ may, on the other hand, be counterintuitive: at a given mean density ρ_0 , an increase of the relative fraction x_1 of heavy particles leads to an increase of γ when the heavy particles are the more elastic (see Fig. 16).

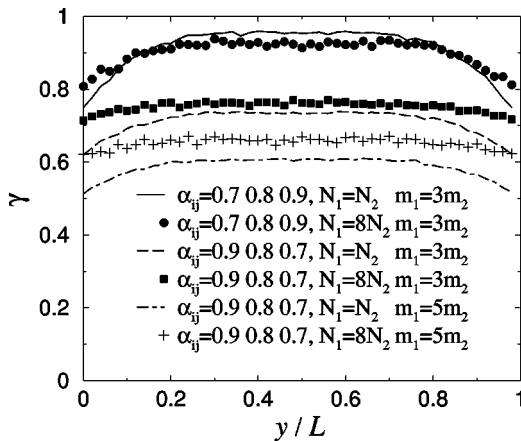


FIG. 16. Influence of number fraction on the temperature ratio T_2/T_1 . The total number of particles is $N = N_1 + N_2 = 500$ (vibrating walls). Given that $\sigma_1 = \sigma_2$, $N_1/N_2 = 8$ corresponds to $\eta_{1,0} = 8\eta_{2,0}$.

TABLE I. Values of γ , γ_x , γ_r in the middle of the system for $N = 500$, $\alpha_{ij} = 0.85$, $\eta_{1,0} = \eta_{2,0}$, $m_1 = 3m_2$ (first three lines), and $m_1 = 5m_2$ (last three lines).

α^t	γ	γ_x	γ_r
-1	0.88	0.92	
-0.5	0.825	0.89	0.83
0	0.79	0.86	0.8
-1	0.79	0.845	
-0.5	0.7	0.78	0.69
0	0.65	0.74	0.66

TABLE II. Values of γ , γ_x , γ_r in the middle of the system for $N=500$, $\alpha_{ij}=0.9,0.8,0.7$ (first three lines), and $\alpha_{ij}=0.7,0.8,0.9$ (last three lines), $m_1=3m_2$, $\eta_{1,0}=\eta_{2,0}$.

α^t	γ	γ_x	γ_r
-1	0.735	0.775	
-0.5	0.69	0.735	0.735
0	0.665	0.72	0.72
-1	0.95	1.0	
-0.5	0.89	0.99	0.84
0	0.85	0.96	0.81

This effect was also clearly observed for the homogeneously heated mixture [17]. On the other hand, an increase of x_1 leads to a relatively weak decrease of γ when the heavier particles are the less elastic, whereas the opposite (albeit also quite weak) trend could be observed in Ref. [17].

C. Velocity distributions

As in the monodisperse case, we have measured the single-particle velocity distributions, which are anisotropic as expected. The vertical velocity distributions are similar to those shown in Fig. 6, and the horizontal velocity distributions show strong non-Gaussian features, as in the monodisperse case. Moreover, it appears in Fig. 17 that the rescaled velocity distributions $P_1(c_x)$ and $P_2(c_x)$ are very close (even if not equal, see also Ref. [23]) for both types of particles. The differences between $P_1(c_x)$ and $P_2(c_x)$ increase if the inelasticities or the mass ratio increase. $P_i(c_x)$ depend slightly on the various parameters, in the same way as the velocity distributions of the monodisperse situation; this dependence would probably be very difficult to measure in an experiment, which would probably lead to the conclusion that $P_1(c_x) \approx P_2(c_x)$.

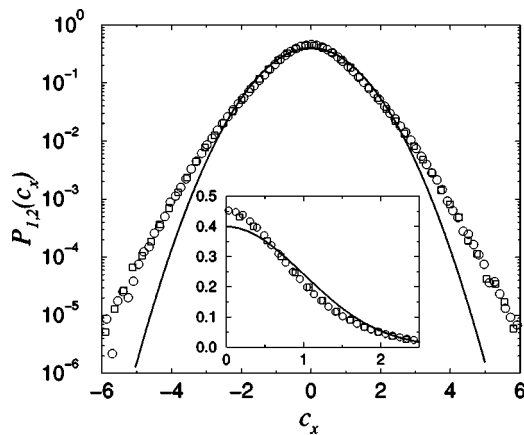


FIG. 17. Probability distribution functions of the rescaled horizontal velocity components $c_{i,x} = v_{i,x}/\sqrt{T_{i,x}}$, for an equimolar mixture. Squares are for P_1 (heavy grains) and circles for P_2 (light grains). Here $\eta_0=0.015$, $N=500$, $\alpha_{ij}=0.9,0.8,0.7$, $m_1=3m_2$, and $\alpha^t=0$. The solid line is the Gaussian with variance 1.

V. CONCLUSION

In this study, we have considered vibrated granular gases outside the Boltzmann limit of (very) low densities. The molecular dynamics simulations performed are free of the approximations underlying the usual kinetic theory or hydrodynamic approaches. Taking due account of the first correction to the ideal gas contribution in the equation of state (second virial order), we, however, found a remarkable constant yy component of the pressure tensor over the whole cell, for monodisperse or bidisperse systems, despite the strong density and temperature heterogeneities due to the realistic energy injection mechanism.

The study of the velocity distributions along the horizontal direction (perpendicular to the energy injection) has revealed non-Gaussian features similar to experiments, which depend weakly on the various parameters involved in the model.

The projection of the dynamics onto the horizontal direction has allowed us to gain insight into the correlations between the effective restitution coefficient α_{1d} and the relative velocities g_x of colliding particles. The measured conditional probability distributions $\mu(\alpha_{1d}|g_x)$ are in agreement with the forms proposed in Ref. [11], based upon partial experimental data. The link between $\mu(\alpha_{1d}|g_x)$ and the velocity probability distribution functions [11] has been confirmed.

In the case of binary mixtures we have analyzed the ratio of granular temperatures as a function of the various parameters, and found a very good qualitative agreement with experiments. The velocity distributions of the two components have, moreover, been shown to be very similar.

ACKNOWLEDGMENTS

We would like to thank K. Feitosa and N. Menon for providing us with valuable unpublished data.

APPENDIX A: INCLUSION OF A TANGENTIAL RESTITUTION COEFFICIENT

In this appendix we give the collision rules when a tangential restitution coefficient is introduced (see also Ref. [12]). The two colliding particles labeled (1) and (2) have masses m_i , diameters σ_i , and moment of inertia $I_i = m_i q \sigma_i^2 / 4$ (with $q=1/2$ for disks and $2/5$ for spheres). The precolliding velocities are $\mathbf{v}_i, \boldsymbol{\omega}_i$, and postcolliding velocities are denoted with primes.

The normal unit vector is defined as

$$\hat{\boldsymbol{\sigma}} = \frac{\mathbf{r}_1 - \mathbf{r}_2}{|\mathbf{r}_1 - \mathbf{r}_2|}. \quad (\text{A1})$$

The relative velocity of the contact point,

$$\mathbf{g} = \mathbf{v}_1 - \mathbf{v}_2 - \left(\frac{\sigma_1}{2} \boldsymbol{\omega}_1 + \frac{\sigma_2}{2} \boldsymbol{\omega}_2 \right) \times \hat{\boldsymbol{\sigma}}, \quad (\text{A2})$$

has normal component $\mathbf{g}_n = (\mathbf{g} \cdot \hat{\boldsymbol{\sigma}}) \hat{\boldsymbol{\sigma}}$ and tangential component $\mathbf{g}_t = \mathbf{g} - \mathbf{g}_n$ (this defines the tangential unit vector $\hat{\mathbf{t}} = \mathbf{g}_t / |\mathbf{g}_t|$).

The postcollisional velocities can be expressed simply in terms of the precollisional velocities through the introduction of the linear momentum change of particle (1),

$$\Delta \mathbf{P} = m_1(\mathbf{v}'_1 - \mathbf{v}_1) = -m_2(\mathbf{v}'_2 - \mathbf{v}_2). \quad (\text{A3})$$

Indeed, the change of angular momentum is

$$\frac{2I_i}{\sigma_i}(\boldsymbol{\omega}'_i - \boldsymbol{\omega}_i) = -\hat{\boldsymbol{\sigma}} \times \Delta \mathbf{P}. \quad (\text{A4})$$

One obtains

$$\mathbf{v}'_1 = \mathbf{v}_1 + \frac{\Delta \mathbf{P}}{m_1}, \quad (\text{A5})$$

$$\mathbf{v}'_2 = \mathbf{v}_2 - \frac{\Delta \mathbf{P}}{m_2}, \quad (\text{A6})$$

$$\boldsymbol{\omega}'_i = \boldsymbol{\omega}_i - \frac{\sigma_i}{2I_i} \hat{\boldsymbol{\sigma}} \times \Delta \mathbf{P}. \quad (\text{A7})$$

The normal and tangential components of $\Delta \mathbf{P}$ are then computed using the definition of the normal and tangential coefficients of restitution:

$$\mathbf{g}'_n = -\alpha \mathbf{g}_n, \quad (\text{A8})$$

$$\mathbf{g}'_t = -\alpha' \mathbf{g}_t. \quad (\text{A9})$$

Since $\mathbf{g}_n = [(\mathbf{v}_1 - \mathbf{v}_2) \cdot \hat{\boldsymbol{\sigma}}] \hat{\boldsymbol{\sigma}}$, the first relation leads to

$$\Delta \mathbf{P} \cdot \hat{\boldsymbol{\sigma}} = -\frac{m_1 m_2}{m_1 + m_2} (1 + \alpha) (\mathbf{v}_1 - \mathbf{v}_2) \cdot \hat{\boldsymbol{\sigma}}. \quad (\text{A10})$$

Using the definition of \mathbf{g}_t , and with $I_i = m_i q \sigma_i^2 / 4$, one also obtains

$$\mathbf{g}'_t = \mathbf{g}_t + \Delta \mathbf{P}_t \left(\frac{1}{m_1} + \frac{1}{m_2} \right) \left(1 + \frac{1}{q} \right), \quad (\text{A11})$$

where $\Delta \mathbf{P}_t = (\Delta \mathbf{P} \cdot \hat{\boldsymbol{\nu}}) \hat{\boldsymbol{\nu}}$. Finally,

$$\Delta \mathbf{P} = -\frac{m_1 m_2}{m_1 + m_2} \left((1 + \alpha) \mathbf{g}_n + \frac{1 + \alpha'}{1 + 1/q} \mathbf{g}_t \right). \quad (\text{A12})$$

APPENDIX B: EQUATION OF STATE FOR A POLYDISPERSE INELASTIC MIXTURE

In this appendix, we adopt a kinetic definition of the total pressure and compute this quantity for an arbitrary homogeneous mixture of species i , with number fraction $x_i = \rho_i / \rho$. Invoking the virial theorem, the excess pressure $P^{\text{ex}} = P - P^{\text{ideal}} = P - \sum_i \rho_i T_i$ is related to the collisional transfer of linear momentum: the partial excess pressure of species i reads (see, e.g., Ref. [39])

$$P_i^{\text{ex}} = \lim_{t \rightarrow \infty} \frac{1}{dV} \frac{1}{t} \sum_{j, \text{collisional partner of } i} \mathbf{r}_{ij} \cdot \delta \mathbf{p}_i \quad (\text{B1})$$

$$= \lim_{t \rightarrow \infty} \frac{1}{dV} \frac{1}{t} \sum_{j, \text{collisional partner of } i} \frac{m_i m_j}{m_i + m_j} (1 + \alpha_{ij})$$

$$\times (\hat{\boldsymbol{\sigma}} \cdot \mathbf{v}_{ij}) \sigma_{ij} \quad \text{where} \quad \sigma_{ij} = \frac{\sigma_i + \sigma_j}{2}. \quad (\text{B2})$$

In these equations, it is understood that the summation runs over all the collision events involving a particle of type i and an arbitrary partner j , in a large volume of measure V . The collisional transfer appearing in Eq. (B2) is readily computed within Enskog-Boltzmann kinetic theory, where the velocity distribution functions $\varphi_i(\mathbf{v})$ obey the set of nonlinear equations,

$$\partial_t \varphi_i(\mathbf{v}_1, t) = \sum_{j=1}^{N_s} \chi_{ij} \sigma_{ij}^{d-1} n_j \int d\mathbf{v}_2 \int d\hat{\boldsymbol{\sigma}} \Theta(\hat{\boldsymbol{\sigma}} \cdot \mathbf{v}_{12}) (\hat{\boldsymbol{\sigma}} \cdot \mathbf{v}_{12}) \left[\frac{1}{\alpha_{ij}^2} \varphi_i(\mathbf{v}_1^*) \varphi_j(\mathbf{v}_2^*) - \varphi_i(\mathbf{v}_1) \varphi_j(\mathbf{v}_2) \right], \quad (\text{B3})$$

where Θ denotes the Heaviside distribution and $(\mathbf{v}_1^*, \mathbf{v}_2^*)$ are the precollisional velocities converted into $(\mathbf{v}_1, \mathbf{v}_2)$ by the collision rules (1) and (2). Equation (B2) may be rewritten as

$$P_i^{\text{ex}} = \frac{1}{2d} \sum_{j=1}^{N_s} \chi_{ij} \sigma_{ij}^{d-1} n_j \int d\mathbf{v}_1 d\mathbf{v}_2 \int d\hat{\boldsymbol{\sigma}} \Theta(\hat{\boldsymbol{\sigma}} \cdot \mathbf{v}_{12}) (\hat{\boldsymbol{\sigma}} \cdot \mathbf{v}_{12}) \varphi_i(\mathbf{v}_1) \varphi_j(\mathbf{v}_2) \frac{m_i m_j}{m_i + m_j} (1 + \alpha_{ij}) (\hat{\boldsymbol{\sigma}} \cdot \mathbf{v}_{12}) \sigma_{ij}. \quad (\text{B4})$$

Summing the contributions of all species, the total excess pressure follows:

$$P^{\text{ex}} = \frac{1}{2d} \sum_{i,j} \chi_{ij} \sigma_{ij}^d n_i n_j \frac{m_i m_j}{m_i + m_j} (1 + \alpha_{ij}) \int d\mathbf{v}_1 d\mathbf{v}_2 \int d\hat{\boldsymbol{\sigma}} \Theta(\hat{\boldsymbol{\sigma}} \cdot \mathbf{v}_{12}) (\hat{\boldsymbol{\sigma}} \cdot \mathbf{v}_{12})^2 \varphi_i(\mathbf{v}_1) \varphi_j(\mathbf{v}_2) \quad (\text{B5})$$

$$= \frac{1}{2d} \sum_{i,j} \chi_{ij} \sigma_{ij}^d n_i n_j \frac{m_i m_j}{m_i + m_j} (1 + \alpha_{ij}) \left[\int d\hat{\boldsymbol{\sigma}} \Theta(\hat{\boldsymbol{\sigma}} \cdot \hat{\mathbf{v}}_{12}) (\hat{\boldsymbol{\sigma}} \cdot \hat{\mathbf{v}}_{12})^2 \right] \int d\mathbf{v}_1 d\mathbf{v}_2 (v_1^2 + v_2^2) \varphi_i(\mathbf{v}_1) \varphi_j(\mathbf{v}_2), \quad (\text{B6})$$

where $\hat{\mathbf{v}}_{12}$ is the unit vector along \mathbf{v}_{12} , and where the contribution from the dot product $\mathbf{v}_1 \cdot \mathbf{v}_2$ vanishes by symmetry in the last integral. The integral over the solid angle $\hat{\boldsymbol{\sigma}}$ is related to the volume V_d of a sphere with diameter 1:

$$\int d\hat{\boldsymbol{\sigma}} \Theta(\hat{\boldsymbol{\sigma}} \cdot \hat{\mathbf{v}}_{12}) (\hat{\boldsymbol{\sigma}} \cdot \hat{\mathbf{v}}_{12})^2 = \frac{\pi^{d/2}}{d\Gamma(d/2)} = 2^{d-1} V_d, \quad (\text{B7})$$

where Γ is the Euler function and it is understood that $\hat{\mathbf{v}}_{12}$ denotes an arbitrary unit vector in Eq. (B7). The volume V_d is itself related to the packing fraction η through $\eta = \rho V_d \langle \sigma^d \rangle$. From the definition of kinetic temperatures $\int v^2 \varphi_i(\mathbf{v}) d\mathbf{v} = dT_i/m_i$, we get

$$P^{\text{ex}} = \rho \eta 2^{d-2} \sum_{i,j} \chi_{ij} x_i x_j \frac{m_i m_j}{m_i + m_j} (1 + \alpha_{ij}) \left(\frac{T_i}{m_i} + \frac{T_j}{m_j} \right) \frac{\sigma_{ij}^d}{\langle \sigma^d \rangle}, \quad (\text{B8})$$

from which we deduce the equation of state (4). In this last step, no approximation (e.g., Gaussian, etc.) is made concerning φ_i . On the other hand, the computation of any other moment $(\hat{\boldsymbol{\sigma}} \cdot \mathbf{v}_{12})^p$ than $p=2$ requires the detailed knowledge of the velocity distributions [25]. It is also noteworthy that the decoupling of velocities \mathbf{v}_1 and \mathbf{v}_2 in Eq. (B6) is a specific property of the momentum transfer, which significantly simplifies the calculation.

APPENDIX C: HYDRODYNAMICS

In this appendix, we recall the hydrodynamical approach considered by Brey *et al.* [1], and adapt it to the case of energy injection at both boundaries $y=0$ and $y=L$. The situation investigated in Ref. [1] is that of a vibrating wall at $y=0$ and a reflecting wall at $y=L$, so that the temperature and density gradients vanish at $y=L$. In our no-flow configuration with two vibrating walls, the gradients vanish by symmetry in the middle of the cell ($y=L/2$), so that restricting to $y \in [0, L/2]$ allows us to use directly the expressions derived in Ref. [1] (which amounts to the formal identification $y \rightarrow 2y$ and $N \rightarrow 2N$). For completeness and clarity, we will, however, adapt the argument to our geometry.

In the case of a stationary system without macroscopic velocity flow, the hydrodynamic equations reduce to

$$\nabla \cdot \mathbf{P} = 0, \quad (\text{C1})$$

$$\frac{2}{\rho d} \nabla \cdot \mathbf{q} + T \zeta = 0. \quad (\text{C2})$$

Here \mathbf{P} is the pressure tensor, \mathbf{q} is the heat flux, and ζ the cooling rate due to the collisional energy dissipation. In the Navier-Stokes approximation for a low-density gas described by the Boltzmann equation modified to account for the inelastic nature of collisions [40],

$$\mathbf{P} = P \mathbf{I}, \quad (\text{C3})$$

$$\mathbf{q} = -\kappa \nabla T - \mu \nabla \rho, \quad (\text{C4})$$

where P is the ideal gas pressure $P = \rho T$. The explicit expressions of the heat conductivity κ , the transport coefficient μ , and cooling rate ζ may be found in Ref. [1]. The important ingredient is that μ is proportional to $T^{3/2}/\rho$ and κ to \sqrt{T} , while $\zeta \propto p/\sqrt{T}$, with coefficients depending on the inelasticity α .

The system is considered homogeneous in the x direction, so that only gradients along the y direction are taken into account. We emphasize that the ideal gas equation of state ($P = \rho T$) is assumed, and this simplification is an important ingredient in the following derivation. The previous equations then reduce to

$$\frac{\partial P}{\partial y} = 0, \quad (\text{C5})$$

$$\frac{2A(\alpha)}{d\rho} \frac{\partial}{\partial y} \left(\sqrt{T} \frac{\partial T}{\partial y} \right) - p \sqrt{T} = 0. \quad (\text{C6})$$

In order to simplify the equation on the temperature, it is convenient to introduce a new variable ξ , defined by

$$d\xi = \sqrt{a(\alpha)} \frac{dy}{\lambda(y)} = C \sigma^{d-1} \sqrt{a(\alpha)} \rho(y) dy, \quad (\text{C7})$$

where $\lambda(y) = [C \sigma^{d-1} \rho(y)]^{-1}$ is the mean free path ($C = 2\sqrt{2}$ for $d=2$), and $a(\alpha)$ includes all the dependence in α . Equation (C6) now reads

$$\frac{\partial^2}{\partial \xi^2} \sqrt{T} = \sqrt{T}. \quad (\text{C8})$$

The variable ξ takes values between 0 and ξ_m , with $\xi_m \propto N$. Then $\sqrt{T} = A \exp(-\xi) + B \exp(\xi)$, where A and B depend on the boundary conditions. In the case of two vibrating walls, the solution is symmetric with respect to $y=L/2$ (or $\xi = \xi_m/2$). With $T(0) = T(\xi_m) = T_0$, one obtains

$$T(\xi) = \frac{T_0}{\sinh^2 \xi_m} [\sinh(\xi_m - \xi) + \sinh \xi]^2. \quad (\text{C9})$$

It is possible to integrate $d\xi = C \sigma^{d-1} \sqrt{a(\alpha)} n(y) dy = C \sigma^{d-1} \sqrt{a(\alpha)} p dy / T(y)$ to obtain $y(\xi)$ and P :

$$P = \frac{T_0}{2C\sigma^{d-1}L\sqrt{a(\alpha)}\cosh^2\frac{\xi_m}{2}} (\xi_m + \sinh\xi_m), \quad (\text{C10})$$

$$\frac{y}{L} = \frac{\xi + \sinh\xi \cosh(\xi_m - \xi)}{\xi_m + \sinh\xi_m}. \quad (\text{C11})$$

Those equations are the same as for the case of one vibrating wall [1], but with $\xi_m \rightarrow 2\xi_m$ and $L \rightarrow 2L$, as expected on the

basis on the symmetry argument proposed above. It is possible to invert $T(\xi)$ and therefore to obtain the profiles $y(T)$ (two symmetric branches):

$$\xi = \frac{\xi_m}{2} \pm \cosh^{-1}\left(\sqrt{\frac{T}{T_0}} \cosh\frac{\xi_m}{2}\right), \quad (\text{C12})$$

$$\frac{y}{L} = \frac{\xi + \sinh\xi \cosh(\xi_m - \xi)}{\xi_m + \sinh\xi_m}. \quad (\text{C13})$$

-
- [1] J.J. Brey, M.J. Ruiz-Montero, and F. Moreno, *Phys. Rev. E* **62**, 5339 (2000).
- [2] J.J. Brey, M.J. Ruiz-Montero, and F. Moreno, *Phys. Rev. E* **63**, 061305 (2001).
- [3] A. Prevost, D.A. Egolf, and J.S. Urbach, *Phys. Rev. Lett.* **89**, 084301 (2002).
- [4] I. Goldhirsch and G. Zanetti, *Phys. Rev. Lett.* **70**, 1619 (1993).
- [5] L.P. Kadanoff, *Rev. Mod. Phys.* **71**, 435 (1999).
- [6] K. Feitosa and N. Menon, *Phys. Rev. Lett.* **88**, 198301 (2002).
- [7] F. Rouyer and N. Menon, *Phys. Rev. Lett.* **85**, 3676 (2000).
- [8] F. Rouyer and N. Menon (unpublished).
- [9] K. Feitosa and N. Menon (private communication).
- [10] A. Barrat, E. Trizac, and J.N. Fuchs, *Eur. Phys. J. E* **5**, 161 (2001).
- [11] A. Barrat and E. Trizac, e-print cond-mat/0202297.
- [12] S. Luding, *Phys. Rev. E* **52**, 4442 (1995).
- [13] W. Losert, D.G.W. Cooper, J. Delour, A. Kudrolli, and J.P. Gollub, *Chaos* **9**, 682 (1999).
- [14] R.D. Wildman and D.J. Parker, *Phys. Rev. Lett.* **88**, 064301 (2002).
- [15] Y. Limon Duparcmeur, Ph.D., thesis, l'Université de Rennes I, 1996 (unpublished).
- [16] V. Garzó and J. Dufty, *Phys. Rev. E* **60**, 5706 (1999).
- [17] A. Barrat and E. Trizac, *Granular Matter* **4**, 57 (2002).
- [18] J.M. Montanero and V. Garzó, *Granular Matter* **4**, 17 (2002).
- [19] R. Clelland and C.M. Hrenya, *Phys. Rev. E* **65**, 031301 (2002).
- [20] S.R. Dahl, C. Hrenya, V. Garzó, and J.W. Dufty, *Phys. Rev. E* **66**, 041301 (2002).
- [21] J.M. Montanero and V. Garzó, e-print cond-mat/0201175.
- [22] U. Marini Bettolo Marconi and A. Puglisi, *Phys. Rev. E* **65**, 051305 (2002); **66**, 011301 (2002).
- [23] R. Pagnani, U.M. Bettolo Marconi, and A. Puglisi, e-print cond-mat/0205619.
- [24] A. Santos, S.B. Yuste, and M. López de Haro, *Mol. Phys.* **96**, 1 (1999).
- [25] I. Pagonabarraga, E. Trizac, T.P.C. van Noije, and M.H. Ernst, *Phys. Rev. E* **65**, 011303 (2002).
- [26] J. Zhang, R. Blaak, E. Trizac, J.A. Cuesta, and D. Frenkel, *J. Chem. Phys.* **110**, 5318 (1999).
- [27] J.T. Willits and B.Ö. Arnason, *Phys. Fluids* **11**, 3116 (1999).
- [28] S. McNamara and J.-L. Barrat, *Phys. Rev. E* **55**, 7767 (1997).
- [29] E.L. Grossman, T. Zhou, and E. Ben-Naim, *Phys. Rev. E* **55**, 4200 (1997).
- [30] K. Helal, T. Biben, and J.-P. Hansen, *Physica A* **240**, 361 (1997).
- [31] D. Henderson, *Mol. Phys.* **30**, 971 (1975).
- [32] The hydrodynamic theory of Ref. [1] predicts the value of ξ_m , which depends on α and is proportional to N . Since the hypothesis of Ref. [1] (isotropic pressure given by the ideal equation of state) is not verified in our simulations, we consider ξ_m as a fitting parameter; the corresponding values are close to the predictions of Brey *et al.*, [1] (with a difference of less than 10%).
- [33] J.J. Breg and M.J. Ruiz-Montero, e-print cond-mat/0210158.
- [34] I.S. Aranson and J.S. Olafsen, e-print cond-mat/0110607.
- [35] The numerical data shown in Fig. 8 display a peak at $\alpha_{1d} = \alpha$, i.e., at the original value of the restitution coefficient in the initial hard-disc model. This peak does not seem to be present in the experimental data either due to a lack of statistics, or because the experimentally measured normal restitution coefficient depends slightly on the collision parameters (relative velocity, impact parameter, etc.), leading to a smoothing of this peak.
- [36] V. Garzó and J.W. Dufty, *Phys. Fluids* **14**, 1476 (2002).
- [37] T. Biben, Ph.A. Martin, and J. Piasecki, *Physica A* **310**, 308 (2002).
- [38] T.P.C. van Noije, M.H. Ernst, E. Trizac, and I. Pagonabarraga, *Phys. Rev. E* **59**, 4326 (1999).
- [39] M.P. Allen and D.J. Tildesley, *Computer Simulation of Liquids* (Clarendon Press, Oxford, 1987).
- [40] J.J. Brey, J.W. Dufty, and A. Santos, *J. Stat. Phys.* **87**, 1051 (1997).

Lack of energy equipartition in homogeneous heated binary granular mixtures

Alain Barrat, Emmanuel Trizac

Abstract We consider the problem of determining the granular temperatures of the components of a homogeneous binary heated mixture of inelastic hard spheres, in the framework of Enskog kinetic theory. Equations are derived for the temperatures of each species and their ratio, which is different from unity, as may be expected since the system is out of equilibrium. We focus on the particular heating mechanism where the inelastic energy loss is compensated by an injection through a random external force (“stochastic thermostat”). The influence of various parameters and their possible experimental relevance is discussed.

Keywords Transport of gases, Theory of gases, Granular mixtures

1

Introduction

Experimental and theoretical studies of rapid granular flows [1] have hitherto mostly focused on assemblies of identical particles, either freely cooling when the energy loss due to inter-particle collisions is not compensated for, or driven in a non-equilibrium stationary state by various energy injection mechanisms. Recently however, interest has grown for the more complicated case of polydisperse systems [2–10]. Theoretical investigations into the homogeneous cooling stage of a binary mixture [2, 3] have shown that the two components have different granular temperatures (i.e. kinetic energies), even if their cooling rates are equal. Such a result, confirmed by detailed Monte Carlo simulations [8] is also obtained when the system is sheared [9, 10], heated by the contact with an elastic granular gas maintained at fixed temperature T [11], or within the Maxwell model framework [12]. Similarly, a tracer particle undergoing inelastic collisions with an equilibrium fluid at temperature T reaches a granular temperature lower than T [13].

This violation of equipartition in a mixture, although in sharp contrast with the behaviour of molecular gases at equilibrium, is not unexpected: the terminology “granular temperature” for the kinetic energy of a granular gas has been coined from the equivalence of temperature and kinetic energy in an elastic gas, but does not have any thermodynamical status in out-of-equilibrium systems like inelastic granular gases.

In recent experiments, the granular temperatures have been measured for binary mixtures, both in 3D vibrofluidized granular beds [6] and in 2D strongly vibrated granular gases [7]. Both studies reported a clear violation of equipartition with a temperature ratio quite insensitive to the relative densities of the two species.

The present article aims at providing a simple theoretical framework where the temperature ratio is readily obtained in a non-equilibrium steady state (NESS). This allows to investigate the influence of many parameters which can be difficult to tune experimentally, such as the masses, sizes, densities and inelasticities of the beads. We consider analytically a heated binary mixture in the framework of the homogeneous non-linear (Enskog-) Boltzmann equation for smooth inelastic hard spheres. Similarly to the case of free cooling described in [3] and restricting to Gaussian velocity distributions, we derive in section 2 equations for the granular temperatures of the mixture components, which are easily solved numerically. The corresponding temperature ratio is in excellent agreement with existing numerical work [11]. In section 3, we consider the NESS sustained by heating through random kicks (“stochastic thermostat” approach), a mechanism which has focused some attention recently for one-component (monodisperse) systems [14–22]. Although finding an energy injection mechanism of experimental relevance is a difficult issue, we expect the approach proposed here to elucidate the basic trends of grain behaviour when varying the controlling parameters. Moreover, as will be shown below, the temperature ratio we obtain provides a reasonable zeroth order approximation to compare with the experiments reported in [6, 7].

Received: 18 February 2002

Alain Barrat (✉), Emmanuel Trizac
Laboratoire de Physique Théorique (UMR 8627 du CNRS),
Bâtiment 210, Université de Paris-Sud,
91405 Orsay Cedex, France
e-mails: Alain.Barrat@th.u-psud.fr,
Emmanuel.Trizac@th.u-psud.fr

We would like to thank T. Biben, R.D. Wildman and C.M. Hrenya for communicating their results prior to publication.

2

Kinetic theory

We consider the model of smooth inelastic hard spheres (IHS) undergoing binary, momentum conserving, inelastic collisions, in the framework of the homogeneous non-linear Enskog equation. The system is a mixture of two types of IHS, with masses m_1 and m_2 , diameters σ_1 and σ_2 . Three types of collisions may occur so that the mixture

is also characterized by three different restitution coefficients: α_{11} , α_{22} , and $\alpha_{12} = \alpha_{21}$.

The velocity distributions in the homogeneous state $f_1(\mathbf{v}, t)$, $f_2(\mathbf{v}, t)$, obey the following kinetic equations:

$$\partial_t f_i(\mathbf{v}_1, t) = \sum_j J_{ij}[\mathbf{v}_1 | f_i, f_j] + \mathcal{F}f_i \quad (1)$$

where the J_{ij} describe the effect of dissipative inter-particle collisions, and $\mathcal{F}f_i$ represents an external forcing which injects energy into the system, allowing it to reach a non-equilibrium steady state. The kernels J_{ij} for collisions between a particle of type i and a particle of type j are given, in dimension d , by

$$J_{ij}[\mathbf{v}_1 | f_i, f_j] = \chi_{ij} \sigma_{ij}^{d-1} \int d\mathbf{v}_2 \int d\hat{\mathbf{c}} (\hat{\mathbf{c}} \cdot \mathbf{v}_{12}) \left(\frac{1}{\alpha_{ij}^2} f_i(\mathbf{v}'_1) f_j(\mathbf{v}'_2) - f_i(\mathbf{v}_1) f_j(\mathbf{v}_2) \right). \quad (2)$$

where the χ_{ij} are the pair distribution functions at contact (a priori unknown, but becoming close to 1 in the limit of low densities); $\hat{\mathbf{c}}$ is a unit vector directed from the center of the particle of type i to the center of particle j [separated at contact by $\sigma_{ij} = (\sigma_i + \sigma_j)/2$], and the prime on the integral is a shortcut for $\int \Theta(\hat{\mathbf{c}} \cdot \mathbf{v}_{12})$. Moreover, $\mathbf{v}_{12} = \mathbf{v}_1 - \mathbf{v}_2$, and the pre-collisional velocities \mathbf{v}'_1 and \mathbf{v}'_2 are given in terms of the post-collisional velocities \mathbf{v}_1 and \mathbf{v}_2 by:

$$\mathbf{v}'_1 = \mathbf{v}_1 - \mu_{ji}(1 + \alpha_{ij}^{-1})(\hat{\mathbf{c}} \cdot \mathbf{v}_{12})\hat{\mathbf{c}} \quad (3)$$

$$\mathbf{v}'_2 = \mathbf{v}_2 + \mu_{ij}(1 + \alpha_{ij}^{-1})(\hat{\mathbf{c}} \cdot \mathbf{v}_{12})\hat{\mathbf{c}} \quad (4)$$

where $\mu_{ij} = m_i/(m_i + m_j)$, so that momentum is conserved but energy dissipated.

The partial granular temperatures are defined from the kinetic energies by

$$\frac{n_i d}{2} T_i(t) = \int d\mathbf{v} \frac{m_i v^2}{2} f_i(\mathbf{v}, t), \quad (5)$$

$n_i = \int d\mathbf{v} f_i(\mathbf{v}, t)$ being the number density of particles of type i with a total temperature of the mixture

$$T = \frac{1}{n_1 + n_2} \sum_i n_i T_i. \quad (6)$$

From (1), the evolution equation for the temperatures reads

$$\partial_t T_i = \frac{m_i}{n_i d} \sum_j \int d\mathbf{v} v^2 J_{ij}[\mathbf{v} | f_i, f_j] + \mathcal{F}T_i, \quad (7)$$

where $\mathcal{F}T_i$ describes the effect of the forcing (source) term $\mathcal{F}f_i$. It is possible to integrate over $\hat{\mathbf{c}}$ (see calculations in the appendix, and also [3]) to obtain, without any further approximation at this stage:

$$\begin{aligned} \partial_t T_i &= \mathcal{F}T_i - \frac{\beta_3 m_i \chi_{ii} \sigma_{ii}^{d-1} (1 - \alpha_{ii}^2)}{4n_i d} \\ &\times \int d\mathbf{v}_1 d\mathbf{v}_2 v_{12}^3 f_i(\mathbf{v}_1) f_i(\mathbf{v}_2) \\ &- \frac{\beta_3 m_i \chi_{ij} \sigma_{ij}^{d-1}}{n_i d} \int d\mathbf{v}_1 d\mathbf{v}_2 f_i(\mathbf{v}_1) f_j(\mathbf{v}_2) \\ &\times [\mu_{ji}^2 (1 - \alpha_{ij}^2) v_{12}^3 + 2\mu_{ji} (1 + \alpha_{ij}) v_{12} (\mathbf{v}_{12} \cdot \mathbf{V}_{ij})] \end{aligned} \quad (8)$$

with $\beta_3 = \pi^{(d-1)/2} / \Gamma[(d+3)/2]$, $\mathbf{V}_{ij} = \mu_{ij} \mathbf{v}_1 + \mu_{ji} \mathbf{v}_2$, and Γ the Euler function.

Since the system reaches a stationary state where the forcing term balances the dissipation due to collisions (the forcing and dissipative terms in (8) generically involve different powers of the temperatures so that its right-hand-side admits a ‘‘physical’’ root), we can write $\partial_t T_i = 0$. It is moreover convenient to scale the velocities with the thermal velocities $v_{0,i} = \sqrt{2T_i/m_i}$, and introduce the functions Φ_i such that

$$f_i(v) = \frac{n_i}{v_{0,i}^d} \Phi_i \left(\frac{v}{v_{0,i}} \right). \quad (9)$$

Equation (8) may then be cast into an equation for the rescaled velocity distributions Φ_i ; no further step can however be taken without some approximations on the unknown distributions Φ_i . It is convenient to study the deviations of Φ_i from the Gaussian $\Phi_i^0(c)$ through an expansion in Sonine polynomials [23]. In single component heated systems, the deviation from a Gaussian remains small, especially for experimentally relevant values of the restitution coefficient [16, 18, 20, 21]. We will here limit our treatment to the Gaussian approximation $\Phi_i(c) = \Phi_i^0(c) = \pi^{d/2} \exp(-c^2)$ (lowest order Sonine expansion). It would of course be possible to go further in a systematic and controlled way, as in [3], but we will see by comparison of our approximate analytical calculations with Monte Carlo simulations that, at least in the cases we consider, the Gaussian approximation provides reliable results.

Assuming Gaussian velocity distributions, it is now possible to carry out the remaining integrations in (8); the calculations are straightforward and some technical details may be found in the appendix of [3]. We only give the resulting equations for the granular temperatures T_i in the NESS:

$$\begin{aligned} \frac{d\Gamma(d/2)}{m_i \pi^{(d-1)/2}} \mathcal{F}T_i &= \chi_{ii} \sigma_{ii}^{d-1} n_i \frac{2(1 - \alpha_{ii}^2)}{m_i^{3/2}} T_i^{3/2} + \chi_{ij} \sigma_{ij}^{d-1} n_j \mu_{ji} \\ &\times \left[\mu_{ji} (1 - \alpha_{ij}^2) \left(\frac{2T_i}{m_i} + \frac{2T_j}{m_j} \right) \right. \\ &\quad \left. + 4(1 + \alpha_{ij}) \frac{T_i - T_j}{m_1 + m_2} \right] \\ &\times \left(\frac{2T_i}{m_i} + \frac{2T_j}{m_j} \right)^{1/2}. \end{aligned} \quad (10)$$

These equations still depend on the particular heating mechanism through the term $\mathcal{F}T_i$; once the latter has been specified, two equations are obtained for T_1 and T_2 ; they are easy to implement and solve numerically varying the various controlling parameters.

Before turning to the heating provided by a stochastic thermostat [which amounts to $(\mathcal{F}T_i)/m_i = \text{constant}$], we consider three particular limiting cases.

a. In the tracer limit [13], i.e. $n_1 \rightarrow 0$, without any forcing term, T_2 is imposed and only the equation for T_1 is considered. As already noted in [3], the result for $\gamma = T_1/T_2$ obtained in [13]

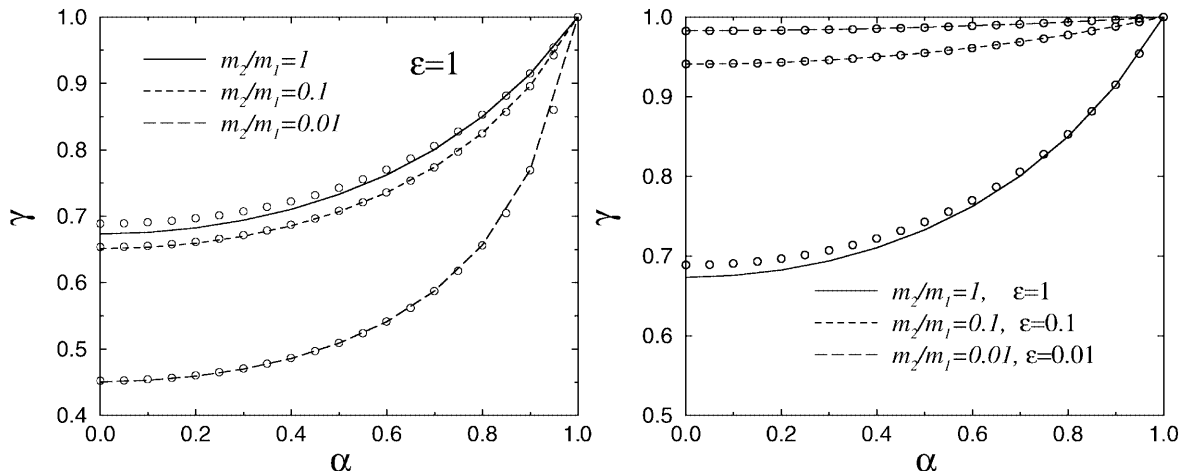


Fig. 1. Comparison of the simulation results found in [11] (lines) with the solution of equation (12) (circles), for various values of the mass ratio and of the parameter ϵ recalled in (12)

$$\gamma = \frac{1 + \alpha_{12}}{2 + \frac{m_2}{m_1}(1 - \alpha_{12})} \quad (11)$$

is easily recovered, irrespective of dimension.

b. Another possibility to obtain a NESS for IHS has been proposed in [11]: the temperature $T_2 = T$ of one population is imposed, with a corresponding Gaussian velocity distribution, and elastic collisions between particles of type 2 as well as for 1–2 collisions: $\alpha_{22} = \alpha_{12} = 1$. Energy is consequently injected into the inelastic population 1 (with restitution coefficient $\alpha_{11} = \alpha < 1$), without the need for any other forcing term. In [11], high precision numerical results were obtained for the distribution function Φ_1 , and temperature T_1 (the system is three-dimensional, and $\chi_{ij} = 1$), by an iterative numerical resolution of the Boltzmann equation. Imposing $\mathcal{F}T_1 = 0$ in (10), it is straightforward to obtain a third order polynomial equation for $\gamma = T_1/T_2$ (this quantity is necessarily smaller than 1)

$$\frac{\epsilon^2(1 - \alpha^2)^2}{32} \left(\frac{m_1}{m_2} + \frac{m_2}{m_1} + 2 \right)^2 \gamma^3 = (1 - \gamma)^2 \left(\gamma + \frac{m_1}{m_2} \right)$$

where, $\epsilon = \frac{4n_1}{n_2(1 + \sigma_2/\sigma_1)^2}$. (12)

In Fig. 1, the solution of equation (12) is compared to the results reported in [11]. The agreement is excellent, which may be traced back to the analysis of [11], showing that the distribution function Φ_1 is very close to a Gaussian, although mathematically different (on the other hand and by definition of the model, Φ_2 is strictly speaking a Gaussian). The slight discrepancy obtained at low α for $m_1 = m_2$ corresponds to values of the parameters for which the deviation of Φ_1 from a Gaussian is stronger.

c. Finally, a forcing term $\mathcal{F}f_i(\mathbf{v}) = \zeta \frac{\partial}{\partial \mathbf{v}} \cdot [\mathbf{v}f(\mathbf{v})]$, which provides an Enskog-Boltzmann equation formally equivalent to the free cooling case (see e.g. [18]), leads back to the results of [3] obtained in this situation: the term $\mathcal{F}T_i$ is indeed proportional to T_i , so that writing $\partial_t T_i = 0$ in (8) yields the same equation for γ as equating the two cooling rates $\partial_t T_i/T_i$ when $\mathcal{F}T_i = 0$.

3 The stochastic thermostat

In this section, we consider the situation of energy supply through random kicks [14–22]: the particles are submitted between collisions to an uncorrelated white noise (e.g. Gaussian). The equation of motion for a particle is then

$$m_i \frac{d\mathbf{v}}{dt} = \mathbf{F}_i + m_i \hat{\xi}_i \quad (13)$$

where \mathbf{F}_i is the force due to inelastic collisions, and $\langle \xi_{i\alpha}(t) \xi_{j\beta}(t') \rangle = \xi_0^2 \delta_{ij} \delta_{\alpha\beta} \delta(t - t')$, where Greek indices refer to Cartesian coordinates. The associated forcing term in the Enskog equation is

$$\mathcal{F}f = \frac{\xi_0^2}{2} \left(\frac{\partial}{\partial \mathbf{v}} \right)^2 f(\mathbf{v}, t),$$

so that $\mathcal{F}T_i = m_i \xi_0^2$. We do not claim that the forcing term considered here is the most suited to describe vibrofluidized beds, but it mimics an important effect of energy injection by a moving piston: in experiments, particles undergoing collisions with the piston (of large mass) gain a velocity that is decorrelated from their masses, so that more kinetic energy is injected into the population of large mass.

The corresponding equation for $\gamma = T_1/T_2$ reads:

$$\begin{aligned} & \chi_{11} \sigma_{11}^{d-1} (1 - \alpha_{11}^2) \frac{n_1}{n_2} \left(\frac{m_2}{m_1} \right)^{3/2} \gamma^{3/2} + \sqrt{2} \chi_{12} \sigma_{12}^{d-1} \\ & \times \left[(1 - \alpha_{12}^2) \left(\mu_{21}^2 - \frac{n_1}{n_2} \mu_{12}^2 \right) \left(1 + \frac{m_2}{m_1} \gamma \right)^{3/2} \right. \\ & \quad \left. + 2\mu_{21}(1 + \alpha_{12}) \left(\mu_{21} + \frac{n_1}{n_2} \mu_{12} \right) \left(1 + \frac{m_2}{m_1} \gamma \right)^{1/2} \right. \\ & \quad \left. \times (\gamma - 1) \right] \\ & = \chi_{22} \sigma_{22}^{d-1} (1 - \alpha_{22}^2). \end{aligned} \quad (14)$$

The temperature ratio γ therefore depends in a non-trivial way on the ratios of masses, densities and diameters, and

also on the inelasticities α_{ij} and pair correlation functions χ_{ij} . It may be checked that in the limit of vanishing inelasticities, $\gamma \rightarrow 1$ as it should. Moreover, for mechanically equivalent particles (i.e. $m_1 = m_2$, $\sigma_1 = \sigma_2$ and $\alpha_{11} = \alpha_{22} = \alpha_{12}$), we should also recover equipartition ($\gamma = 1$) irrespective of densities. This is the case in the Boltzmann limit (low densities where all pair correlation functions $\chi_{ij} \rightarrow 1$). At arbitrary packing fraction, the various approximations for the χ_{ij} that may be found in the literature [24,25] are such that χ_{ij} no longer depends on i and j when $\sigma_1 = \sigma_2$, so that equipartition holds for mechanically equivalent particles.

Since equation (14) relies on a Gaussian approximation for Φ_i , we have compared our approach to the results of Monte Carlo simulations (the so-called DSMC technique [26]) where the non-linear Boltzmann equation is solved numerically for both species. As we solve numerically the *homogeneous* Boltzmann equation, the phenomena of segregation or clustering are explicitly discarded.

In the following sections, we will study more precisely some cases that could have experimental relevance, and for the sake of simplicity, we considered $\chi_{ij} = 1$. All the results are given for the three dimensional case; note however that for $\sigma_1 = \sigma_2$ the temperature ratio becomes d -independent.

3.1

Equal inelasticities: $\alpha_{ij} = \alpha$

We first consider the case of equal restitution coefficients ($\alpha_{ij} = \alpha$), for materials having similar elastic properties. The dependence of γ on the mass and number density ratios, for equal sizes, is shown in Figure 2. Excellent agree-

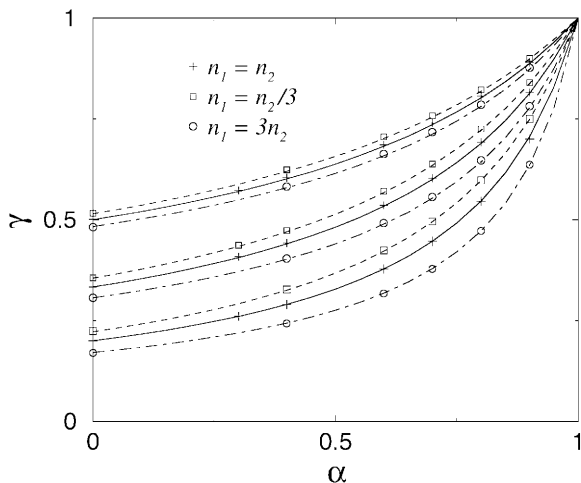


Fig. 2. Temperature ratio $\gamma = T_1/T_2$ as a function of inelasticity, for $\alpha_{11} = \alpha_{22} = \alpha_{12} = \alpha$, and grains of equal radii ($\sigma_1 = \sigma_2$). The curves show the solutions of equation (14) whereas the symbols display the results of DSMC simulations. The top three curves correspond to a mass ratio $m_2/m_1 = 2$, the three intermediate ones to $m_2/m_1 = 3$ and $m_2/m_1 = 5$ for the three bottom curves. For each mass ratio, several density ratios have been considered: $n_2/n_1 = 3$ (squares and dashed lines), $n_2/n_1 = 1$ (pluses and continuous lines), and $n_2/n_1 = 1/3$ (circles and dot-dashed lines)

ment is found between DSMC simulations (symbols) and the solution of equation (14). It turns out indeed that the velocity distributions measured in Monte Carlo simulations are very close to Gaussians. As may be expected, γ is a decreasing function of m_2/m_1 . The density dependence is relatively weak (the temperature ratio slightly increases when n_2/n_1 increases by an order of magnitude).

We have also considered two types of beads of the same material, i.e. the same restitution coefficient $\alpha_{11} = \alpha_{22} = \alpha_{12}$ and same mass density ρ : the ratio of masses m_2/m_1 is then equal to $(\sigma_2/\sigma_1)^3$ for three-dimensional beads. Figure 3 shows a strong influence of the size ratio, for two experimentally relevant values of α : γ decreases very strongly as soon as σ_2 is two or three times σ_1 . Once again, the number density ratio has a relatively small incidence on γ . It is interesting to disentangle the effects of σ_2/σ_1 and m_2/m_1 , by varying one parameter alone, the other being kept constant. It appears that the leading effect in the decrease of γ observed in Figure 3 is ascribable to a change in mass ratio, and not in size: the results obtained at $\sigma_1 = \sigma_2$ varying m_2/m_1 are close to those reported in Fig. 3, but surprisingly give a lower γ (e.g. the results displayed in Figure 3 for $\alpha = 0.9$ and equal densities are $\gamma = 0.66$ and 0.38 for $\sigma_2/\sigma_1 = 2$ and 3 respectively, whereas with $\sigma_1 = \sigma_2$, we obtain $\gamma = 0.59$ for $m_2/m_1 = 2^3$ and $\gamma = 0.29$ for $m_2/m_1 = 3^3$).

3.2

Comparison with experiments

For glass spheres with size ratio $\sigma_2/\sigma_1 = 1.25$, Wildman and Parker have measured a temperature ratio $\gamma = T_1/T_2$ in the range 0.75–0.8 [6], with a weak dependence on densities (except may be in the limit of large grains predominance where $n_2 \gg n_1$). Estimating the relevant restitution coefficient to be $\alpha \simeq 0.9$ [6], we obtain from Eq. (14) $\gamma \simeq 0.9$ (see also Fig. 3), with also

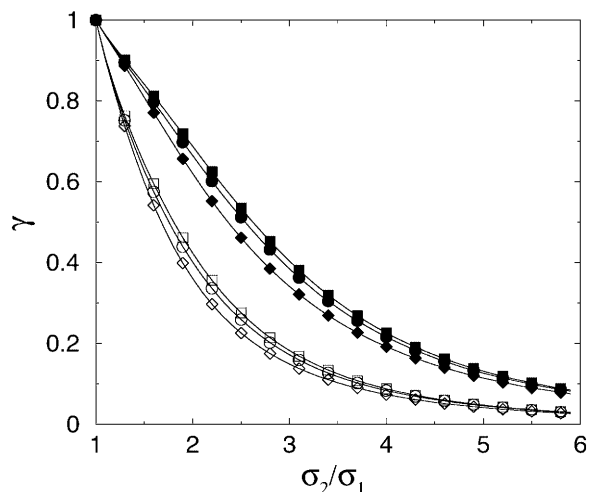


Fig. 3. Temperature ratio from eq (14) for grains made of the same material, i.e. for $m_2/m_1 = (\sigma_2/\sigma_1)^3$, and $\alpha_{ij} = \alpha$. Filled symbols correspond to $\alpha = 0.9$, open ones to $\alpha = 0.7$. The squares are for $n_2/n_1 = 3$, the circles for $n_2/n_1 = 1$ and the diamonds for $n_2/n_1 = 1/3$

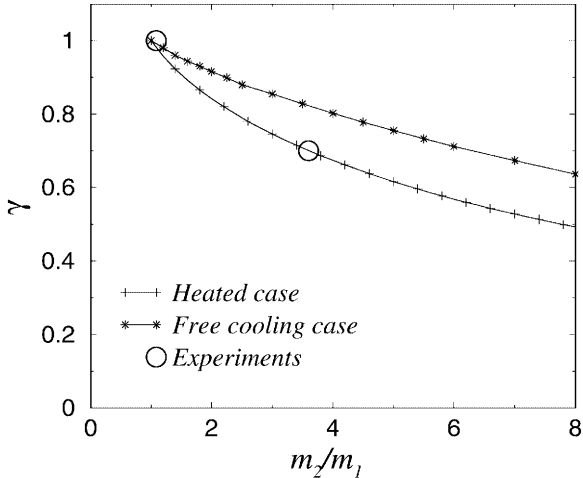


Fig. 4. T_1/T_2 as a function of mass ratio, for $\alpha_{ij} = 0.85$ and $\sigma_1 = \sigma_2$, for the stochastic thermostat and for the free cooling regime, together with the experimental data of [7]. Note that the values $\alpha_{ij} = 0.85$ are only schematic and cannot be intended as an exact description of the experimental situation

a weak dependence on n_2/n_1 . It is however noteworthy that this weak dependence is opposite to that observed experimentally: when the proportion of large grains is increased, we obtain an increase of γ . For comparison, the temperature ratio obtained for the same parameters in the homogeneous cooling stage [3] is $\gamma \simeq 0.96$ and the authors of [6] proposed a simplified theory for which γ is in the range 0.4–0.7.

The results obtained by Feitosa and Menon [7] confirm the very weak influence of n_2/n_1 when the grains (of equal size) are made of two different materials. For a mixture glass/aluminum with mass ratio $m_2/m_1 = 1.09$, γ is measured very close to 1, whereas for a more asymmetric mixture of glass and brass with $m_2/m_1 \simeq 3.6$, $\gamma \simeq 0.7$. Making use of equation (14) with schematic inelasticities $\alpha_{11} = \alpha_{12} = \alpha_{22} = 0.85$, we obtain $\gamma = 0.98$ for $m_2/m_1 = 1.09$ and $\gamma = 0.7$ for $m_2/m_1 = 3.6$. In the free cooling regime, the corresponding ratios are 0.99 and 0.82. These results are displayed in Fig. 4.

Other results are given in Figures 5 and 6, where the partial inelasticities are not taken equal, but are given values that we expect to be of experimental relevance: the experimental data of [7] are therefore also reported in Fig. 5(b). In Fig. 5, the sizes of the particles are taken equal and the mass ratio changes, while Fig. 6 displays the influence of the size ratio when the density ratios are fixed.

The situation reported in [7] corresponds to that of the Figures 5b and 6b, where the heavier grains are also the more dissipative. As may be observed in Fig. 5b, a variation of n_1/n_2 from 1/3 to 3 leaves γ roughly unaffected for $m_2/m_1 \leq 3$.

It may be noted that γ is not bounded from above by 1, and values slightly above 1 are obtained even when $m_2 > m_1$ by conveniently choosing the inelasticities (or, at fixed inelasticities and densities, by conveniently choosing the sizes). γ is nevertheless generically smaller than 1 for $m_2 > m_1$: the heavier particles have a larger kinetic energy.

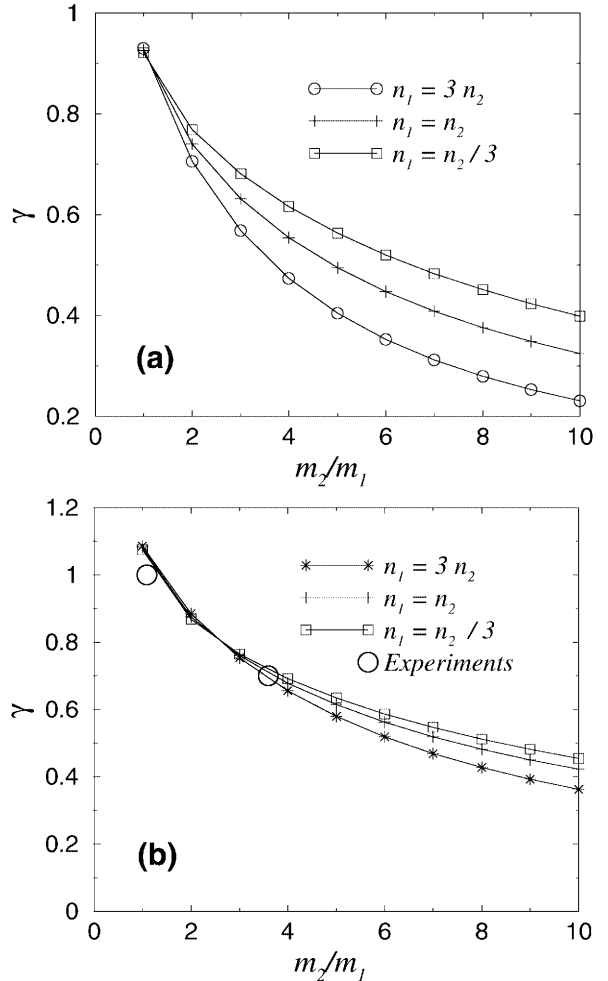


Fig. 5. **a** T_1/T_2 as a function of mass ratio, for $\alpha_{11} = 0.7$, $\alpha_{12} = 0.8$, $\alpha_{22} = 0.9$ and $\sigma_1 = \sigma_2$. **b** same with “reversed” inelasticities ($\alpha_{11} = 0.9$, $\alpha_{12} = 0.8$ and $\alpha_{22} = 0.7$), together with the experimental values of [7]

4 Conclusion

We have considered heated binary granular mixtures from the point of view of kinetic theory. As in the free cooling case, and in agreement with recent experimental data, the granular temperatures of the components of the mixture differ. This finding is not surprising in a non-equilibrium system, where the “temperature” does not have any thermodynamical relevance.

Using a mean-field approach with the assumption of isotropic Gaussian velocity distributions, we have derived an equation for the temperature ratio γ that may be adapted for various kinds of heating mechanisms, and easily solved once the controlling parameters have been chosen. In particular, the values obtained within the stochastic thermostat framework are compatible with those measured in the experiments reported in [6,7]. Even if a quantitative comparison with experiments is somehow pointless given the simplicity of our approach, similar trends are observed. For example, the heavier particles carry generically more kinetic energy than the lighter ones, the ratio being insensitive to the relative

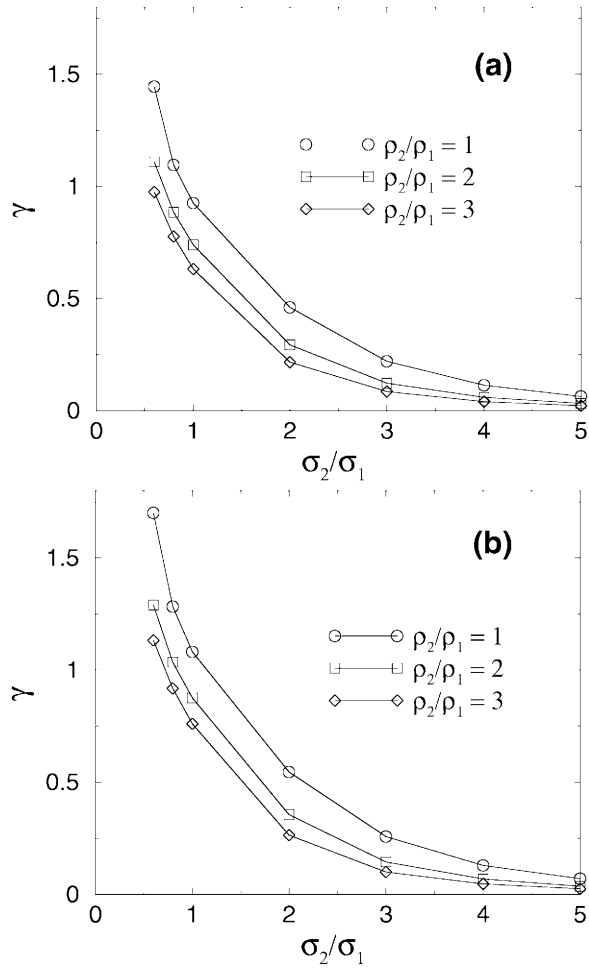


Fig. 6. **a** γ versus size ratio for an equimolar mixture ($n_2 = n_1$) with $\alpha_{11} = 0.7$, $\alpha_{12} = 0.8$, $\alpha_{22} = 0.9$ and different mass density ratios ρ_2/ρ_1 . **b** same with $\alpha_{11} = 0.9$, $\alpha_{12} = 0.8$, $\alpha_{22} = 0.7$ and again $n_2 = n_1$

number fraction of both species. It also appears that the breakdown of energy equipartition is all the more pronounced as the mass ratio is increased, the size ratio playing only a minor role.

Appendix

In this appendix we show how to perform the integrals over $\hat{\mathbf{c}}$, in order to obtain equation (8). We start from the identity

$$\int d\mathbf{v} v^2 J_{ij}[\mathbf{v}|f_i, f_j] = \chi_{ij} \sigma_{ij}^{d-1} \int d\mathbf{v}_1 d\mathbf{v}_2 \int d\hat{\mathbf{c}} (\hat{\mathbf{c}} \cdot \mathbf{v}_{12}) f_i(\mathbf{v}_1) f_j(\mathbf{v}_2) (v_1''^2 - v_1^2), \quad (15)$$

with $\mathbf{v}_1'' = \mathbf{v}_1 - \mu_{ji}(\mathbf{1} + \alpha_{ij})(\hat{\mathbf{c}} \cdot \mathbf{v}_{12})\hat{\mathbf{c}}$, i.e. where

$$v_1''^2 - v_1^2 = \mu_{ji}^2 (1 + \alpha_{ij})^2 (\hat{\mathbf{c}} \cdot \mathbf{v}_{12})^2 - 2\mu_{ji} (1 + \alpha_{ij}) (\hat{\mathbf{c}} \cdot \mathbf{v}_{12}) (\hat{\mathbf{c}} \cdot \mathbf{v}_1).$$

Using the unit vector $\hat{\mathbf{c}}_{12} = \mathbf{v}_{12}/v_{12}$, and the known integrals $\beta_n = \int d\hat{\mathbf{c}} (\hat{\mathbf{c}} \cdot \mathbf{c}_{12})^n$ (see e.g. [16]), the first term is readily computed and yields:

$$\beta_3 \chi_{ij} \sigma_{ij}^{d-1} \mu_{ji}^2 (1 + \alpha_{ij})^2 \int d\mathbf{v}_1 d\mathbf{v}_2 f_i(\mathbf{v}_1) f_j(\mathbf{v}_2) v_{12}^3. \quad (16)$$

To compute the term containing $(\hat{\mathbf{c}} \cdot \mathbf{v}_1)$, we choose one of the unit vectors to be along \mathbf{v}_{12} , and decompose:

$$\mathbf{v}_{12} = v_{12} \hat{\mathbf{e}}_1, \quad \mathbf{v}_1 = \frac{\mathbf{v}_1 \cdot \mathbf{v}_{12}}{v_{12}} \hat{\mathbf{e}}_1 + \mathbf{v}_1^\perp, \\ \hat{\mathbf{c}} = \frac{\hat{\mathbf{c}} \cdot \mathbf{v}_{12}}{v_{12}} \hat{\mathbf{e}}_1 + \hat{\mathbf{c}}^\perp. \quad (17)$$

$(\hat{\mathbf{c}} \cdot \mathbf{v}_1)$ is then written as

$$\frac{(\mathbf{v}_1 \cdot \mathbf{v}_{12})(\hat{\mathbf{c}} \cdot \mathbf{v}_{12})}{v_{12}^2} + \hat{\mathbf{c}}^\perp \cdot \mathbf{v}_1^\perp,$$

and the term $\hat{\mathbf{c}}^\perp \cdot \mathbf{v}_1^\perp$ gives a vanishing contribution in the integral over $\hat{\mathbf{c}}$ for symmetry reasons. We are therefore left with

$$\int d\hat{\mathbf{c}} \frac{(\mathbf{v}_1 \cdot \mathbf{v}_{12})(\hat{\mathbf{c}} \cdot \mathbf{v}_{12})^3}{v_{12}^2} = v_{12} \beta_3 (\mathbf{v}_1 \cdot \mathbf{v}_{12}).$$

Rearranging terms and writing $\mathbf{v}_1 = \mu_{ji} \mathbf{v}_{12} + \mu_{ij} \mathbf{v}_1 + \mu_{ji} \mathbf{v}_2 = \mu_{ji} \mathbf{v}_{12} + \mathbf{V}_{ij}$, one finally obtains equation (8).

References

1. H. M. Jaeger, S. R. Nagel & R. P. Behringer, Rev. Mod. Phys., 68, 1259 (1996); L.P. Kadanoff, Rev. Mod. Phys., 71, 435 (1999)
2. Y. Limon Duparcmeur, Thèse de l'université de Rennes I (1996)
3. V. Garzó & J. Dufty, Phys. Rev. E, 60 5706 (1999)
4. L. Huilin, L. Wenti, B. Rushan, Y. Lidán & D. Gidaspow, Physica A, 284, 265 (1999)
5. W. Losert, D.G.W. Cooper, J. Delour, A. Kudrolli & J.P. Gollub, Chaos 9, 682 (1999)
6. R. D. Wildman & D. J. Parker, Phys. Rev. Lett., 88, 064301 (2002)
7. K. Feitosa & N. Menon, Phys. Rev. Lett., 88, 198301 (2002)
8. J. M. Montanero & V. Garzó, Gran. Matter, 4, 17 (2002)
9. R. Clelland & C. M. Hrenya, Phys. Rev. E, 65, 031301 (2002)
10. J. M. Montanero & V. Garzó, preprint cond-mat/0201175
11. T. Biben, Ph. A. Martin & J. Piasecki, preprint
12. U. Marini Bettolo Marconi & A. Puglisi, cond-mat/0112336 Phys. Rev. E (2002) and cond-mat/0202267
13. Ph. A. Martin & J. Piasecki, Europhys. Lett., 46, 613 (1999)
14. D. R. M. Williams & F. C. MacKintosh, Phys. Rev E, 54, R9 (1996)
15. A. Puglisi, V. Loreto, U. Marini Bettolo Marconi & A. Vulpiani, Phys. Rev. E, 59, 5582 (1999)
16. T.P.C. van Noije & M.H. Ernst, Gran. Matter, 1, 57 (1998)
17. T.P.C. van Noije, M.H. Ernst, E. Trizac & I. Pagonabarraga, Phys. Rev. E, 59, 4326 (1999)
18. J.M. Montanero & A. Santos, Granular Matter, 2, 53 (2000)
19. R. Cafiero, S. Luding & H.J. Herrmann, Phys. Rev. Lett., 84, 6014 (2000)
20. S. J. Moon, M. D. Shattuck & J. B. Swift, Phys. Rev. E, 64, 031303 (2001)

21. I. Pagonabarraga, E. Trizac, T.P.C. van Noije, & M.H. Ernst, *Phys. Rev. E*, 65, 011303 (2002)
22. V. Garzó & J. M. Montanero, cond-mat/0112241
23. L. Landau & E. Lifshitz, *Physical Kinetics*, Pergamon Press (1981)
24. L. L. Lee & D. Levesque, *Mol. Phys.*, 24, 269 (1972)
25. A general procedure to infer the pair correlation functions in a multi-component d -dimensional hard-sphere fluid from the equation of state of the monodisperse system has been proposed by A. Santos, S. B. Yuste and M. López de Haro, *Mol. Phys.*, 96, 1 (1999)
26. G. Bird, “Molecular Gas Dynamics” (Oxford University Press, New York, 1976) and “Molecular Gas Dynamics and the Direct Simulation of Gas flows” (Clarendon Press, Oxford, 1994)

Chapitre A

Qu'est-ce qu'une dispersion colloïdale ?

RESEARCH NOTE

Stability of the AB crystal for asymmetric binary hard sphere mixtures

By E. TRIZAC, M. D. ELDRIDGE and P. A. MADDEN

Physical Chemistry Laboratory, Oxford University, South Parks Road, Oxford OX1 3QZ, UK

(Received 5 September 1996; accepted 23 September 1996)

The thermodynamic stability of the AB (rocksalt) structure for binary mixtures of hard spheres is established by means of Monte Carlo and molecular dynamics simulations. Constant pressure and constant volume phase diagrams are presented for size ratios $\sqrt{2} - 1$ and 0.45. A phase-separation molecular dynamics experiment is described, confirming the predictions of the phase diagram.

The finding that binary mixtures of hard spheres may crystallize spontaneously into ordered superlattices has provoked considerable interest. Crystals of stoichiometry AB_{13} and AB_2 (where A is the large particle) were observed in colloidal suspensions of particles with steeply repulsive potentials by Bartlett *et al.* [1] and the thermodynamic stability of these structures for true hard spheres was confirmed in computer simulations by Eldridge and co-workers [2, 3]. This appears to present a paradox [4] as the formation of these ordered structures is caused by the entropy, normally associated with the driving force for disorder, since the potential energy in hard-particle systems is zero. Understanding the factors which control crystal structures in colloids has become a matter of technical importance, since colloidal crystals may exhibit potentially useful optical [5] and acoustic properties. More generally, it has been suggested that the same packing considerations which dictate the ordered structures of hard particles may govern the stoichiometry of the compounds which form in van der Waals mixtures (e.g., CH_4/H_2) at very high pressures [6] though other workers have maintained the importance of energetic factors [7] in these systems. Certainly, the hard sphere model is an important reference system for perturbation theories of mixtures, which can be applied to alloys or van der Waals crystals [8].

The entropy 'paradox' is resolved by noting that in an ordered system at high density a particle may explore a larger volume about its lattice site than is available in a disordered system at the same density, and that the consequential gain in translational entropy may compensate for the loss of entropy associated with the formation of

the ordered structure [4]. Murray and Sanders [9] formulated the principle that an ordered compound would form only if its packing fraction ϕ (the fraction of space contained in the interior of the particles) when close packed exceeded that of the one-component crystals into which it would separate ($\phi_{cp}^{(1)} = \pi\sqrt{2}/6 \approx 0.7405$ for fcc or hcp structures). For a lower packing fraction the particles in such a compound will have a larger free volume in which to move, and thus a higher entropy. This principle accounts for the stability of the AB_2 system, for a particle radius ratio α , $0.48 < \alpha < 0.62$, which is (roughly) where it is observed. It also predicts a window of stability for an AB compound, of the NaCl structure, for $\alpha \sim 0.414 \approx \sqrt{2} - 1$, for which $\phi_{cp}(\alpha = \sqrt{2} - 1) = 0.793$ comfortably exceeds that of monodisperse hard spheres. The principle does not, however, predict the observed stability of the AB_{13} system for which the maximum packing fraction $\phi_{cp}(\alpha = 0.558) = 0.738$. Recently, Cottin and Monson [10] have developed a cell theory of binary hard particle crystals, which contains a more precise estimate of the free volume. Their results for the free energies of the AB_2 and AB_{13} crystals and for the binary phase diagrams involving them are in remarkably good agreement with those obtained in the computer simulations.

The purpose of the present work is to report on the thermodynamic stability of the AB (rocksalt) phase on the basis of the same free-energy calculations used previously [2] (we have already reported that AB (CsCl) is unstable [3]). This phase has not been detected experimentally in colloidal suspensions. The appearance of the AB phase, expected on packing arguments for a relatively small size ratio ($\alpha < 0.45$), would set a lower

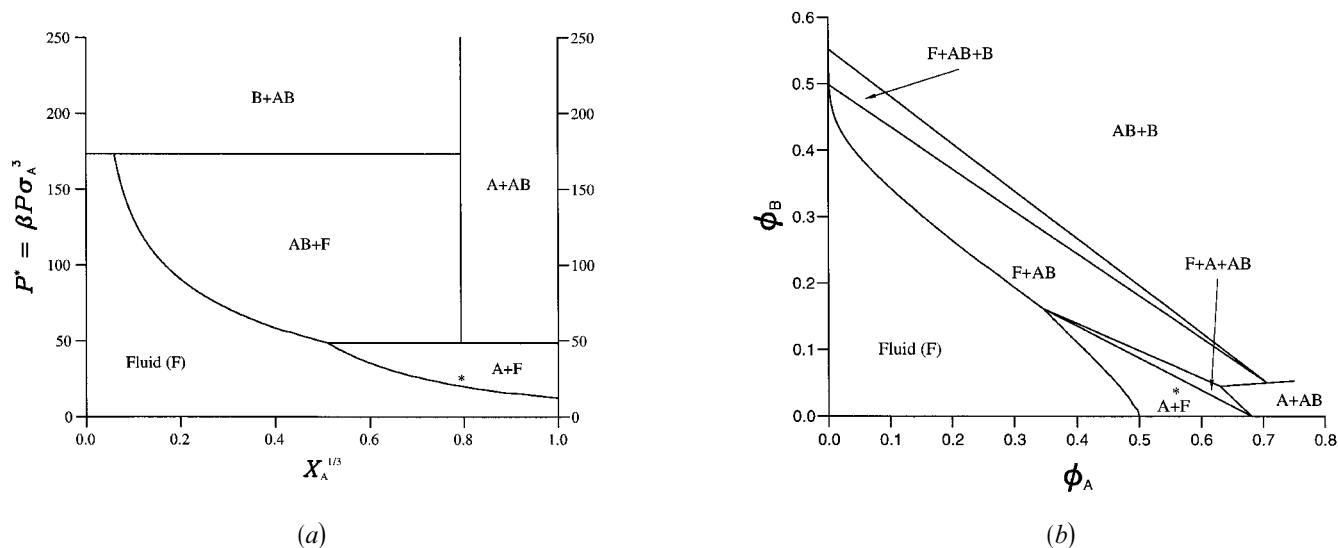


Figure 1. (a) P - X phase diagram of a binary mixture of hard spheres with a diameter ratio $\alpha = 0.414$, (b) Constant volume diagram: the lines indicate boundaries of two or three phase regions. Note that the ordinate in (a) is $X_A^{1/3}$. The star marks the phase point used as the starting point of the MD run.

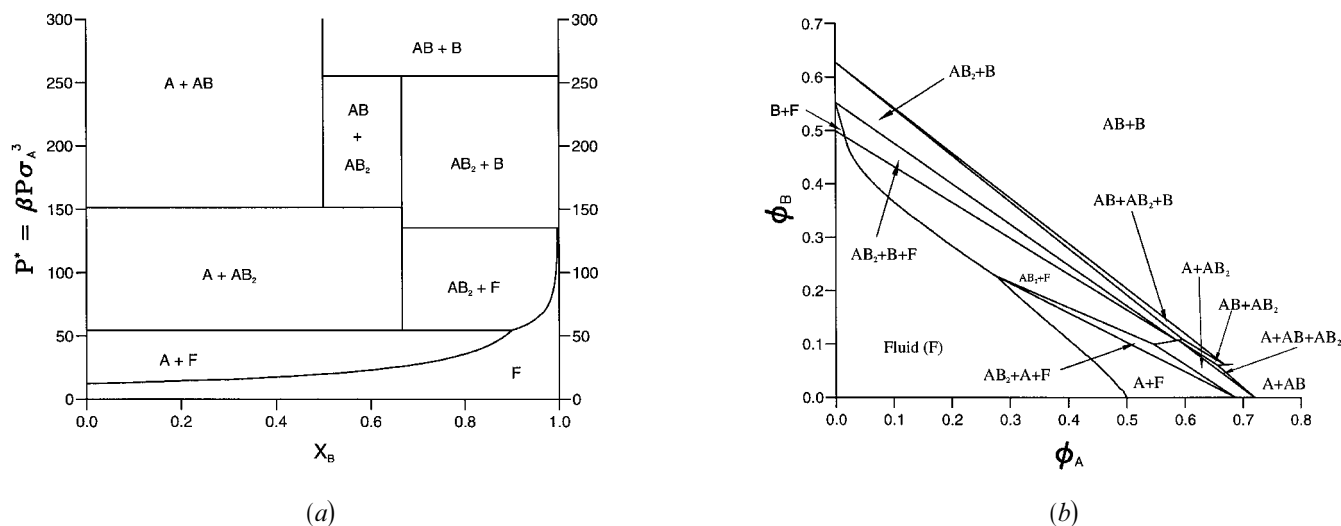


Figure 2. Constant P and V phase diagrams for $\alpha = 0.45$.

bound in α to the range of observability of the more exotic AB_2 crystal. It was not included in the phase diagrams reported previously [3] but it has already been considered in cell theory calculations [10]

Results are reported at $\alpha = 0.414$, where AB should be most stable (since the small particles will just fill the octahedral holes in the fcc lattice of large particles) and at $\alpha = 0.45$ which might be expected to be close to its upper limit of stability. The competing phases considered are the binary fluid (expected at low packing fractions), pure fcc crystal (A and B), and AB_2 . The data concerning the AB_2 superlattice were taken from [2] for the diameter ratios considered ($\alpha \leq 0.45$) AB_{13} cannot

be found (cf. [2]). The Gibbs free energies of all phases were determined by thermodynamic integration [11] For the binary fluid, the semi-empirical equation of state of Mansoori *et al.* [12] was used, allowing the free energy to be known analytically. For the solid state, the method of Frenkel and Ladd [13] was implemented, taking the reference state, of known free energy, as the corresponding Einstein crystal, which can be reached by slowly turning on harmonic springs to bind the particles to their lattice sites. The method is discussed in detail in [2] and requires Monte Carlo calculations. The results were checked by direct integration of the equation of state between selected state points.

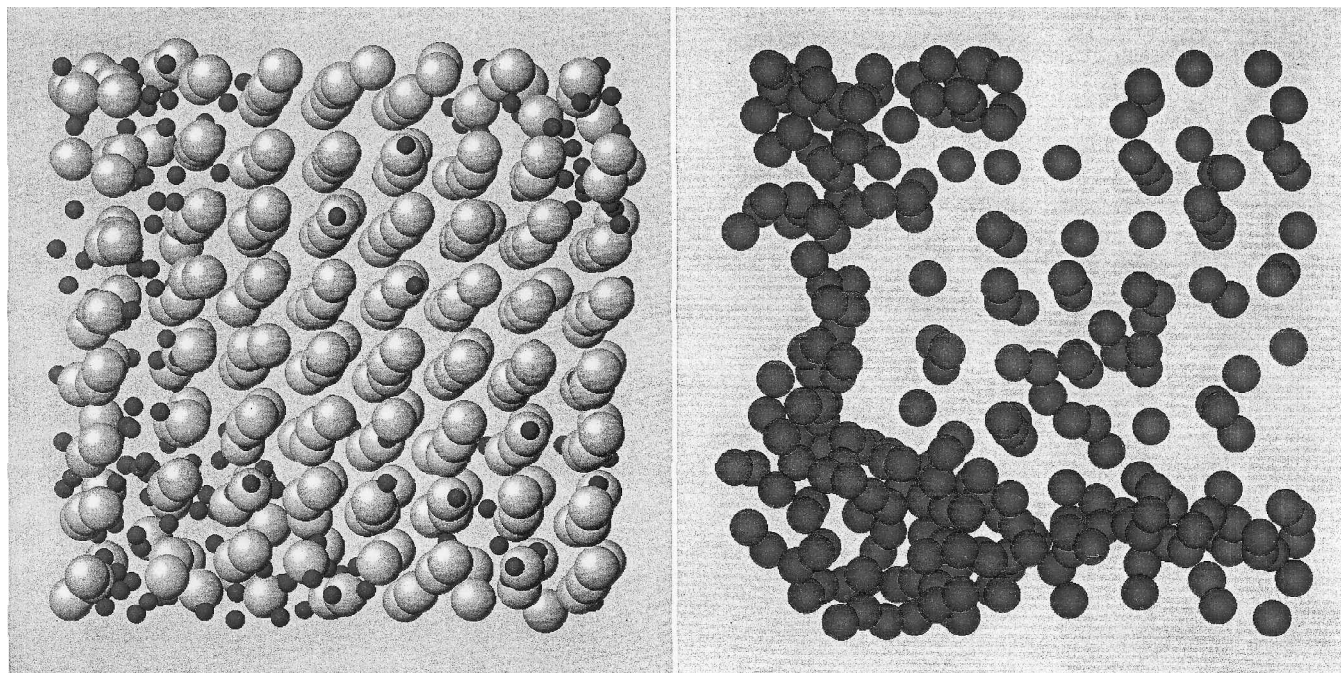


Figure 3. The left hand panel shows the arrangement of large (yellow) and small (red) spheres in the last configuration of the molecular dynamics simulation. For convenience, the radii of each species have been drawn half their actual value. The right hand panel shows the small spheres full-size and the large spheres are omitted.

We present the pressure–composition phase diagrams, derived from the classical double-tangent construction (see [3]), for diameter ratios $\alpha = 0.414$ in figure 1(a) and $\alpha = 0.45$ in figure 2(a). As anticipated, at $\alpha = 0.414$ AB is the dominant compound observed in the solid part of the phase diagram, and AB_2 is no longer observed at such small diameter ratios. Note that a pure A solid would crystallize out of an equimolar fluid mixture ($x_A = x_B = 1/2$), rather than AB, in agreement with Denton and Ashcroft's theoretical finding that the AB crystal was unstable in such a mixture [14]. For $\alpha = 0.45$, the AB structure coexists with the AB_2 superlattice, but is observable only at very high pressures, showing that it is very close to its upper stability limit. For intermediate pressures, there is a tendency for fcc solid A (large spheres) to precipitate, but the AB + fcc B + fluid eutectic corresponds to a composition $x_B \simeq 1$ so that the B + fluid coexistence is confined to a very tiny region. Overall, the calculated phase diagrams are in good agreement with the cell model theoretical results [10] although the predicted stability limits of each phase differ somewhat.

Pressure–composition phase diagrams are not very relevant when it comes to comparing the data with experiments on colloidal suspensions [1]. The total volume accessible to a colloidal mixture is set by the suspending fluid. Hence, constant volume phase diagrams have been computed [3] using the partial packing

fractions as independent coordinates. In such a diagram, the lines passing through the origin correspond to a constant composition and the lines parallel to the second bisectrix are of equal total packing fraction. Figures 1(b) and 2(b) show the representations obtained for $\alpha = 0.414$ and $\alpha = 0.45$. Figure 1(b) shows that AB crystals should be readily preparable in colloidal suspensions of this size ratio, but a large excess of the smaller B particles is required in the mixture.

As a final step we examine by means of molecular dynamics simulations whether the system can reach the predicted equilibrium state. The calculation provides a check on the accuracy of the thermodynamically deduced phase diagram and also gives some insight into the phase kinetics of the hard-particle system. We consider an MD simulation started from an AB crystal with $\alpha = \sqrt{2} - 1$ and with a packing fraction of 0.6. As figure 1 shows (the relevant composition is shown by the stars in the figures) the AB crystal is metastable under these conditions (at $P^* = 28$ in figure 1(a)); the thermodynamic equilibrium state should be coexistence of fcc A + fluid with $x_{\text{fluid}}B = 0.7$. Applying the lever rule to figure 1(a) gives the following equilibrium composition for the system; 71.7% fluid and 28.3% fcc A. Thus, 56.6% of the large spheres should stay on lattice sites and the remainder should be found in a fluid state with all the small ones. The evolution of the system can be followed by saving periodically the diffusion constants

of large and small spheres, and a 'melting factor' \mathcal{M} defined as the average of (200), (020) and (002) structure factors of the crystal ($N^{-1} \sum_{i=1}^N \sum_{j=1}^N \exp\{\mathbf{i}\mathbf{k} \cdot \mathbf{r}^{ij}\}$) where N is the total number of atoms, 512). For the perfect AB structure, $\mathcal{M} = N$, whereas in the liquid state, $\mathcal{M} \simeq 1$. Consistently with the predictions of the phase diagram, the melting factor after 10^5 collisions per particle has converged to a result remarkably close to the theoretical value $\mathcal{M} \sim (0.283)^2 N$ and the diffusion constants for the small spheres have reached a constant value. Finally, a useful probe is the direct visualization of the final configuration of the molecular dynamics simulations. Figure 3 shows the last configuration of the 30 million collision run. A central, crystalline region of large spheres depleted in small ones is seen to coexist with a fluid of large and small spheres. For the central domain, the former fcc structure remains with an A—A separation very similar to that in the parent AB crystal, indicating that phase separation has occurred in accordance with the predictions of the phase diagram. Given the relatively weak thermodynamic driving forces which one imagines to be associated with the entropy, it seems remarkable that this mesoscopic reorganization is observed on this timescale.

Overall, these results provide further confirmation of the reliability of the predictions emerging from cell model theory [10] which are achieved with far less effort. Some quantitative differences are seen in the phase diagrams but, given the sensitivity of these diagrams to the thermodynamic properties of the pure phases, this is unsurprising. Cottin and Monson [10] have surveyed the possible compounds which might be found in hard sphere mixtures and concluded that AB_{13} , AB_2 and AB (rocksalt) are the only ones likely to form.

This observation would seem to suggest that energetic factors play a role in the formation of van der Waals compounds [6, 7] since other stoichiometries have, so far, been observed.

This work was sponsored by the Engineering and Physical Sciences Research Council through grant No. GR/K14386.

References

- [1] BARTLETT, P., OTTEWILL, R. H., and PUSEY, P. N., 1990, *J. chem. Phys.*, **93**, 1299; 1992, *Phys. Rev. Lett.*, **68**, 3801.
- [2] ELDRIDGE, M. D., MADDEN, P. A., and FRENKEL, D., 1993, *Molec. Phys.*, **79**, 105; **80**, 987; *Nature*, **365**, 35.
- [3] ELDRIDGE, M. D., MADDEN, P. A., PUSEY, P. N., and BARTLETT, P., 1995, *Molec. Phys.*, **84**, 395.
- [4] FRENKEL, D., 1993, *Physics World*, **6**, 24.
- [5] TARHAN, I. I., and WATSON, G. H., 1996, *Phys. Rev. Lett.*, **76**, 315.
- [6] SOMAYAZULU, M. S., FINGER, L. W., HEMLEY, R. J., and MAO, H. L., 1996, *Science*, **271**, 1400.
- [7] VOS, W. L., and SCHOUTEN, J. A., 1993, *Low Temp. Phys.*, **19**, 338.
- [8] YOUNG, D. A., 1993, *J. chem. Phys.*, **98**, 9819.
- [9] MURRAY, M. J., and SANDERS, J. V., 1980, *Phil. Mag. A*, **42**, 721.
- [10] COTTIN, X., and MONSON, P. A., 1995, *J. chem. Phys.*, **102**, 3354.
- [11] FRENKEL, D., 1986, *Molecular Dynamics Simulations of Statistical Mechanical Systems Proceedings*, edited by G. Ciccotti and W. G. Hoover (Amsterdam: North-Holland) pp. 151–188.
- [12] MANSOORI, G. A., CARNAHAN, N. F., STARLING, K. E., and LELAND, T. W., 1971, *J. chem. Phys.*, **54**, 1523.
- [13] FRENKEL, D., and LADD, A. J. C., 1984, *J. chem. Phys.*, **81**, 3188.
- [14] DENTON, A. R., and ASHCROFT, N. W., 1990, *Phys. Rev. A*, **42**, 7312.

Chapitre B

Compacité et polydispersité optimale

Optimal packing of polydisperse hard-sphere fluids

Junfang Zhang, Ronald Blaak, Emmanuel Trizac,^{a)} José A. Cuesta,^{b)} and Daan Frenkel
*FOM Institute for Atomic and Molecular Physics, Kruislaan 407, 1098 SJ, Amsterdam,
The Netherlands*

(Received 14 October 1998; accepted 9 December 1998)

We consider the effect of intermolecular interactions on the optimal size-distribution of N hard spheres that occupy a fixed total volume. When we minimize the free-energy of this system, within the Percus–Yevick approximation, we find that no solution exists beyond a quite low threshold ($\eta \approx 0.260$). Monte Carlo simulations reveal that beyond this density, the size-distribution becomes bimodal. Such distributions cannot be reproduced within the Percus–Yevick approximation. We present a theoretical argument that supports the occurrence of a nonmonotonic size-distribution and emphasize the importance of finite size effects. © 1999 American Institute of Physics.
[S0021-9606(99)50111-6]

I. INTRODUCTION

Synthetic colloids are never perfectly monodisperse. Often, this polydispersity is a drawback, for instance, polydispersity is a problem in the preparation of high-quality colloidal crystals, that are needed in photonic band gap materials. However, occasionally, polydispersity is desirable, because it allows us to achieve material properties that cannot be realized with monodisperse colloids. For instance, monodisperse colloidal systems can fill at most 74.05% of space in the crystalline phase (regular close packing) and some 63% in the liquid/glassy state (random close packing). In contrast, colloids with a properly chosen particle-size distribution can be made essentially space filling, both in the crystalline solid (Appolonian packing) and in the liquid. In practice, perfect space filling structures are never achieved because this requires an infinite number of (predominantly small) particles per unit volume. Here, we consider a somewhat simpler problem, namely the filling of a given volume V by a fixed number of particles N , that occupy a prescribed total volume fraction η . We assume that the particles are free to exchange volume. As we have fixed both the number and the total volume of the particles, the average volume per particle is fixed—it defines the natural length-scale in the model. Clearly, the Helmholtz free energy of the system will depend on the nonfixed particle-size distribution. The distribution, however, is restricted by the two constraints of fixed number of particles and fixed total volume. We define the optimal size distribution to be the one that minimizes the Helmholtz free energy under both constraints. In the Monte Carlo simulations (performed in the isothermal–isobaric ensemble) that we report in this paper, we study the density dependence of the particle-size distribution. We compare the simulation re-

sults for the size distribution with an analytical estimate that is obtained by solving the Percus–Yevick (PY) equation for an N -component hard-sphere mixture.¹ Not surprisingly, the PY equation works very well at low densities. However, the theory breaks down at a surprisingly low density ($\eta \approx 0.26$). Of course, the fact that an approximate theory fails at a given density, does not imply that there is anything special going on in the system at that density. Yet, our simulations indicate that there is—the size distribution that was initially unimodal, becomes bimodal. We present a theoretical argument supporting this scenario.

The remainder of this paper is organized as follows: in Sec. II we describe the constant-pressure Monte Carlo simulations. The Percus–Yevick expression for the free energy of a system of polydisperse hard spheres with variable size distribution is discussed in Secs. III and IV. Section V is devoted to the derivation of analytical results turning useful when interpreting the simulation data. The mechanism behind the transition from unimodal to bimodal size distribution is also discussed.

II. MONTE CARLO SIMULATIONS

Monte Carlo simulations were performed in the isothermal–isobaric (constant NPT) ensemble.² This means that the number of particles N , the pressure P , and the temperature T are fixed. We attempt three distinct types of trial moves. We change the positions of the particles and allow the volume of simulation box to fluctuate, in order to equilibrate with respect to the applied pressure. Since we do not expect any crystalline order at low pressures, a cubic box shape is maintained. The third type of move is the one related to sampling the polydispersity of the system. To this end, we select two particles at random, between which we exchange an amount of volume drawn uniformly from the interval $[-\Delta V_{\max}, \Delta V_{\max}]$ (Fig. 1). The maximum volume change ΔV_{\max} was chosen such that the acceptance of a volume exchange move is between 35% and 50%. The relative

^{a)}Present address: Laboratoire de Physique Théorique et Hautes Energies (URA D00063 du CNRS), Bâtiment 211, Université Paris-Sud, 91405 Orsay Cedex, France.

^{b)}Permanent address: Grupo Interdisciplinar de Sistemas Complicados (GISC), Departamento de Matemáticas, Escuela Politécnica Superior, Universidad Carlos III de Madrid, c/Butarque, 15, 28911-Leganés, Madrid, Spain.

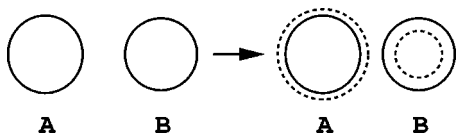


FIG. 1. Schematic drawing of the Monte Carlo trial used to sample the polydispersity. Of two randomly chosen particles the volume of one is increased, while the other is decreased in volume by the same amount.

frequency of the three moves is given by $N:1:N/2$. The initial configurations are made by N monodisperse spheres on a simple cubic lattice.

Simulations were performed for system sizes of $N = 512$ or 1000 , and several different reduced pressures $P^* = (k_B T)^{-1} P \langle \sigma^3 \rangle$, where σ is the diameter of particles, and $\langle \cdot \rangle$ denotes an average over particle-size distribution. As $\langle \sigma^3 \rangle$ is fixed, we choose $\langle \sigma^3 \rangle^{1/3}$ to define the unit of length that we will use in the remainder of this paper. We use $k_B T$ as our unit of energy. All other units that we need, follow from these definitions. The equation of state [P^* as a function of $\rho^* (\equiv \rho \langle \sigma^3 \rangle)$] and the particle size distribution were determined in the simulations. The results for the equation of state are shown in Fig. 2. The simulation data have been collected in Table I. At low pressures the particle-size distribution function is a single-peaked function with its maximum at $v=0$ (Figs. 3, 4 and 5). At higher pressures (typically, $P^* > 2.0$), the particle-size distribution develops a second peak. Actually, this second peak is quite small (i.e., only a small fraction of all particles becomes “large”). However, these particles contribute appreciably to the total volume fraction (Fig. 6). Depending on the pressure this contribution can get as large as 75%.

The formation of big particles in these MC simulations is a rather slow “dynamical” process. In order to speed up calculations, we did additional simulations, in which we started with a bidisperse distribution, with one or several big particles containing 99% of the total volume occupied by the

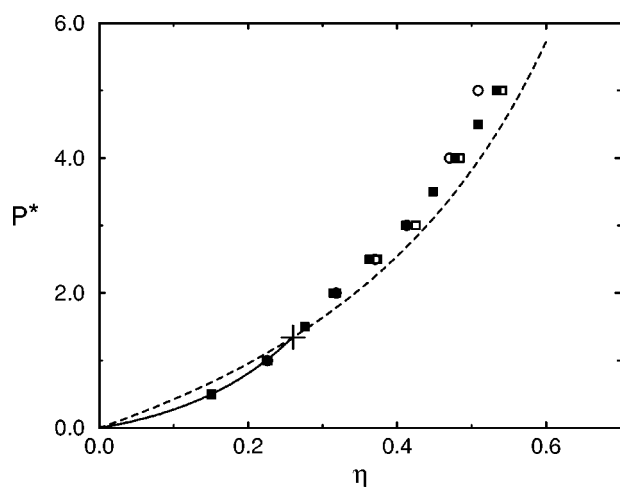


FIG. 2. The equation of state of the polydisperse system. The solid line is the PY prediction, which can not be extended beyond the cross. The circles correspond to a system initially prepared monodisperse, while the squares are final values in which we initially started with one big particle. The solid squares and the open symbols are from a 512 and 1000 particle system, respectively. The dashed line is the upper bound (26) for the pressure.

TABLE I. Equation of state of polydisperse hard spheres, obtained from MC simulations with 1000 particles. The estimated error in the last digit of the packing fraction η is indicated in parentheses.

η	P^*
0.0052(3)	0.01
0.244(1)	1.00
0.314(3)	2.00
0.374(2)	2.50
0.425(4)	3.00
0.484(2)	4.00
0.541(3)	5.00

spheres, surrounded by a sea of small particles containing the remaining volume. In the 512 particle system, only one or two big particles remain for the lower pressures ($P^* = 2.5$ and $P^* = 3.0$). For higher pressures the number of big particles can stabilize at higher values as well. For the 1000 particle system the maximum number of big particles observed at the lower pressures is three. In addition, the size of these big particles is not the same. It is not clear whether this suggests a further possible fractionation or that it is a consequence of the slow equilibration and that one or more of the big particles are still shrinking.

Below, we discuss these simulation results in the context of the relevant theoretical predictions, but first let us stop to make certain considerations on the ideal entropy associated with this system.

III. IDEAL ENTROPY OF A POLYDISPERSE SYSTEM

Strictly speaking, the ideal entropy of a polydisperse system is infinite.¹ In a multicomponent system such an entropy is exactly given by

$$-Nk_B \sum_i w_i \ln(\Lambda_i^3 \rho w_i), \quad (1)$$

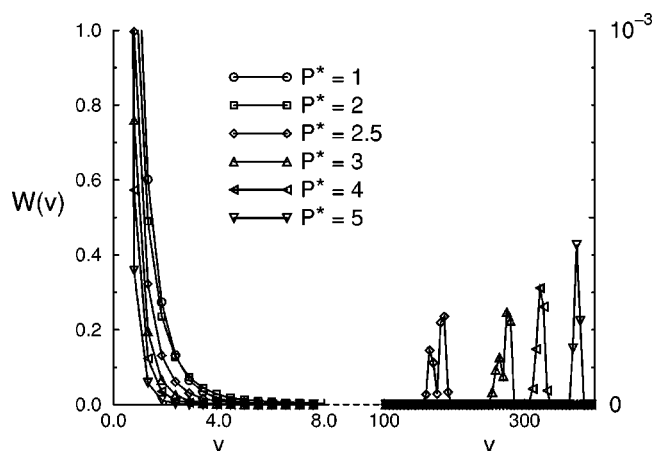


FIG. 3. The Monte Carlo results for the distribution of particle volumes, $W(v)$, as a function of v , for several reduced pressures for a 1000 particle system. For $P^* > 2.0$ the distribution develops a second peak (with statistical noise) at much larger volumes (note the change in scale on the right-hand side of the figure). Although there are only one or several of these big particles, they can contribute over 30% of the total volume of all particles. The diameters can get larger than a third of the length of the simulation box.

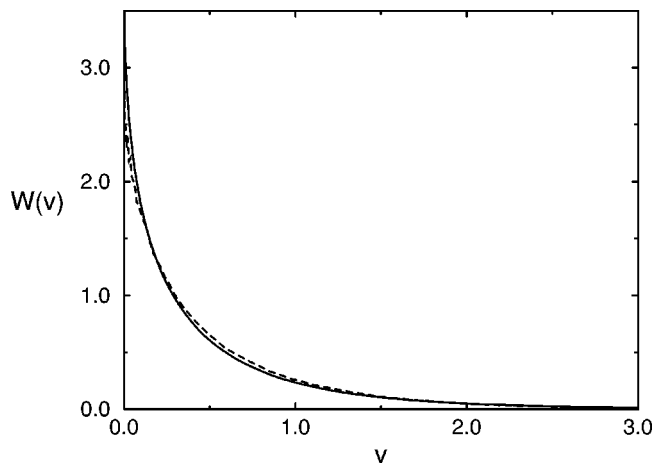


FIG. 4. Comparison of the numerical results (dashed line) for the particle-size distribution $W(v)$, with the corresponding prediction of the PY theory (solid line). These results were obtained at a relatively low pressure ($P^* = 0.5$), which corresponds to a volume fraction $\eta = 0.151$. Note that at this density, simulation and theory are in quite good agreement.

where w_i is the molar fraction of species i and Λ_i its thermal wavelength. The usual path towards the entropy of a polydisperse system¹ (or for that matter, towards the entropy of continuous signals in Information Theory³) is to classify the species into “boxes” according to a certain property which distinguishes them (diameter, volume, molecular weight, etc.). If x denotes such a property species i will denote the box having particles with x between $i\Delta x$ and $(i+1)\Delta x$, for a given Δx which defines the boxes. If $W(x)$ denotes the probability density of a particle having the value x for that property, then $w_i = W(x_i)\Delta x$ where x_i is a typical value of the i th box. Then Eq. (1) adopts the form

$$-Nk_B \sum_i W(x_i)\Delta x \ln(\Lambda_i^3 \rho W(x_i)/\Delta x). \quad (2)$$

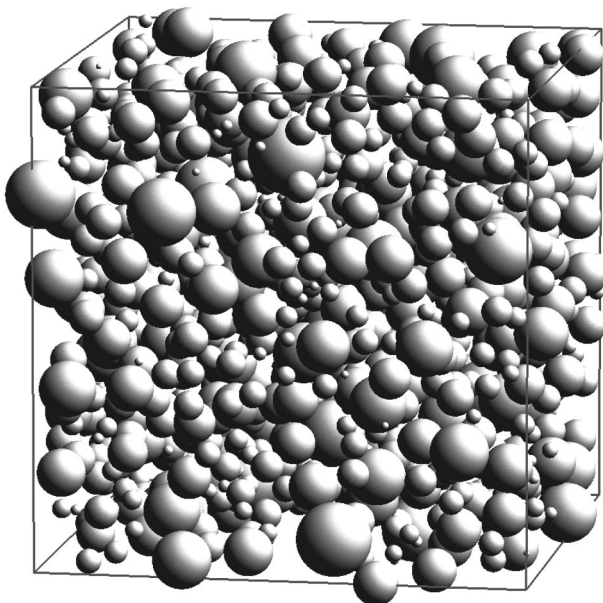


FIG. 5. Snapshot of a typical configuration at reduced pressure $P^* = 1.0$ and volume fraction $\eta = 0.244$.

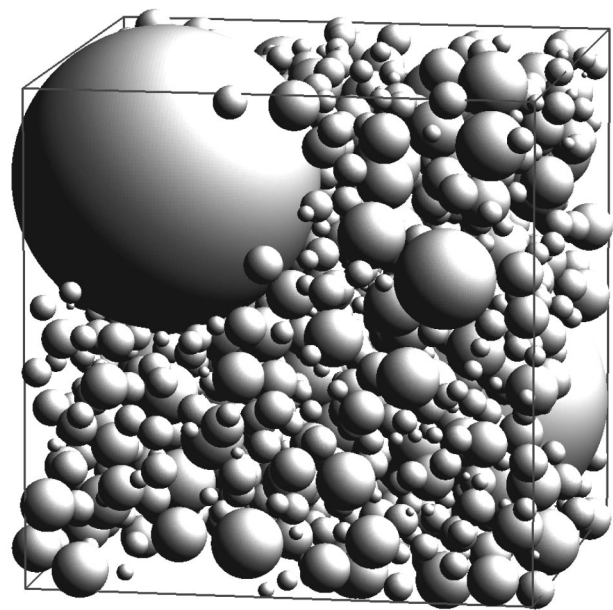


FIG. 6. Snapshot of a typical configuration at reduced pressure $P^* = 3.0$ and volume fraction $\eta = 0.425$. In this case there are two big particles.

The entropy of the polydisperse system is obtained from Eq. (2) taking the limit $\Delta \rightarrow 0$, and we can clearly see that, besides obtaining the usual expression^{1,3}

$$S_{\text{poly}} = -NK_B \int dx W(x) \ln[\Lambda(x)^3 W(x)], \quad (3)$$

there is also a divergent $-\ln \Delta x$, which is simply taken as a “constant” ignorable term.

But expression (3) is not well defined. Suppose we simply change coordinates to label the species from x to y (say, from the diameter to the volume). Then the probability density in the new variable will be $\tilde{W}(y) = W(x)|dx/dy|$. It is straightforward to show that in the new labeling the entropy becomes

$$S_{\text{poly}} = -NK_B \int dy \tilde{W}(y) \ln[\Lambda(x(y))^3 \tilde{W}(y)] \\ + Nk_B \int dy \tilde{W}(y) \ln \left| \frac{dy}{dx} \right|, \quad (4)$$

which is different of what we would have obtained had we began with the labeling y .

This is a well known fact in Information Theory.³ In the study of fluid equilibria of *quenched* polydisperse systems this fact turns out to be irrelevant because the new term simply adds the same constant to both sides of the equilibrium equations.⁴ However when studying *annealed* polydispersity this results tells us that the labeling is crucial and has to be dictated by the physical process underlying the polydispersity. In our case the Monte Carlo movements described in Sec. II are a large scale description of a hypothetical microscopic system of tiny particles of exactly the same size distributed among N aggregates of a variable number of particles. The constant volume constraint would correspond to the conservation of the number of tiny particles, and the natural labeling of the aggregates would be the number of

tiny particles which form it. As this number is proportional to the volume of the aggregate, in the continuum description is the volume, instead of the diameter, what turns out to be the natural labeling.

Notice that we could have described another model in which the tiny particles aggregated into spherical surfaces. In that case it would be the total surface what would be preserved and the natural labeling of aggregates would be their respective surfaces. As we will discuss in the conclusions, the physics of this model would be completely different.

IV. PERCUS–YEVICK THEORY

The Percus–Yevick equation for an n -component hard-sphere mixture can be solved analytically, to yield the following equation of state:¹

$$\frac{\pi}{6} P^* = \frac{\xi_0}{1-\xi_3} + \frac{3\xi_1\xi_2}{(1-\xi_3)^2} + \frac{3\xi_2^3}{(1-\xi_3)^3}. \quad (5)$$

The j th moment of the particle-size distribution ξ_j is defined as

$$\xi_j = \frac{\pi}{6} \sum_i \rho_i \left(\frac{6v_i}{\pi} \right)^{j/3}, \quad (6)$$

where $\rho_i = N_i/V$, the index i is used to denote the different particle species, and v_i is the volume of the i th species.

Equation (5) is also valid for a continuous size distribution, in which case the sum in Eq. (6) is replaced by an integral. The corresponding expression for the chemical potential of a species with radius R is⁵

$$\begin{aligned} \mu^* = \ln[\rho\Lambda^3 W(v)] - \ln(1-\xi_3) + \frac{6\xi_2 R}{(1-\xi_3)} + \frac{12\xi_1 R^2}{(1-\xi_3)} \\ + \frac{18\xi_2^2 R^2}{(1-\xi_3)^2} + \frac{4\pi}{3} P^* R^3, \end{aligned} \quad (7)$$

where Λ is the de-Broglie thermal wavelength, $\sqrt{h^2/(2\pi mkT)}$, and $W(v)$ is the probability density to find a particle with a volume around $v = (4\pi/3)R^3$. The pressure P^* is given by Eq. (5).

In an (NPT) description, the Gibbs free energy of the system fulfilling the constraints, must be at a minimum. The conservation of the number of particles and of the solid volume fraction, imply that $W(v)$ must be of the form,

$$W(v) = \exp\left\{ \sum_{i=0}^3 \alpha_i R^i \right\}, \quad (8)$$

where

$$\alpha_1 = -\frac{6\xi_2}{1-\xi_3}, \quad (9)$$

$$\alpha_2 = -12 \left[\frac{\xi_1}{1-\xi_3} + \frac{3\xi_2^2}{2(1-\xi_3)^2} \right]. \quad (10)$$

The coefficients α_0 and α_3 are determined by the constraints that the number of particles and the solid volume fraction are fixed. Note that all ξ_i ($i=1,2,3$) are positive. Moreover, ξ_3 is equal to the volume fraction η , and is therefore necessarily

less than one. Hence, α_1 and α_2 are always negative. The last coefficient, α_3 , should be negative or zero, because otherwise the particle-size distribution cannot be normalized. Since α_1 , α_2 and α_3 are always negative the Percus–Yevick equation predicts that $W(v)$ is a monotonically decreasing function of v . This implies that the size-distribution given by Eq. (8) can never be bimodal.

Note that these conclusions also hold for the more accurate equation of state of Mansoori *et al.*⁶ This equation adds an extra term to the pressure given in Eq. (5) depending on ξ_3 . Thus Eq. (7) is the same with the new expression for P , which turns out to be irrelevant because the R^3 term is controlled by the Lagrange multiplier associated with the constraint on the total solid particle volume. In other respect, the analysis for the Mansoori equation-of-state is identical to that for PY.

In practice, we solve Eq. (8) numerically. To this end, we represent $W(v)$ as a histogram. Initially, the value of $W(v)$ in the different bins is assigned an arbitrary non-negative value, compatible with the constraint that $W(v)$ is normalized and that $\langle v \rangle$ is fixed. We fix the density at the desired value. We determine the optimal $W(v)$ using the following scheme: we select a bin (say i) at random and change the value of $W(v_i)$ by a random amount ΔW , distributed uniformly in the interval $[-\Delta W_{\max}, \Delta W_{\max}]$. We first check if the new value $W(v_i)$ is non-negative. If it is, we satisfy the constraints by scaling the width of all bins and the height of the function by two appropriately chosen factors. We then compute all moments ξ_j , the pressure and the free energy, and we check if the Helmholtz free energy is smaller than the previous one. If it is, we accept the new value for $W(v_i)$, otherwise we reject it. We repeat the procedure until the free energy no longer decreases. We have verified that $W(v)$ is indeed of the form given by Eqs. (8)–(10). Figure 4 shows a comparison of the PY estimate for $W(v)$, determined in this way, with the results of the full Monte Carlo simulations. We find that α_3 is a monotonically increasing function of density. A comparison between simulation and PY theory for the equation of state is shown in Fig. 2. Note that, in this figure, the PY solution terminates at pressure $P_c \approx 1.34$ (the cross in Fig. 2). This is the point where α_3 becomes zero. Beyond this point we can no longer find a solution for $W(v)$ that is of the form given by Eq. (8). In Appendix A, we consider the breakdown of the PY theory in more detail and obtain the packing fraction beyond which the PY approximation breaks down: $\eta_c = 0.260$, the corresponding pressure being $P_c^* = 1.343$. This breakdown of the PY equation at a relatively low density is surprising, as the PY equation works well up to quite high densities for *fixed* particle size distributions.^{7–9} That it breaks down regardless the accuracy of the equation of state can be inferred from the fact that Mansoori *et al.*'s equation of state undergoes exactly the same breakdown, though for slightly different values of η and P . Besides, from the analysis that we have carried out, it can be seen that a similar breakdown will appear for any other theory yielding an equation of state depending only on ξ_i , $i=0,1,2,3$.

V. ANALYTICAL RESULTS

In this section, we derive a theoretical bound for the pressure of the polydisperse system, providing the equation of state at the packing fraction where the size distribution becomes bimodal. To this end, we work in the (NVT) ensemble and take advantage of the extremality of the Helmholtz free energy under the constraints of constant N and η ; the “grand potential”

$$\mathcal{R} = \mathcal{F}\{W\} - \mathcal{L}_0 \int W(v) dv - \mathcal{L}_1 \int v W(v) dv, \quad (11)$$

where \mathcal{L}_0 and \mathcal{L}_1 are Lagrange multipliers, has to be minimum for the optimal size distribution. In the above relation, the free energy functional \mathcal{F} can be cast into the usual ideal and excess contributions

$$\begin{aligned} \mathcal{F}\{W\} = & Nk_B T \int dv W(v) [\ln(\Lambda^3 \rho W(v)) - 1] \\ & + \mathcal{F}_{\text{excess}}\{W\}. \end{aligned} \quad (12)$$

We attempt the following change in the system: the volume of a given particle v_0 is increased by an amount δv_0 , before a rescaling of all volumes by a factor λ (e.g., $v \rightarrow \lambda v$) such that the overall volume change vanishes. This imposes

$$\lambda = 1 - \frac{\delta v_0}{N\langle v \rangle} + \mathcal{O}([\delta v_0]^2). \quad (13)$$

The effect of the expansion of particle v_0 on the size-distribution can be written

$$\delta W(v) = \frac{1}{N} [\delta(v - v_0 - \delta v_0) - \delta(v - v_0)], \quad (14)$$

where $\delta(\dots)$ denotes the Dirac distribution. The scaling procedure affects W according to

$$\delta W(v) = \frac{1}{\lambda} W\left(\frac{v}{\lambda}\right) - W(v) \quad (15)$$

$$= \frac{\delta v_0}{N\langle v \rangle} \frac{d[vW]}{dv} + \mathcal{O}([\delta v_0]^2). \quad (16)$$

The corresponding variation of the ideal contribution to \mathcal{F} reads

$$\delta \mathcal{F}_{\text{id}} = \int dv \frac{\delta \mathcal{F}_{\text{id}}\{W\}}{\delta W(v)} \delta W(v), \quad (17)$$

with the functional derivative

$$\frac{\delta \mathcal{F}_{\text{id}}\{W\}}{\delta W(v)} = Nk_B T \ln[\Lambda^3 W(v)]. \quad (18)$$

We then get the entropic term

$$\begin{aligned} \delta \mathcal{F}_{\text{id}} = & k_B T \int dv \ln[\Lambda^3 W] \\ & \times \left[\delta(v - v_0 - \delta v_0) - \delta(v - v_0) + \frac{\delta v_0}{\langle v \rangle} \frac{d[vW]}{dv} \right] \end{aligned} \quad (19)$$

$$= k_B T \left\{ \frac{W'(v_0)}{W(v_0)} + \frac{1}{\langle v \rangle} \right\} \delta v_0, \quad (20)$$

where W' is the derivative of W .

The variation of the excess free energy reduces to the reversible work needed to perform the transformation, and is derived in Appendix B,

$$\frac{\delta W_{\text{rev}}}{\delta v_0} = \rho k_B T \int dv W(v) g\left(\frac{\sigma_0 + \sigma}{2}\right) \left(1 + \frac{\sigma}{\sigma_0}\right)^2 - \frac{P_{\text{excess}}}{\eta}, \quad (21)$$

where $g(\sigma_0/2 + \sigma/2)$ denotes the radial distribution function evaluated at contact between species of diameters σ_0 (having volume v_0) and σ (having volume v). When $\sigma_0 \gg \langle \sigma \rangle$, we can replace the density at the surface of particle v_0 by that at a planar wall, and Eq. (21) becomes

$$\delta W_{\text{rev}} = \left[P - \frac{P_{\text{excess}}}{\eta} \right] \delta v_0. \quad (22)$$

In this limit $v_0 \gg \langle v \rangle$

$$\frac{\delta \mathcal{R}}{\delta v_0} = \frac{\delta \mathcal{F}}{\delta v_0} = k_B T \left\{ \frac{W'(v_0)}{W(v_0)} + \frac{1}{\langle v \rangle} \right\} + P - \frac{P_{\text{excess}}}{\eta}. \quad (23)$$

For the optimal size distribution, $\delta \mathcal{F}$ vanishes so that

$$k_B T \frac{W'(v_0)}{W(v_0)} + \frac{1 - \eta}{\eta} \left[\frac{2\rho k_B T}{1 - \eta} - P \right] = 0. \quad (24)$$

Assuming $W(v)$ to be a normalizable distribution, $W'(v)$ has to be negative for large arguments, which sets the upper bound,

$$P < 2 \frac{\rho k_B T}{1 - \eta} \quad \text{or} \quad P^* < \frac{12\eta}{\pi(1 - \eta)} \quad (25)$$

for the rescaled pressure. For low packing fractions ($\eta < \eta_c$) where the PY solution is available, the above inequality is fulfilled (Fig. 2). At the threshold $\eta = \eta_c$ where the second polydispersity peak appears, W' changes sign which means

$$P_c^* = \frac{12\eta_c}{\pi(1 - \eta_c)}. \quad (26)$$

The above relation is remarkably well obeyed within the PY approximation [see the data of Sec. IV or Fig. 2; the PY expression crosses the line given by Eq. (25) exactly at η_c]. For $\eta > \eta_c$, the upper bound is violated by the simulation results reported in Table I and Fig. 2. However, the data suggest non-negligible finite-size effects; increasing N shifts the pressure closer to the theoretical bound. Besides, starting from bidisperse initial conditions (cf. the procedure described in Sec. II), supposed to be closer to the expected polydispersity, has the same effect. According to expressions (23) and (24), the violation of Eq. (25) means that $\delta \mathcal{R} = \delta \mathcal{F} < 0$ for $\delta v_0 > 0$, so that the biggest particle tends to expand. Its growth is however necessarily limited by the length L of the simulation box. This is supported by the observation that, even for the largest system investigated ($N = 10^3$ particles), the size of the biggest particle obtained is determined by L ($\sigma_{\text{biggest}} > L/3$, irrespective of the packing

fraction, see, for example, Fig. 6). This suggests that system sizes that would presumably allow the system to reach thermodynamic equilibrium [and fulfill inequality (25)] are numerically out of reach. Consequently, the question of the extensivity/intensivity of the number of large particles cannot be addressed by simulations; a theoretical investigation seems to require the detailed knowledge of the interfacial free energy between “large” and “small” species. At this stage, we cannot tell whether a true phase transition is associated with the occurrence of the second peak in the particle-size distribution. The available data certainly do not rule out this possibility.

Finally, the integration of Eq. (24) yields the tail of the optimal size-distribution

$$\ln W(v) \propto -v/\langle v \rangle \text{ for } v \gg \langle v \rangle. \quad (27)$$

Equation (8) obeys this relation, which cannot be tested against simulation results because of the lack of statistics for very large particles (not more than 5 in a typical run).

VI. CONCLUSION

At this stage, we can only speculate what will happen at larger N and/or larger densities. Conceivably, once the volume-fraction of the large particles exceeds a certain threshold, proliferation of still larger particles can occur, and so on, until eventually an “Appolonian” packing of the liquid is achieved. The theoretical analysis of this scenario is nontrivial, as the small particles now induce attractive depletion forces between the large particles. Unfortunately, the systems that we can conveniently study by simulation are too small to allow us to investigate this regime.

We stress that the specific model we have chosen to study is somewhat arbitrary. For instance, rather than fixing the number of particles, one might have chosen to fix the total surface area of the particles. The latter constraint would be logical if one aims to model the size distribution of droplets covered with a fixed amount of surfactant. In addition, we assume that the surface free energy of the spheres is negligible. Again, this constraint can be removed. We hope that the rather surprising results of the present study will stimulate research into these related models.

ACKNOWLEDGMENTS

We thank Bela Mulder for critical discussions. The work of the FOM Institute is part of the research program of FOM and is made possible by financial support from the Netherlands Organization for Scientific Research (NWO). Junfang Zhang acknowledges financial support from the Chinese government. José Cuesta participated in this work during a stay at AMOLF financed by Project No. PR95-558 from the Dirección General de Enseñanza Superior (DGES). His work is also part of the DGES Project No. PB96-0119. He also wants to thank the hospitality found at AMOLF, especially from Daan Frenkel’s and Bela Mulder’s groups.

APPENDIX A:

Let us consider the range of densities where a solution of the Percus–Yevick equation is possible. As stated in Sec. IV,

it is essential that α_3 be nonpositive. Hence, the pressure at which $\alpha_3=0$ defines the end point of the theory. To locate this point, consider the form of the solution at the point where $\alpha_3=0$. Then the distribution function reduces to

$$W(v) = \exp\left\{ \sum_{i=0}^2 \alpha_i R^i \right\},$$

where R hereafter denotes a reduced radius measured in units of $\langle \sigma^3 \rangle^{1/3}$. Using the two constraints for normalization and for the average volume of the particles, we can express the coefficients α_0 and α_2 in terms of α_1 . If we combine Eqs. (9) and (10) to eliminate ξ_3 , we obtain

$$\begin{aligned} \alpha_2 &= 2\alpha_1 \frac{\xi_1}{\xi_2} - \frac{1}{2} \alpha_1^2 \\ &= \alpha_1 \frac{\langle R \rangle}{\langle R^2 \rangle} - \frac{1}{2} \alpha_1^2, \end{aligned} \quad (A1)$$

where the ratio of the moments ξ_1/ξ_2 does not depend explicitly on the density ρ or on α_0 , but it only depends on α_1 itself. In the second line we have used the definition

$$\langle R^i \rangle = \int_0^\infty R^i W(v) 4\pi R^2 dR. \quad (A2)$$

But we have another relation between the moments of the particle-size distribution; partial integration of $\int R^n W(v) dv$ yields

$$\begin{aligned} [R^{n+1}W(v)]_0^\infty &= \int_0^\infty (2\alpha_2 R^{n+2} + \alpha_1 R^{n+1} \\ &\quad + (n+1)R^n)W(v) dR = 0 \end{aligned} \quad (A3)$$

for $n \geq 0$. This leads to the identities

$$\langle R^3 \rangle = \frac{-\alpha_1}{2\alpha_2} \langle R^2 \rangle - \frac{4}{2\alpha_2} \langle R \rangle, \quad (A4)$$

$$\langle R^2 \rangle = \frac{-\alpha_1}{2\alpha_2} \langle R \rangle - \frac{3}{2\alpha_2} \langle R^0 \rangle. \quad (A5)$$

This allows us to write $\langle R \rangle$ and $\langle R^2 \rangle$ as a function of α_1 , α_2 , $\langle R^0 \rangle$ and $\langle R^3 \rangle$; i.e.,

$$\langle R \rangle = \frac{-3\alpha_1 \langle R^0 \rangle + 4\alpha_2^2 \langle R^3 \rangle}{\alpha_1^2 - 8\alpha_2}, \quad (A6)$$

$$\langle R^2 \rangle = \frac{12\langle R^0 \rangle - 2\alpha_1 \alpha_2 \langle R^3 \rangle}{\alpha_1^2 - 8\alpha_2}. \quad (A7)$$

But $\langle R^0 \rangle = 1$ and $\langle R^3 \rangle = 1/8$; hence

$$\frac{\langle R \rangle}{\langle R^2 \rangle} = \frac{-3\alpha_1 + (\frac{1}{2})\alpha_2^2}{12 - (\frac{1}{4})\alpha_1\alpha_2}. \quad (A8)$$

Substituting this expression in Eq. (A1), we can eliminate $\langle R \rangle/\langle R^2 \rangle$ to obtain

$$\alpha_2 + \frac{1}{2} \alpha_1^2 = \alpha_1 \frac{-3\alpha_1 + (1/2)\alpha_2^2}{12 - (1/4)\alpha_1\alpha_2}. \quad (A9)$$

For what follows, it is convenient to introduce two new variables f and c ,

$$\alpha_1 = -fc, \quad (\text{A10})$$

$$\alpha_2 = -f^2;$$

then

$$\langle R^i \rangle = \frac{1}{f^{i+3}} \langle R^i \rangle_{f=1}. \quad (\text{A11})$$

We can use this relation to express f as function of c . We use the fact that the average volume per particle is fixed, to rewrite

$$\frac{\langle R^3 \rangle}{\langle R^0 \rangle} = \frac{1}{8} = \frac{1}{f^3} \frac{\langle R^3 \rangle_{f=1}(c)}{\langle R^0 \rangle_{f=1}(c)} \equiv \frac{1}{f^3} Y(c), \quad (\text{A12})$$

where the second line defines the function $Y(c)$. Hence

$$f = 2Y^{1/3}(c). \quad (\text{A13})$$

As $Y(c)$ can be expressed explicitly in terms of error functions, we now know f as a function of c . Equation (A10) allows us to express both α_1 and α_2 as explicit functions of c . We can then use Eq. (A9) to determine c numerically. We find that this equation has a unique solution. Once the value of c has been determined, we know α_1, α_2 and α_0 (from the normalization condition). Equation (9) finally yields the packing fraction beyond which the PY approximation breaks down, $\eta_c = 0.260198$. The corresponding pressure is $P_c^* = 1.343442$.

APPENDIX B:

We first note that the reversible work done by an operator rescaling both particle volumes ($v_i \rightarrow \lambda v_i, \forall i$) and container volume ($V \rightarrow V' = \lambda V$), is

$$\delta W_1 = -P_{\text{ideal}} \delta V = -\rho k_B T \delta V, \quad \text{where } \delta V = (\lambda - 1)V. \quad (\text{B1})$$

In the transformation, the total volume V_p of the particles changes according to

$$\frac{\delta V_p}{V_p} = \frac{\delta V}{V} \Rightarrow \delta V_p = \eta \delta V. \quad (\text{B2})$$

Keeping the particle volumes fixed and going back to the original container volume ($V' \rightarrow V'/\lambda$) requires the reversible work

$$\delta W_2 = -P(V - V') = P \delta V. \quad (\text{B3})$$

It is then straightforward to obtain the work associated with a rescaling of particle volumes at constant accessible volume V ,

$$\delta W_{v \rightarrow \lambda v} = \delta W_1 + \delta W_2 = \frac{P_{\text{excess}}}{\eta} \delta V_p, \quad (\text{B4})$$

valid for all polydispersities $W(v)$.

In the remainder, they shall derive the work needed to grow a particle v_0 by an amount δv_0 ($\delta v_0 = \pi \sigma_0^2 \delta \sigma_0 / 2$). We assume the normalization $\int W dv = 1$ to hold. Consider species having volumes between v and $v + \delta v$ (diameters be-

tween σ and $\sigma + \delta \sigma$). They exert a pressure $\rho k_B T W(v) dv g(\sigma_0/2 + \sigma/2)$ on particle v_0 , involving the radial distribution function at contact between species σ_0 and σ . For the above pair (σ_0, σ) , the excluded volume sphere has diameter $\sigma_0 + \sigma$, and sweeps a volume

$$\delta V_{\text{sweep}} = \pi (\sigma_0 + \sigma)^2 \frac{\delta \sigma_0}{2} = \left(1 + \frac{\sigma}{\sigma_0}\right)^2 \delta v_0 \quad (\text{B5})$$

during the growth of particle v_0 . Summing over all species v , the work performed by the operator takes the form

$$\delta W_{\text{growth } v_0} = \rho k_B T \delta v_0 \int dv W(v) g\left(\frac{\sigma_0 + \sigma}{2}\right) \left(1 + \frac{\sigma}{\sigma_0}\right)^2. \quad (\text{B6})$$

For the size modification considered in Sec. V, the global volume change of the particles vanishes, such that $\delta V_p + \delta v_0 = 0$. Summing the contributions arising from Eqs. (B4) and (B6), the results of Eq. (21) is recovered,

$$\frac{\delta W_{\text{rev}}}{\delta v_0} = \rho k_B T \int dv W(v) g\left(\frac{\sigma_0 + \sigma}{2}\right) \left(1 + \frac{\sigma}{\sigma_0}\right)^2 - \frac{P_{\text{excess}}}{\eta}. \quad (\text{B7})$$

Note that a similar argument can be invoked to compute the reversible work needed to rescale all particle diameters, at constant V . After integration of Eq. (B6) over all $W(v_0) dv_0$, we obtain

$$\begin{aligned} \delta W_{v \rightarrow \lambda v} &= \rho k_B T \int dv dv' W(v) W(v') g\left(\frac{\sigma + \sigma'}{2}\right) \\ &\quad \times (\sigma + \sigma')^2 \sigma \frac{\delta V_p}{\langle \sigma \rangle^3}. \end{aligned} \quad (\text{B8})$$

Inserting this result into Eq. (B4) provides the equation of state for a polydisperse fluid of hard spheres

$$\begin{aligned} \frac{P}{\rho k_B T} &= 1 + \eta \int dv dv' W(v) W(v') g\left(\frac{\sigma + \sigma'}{2}\right) \\ &\quad \times (\sigma + \sigma')^2 \frac{\sigma}{\langle \sigma \rangle^3}. \end{aligned} \quad (\text{B9})$$

For a monodisperse fluid, $W(v) = \delta(v - v_0)$ and we recover the well known relation

$$\frac{P}{\rho k_B T} = 1 + 4 \eta g(\sigma_0). \quad (\text{B10})$$

¹J. J. Salacuse and G. Stell, J. Chem. Phys. **77**, 3714 (1982).

²D. Frenkel and B. Smit, *Understanding Molecular Simulation: From Algorithms to Applications* (Academic, San Diego, 1996).

³F. M. Reza, *An Introduction to Information Theory* (Dover, New York, 1994).

⁴J. A. Gualtieri, J. M. Kincaid, and G. Morrison, J. Chem. Phys. **77**, 521 (1982).

⁵R. J. Baxter, J. Chem. Phys. **52**, 4559 (1970).

⁶G. A. Mansoori, N. F. Carnahan, K. E. Starling, and T. W. Leland, Jr., J. Chem. Phys. **54**, 1523 (1971).

⁷G. Jackson, J. S. Rowlinson, and F. van Swol, J. Phys. Chem. **91**, 4907 (1987).

⁸D. Frenkel, R. J. Vos, C. G. de Kruif, and A. Vrij, J. Chem. Phys. **84**, 4625 (1986).

⁹W. G. T. Kranendonk and D. Frenkel, Mol. Phys. **72**, 715 (1991).

Chapitre C

Renormalisation de charge pour les colloïdes en suspension

Simple Approach for Charge Renormalization in Highly Charged Macroions

Emmanuel Trizac,¹ Lydéric Bocquet,² and Miguel Aubouy³

¹Laboratoire de Physique Théorique, UMR CNRS 8627, Bâtiment 210, Université Paris-Sud, 91405 Orsay Cedex, France

²Laboratoire de Physique de l'E.N.S. de Lyon, UMR CNRS 5672, 46 Allée d'Italie, 69364 Lyon Cedex, France

³S.I.3M., D.R.F.M.C., UMR CNRS 5819, CEA-DSM Grenoble, 17 rue des Martyrs, 38054 Grenoble Cedex 9, France

(Received 28 January 2002; published 20 November 2002)

We revisit the notion of renormalized charge, which is a concept of central importance in the field of highly charged colloidal or polyelectrolyte solutions. Working at the level of a linear Debye–Hückel-like theory only, we propose a versatile method to predict the saturated amount of charge renormalization, which is, however, a nonlinear effect arising at strong electrostatic coupling. The results are successfully tested against nonlinear Poisson-Boltzmann theory for polyions of various shapes (planar, cylindrical, and spherical), both in the infinite dilution limit or in confined geometry, with or without added electrolyte. Our approach, accurate for monovalent microions in solvents such as water, is finally confronted against experimental results on charged colloids and *B*-DNA solutions.

DOI: 10.1103/PhysRevLett.89.248301

PACS numbers: 82.70.Dd, 61.20.Gy, 64.70.–p

Our present understanding of charged macroion suspensions is essentially based on the DLVO theory, named after Derjaguin, Landau, Verwey, and Overbeek [1]. This approach relies on a Poisson-Boltzmann (PB) mean-field description of the microion clouds. An important prediction of the theory is the effective interaction pair potential between two macroions (e.g., colloids) in the solvent which, within a linearization approximation, takes the well-known Yukawa or Debye-Hückel (DH) form: $v(r) \sim Z^2 \exp(-\kappa r)/r$, where Z is the charge of the object and κ denotes the inverse Debye screening length. However, this approach becomes inadequate to describe highly charged objects for which the electrostatic energy of a microion near the macroion surface largely exceeds $k_B T$, the thermal energy, and the linearization of PB equations is *a priori* not justified. In this case, however, the electrostatic potential in exact [2] or mean-field [3–5] theories still takes a Debye-Hückel form far from the charged bodies, provided that the source of the potential is renormalized ($Z \rightarrow Z_{\text{eff}}$). The essential idea is that the microions which suffer a high electrostatic coupling with the macroion accumulate in its immediate vicinity so that the decorated object (macroion *plus* captive counterions) may be considered as a single entity which carries an effective charge Z_{eff} , much lower (in absolute value) than the structural one. Within PB theory, Z and Z_{eff} coincide for low values of the structural charge, but Z_{eff} eventually reaches a saturation value Z_{sat} independent of Z when the bare charge increases [5,6].

Of course, the difficulty remains to predict Z_{sat} for a given suspension of macroions [4–7]. In the absence of any general analytical framework for the computation of the effective charge, this quantity is often considered as an adjustable parameter to fit experimental data [8,9]. In this Letter, we show that a simple physical argument, at the level of the DH linearized description only, yields explicit (and in some favorable cases analytical) expressions for the effective charges at saturation, which com-

pare well with both numerical solutions of nonlinear PB theory and available experimental data with monovalent microions.

For simplicity, we start by considering a unique highly (positively) charged sphere immersed in a symmetric 1:1 electrolyte of bulk ionic strength $I_0 = \kappa^2/8\pi\ell_B$, where $\ell_B = e^2/4\pi\epsilon k_B T$ is the Bjerrum length (ϵ being the dielectric constant of the solvent): $\ell_B = 7 \text{ \AA}$ for water at room temperature. Within PB theory, the dimensionless electrostatic potential $\Phi = eV/k_B T$ obeys the relation

$$\nabla^2 \Phi = \kappa^2 \sinh \Phi. \quad (1)$$

Far from macroion (where it is understood that Φ vanishes), the solution Φ_{PB} of Eq. (1) also obeys the linearized Poisson-Boltzmann (LPB) equation $\nabla^2 \Phi = \kappa^2 \Phi$, and therefore takes the Yukawa form $\Phi_{\text{LPB}} = Z_{\text{eff}} \ell_B \exp[\kappa(a-r)]/[r(1+\kappa a)]$, with a the radius of the sphere. Z_{eff} (in e units) is consequently defined here without ambiguity from the far field behavior of Φ_{PB} (see [4,10,11] for alternative definitions of effective charges). Accordingly, a “nonlinear” region may be defined ($r \in [a, r^*]$), corresponding to Φ_{PB} larger than unity, where by definition of the cutoff r^* , $\Phi_{\text{LPB}}(r^*)$ is of order 1. In the limit of large κa , this nonlinear region is, however, confined to the immediate vicinity of the macroion: $r^* \simeq a$. We consequently have the effective boundary condition $\Phi_{\text{LPB}}(a) \simeq \Phi_{\text{PB}}(r^*) = C$, where C is a constant of order 1, which yields immediately $Z_{\text{eff}} = Ca(1 + \kappa a)/\ell_B$. This argument assumes that the bare charge Z is high enough to have Φ_{PB} larger than unity close to the macroion and, therefore, provides the saturation value of Z_{eff} , denoted hereafter as Z_{sat} [12]. We therefore easily obtain the nontrivial dependence of this quantity upon physicochemical parameters.

This picture of a decorated macroion—where the “bound” counterions renormalizing the charge appear to have an electrostatic energy eV_0 balancing the thermal

energy $k_B T$ —may be rationalized as follows. In the limit of large κa , we perform an asymptotic matching of the nonlinear PB planar solution (see [1]) to the linear solution Φ_{LPB} in curved geometry. We obtain for high bare charges the same value of the contact potential $\Phi_{\text{LPB}}(a) = 4$ (of order 1 as expected) so that $Z_{\text{sat}} = 4a(1 + \kappa a)/\ell_B$ [13]. Such a procedure provides by construction the correct large κa (low curvature) behavior of Z_{sat} , but we show below that it remains fairly accurate down to κa of order 1.

Generalizing this approach, we consequently obtain the leading curvature saturated effective charge from the following analysis. For an isolated macroion of arbitrary shape in an electrolyte: (a) find the electrostatic potential, Φ_{LPB} , solution of the *linearized* PB equations, supplemented by a *fixed potential boundary condition*: $\Phi_{\text{LPB}}(\text{surface}) = C$, where $C = 4$ at leading order in curvature; (b) deduce Z_{sat} from Gauss theorem at the surface of the object. In the case of an infinite cylinder (radius a , bare line charge λ), we obtain $\lambda_{\text{sat}} = 2(\kappa a/\ell_B)K_1(\kappa a)/K_0(\kappa a)$, where K_0 and K_1 are the modified Bessel functions of orders 0 and 1.

In order to test the validity of our results, we have numerically solved the nonlinear PB equation (1) for high Z values corresponding to the saturation regime and computed the effective charge from the electrostatic potential at large distances (i.e., the value required to match Φ_{LPB} to the far field Φ_{PB} obtained numerically). Figure 1 compares the resulting PB effective charge to our expressions, for spherical and cylindrical macroions. The agreement becomes excellent at large κa as it should, and in the case of cylinders, even holds down to very small κa (0.01), a point which is not *a priori* expected. Finally, in the planar geometry our approach provides by construction the correct effective charge (compared to PB).

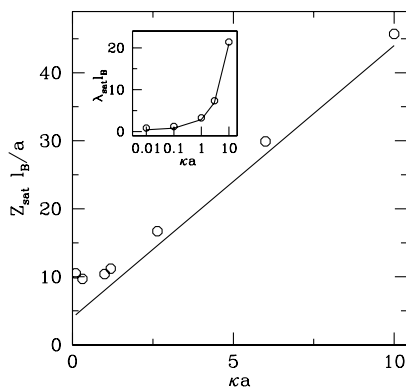


FIG. 1. Effective charge at saturation of an isolated spherical macroion (radius a) as a function of κa . The continuous line is the analytical expression given in the text, while the dots are the results extracted from the far-field behavior of the nonlinear PB potential. In the inset, the same results for the cylinder geometry are shown on a log-linear scale.

For spherical colloids, expressions reminiscent of that reported above can be found in the literature [4,14,15]. It seems, however, that the generality of the underlying method has been overlooked. In particular, our procedure may be extended to the finite concentration case, using the concept of Wigner Seitz (WS) cell [5]: the influence of the other macroions is accounted for by confining the macroion into a cell, with global electroneutrality. The size of the cell, R_{WS} , is computed from the density of macroions, while its geometry is chosen as to mimic the spatial structure of the macroions in the solution. Suppose that the system is in equilibrium with a reservoir of salt defined in terms of its Debye length κ^{-1} . We first linearize Eq. (1) around the value of potential at the cell boundary, $\Phi_R = \Phi(R_{\text{WS}})$, unknown at this point, which yields

$$\nabla^2 \delta\Phi = \kappa_*^2 (\gamma_0 + \delta\Phi), \quad (2)$$

where $\delta\Phi = \Phi - \Phi_R$, $\kappa_*^2 = \kappa^2 \cosh(\Phi_R)$, and $\gamma_0 = \sqrt{1 - (\kappa/\kappa_*)^4}$. Note that the relevant screening length κ_*^{-1} (always smaller than κ^{-1} , a general feature for finite concentration) is not a parameter and should be determined at the end of the calculation. Equation (2) is supplemented by two boundary conditions: the consistency constraint [$\delta\Phi(R_{\text{WS}}) = 0$] and the global electroneutrality (which imposes a vanishing normal electric field at the WS boundary). To generalize the approach discussed in the limit of infinite dilution, we propose the following prescription (providing a third boundary condition): the *difference of potential* between the macroion and the WS surface is $\delta\Phi(a) = 4$. Here again, the effective charge is obtained from Gauss theorem at the macroion's surface.

This generalized procedure is now applied to a solution of spherical macroions with concentration ρ . The radius of the WS spherical cell is given as $R_{\text{WS}} = (4\pi\rho/3)^{-1/3}$. In this geometry, the (LPB) solution of Eq. (2) reads

$$\delta\Phi(r) = \gamma_0 \left[-1 + f_+ \frac{e^{\kappa_* r}}{r} + f_- \frac{e^{-\kappa_* r}}{r} \right], \quad (3)$$

where $f_{\pm} = [(\kappa_* R_{\text{WS}} \pm 1)/2\kappa_*] \exp(\mp \kappa_* R_{\text{WS}})$. Our prescription allows one to compute κ_* , such that $\delta\Phi(a) = 4$. This equation is solved numerically for κ_* using a simple numerical Newton procedure. The effective charge follows from the gradient of $\delta\Phi(r)$ in Eq. (3) taken at $r = a$. The corresponding Z_{sat} as a function of volume fraction $\eta = 4\pi\rho a^3/3$ is displayed in Fig. 2, with a comparison to its counterpart deduced from the numerical solution of PB theory supplemented with the popular procedure proposed by Alexander *et al.* [5]. In this figure, we have also plotted the results obtained without added salt [where the term $\sinh\Phi$ on the right-hand side of Eq. (1) is replaced by $(\exp\Phi)/2$, due to the absence of coions]. Our results are fully compatible with those obtained from Alexander's method, with a similar agreement for

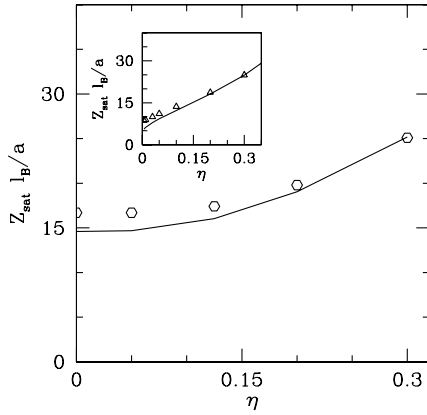


FIG. 2. Effective saturated charge of spherical macroions (radius a) as a function of volume fraction η for $\kappa a = 2.6$. The continuous line shows the effective charge computed using the prescription, while the dots are the results of the nonlinear PB theory, following Ref. [5]. Inset: no-salt situation.

cylindrical macroions (not shown). It is eventually instructive to note that, for a charged plane confined without added salt in a WS slab of width $2h$, Alexander's saturation surface charge may be computed analytically with the result [13] $\sigma_{\text{sat}} = 2^{-3/2} \sinh(\pi/\sqrt{2})/\ell_B h$, whereas we obtain $\sigma_{\text{sat}} = \sqrt{6} \operatorname{argcosh}(5)/\pi \ell_B h$ following our prescription. Both expressions agree within 10% and remarkably exhibit the same functional dependence on ℓ_B and density (through h).

That our prescription compares favorably with Alexander's procedure for the planar, cylindrical, and spherical geometries, calls for the more stringent test of confronting our predictions against experimental data. We consider two specific situations corresponding to two different geometries: crystallization of charged colloidal suspensions and osmotic pressure in B -DNA solutions.

Crystallization of charged spheres.—Investigation into the phase diagram of charged polystyrene colloids has been conducted experimentally by Monovoukas and Gast [8] and compared to the phase diagram of a system where particles interact through a Yukawa potential (deduced from extensive molecular dynamics simulations [16]). However, this comparison requires an *ad hoc* choice for Z_{eff} . We use here the results we found for the effective charge as a function of ionic strength, which we insert into the numerical generic phase diagram of Yukawa systems [16]. We emphasize that there is *no adjustable parameter* in our equations since the radius of the polystyrene beads, the only parameter entering our description, was independently measured to be $a = 667 \text{ \AA}$. We only make the (reasonable) assumption that the bare charge Z of the colloids is large enough to have $Z_{\text{eff}} \approx Z_{\text{sat}}$. The results for the melting line using our prescription for the effective charge are confronted to the experimental data in Fig. 3. We also plot the result for the melting

line for an *ad hoc* constant effective charge, $Z_{\text{eff}} = 880$, as was proposed in Ref. [8] (while in our case the latter varies between 500 and 2000 on the melting curve). The observed agreement of our results illustrates both the pertinence of our prescription for Z_{sat} and the relevance of the PB saturation picture for macroions of large bare charge, for monovalent microions in water.

Osmotic coefficient of B-DNA.—A similar test of our method may be performed for the cylindrical geometry using the experimental results for rigid cylindrical polyelectrolytes such as B -DNA [17]. We specifically consider the measurements of the osmotic coefficient $\phi = \Pi_{\text{osm}}/\Pi_c$, defined as the ratio between the osmotic pressure Π_{osm} to the pressure Π_c of releasable counterions having bare density c_c ($\Pi_c = k_B T c_c$). Within the WS model, B -DNA macroions are confined into cylindrical cells, whose radius R_{WS} is related to the bare concentration of DNA counterions as $c_c = (\ell_{\text{DNA}} \pi R_{\text{WS}}^2)^{-1}$, with $\ell_{\text{DNA}} = 1.7 \text{ \AA}$ the distance between charges along DNA. The osmotic pressure is related to the densities of microions at the cell boundary: $\Pi_{\text{osm}} = k_B T (\rho_+ + \rho_- - 2I_0)$ [18], which can be recast in the form $\Pi_{\text{osm}} = k_B T (\kappa_*^2 - \kappa^2)/4\pi \ell_B$ introducing the screening factor κ_* defined previously. This latter quantity is computed from our prescription, following the same lines as for the spherical case [see Eq. (3)].

In Fig. 4, the corresponding results for the osmotic coefficient are confronted against the experimental data of Ref. [17], showing again a good quantitative agreement. As in Ref. [18], we report the prediction of classical Oosawa-Manning condensation theory, for which the osmotic coefficient is constant [$\phi = \ell_{\text{DNA}}/(2\ell_B)$] at complete variance with the experiments. Again we emphasize that the only quantity introduced in our description is the

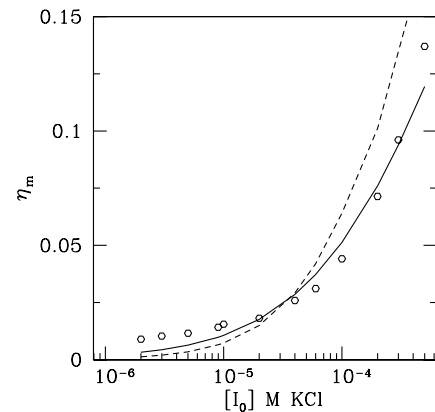


FIG. 3. Liquid-solid transition of charged polystyrene colloids: volume fraction for melting η_m as a function of salt ionic strength I_0 . Dots are experimental points for the melting line extracted from Ref. [8]. The solid line is the theoretical prediction for the melting transition using our prescription for effective charges. The dashed line corresponds to $Z_{\text{eff}} = 880$ (see text).

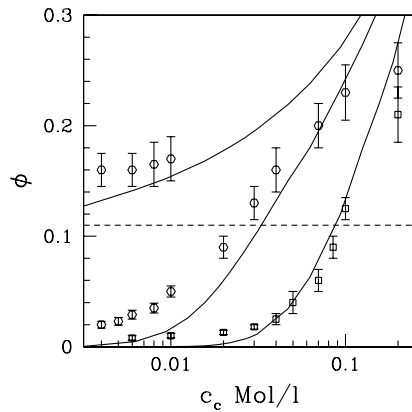


FIG. 4. Osmotic coefficient of *B*-DNA vs density of DNA phosphate ions c_c , for $I_0 = 10, 2,$ and 0 mM (from bottom to top). Dots: experiments of Ref. [17]; solid lines: present prescription; dashed line: prediction of Oosawa-Manning condensation theory.

diameter ($a = 10 \text{ \AA}$) of DNA, known from independent measurements.

In conclusion, we have put forward a simple method of asymptotic matching to compute the effective charge at saturation for isolated macroions. In the situation of finite density, this method has been translated into a prescription, the validity of which has been assessed. This approach (mostly suited to describe the colloidal limit $\kappa a \gg 1$) amounts to considering the highly charged macroions as objects with constant electrostatic potential $\sim 4kT/e$, independently of shape and physicochemical parameters (size, added 1:1 electrolyte...). As a general result, we find that the effective charge is an *increasing* function of κ , which stems from the reduction of the attraction between the counterions and the macroion. Addition of salt consequently brings two antagonist effects on the effective Coulombic interaction between macroions: the range of the interaction decreases due to screening, while the amplitude increases due to the effective charge. The competition between these two effects might be a key point in the understanding of these systems.

An important question concerning our approach is that of the validity of PB theory for highly charged macroions. Within PB, microion correlations are neglected, but the approach may still allow one to describe high macro/microion couplings: in particular, for monovalent microions in water at room temperature, microion correlations are negligible for all known macroions. This may no longer be the case in presence of multivalent microions. More generally, PB is a reasonable approximation when the macroion size a is much larger than ℓ_B [19], and the

saturation plateau of Z_{eff} as a function of the bare charge Z is an important physical phenomenon that our approach allows one to capture. When a becomes of the same order as ℓ_B , the amount of counterion “condensation” found in molecular dynamics or Monte Carlo simulations is larger than predicted by PB [19,20]; our method for Z_{sat} therefore provides an upper bound for the effective charge. It is, moreover, noteworthy that for *B*-DNA where $a/\ell_B \approx 1.4$, our approach still gives a valuable first approximation and that omission of charge renormalization leads to spurious results (such as negative osmotic coefficients corresponding to an unphysical phase transition at physiological salt concentrations).

-
- [1] E. J. W. Verwey and J. T. G. Overbeek, *Theory of the Stability of Lyophobic Colloids* (Elsevier, Amsterdam, 1948).
 - [2] R. Kjellander, in *Electrostatic Effects in Soft Matter and Biology*, edited by C. Holm *et al.* (Kluwer, Dordrecht, 2001).
 - [3] G. S. Manning, *J. Chem. Phys.* **51**, 924 (1969).
 - [4] L. Belloni, *Colloids Surf. A* **140**, 227 (1998).
 - [5] S. Alexander, P. M. Chaikin, P. Grant, G. J. Morales, and P. Pincus, *J. Chem. Phys.* **80**, 5776 (1984).
 - [6] J.-P. Hansen and H. Löwen, *Annu. Rev. Phys. Chem.* **51**, 209 (2000).
 - [7] A. Diehl, M. C. Barbosa, and Y. Levin, *Europhys. Lett.* **53**, 86 (2001).
 - [8] Y. Monovoukas and A. P. Gast, *J. Colloid Interface Sci.* **128**, 533 (1989).
 - [9] M. J. Stevens, M. L. Falk, and M. O. Robbins, *J. Chem. Phys.* **104**, 5209 (1996).
 - [10] M. Deserno, C. Holm, and S. May, *Macromolecules* **33**, 199 (2000).
 - [11] D. B. Lukatsky and S. A. Safran, *Phys. Rev. E* **63**, 011405 (2001).
 - [12] If, on the other hand, Z is low, we have $Z_{\text{eff}} = Z$.
 - [13] L. Bocquet, E. Trizac, and M. Aubouy, *J. Chem. Phys.* **117**, 8138 (2002).
 - [14] J. C. Crocker and D. G. Grier, *Phys. Rev. Lett.* **77**, 1897 (1996).
 - [15] S. H. Behrens and D. G. Grier, *J. Chem. Phys.* **115**, 6716 (2001).
 - [16] M. O. Robbins, K. Kremer, and G. S. Grest, *J. Chem. Phys.* **88**, 3286 (1988).
 - [17] H. E. Auer and Z. Alexandrowicz, *Biopolymers* **8**, 1 (1969); E. Raspaud, M. da Conceicao, and F. Livolant, *Phys. Rev. Lett.* **84**, 2533 (2000).
 - [18] P. L. Hansen, R. Podgornik, and V. A. Parsegian, *Phys. Rev. E* **64**, 021907 (2001).
 - [19] R. D. Groot, *J. Chem. Phys.* **95**, 9191 (1991).
 - [20] M. Deserno and C. Holm, cond-mat/0203599.

Analytical estimation of effective charges at saturation in Poisson–Boltzmann cell models

Emmanuel Trizac¹, Miguel Aubouy² and Lydéric Bocquet³

¹ Laboratoire de Physique Théorique, UMR CNRS 8627, Bâtiment 210, Université Paris-Sud, 91405 Orsay Cedex, France

² SI3M, DRFMC, CEA-DSM Grenoble, 17 rue des Martyrs, 38054 Grenoble Cedex 9, France

³ Département de Physique des Matériaux, UMR CNRS 5586, Université Lyon-I, 43 Bd du 11 Novembre 1918, 69622 Villeurbanne Cedex, France

Received 16 October 2002

Published 16 December 2002

Online at stacks.iop.org/JPhysCM/15/S291

Abstract

We propose a simple approximation scheme for computing the effective charges of highly charged colloids (spherical or cylindrical with infinite length). Within non-linear Poisson–Boltzmann theory, we start from an expression for the effective charge in the infinite-dilution limit which is asymptotically valid for large salt concentrations; this result is then extended to finite colloidal concentration, approximating the salt partitioning effect which relates the salt content in the suspension to that of a dialysing reservoir. This leads to an analytical expression for the effective charge as a function of colloid volume fraction and salt concentration. These results compare favourably with the effective charges *at saturation* (i.e. in the limit of large bare charge) computed numerically following the standard prescription proposed by Alexander *et al* within the cell model.

1. Introduction

In colloidal suspensions, the charge ratio between the poly-ions (colloids) and the counter-ions or salt ions may be larger than 10^4 . This considerable asymmetry invalidates most of standard liquid state theories. The concept of charge renormalization, however, allows one to significantly simplify the description of such systems: the electrostatic coupling between the poly-ions and oppositely charged micro-species induces a strong accumulation (or ‘condensation’) near the poly-ion surface. The idea is then to consider a colloid plus its ‘captive’ micro-ions as an entity carrying an effective (or renormalized) charge Z_{eff} , *a priori* much smaller than the bare charge Z_{bare} . Consequently, except in the immediate vicinity of the colloids where linearization schemes fail, the interactions in the suspension are well described by Debye–Hückel-like linearized theories, provided that the bare charge is replaced by the renormalized one Z_{eff} . Schematically, the linear effects of screening by an electrolyte induce a dressing of the bare Coulomb potential ($Z_{\text{bare}}/r \rightarrow Z_{\text{bare}} \exp(-\kappa r)/r$ where κ^{-1} is the

Debye length; see below), while the non-linear effects of screening imply the identification $Z_{\text{bare}} \exp(-\kappa r)/r \rightarrow Z_{\text{eff}} \exp(-\kappa' r)/r$ (with possibly $\kappa' \neq \kappa$ [1]).

Several reviews discussing the notion of charge renormalization have appeared recently [1–4]. In the colloid science field this concept has been introduced by Alexander *et al* [5] in the context of the Poisson–Boltzmann (PB) cell model, but it had been widely accepted since the 1950s in the field of linear polyelectrolytes [6, 7]. The definition of an effective charge from the far-field potential created by an isolated macro-ion in an electrolyte is unambiguous [2, 8a, 9a], at least for the simple cases of spherical or infinitely long cylindrical macro-ions that we shall consider here, even if the case of less symmetric poly-ions deserves more attention (see e.g. [10]). Within a cell model, introduced to replace the complicated many-body problem of colloids in solution by a simpler one-particle system [11–14], the definition of an effective charge is more elusive, but the celebrated proposal made by Alexander *et al* amounts to finding the optimal linearized PB potential matching the non-linear one at the cell boundary. The cell approach, whose validity has been assessed by several studies [16–21], appears to provide a reasonable description of solutions containing monovalent counter-ions [22–24]. The effective charge is obtained by integrating the charge density deduced from the linearized potential over the region accessible to micro-ions, or equivalently from Gauss’s theorem at the colloid’s surface. Note that a renormalization of Z also implies a renormalization of the screening constant κ . For low poly-ion bare charges Z_{bare} , linearizing the PB equation is a valid approximation, so $Z_{\text{eff}} \simeq Z_{\text{bare}}$ —whereas in the opposite limit of high bare charges, Z_{eff} was found numerically to saturate to a value independent of Z_{bare} : $Z_{\text{eff}} \simeq Z_{\text{sat}}$. The saturation value Z_{sat} depends on the geometry of the colloid, and the temperature or the quantity of added salt. Unfortunately, no analytical prediction is available for these dependences.

In this paper, we propose an approximate analytical expression for the effective charge of spherical or rod-like macro-ions, as a function of macro-ion density or salt content. Our approach starts with an estimation of the saturation value of the effective charge in the infinite-dilution limit, as deduced from recent analytical results [25]. In the case of finite colloidal dilution, the osmotic equilibrium of the suspension with a salt reservoir is modelled using a Donnan equilibrium approximation. This allows us to derive a simple polynomial equation of degree 4 fulfilled by the *saturation value* Z_{sat} of the effective charge Z_{eff} , in the case of a symmetric 1:1 electrolyte. In the limiting case of no added salt, the above equation is easily solved analytically and provides results in quantitative agreement with the saturation effective charges following Alexander’s prescription.

2. General framework and method

We consider first the situation of an isolated macro-ion of given surface charge density in a electrolyte of bulk density n_0 (no confinement). The solvent is considered as a medium of uniform dielectric (CGS) permittivity ϵ . Within PB theory, the electrostatic potential, when assumed to vanish far from the macro-ion, obeys the equation

$$\nabla^2 \phi = \kappa_0^2 \sinh \phi, \quad (1)$$

where the screening factor κ_0 is defined as $\kappa_0^2 = 8\pi \ell_B n_0$ and the Bjerrum length quantifies the strength of electrostatic coupling: $\ell_B = e^2/(\epsilon kT)$ ($e > 0$ denotes the elementary charge and kT is the thermal energy). A complete asymptotic solution of equation (1) has been obtained recently by Shkel *et al* [25] in spherical and cylindrical geometries. From the far-field behaviour of the corresponding solutions, one obtains after some algebra the effective

charges at saturation:

$$Z_{\text{sat}} \frac{\ell_B}{a} = 4\kappa_0 a + 6 + \mathcal{O}\left(\frac{1}{\kappa_0 a}\right) \quad \text{for spheres} \quad (2)$$

$$\lambda_{\text{sat}} \ell_B = 2\kappa_0 a + \frac{3}{2} + \mathcal{O}\left(\frac{1}{\kappa_0 a}\right) \quad \text{for cylinders.} \quad (3)$$

In these equations, a denotes the radius of the macro-ion under consideration, Ze the total charge in the case of spheres, and λe the line charge density in the case of cylinders (with infinite length). Expressions (2) and (3) are the exact expansions of the saturation charges in the limit of large $\kappa_0 a$ but are in practice accurate as soon as $\kappa_0 a > 1$ (not shown).

Our goal is to translate these relations into expressions that would approximate the effective charges in confined geometry, where the macro-ion is enclosed in a cell [5]. To this end, we first find an approximation for the relevant screening factor κ_* before inserting it into (2) and (3), making the substitution $\kappa_* \leftrightarrow \kappa_0$. The implicit assumption is that the mean salt density in the cell is related to the effective charge in a similar manner to in the infinite-dilution limit.

In confined geometry, the PB equation still takes the form (1), where $\kappa_0 = (8\pi \ell_B n_0)^{1/2}$ should now be considered as the inverse screening length in a (neutral) salt reservoir in osmotic equilibrium with the solution, through a membrane permeable to micro-species (n_0 is thus now the salt density in the reservoir). It may be shown that the relevant screening factor in the cell is related to the micro-ion density at the cell boundary [8]:

$$\kappa_*^2 = 4\pi \ell_B [\rho^+(R_{WS}) + \rho^-(R_{WS})]. \quad (4)$$

In this equation R_{WS} is the radius of the Wigner–Seitz (WS) confining cell. We have recently proposed an efficient prescription for computing κ_* without solving the complicated non-linear problem [8]. It is however impossible to deduce an analytical expression for κ_* from this approach and we resort to the following approximation. We assume that the micro-ion densities are slowly varying in the WS cell so that the mean densities n^\pm provide a reasonable estimation of the boundary densities $\rho^\pm(R_{WS})$. We thus write

$$\kappa_*^2 = 4\pi \ell_B (n^+ + n^-) = 4\pi \ell_B (2n^+ + Z_{\text{sat}} \rho), \quad (5)$$

where the last equality follows from the electroneutrality constraint (ρ is the density of colloids, assumed positively charged without loss of generality). Note that at the level of a linear theory, the effective charge Z_{sat} and not the bare one Z_{bare} enters this expression.

We now need to relate the mean densities n^\pm to n_0 , the concentration in the reservoir (the so-called Donnan effect; see e.g. [14, 26]). Chemical equilibrium imposes $\rho^+ \rho^- = n_0^2$ at any point in the cell. We again assume this relation to hold for the mean densities, so that $n^+ n^- = n_0^2$. This leads to

$$\kappa_*^4 = \kappa_0^4 + (4\pi \ell_B Z_{\text{sat}} \rho)^2. \quad (6)$$

Up to now the reasoning has been quite general and independent of the geometry. For spheres with radius a and packing fraction $\eta = 4\pi \rho a^3/3 = (a/R_{WS})^3$, and for rods with packing fraction $\eta = (a/R_{WS})^2$, we obtain

$$(\kappa_* a)^4 = \begin{cases} (\kappa_0 a)^4 + (3\eta Z_{\text{sat}} \ell_B / a)^2 & \text{(spheres)} \\ (\kappa_0 a)^4 + (4\eta \lambda_{\text{sat}} \ell_B)^2 & \text{(cylinders).} \end{cases} \quad (7)$$

Supplementing these equations with the κ -dependence of Z_{sat} obtained in equation (2) for spheres and (3) for cylinders, leads to an equation of degree 4 satisfied by κ_* (or equivalently Z_{sat}).

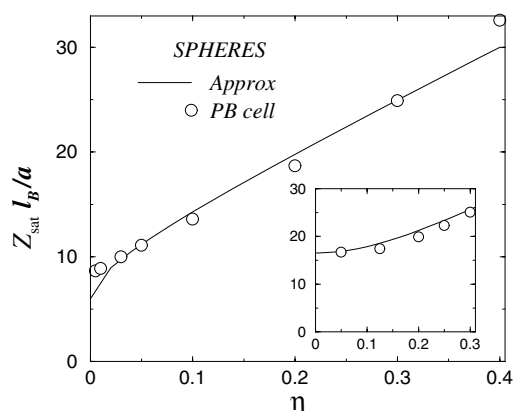


Figure 1. Effective charge at saturation Z_{sat} (in units of the radius over the Bjerrum length ℓ_B) as a function of packing fraction for a spherical macro-ion of radius a enclosed in a concentric spherical cell of radius $a\eta^{-1/3}$. The situation is without added salt. The analytical expression (8) is shown by the continuous curve while the non-linear PB values computed numerically following Alexander *et al* [5] are represented with circles. Inset: the same, but with added salt for $\kappa_0 a = 2.6$.

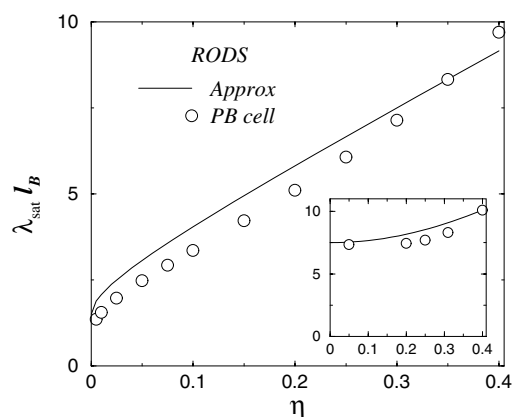


Figure 2. Effective line charge density at saturation λ_{sat} (in units of $1/\ell_B$) as a function of packing fraction for a cylindrical macro-ion of radius a enclosed in a concentric cylindrical cell of radius $a\eta^{-1/2}$ (no added salt). The analytical expression (9) is shown by the continuous curve while the non-linear PB values computed numerically following Alexander *et al* [5] are represented with circles. The inset shows the same quantity, but with added electrolyte ($\kappa_0 a = 3.0$).

This equation can be solved analytically. We give the general solution in the appendix. However, without added salt (formally $\kappa_0 = 0$), the solutions of these equations take a particularly simple form:

$$Z_{\text{sat}} \frac{\ell_B}{a} = 6 + 24\eta + 12\sqrt{2\eta + 4\eta^2} \quad (8)$$

$$\lambda_{\text{sat}} \ell_B = \frac{3}{2} + 8\eta + 2\sqrt{6\eta + 16\eta^2}. \quad (9)$$

We compare in figures 1 and 2 the results obtained following this route with the full PB estimate following Alexander's prescription. The latter involves a numerical resolution of the PB equation. Both the no-salt and the finite-ionic-strength case are considered. The agreement is seen to be quite good in view of the minimum number of ingredients involved in the present approach.

3. Conclusions

In this contribution, we propose a simple approximation scheme for computing the saturation value of the effective charge in concentrated suspensions of highly charged colloidal particles. Our estimation starts with an asymptotic expression of the effective charge in the infinite-dilution limit, obtained from recent analytical results [25]. The case of finite colloidal dilution is described using a Donnan equilibrium approximation for the osmotic equilibrium of the suspension with a salt reservoir. This calculation leads to an analytical estimate of Z_{sat} , the saturation value of the effective charge, as a function of the density of colloids and salt concentration. Our starting points (equations (2) and (3)) neglect contributions of order $(\kappa_0 a)^{-1}$ and become inaccurate for $\kappa a < 1$. This implies that our effective charges at finite density becomes less reliable in the salt-free case for small packing fractions η . However, this is seen to occur for very small η only (see e.g. figure 1).

These results are obtained at the level of the mean-field PB theory. We note however that the existence of a saturation value of the effective charge, Z_{sat} , independent of the bare charge, is indeed confirmed in more refined approaches in the *colloidal limit* $a \gg \ell_B$, with a the colloid size and ℓ_B the Bjerrum length (see e.g. Groot [22], using the primitive model). These results show moreover that PB theory becomes successful in the aforementioned colloidal limit, $a \gg \ell_B$ [20, 22]. Eventually the saturation picture within PB theory becomes in quantitative agreement with experimental data for the osmotic pressure [8, 27, 28].

It is finally instructive to reconsider the results reported by Alexander *et al* [5] in their original paper. At a packing fraction $\eta = 0.125$, they find numerically a saturation value for Z_{eff} of the order of 15, in units of a/ℓ_B (spherical colloid). On the other hand, our expression (8) for the same η gives $Z_{\text{sat}} \ell_B/a = 9 + 3\sqrt{5} \simeq 15.7$, i.e. very close to the value found in [5]. Note that this number, 15, has subsequently been often quoted in the literature as a ‘standard’ value of the effective charge. The saturation value of the effective charge however crucially depends on the colloid volume fraction, and the full density dependence of Z_{sat} should be taken into account in finite-concentration cases.

Acknowledgments

We would like to thank M Deserno and H H von Grünberg for useful discussions.

Appendix. Analytical expression for the effective charge

We give here the explicit expression for the effective charge as a function of the colloid packing fraction η and salt concentration in the reservoir, $n_0 = \kappa_0^2/8\pi\ell_B$.

Inserting equation (2) or (3) into (7), one gets the quartic equation for $X = \kappa_* a$:

$$X^4 = X_0^4 + \eta^2(\alpha + \beta X)^2 \quad (\text{A.1})$$

with $X_0 = \kappa_0 a$. The values for α , β are respectively $\alpha = 12$ and $\beta = 18$ for spheres, and $\alpha = 8$ and $\beta = 6$ for cylinders.

Let us introduce the following quantities:

$$\begin{aligned} \Lambda &= -12X_0^4 - 12\beta^2\eta^2 + \alpha^4\eta^4 \\ \Gamma &= 108\alpha^2\beta^2\eta^4 - 2\alpha^6\eta^6 - 72\alpha^2\eta^2(X_0^4 + \beta^2\eta^2) \\ \Phi &= -72X_0^4\alpha^2\eta^2 + 36\alpha^2\beta^2\eta^4 - 2\alpha^6\eta^6 \\ \Psi &= \frac{1}{3 \cdot 2^{1/3}} \left(\Phi + \sqrt{\Gamma^2 - 4\Lambda^3} \right)^{1/3} \\ \Theta &= \frac{\Lambda}{9\Psi} + \Psi. \end{aligned} \quad (\text{A.2})$$

The solution $X = \kappa_* a$ is then found as

$$\kappa_* a = \frac{1}{2} \sqrt{\frac{2\alpha^2 \eta^2}{3} + \Theta} + \frac{1}{2} \left(\frac{4\alpha^2 \eta^2}{3} - \Theta + \frac{4\alpha\beta\eta^2}{\sqrt{\frac{2\alpha^2 \eta^2}{3} + \Theta}} \right)^{1/2}. \quad (\text{A.3})$$

The effective charge is then obtained by replacing this value for κ_* in equation (2) for spherical macro-ions, and in equation (3) for rod-like macro-ions.

In the no-added-salt case, these expressions reduce to equations (8) and (9), as indicated in the text.

References

- [1] Kjellander R 2001 *Electrostatic Effects in Soft Matter and Biophysics (NATO ASI Series)* ed C Holm *et al* (Dordrecht: Kluwer) p 317
- [2] Belloni L 1998 *Colloids Surf. A* **140** 227
- [3] Hansen J-P and Löwen H 2000 *Annu. Rev. Phys. Chem.* **51** 209
- [4] Levin Y 2002 Electrostatic correlations: from plasma to biology *Preprint cond-mat/0207086*
- [5] Alexander S, Chaikin P M, Grant P, Morales G J and Pincus P 1984 *J. Chem. Phys.* **80** 5776
- [6] Fuoss R M, Katchalsky A and Lifson S 1951 *Proc. Natl Acad. Sci. USA* **37** 579
- See also
- Alfrey T, Berg P and Morawetz H J 1951 *J. Polym. Sci.* **7** 543
- [7] Manning G S 1969 *J. Chem. Phys.* **51** 924
- Oosawa F 1971 *Polyelectrolytes* (New York: Dekker)
- [8] Trizac E, Bocquet L and Aubouy M 2002 *Phys. Rev. Lett.* **89** 24830
- Bocquet L, Trizac E and Aubouy M 2002 *J. Chem. Phys.* **117** 8138
- [9] For alternative definitions, see e.g.
- Diehl A, Barbosa M C and Levin Y 2001 *Europhys. Lett.* **53** 86
- Deserno M, Holm C and May S 2000 *Macromolecules* **33** 199
- [10] Trizac E, Bocquet L, Agra R, Weis J-J and Aubouy M 2002 *J. Phys.: Condens. Matter* **14** 9339
- [11] Marcus R A 1955 *J. Chem. Phys.* **23** 1057
- [12] Trizac E and Hansen J-P 1996 *J. Phys.: Condens. Matter* **8** 9191
- [13] Trizac E and Hansen J-P 1997 *Phys. Rev. E* **56** 3137
- [14] Deserno M and von Grünberg H H 2002 *Phys. Rev. E* **66** 011401
- [15] Dubois M, Zemb T, Belloni L, Delville A, Levitz P and Setton R 1992 *J. Chem. Phys.* **75** 944
- [16] Härtl W and Versmold H 1988 *J. Chem. Phys.* **88** 7157
- [17] Bitzer F, Palberg T, Löwen H, Simon R and Leiderer P 1994 *Phys. Rev. E* **50** 2821
- Palberg T, Mönch W, Bitzer F, Piazza R and Bellini T 1995 *Phys. Rev. Lett.* **74** 4555
- [18] Löwen H 1994 *J. Chem. Phys.* **100** 6738
- [19] Gisler T *et al* 1994 *J. Chem. Phys.* **101** 9924
- [20] Stevens M J, Falk M L and Robbins M O 1996 *J. Chem. Phys.* **104** 5209
- [21] Lobaskin V and Linse P 1999 *J. Chem. Phys.* **111** 4300
- [22] Groot R D 1991 *J. Chem. Phys.* **95** 9191
- [23] Hribar B, Vlachy V, Bhuiyan L B and Outhwaite C W 2000 *J. Phys. Chem. B* **104** 11522
- [24] Evilevitch A, Lobaskin V, Olsson U, Linse P and Schurtenberger P 2001 *Langmuir* **17** 1043
- [25] Shkel I A, Tsodirov O V and Record M T 2000 *J. Phys. Chem. B* **104** 5161
- [26] Hansen J-P and Trizac E 1997 *Physica A* **235** 257
- [27] Reus V, Belloni L, Zemb T, Lutterbach N and Versmold H 1997 *J. Physique II* **7** 603
- [28] Raspaud E, da Conceicao L and Livolant F 2000 *Phys. Rev. Lett.* **84** 2533

Chapitre D

Interactions effectives entre poly-ions de même charge

Effective interactions between like-charged macromolecules

Emmanuel Trizac*

*Laboratoire de Physique Théorique, Unité Mixte de Recherche UMR 8627 du CNRS, Bâtiment 210, Université de Paris-Sud,
91405 Orsay Cedex, France*

(Received 19 January 2000)

We investigate, within a local density functional theory formalism, the interactions between like-charged polyions immersed in a confined electrolyte. We obtain a simple condition for a repulsive effective pair potential, which can be related to the thermodynamic stability criterion of the uncharged counterpart of microscopic species constituting the electrolyte. Under the same condition, the phenomenon of charge inversion (over-charging), where the polyion bare charge is over-screened by its electric double layer, is shown to be impossible. These results hold beyond standard mean-field theories (such as Poisson-Boltzmann or modified Poisson-Boltzmann approaches).

PACS number(s): 05.70.Np, 64.10.+h, 82.60.Lf, 82.70.Dd

Electrostatic forces play a key role in determining the stability, phase, and structural properties of colloids or macroions suspended in polar solvents (usually aqueous media). Such suspensions are ubiquitous in many biological and technologically important systems, from superabsorbants or water-soluble paints to DNA solutions. Their behavior is, however, far from being well understood, despite an intense theoretical effort over the last 50 years.

Upon dispersion in water, mesoscopic colloidal polyions bearing ionizable groups gain a (large) bare charge, and strongly attract counterions while repelling coions, thus giving rise to electric double layers characterized by strong inhomogeneities in the local density of these microions in the vicinity of the polyions. From the electrostatic part of the traditional Derjaguin-Landau-Verwey-Overbeek (DLVO) theory [1], the effective interactions (solvent and microion mediated) between two like-charged colloidal particles are expected to be repulsive [2], whereas experiments [3] and numerical simulations [4] provide evidence for attraction, particularly within confined geometries (e.g., when the two macroions are close to a charged wall or between two glass plates).

We consider a mixture of N microions, where species α has charge number z_α and local density $c_\alpha(\mathbf{r})$. Disregarding the molecular nature of the solvent, considered to be a confined electrolyte of dielectric permittivity ϵ , the effective interactions between two like-charge colloids are then analyzed within a generic local density functional theory. We show that the convexity of the free energy density with respect to the microions densities is a sufficient condition for having repulsive effective interactions and for preventing charge inversion. The physical implications of this result are considered in the final discussion (in particular the repulsion “often” follows from the thermodynamic stability criterion of the corresponding uncharged mixture of micro-species). The proof makes use of the results established in Refs. [5–7], and considers a geometry which encompasses many cases of experimental relevance: the confining region \mathcal{R} is a cylinder of arbitrary cross section and length $2L$ (in the limit

of large L) while the medium \mathcal{R}' outside \mathcal{R} is a dielectric continuum of permittivity ϵ' with the possibility of a uniform density of surface charges σ on the boundary $\partial\mathcal{R}$. The standard Neuman and Dirichlet boundary conditions (constant normal electric field and constant potential respectively) belong to the above class, and the dielectric medium in \mathcal{R}' may contain an electrolyte solution (this possibility was not considered in Refs [5,6]). We assume global electroneutrality in both \mathcal{R} and \mathcal{R}' and the two macroions we shall focus on may be of arbitrary shape provided the electrostatic potential possesses mirror symmetry with respect to a plane Oxy between the macroions. Our approach holds irrespective of the specific boundary conditions to be applied on the macroions (constant charge or constant potential) and is independent of the sign of the surface charge σ .

Omitting, for the sake of simplicity, their temperature dependence, the local [8] density free energy functionals [9] considered here are of the form

$$\mathcal{F}(\{c_\alpha\}) = \int_{\mathcal{R}} f(\{c_\alpha(\mathbf{r})\}) d\mathbf{r} + \frac{1}{2} \int_{\mathcal{R}} \rho_c(\mathbf{r}) G(\mathbf{r}, \mathbf{r}') \rho_c(\mathbf{r}') d\mathbf{r} d\mathbf{r}', \quad (1)$$

where the Helmholtz free energy density f is a function of all N microions densities and the local charge density includes the contributions from the macroions $q_{\mathcal{M}}(\mathbf{r})$ as well as from the microions:

$$\rho_c(\mathbf{r}) = \sum_{\alpha=1}^N z_\alpha e c_\alpha(\mathbf{r}) + q_{\mathcal{M}}(\mathbf{r}). \quad (2)$$

In Eq. (1), $G(\mathbf{r}, \mathbf{r}')$ denotes the Green’s function such that the electrostatic potential $\psi(\mathbf{r})$, which is a solution of Poisson’s equation $\nabla^2 \psi = -(4\pi/\epsilon)\rho_c(\mathbf{r})$ with the required boundary conditions on the surface $\partial\mathcal{R}$, can be cast in the form

$$\psi(\mathbf{r}) = \int_{\mathcal{R}} \rho_c(\mathbf{r}') G(\mathbf{r}, \mathbf{r}') d\mathbf{r}'. \quad (3)$$

*Electronic address: Emmanuel.Trizac@th.u-psud.fr

G reduces to the usual Coulomb potential in the absence of confinement. The density functional formulation provided by Eq. (1) encompasses a large class of modelizations, including (i) the standard Poisson-Boltzmann theory when the ideal gas expression $f = \sum_{\alpha} k T c_{\alpha} [\ln(c_{\alpha} \Lambda_{\alpha}^3) - 1]$ is chosen for the free energy density, (ii) modified Poisson-Boltzmann theories derived to account for steric effects [10] or more general nonelectrostatic interactions [11], and (iii) recent improvements over standard mean-field approximations incorporating ion-ion correlations in the form of a one component plasma correction [12]. This last case involves a free energy density which does not only depend on the local densities of microions but also on the elementary charge e , and will be examined in the concluding discussion. In general, the present analysis allows one to incorporate correlation or non-mean-field contributions, provided these effects translate into a local free energy density.

Minimization of the functional (1) subject to the normalization constraints $\int_{\mathcal{R}} c_{\alpha}(\mathbf{r}) d\mathbf{r} = N_{\alpha}$ yields the implicit relation between the densities $c_{\alpha}(\mathbf{r})$ and the electrostatic potential,

$$\frac{\partial f}{\partial c_{\alpha}} + e z_{\alpha} \psi(\mathbf{r}) = \mu_{\alpha}^*, \quad 1 \leq \alpha \leq N, \quad (4)$$

where μ_{α}^* is the (electro)chemical potential of species α . The effective force acting on a colloid is obtained from integration of the generalized Maxwell stress tensor $\mathbf{\Pi}$ over the surface S of the macroion,

$$\mathbf{F} = \oint_S \mathbf{\Pi} \cdot \mathbf{n} dS, \quad (5)$$

where the unit vector \mathbf{n} points outward from the surface of integration. The local stress tensor follows from the computation of the reversible work required to locally deform the shape of the confining cylinder, with the result

$$\mathbf{\Pi} = - \left[P + \frac{\epsilon}{2} \nabla \psi \cdot \nabla \psi \right] \mathbf{I} + \epsilon \nabla \psi \otimes \nabla \psi, \quad (6)$$

where the osmotic pressure $P(\{c_{\alpha}\})$, which depends on position via the local densities $c_{\alpha}(\mathbf{r})$, is the pressure that would be found in the medium in the absence of an electric field, with the same densities $c_{\alpha}(\mathbf{r})$ [13], and can be written as the Legendre transform of the free energy density,

$$P(\{c_{\alpha}\}) = -f(\{c_{\alpha}\}) + \sum_{\alpha=1}^N c_{\alpha} \frac{\partial f}{\partial c_{\alpha}}. \quad (7)$$

For any stress tensor of the form (6), it has been shown in Refs. [5–7] that the effective force \mathbf{F} given by Eq. (5) has a component F_z along the axis of the cylinder that can be cast in the form

$$F_z = \int_{Oxy} \left[P(\psi)_{z=0} - P(\psi)_{z=L} - (\psi_{z=0} - \psi_{z=L}) \frac{\partial P}{\partial \psi}(\psi_{z=L}) \right] dx dy + \frac{\epsilon}{2} \int_{Oxy} (\nabla \psi_{z=0} - \nabla \psi_{z=L})^2 dx dy, \quad (8)$$

where ϵ denotes ϵ (respectively ϵ') for the part of the symmetry plane, denoted Oxy , belonging to \mathcal{R} (respectively \mathcal{R}'). In Eq. (8), it is understood that the pressure depends on the potential via Eqs. (7) and (4), the latter giving sense to the notation $\partial P / \partial \psi$. The subsequent analysis is devoted to the proof that P is a convex-up function of ψ provided that the free energy density is itself convex-up with respect to the densities $\{c_{\alpha}\}$. Remembering the orientation convention chosen in Refs. [5–7], this in turn establishes the repulsive nature of the effective interactions ($F_z > 0$). From the direct differentiation of Eq. (7) we get

$$\frac{\partial P}{\partial \psi} = -\rho_c(\mathbf{r}), \quad (9)$$

where use was made of the stationary condition (4). The relation (9) can be recovered from the mechanical equilibrium condition of a fluid element of microions: the balance between the electric force and the osmotic constraint acting on such a fluid element located at point \mathbf{r} can indeed be written as

$$-\nabla P = \rho_c(\mathbf{r}) \nabla \psi \quad (10)$$

$$\Leftrightarrow \left[\frac{\partial P}{\partial \psi} + \rho_c \right] \nabla \psi = \mathbf{0}. \quad (11)$$

Equation (9) equivalently implies that the tensor $\mathbf{\Pi}$ is divergence free, as already invoked in Ref. [7] to obtain the osmotic equation of state in the specific case of a modified Poisson Boltzmann theory.

The second derivative of the osmotic pressure,

$$\frac{\partial^2 P}{\partial \psi^2} = -e \sum_{\alpha} z_{\alpha} \frac{\partial c_{\alpha}}{\partial \psi}, \quad (12)$$

involves the quantities $\partial c_{\alpha} / \partial \psi$ which may be determined from the condition (4):

$$\sum_{\beta=1}^N \frac{\partial^2 f}{\partial c_{\alpha} \partial c_{\beta}} \frac{\partial c_{\beta}}{\partial \psi} = -e z_{\alpha}. \quad (13)$$

Assuming the free energy density to be a convex-up function of the $\{c_{\alpha}\}$ implies that the matrix \mathbf{H} with elements

$$H_{\alpha\beta} \equiv \frac{\partial^2 f}{\partial c_{\alpha} \partial c_{\beta}} \quad (14)$$

is positive definite. Its inverse \mathbf{H}^{-1} is consequently positive definite from which we can invert relation (13):

$$\frac{\partial c_{\alpha}}{\partial \psi} = -e \sum_{\beta=1}^N (\mathbf{H}^{-1})_{\alpha\beta} z_{\beta}. \quad (15)$$

Upon substitution of Eq. (15) into (12) we finally obtain

$$\frac{\partial^2 P}{\partial \psi^2} = e^2 \sum_{\alpha, \beta} (\mathbf{H}^{-1})_{\alpha\beta} z_\alpha z_\beta > 0. \quad (16)$$

The pressure P is therefore a convex-up function of the electrostatic potential, which establishes the aforementioned connection between the convexity of f and the sign of the polyion-polyion effective interactions. Note that the nonconvexity of the free energy density is a necessary though insufficient condition for the existence of attraction within a local density approximation formalism.

We now address the question of charge reversal, where the nominal charge of a bare polyion can be over-screened by its condensed counterions. This interesting phenomenon (occurring for instance in DNA salt systems [14]) requires, from Gauss's theorem, the vanishing of the normal component of the electric field ($-\mathbf{n} \cdot \nabla \psi$) on a closed surface with normal \mathbf{n} around the polyion. Taking the gradient of Eq. (4) then implies, without any symmetry assumption,

$$\sum_{\beta=1}^N \frac{\partial^2 f}{\partial c_\alpha \partial c_\beta} [\mathbf{n} \cdot \nabla c_\beta] = 0, \quad (17)$$

hence, the existence of a vanishing eigenvalue [with eigenvector $(\mathbf{n} \cdot \nabla c_\beta)_{\beta=1 \dots N}$] of the stability matrix \mathbf{H} , which is impossible under the assumption of positive definiteness.

Within the framework of Poisson-Boltzmann theory, the repulsive nature of the effective electrostatic force between two similar colloidal bodies [5–7] and the impossibility of charge reversal immediately follows from the previous analysis. However, if for the sake of analytical tractability and in the spirit of Ref. [15], the ideal free energy density is further Taylor expanded up to order \mathcal{N} around the mean densities $\{\bar{c}_\alpha\}$, we obtain

$$H_{\alpha\beta} = \frac{\delta_{\alpha\beta}}{c_\alpha} \sum_{i=0}^{\mathcal{N}-2} \left(1 - \frac{c_\alpha}{\bar{c}_\alpha}\right)^i = \left[1 - \left(1 - \frac{c_\alpha}{\bar{c}_\alpha}\right)^{\mathcal{N}-1}\right] \frac{\delta_{\alpha\beta}}{c_\alpha}. \quad (18)$$

The truncated Hessian \mathbf{H} is therefore positive definite and gives a repulsive force for even values of \mathcal{N} (as in the nonlinear Poisson-Boltzmann theory), while it can be nonpositive definite and the force attractive for odd orders \mathcal{N} provided the local density of one counterion species exceeds twice its mean density. This explains the repulsion within linearized Poisson-Boltzmann theory [16] (where linearization amounts to taking $\mathcal{N}=2$ [9]), and the attraction seen in Ref. [15] with an expansion pushed one order further and

truncated after third order to account for the triplet interactions between two polyions and a charged wall.

We have shown that effective attractive pair potentials and over-charging are both ruled out under the assumption of positive definiteness for the stability matrix \mathbf{H} . This is a necessary requirement when the free energy density does not depend on the elementary charge e . The key ingredient here is the existence of a *thermodynamically stable* neutral mixture of microspecies described by the same density $f\{c_\alpha\}$ as its charged counterpart. On the other hand, the inclusion of correlations and/or fluctuations corrections is believed to be essential in order to describe the appearance of attractive interactions. If their correction to the mean-field electrostatic term $\int \rho_c G \rho_c$ on the right-hand side of Eq. (1) is taken into account, and translated into an e -dependent free energy density [12,18], the thermodynamic stability condition is now the positive definiteness of the integral operator whose kernel is defined by

$$\frac{\partial^2 f}{\partial c_\alpha \partial c_\beta} \delta(\mathbf{r}-\mathbf{r}') + e^2 z_\alpha z_\beta G(\mathbf{r}, \mathbf{r}'), \quad (19)$$

and it is in general impossible to find a *locally* neutral mixture described by the same density f . \mathbf{H} need not therefore be positive definite. However, non-convex-up densities f such as the correction put forward by Stevens and Robbins [17] by extrapolation of the Monte Carlo data for the homogeneous one-component plasma lead to an instability at high densities (the so-called structuring catastrophe), and cannot be used in a thermodynamically stable way within a local density functional theory [12,18]. The recent attempt of Barbosa *et al.* [12] to circumvent this instability gives rise to a convex-up f , with results reproducing satisfactorily the ionic correlations present in molecular dynamics simulations. The present work indicates that the effective interactions are then necessarily repulsive and charge inversion impossible, regardless of the analytical complexity of the formalism.

To conclude, repulsive effective pair potentials seem generic within local density approximations. The description of attraction and over-charging thus requires involved density functional theories, and it is not sufficient to incorporate correlation effects in a local formulation. Our analysis points to the importance of nonlocal effects, which can be accounted for by weighted density functionals [17,18], or simpler approaches relying on nonelectrostatic depletion interactions [19].

The author would like to thank J.L. Raimbault, D. Levesque, J.P. Hansen, B. Jancovici, H. Hilhorst, M. Deserno, and D. Rowan for helpful discussions.

- [1] B.V. Derjaguin and L. Landau, *Acta Physicochim. URSS* **14**, 633 (1941); E.J.W. Verwey and J.Th.G. Overbeek, *Theory of the Stability of Lyophobic Colloids* (Elsevier, New York, 1948).
 [2] J. Chakrabarti and H. Löwen, *Phys. Rev. E* **58**, 3400 (1998); A. Denton and H. Löwen, *Thin Solid Films* **330**, 7 (1998); K. Vondermasson, J. Bongers, A. Mueller, and H. Versmold, *Langmuir* **10**, 1351 (1994); J.C. Crocker and D.G. Grier, *Phys.*

Rev. Lett. **73**, 352 (1994).

- [3] G.M. Kepler and S. Fraden, *Phys. Rev. Lett.* **73**, 356 (1994); M.D. Carbajal-Tinoco, F. Castro-Román, and J.L. Arauz-Lara, *Phys. Rev. E* **53**, 3745 (1996); A.M. Larsen and D.G. Grier, *Nature (London)* **385**, 230 (1997); J.C. Crocker and D.G. Grier, *Phys. Rev. Lett.* **77**, 1897 (1996); D.G. Grier, *Nature (London)* **393**, 621 (1998).
 [4] N. Grønbech-Jensen, K.M. Beardmore, and P. Pincus, *Physica*

- A **261**, 74 (1998); E. Allahyarov, I. D'Amico, and H. Löwen, Phys. Rev. E **60**, 3199 (1999); P. Linse and V. Lobaskin, Phys. Rev. Lett. **83**, 4208 (1999).
- [5] J.C. Neu, Phys. Rev. Lett. **82**, 1072 (1999).
- [6] J.E. Sader and D.Y. Chan, J. Colloid Interface Sci. **213**, 268 (1999); J.E. Sader and D.Y. Chan, Langmuir **16**, 324 (2000).
- [7] E. Trizac and J.L. Raimbault, Phys. Rev. E **60**, 6530 (1999).
- [8] The "locality" does not refer to the van der Waals-like mean-field term $\int \rho_c \tilde{G} \rho_c$ but to the term $\int f$ that may contain correlation contributions besides the usual ideal part [9].
- [9] For a review, see J.P. Hansen and E. Smargiassi, in *Monte Carlo and Molecular Dynamics of Condensed Matter Systems*, edited by K. Binder and G. Ciccotti (SIF, Bologna, 1996), or R. Evans, in *Fundamentals of Inhomogeneous Fluids*, edited by D. Henderson (Marcel Dekker, New York, 1992).
- [10] M. Eigen and E. Wicke, J. Phys. Chem. **58**, 702 (1954); V. Kralj-Iglič and A. Iglič, J. Phys. II **6**, 477 (1996); I. Borukhov, D. Andelman, and H. Orland, Phys. Rev. Lett. **79**, 435 (1997).
- [11] L. Lue, N. Zoeller, and D. Blankschtein, Langmuir **15**, 3726 (1999).
- [12] M.C. Barbosa, M. Deserno, and C. Holm, e-print cond-mat/9910364.
- [13] L.D. Landau and E.M. Lifschitz, *Electrodynamics of Continuous Media* (Pergamon Press, Oxford, 1984).
- [14] B.I. Shklovskii, Phys. Rev. E **60**, 5802 (1999); T. Das, D. Bratko, L.B. Bhuiyan, and C.W. Outhwaite, J. Chem. Phys. **107**, 9197 (1999); C.N. Patra and A. Yethiraj, J. Phys. Chem. B **103**, 6080 (1999); P.S. Kuhn, Y. Levin, and M.C. Barbosa, Physica A **274**, 8 (1999).
- [15] D. Goulding and J.P. Hansen, Europhys. Lett. **46**, 407 (1999).
- [16] D. Goulding and J.P. Hansen, Mol. Phys. **95**, 649 (1998).
- [17] M.J. Stevens and M.O. Robbins, Europhys. Lett. **12**, 81 (1990).
- [18] A. Diehl, M.N. Tamashiro, M.C. Barbosa, and Y. Levin, Physica A **274**, 433 (1999).
- [19] M.N. Tamashiro and P. Pincus, Phys. Rev. E **60**, 6549 (1999).

On the bulk modulus of the cell model of charged macromolecules suspensions

Gabriel Téllez^{a)}

Grupo de Física Teórica de la Materia Condensada, Departamento de Física, Universidad de Los Andes, A.A. 4976, Bogotá, Colombia

Emmanuel Trizac^{b)}

Laboratoire de Physique Théorique, Bâtiment 210, Université de Paris-Sud, 91405 Orsay, France (Unité Mixte de Recherche 8627 du CNRS)

(Received 4 September 2002; accepted 22 November 2002)

We study theoretically the bulk modulus (inverse of the compressibility) of a suspension of charged objects (macroions), making use of a cell model to account for the finite density of macroions. The diffuse layer of charged microspecies around a macroion is described by a generic local density functional theory. Within this general framework, we obtain the condition for a positive bulk modulus, which is fulfilled by several proposals made in the literature and rules out the possibility of a critical point. We show that a sufficient condition for a positive compressibility also ensures that the same theory produces repulsive effective pair potentials. © 2003 American Institute of Physics. [DOI: 10.1063/1.1538604]

I. INTRODUCTION

Macromolecules soluble in aqueous suspensions usually acquire an electric charge. Such systems are of considerable theoretical and experimental interest. Examples include proteins in living cells, dispersion paints, or superabsorbants. Their theoretical description is however a tremendous task, and operational approximate treatments are needed.

In this work, we consider a cell model to account for the macroions correlations,¹ in conjunction with a local density functional theory to describe the inhomogeneous electric double layer around a macroion.^{2,3} This framework encompasses the standard mean-field Poisson–Boltzmann (PB) theory, but also more recent approaches proposed to account for microions excluded volume,⁴ more general nonelectrostatic effects,⁵ or to incorporate correlations between the screening microions,^{6,7} that are neglected within PB theory. The cell model description may be considered as one of the simplest starting points, and provides an important benchmark against which experiments and more refined theories are tested. The resulting differential equations are however highly nonlinear, and even with the simplest of the approaches under consideration here (PB), can only be solved analytically in 1 or 2 dimensions without added salt (i.e., for the situation of a flat double layer in a confining slab, or for that of a rod-like macroion of infinite length enclosed in a concentric confining cylinder⁸). The linearized version of the above problem has therefore always been an important alternative, but is not free of internal inconsistencies. In particular, the linearized PB theory may lead to negative osmotic pressures^{9,10} and negative bulk modulus (inverse of the compressibility),¹⁰ whereas within the original nonlinear PB theory, it is straightforward to show that the osmotic pressure is necessarily positive. For the bulk modulus, the situation is

less clear: although this quantity is found positive in the numerical solution of PB equation, it seems that no formal proof exists concerning its sign. In this article, we derive such a proof and obtain the conditions under which a general local density functional theory leads to a positive compressibility within the cell model.

The article is organized as follows. The density functional theory formalism is presented in Sec. II, where a few useful identities are derived. The bulk modulus is then computed in Sec. III and cast in a form where a sufficient condition for its positivity clearly appears. Conclusions are drawn in the final section.

II. GENERAL FORMALISM

A. Density functional theory

We consider a ν -dimensional colloid with spherical symmetry confined in its (concentric) Wigner–Seitz cell ($\nu=2$ for a cylindrical colloid, $\nu=3$ for a colloidal sphere). The cell is a spherical region \mathcal{R} of radius R and volume $V = S_\nu R^\nu / \nu$ (S_ν is the area of the unit radius ν -dimensional sphere, $S_2 = 2\pi$, $S_3 = 4\pi$). The colloid (of fixed uniform surface charge density) is immersed in an electrolyte solution with several different species of ions with charges $\{q_\alpha\}$, and the local density of the species α is denoted $n_\alpha(\mathbf{r})$. The system inside the cell is globally neutral. In what follows, we explicitly consider the semi-grand-canonical situation where the macroion's suspension is in osmotic equilibrium with a salt reservoir through a semipermeable membrane (permeable to microspecies only). We therefore consider the grand potential $\Omega\{n_\alpha\}$, which is a functional of microion densities that we write

$$\begin{aligned} \Omega\{n_\alpha\} = & \int_{\mathcal{R}} \omega(\{n_\alpha(\mathbf{r})\}) d\mathbf{r} + \frac{1}{2} \int_{\mathcal{R}} \rho(\mathbf{r}) \psi(\mathbf{r}) d\mathbf{r} \\ & + \lambda \int_{\mathcal{R}} \rho(\mathbf{r}) d\mathbf{r}, \end{aligned} \quad (2.1)$$

^{a)}Electronic mail: gtellez@uniandes.edu.co

^{b)}Electronic mail: emmanuel.trizac@th.u-psud.fr

where

$$\rho(\mathbf{r}) = \sum_{\alpha} q_{\alpha} n_{\alpha}(\mathbf{r}) + \rho_{\text{col}}(\mathbf{r}) \quad (2.2)$$

is the total charge density including that of the colloid (denoted ρ_{col}), λ is a Lagrange multiplier to ensure global electroneutrality ($\partial\Omega/\partial\lambda = \int\rho = 0$), and $\psi(\mathbf{r})$ is the electrostatic potential. Within PB theory, the local part of the functional (2.1) embodied in ω is entirely of entropic origin. In other words, electrostatic interactions are taken into account at mean-field level only, through the term $\int\rho\psi/2$. This feature is shared by the theories of Refs. 4 and 5, but is not the case of the formalism put forward by Barbosa *et al.*,^{6,7} where the term ω contains electrostatic corrections to the mean-field Coulomb contribution. By comparison with the results of molecular dynamics simulations, this framework was shown to capture important correlations missed by the mean-field Poisson–Boltzmann.⁶

Within the standard Poisson–Boltzmann theory, the microions are treated as an ideal gas of charged particles reacting to the mean electrostatic potential. The free-energy density therefore reads $f(\{n_{\alpha}\}) = f_{\text{id}}(\{n_{\alpha}\}) = \beta^{-1} \sum_{\alpha} n_{\alpha} \{\ln[\Lambda^3 n_{\alpha}] - 1\}$, where Λ is an irrelevant length scale and $\beta = 1/(k_B T)$ the inverse temperature. The grand potential functional describing the osmotic equilibrium with a salt reservoir is thus $\Omega = \int f - \sum_{\alpha} \mu_{\alpha}^b \int n_{\alpha} + \int \rho\psi/2 + \lambda \int \rho$, where the chemical potentials $\mu_{\alpha}^b = \partial f_{\text{id}}(\{n_{\alpha}^b\})/\partial n_{\alpha}^b = \beta^{-1} \ln(\Lambda^3 n_{\alpha}^b)$ are defined from the bulk densities n_{α}^b of microspecies in the reservoir. The local grand potential density finally takes the form

$$\begin{aligned} \omega(\{n_{\alpha}(\mathbf{r})\}) &= f(\{n_{\alpha}(\mathbf{r})\}) - \sum_{\alpha} \mu_{\alpha}^b n_{\alpha}(\mathbf{r}) \\ &= \beta^{-1} \sum_{\alpha} n_{\alpha}(\mathbf{r}) \left(\ln \frac{n_{\alpha}(\mathbf{r})}{n_{\alpha}^b} - 1 \right). \end{aligned} \quad (2.3)$$

As mentioned in the Introduction, other theories may be described by our formalism, such as those proposed to account for steric effects,⁴ more general nonelectrostatic interactions,⁵ or to go beyond mean field and include correlations.^{6,7}

The mean-field Coulomb term $\frac{1}{2} \int \rho(\mathbf{r})\psi(\mathbf{r})d\mathbf{r}$ in Eq. (2.1) is actually quadratic in the densities if one writes the potential in term of the set $\{n_{\alpha}\}$. Introducing the proper Green’s function $G(\mathbf{r}, \mathbf{r}')$ for the electrostatic problem in the region \mathcal{R} , it is always possible to write the electrostatic potential in the form (see the Appendix)

$$\psi(\mathbf{r}) = \int_{\mathcal{R}} \rho(\mathbf{r}') G(\mathbf{r}, \mathbf{r}') d\mathbf{r}', \quad (2.4)$$

with the cell boundary chosen as the potential reference, $\psi(R) = 0$.

The variational problem defined by the functional (2.1) leads to the stationary condition

$$\frac{\partial\omega(\{n_{\alpha}(\mathbf{r})\})}{\partial n_{\alpha}} + q_{\alpha}(\psi(\mathbf{r}) + \lambda) = 0, \quad (2.5)$$

which, in the Poisson–Boltzmann theory, reduces to

$$n_{\alpha}(\mathbf{r}) = n_{\alpha}^b e^{-\beta q_{\alpha}[\psi(\mathbf{r}) + \lambda]}. \quad (2.6)$$

Since the potential vanishes at the boundary of the cell, it can be seen in this equation that the Lagrange multiplier λ coincides with the so-called Donnan potential (potential drop across the interface of the cell and the bulk reservoir, which is formally at a potential $-\lambda$).

Finally, discriminating between the optimal density profiles fulfilling Eq. (2.5) and the generic arguments of the grand potential functional leads to unnecessary heavy notations and will not be useful for the subsequent analysis.

B. A few useful identities

Consider a functional \mathcal{Q} of the density profiles $n_{\alpha}(\mathbf{r})$ having an explicit dependence on the volume V of the cell and the potential drop λ (later, we shall be interested in $\mathcal{Q} = \Omega$). The total derivative $d\mathcal{Q}/dV$ of \mathcal{Q} when the volume of the cell varies is¹⁰

$$\frac{d\mathcal{Q}}{dV} = \frac{\partial\mathcal{Q}}{\partial V} + \int_{\mathcal{R}} \sum_{\alpha} \frac{\delta\mathcal{Q}}{\delta n_{\alpha}(\mathbf{r})} \frac{dn_{\alpha}(\mathbf{r})}{dV} d\mathbf{r} + \frac{\partial\mathcal{Q}}{\partial\lambda} \frac{d\lambda}{dV}, \quad (2.7)$$

where the first term is the variation due to the explicit dependence of \mathcal{Q} on V , the second is due to the variation of the density profiles when the volume changes, and the last is due to the variation of the potential drop with the volume. Computing $dn_{\alpha}(\mathbf{r})/dV$ and $d\lambda/dV$ would require to solve the variational problem (2.5) subject to the neutrality condition for a cell of volume $V+dV$ and for a cell of volume V , before computing the difference of the two solutions. However, this will not be necessary for our purposes.

We will be interested most of the time in quantities defined by a local density. In general, the partial derivative with respect to the volume (explicit dependence) of such a quantity may be computed by means of the dilatation method

$$\begin{aligned} \frac{\partial}{\partial V} \left[\int_{\mathcal{R}} g(\mathbf{r}) d\mathbf{r} \right] &= \frac{\partial}{\partial V} \left[V \int_{\tilde{\mathcal{R}}} g(V^{1/\nu} \tilde{\mathbf{r}}) d\tilde{\mathbf{r}} \right] \\ &= \frac{1}{V} \int_{\mathcal{R}} g(\mathbf{r}) d\mathbf{r} + \frac{1}{V\nu} \int_{\mathcal{R}} \mathbf{r} \cdot \frac{\partial g(\mathbf{r})}{\partial \mathbf{r}} d\mathbf{r} \\ &= \frac{1}{V} \int_{\mathcal{R}} g(\mathbf{r}) d\mathbf{r} + \frac{1}{V\nu} \int_{\partial\mathcal{R}} g(\mathbf{r}) \mathbf{r} \cdot d\mathbf{S} \\ &\quad - \frac{1}{V\nu} \int_{\mathcal{R}} \nu g(\mathbf{r}) d\mathbf{r} \end{aligned} \quad (2.8)$$

$$= \frac{1}{V\nu} \int_{\partial\mathcal{R}} g(\mathbf{r}) \mathbf{r} \cdot d\mathbf{S}. \quad (2.9)$$

We first made a change of variable $\mathbf{r} = V^{1/\nu} \tilde{\mathbf{r}}$ to show explicitly the volume dependence of the integral. After computing the derivatives and returning to the unscaled variable \mathbf{r} we made an integration by parts (ν is the dimensionality of the cell $\nu = 2, 3$). For the spherical isotropic geometry we are interested in, this result reduces to

$$\frac{\partial}{\partial V} \left[\int_{\mathcal{R}} g(\mathbf{r}) d\mathbf{r} \right] = g(R). \quad (2.10)$$

We will need also to compute the derivative of some terms given by a double integral. Following the same steps as above, this derivative is given by

$$\begin{aligned} \frac{\partial}{\partial V} \left[\int_{\mathcal{R}} g(\mathbf{r}, \mathbf{r}') d\mathbf{r} d\mathbf{r}' \right] \\ = \int_{\mathcal{R}} g(\mathbf{R}, \mathbf{r}') d\mathbf{r}' + \int_{\mathcal{R}} g(\mathbf{r}, \mathbf{R}) d\mathbf{r}. \end{aligned} \quad (2.11)$$

The key assumption here is that both quantities $\int g(\mathbf{r}, \mathbf{R}) d\mathbf{r}$ and $\int g(\mathbf{R}, \mathbf{r}) d\mathbf{r}$ only depend on the modulus $R = |\mathbf{R}|$. Another important point to notice is that the volume total derivative is taken at constant total electric charge because the system is neutral. Applying Eq. (2.7) to $\sum_{\alpha} q_{\alpha} N_{\alpha} = \int \sum_{\alpha} q_{\alpha} n_{\alpha}(\mathbf{r}) d\mathbf{r}$ then gives

$$\sum_{\alpha} q_{\alpha} \frac{dN_{\alpha}}{dV} = 0 = \rho(R) + \int_{\mathcal{R}} \sum_{\alpha} q_{\alpha} \frac{dn_{\alpha}(\mathbf{r})}{dV} d\mathbf{r}. \quad (2.12)$$

III. THE COMPRESSIBILITY

A. Derivation from the grand potential

Applying formula (2.7) to the grand potential once gives minus the pressure. However, as noticed in Ref. 10, the second and third terms vanish at the solution of the variational problem. Making use of Eqs. (2.10) and (2.11), we consequently have

$$\frac{\partial \Omega}{\partial V} = \omega(\{n_{\alpha}(R)\}) + \rho(R) [\psi(R) + \lambda] \quad (3.1a)$$

$$= \omega(\{n_{\alpha}(R)\}) + \lambda \rho(R). \quad (3.1b)$$

The last equality follows from $\psi(R) = 0$ [see the property (A10)] and is valid in general for arbitrary isotropic densities *even* if they differ from the optimal ones solving the variational problem. This will be used later. Note that the symmetry property of the Green's function [$G(\mathbf{r}, \mathbf{r}') = G(\mathbf{r}', \mathbf{r})$] is an important ingredient in obtaining the above equations.¹²

Using the stationary condition (2.5) one finds the usual result^{1,3,10}

$$p = \sum_{\alpha} n_{\alpha}(R) \frac{\partial \omega}{\partial n_{\alpha}(R)} - \omega(\{n_{\alpha}(R)\}), \quad (3.2)$$

which reduces to $p = k_B T \sum_{\alpha} n_{\alpha}(R)$ within PB theory (see Ref. 13 for a general derivation of this result, valid beyond PB).

When computing the second total derivative with respect to the volume of Ω to obtain the bulk modulus, one should not disregard the second and third terms of Eq. (2.7) too early.

$$\frac{d^2 \Omega}{dV^2} = \frac{\partial^2 \Omega}{\partial V^2} \quad (3.3a)$$

$$+ 2 \int_{\mathcal{R}} \sum_{\alpha} \frac{\delta}{\delta n_{\alpha}(\mathbf{r})} \left[\frac{\partial \Omega}{\partial V} \right] \frac{dn_{\alpha}(\mathbf{r})}{dV} d\mathbf{r} \quad (3.3b)$$

$$+ 2 \frac{\partial^2 \Omega}{\partial V \partial \lambda} \frac{d\lambda}{dV} \quad (3.3c)$$

$$+ \int_{\mathcal{R}^2} \sum_{\alpha\gamma} \frac{\delta^2 \Omega}{\delta n_{\alpha}(\mathbf{r}) \delta n_{\gamma}(\mathbf{r}')} \frac{dn_{\alpha}(\mathbf{r})}{dV} \frac{dn_{\gamma}(\mathbf{r}')}{dV} d\mathbf{r} d\mathbf{r}' \quad (3.3d)$$

$$+ 2 \int_{\mathcal{R}} \sum_{\alpha} \frac{\delta}{\delta n_{\alpha}(\mathbf{r})} \left[\frac{\partial \Omega}{\partial \lambda} \right] \frac{dn_{\alpha}(\mathbf{r})}{dV} \frac{d\lambda}{dV} d\mathbf{r} \quad (3.3e)$$

$$+ \frac{\partial^2 \Omega}{\partial \lambda^2} \left[\frac{d\lambda}{dV} \right]^2. \quad (3.3f)$$

At the solution of the variational problem most of these terms vanish, as it will be shown below. The first term (3.3a) is obtained taking the partial derivative of (3.1b) with respect to V

$$\begin{aligned} \frac{\partial}{\partial V} [\omega(\{n_{\alpha}(R)\}) + \lambda \rho(R)] \\ = \frac{1}{S_{\nu} R^{\nu-1}} \left\{ \sum_{\alpha} \frac{\partial n_{\alpha}(R)}{\partial R} \left[\frac{\partial \omega}{\partial n_{\alpha}(R)} + q_{\alpha} \lambda \right] \right\} = 0. \end{aligned} \quad (3.4)$$

We have used the variational equation (2.5) at $\mathbf{r} = \mathbf{R} \in \partial \mathcal{R}$ and the fact that $\psi(R) = 0$. The second term (3.3b) is obtained replacing the expression (3.1b) for $\partial \Omega / \partial V$ into (3.3b)

$$2 \sum_{\alpha} \left[\frac{\partial \omega}{\partial n_{\alpha}(R)} + q_{\alpha} \lambda \right] \frac{dn_{\alpha}(R)}{dV} = 0, \quad (3.5)$$

where we have once more used Eq. (2.5) at $\mathbf{r} = \mathbf{R} \in \partial \mathcal{R}$.

The third term (3.3c) is equal to

$$2\rho(R) \frac{d\lambda}{dV}, \quad (3.6)$$

and with the fifth term (3.3e)

$$\begin{aligned} 2 \frac{\partial}{\partial \lambda} \int_{\mathcal{R}} \sum_{\alpha} \left[\frac{\partial \omega}{\partial n_{\alpha}} + q_{\alpha} (\psi(\mathbf{r}) + \lambda) \right] \frac{dn_{\alpha}(\mathbf{r})}{dV} \frac{d\lambda}{dV} d\mathbf{r} \\ = 2 \int_{\mathcal{R}} \sum_{\alpha} q_{\alpha} \frac{dn_{\alpha}(\mathbf{r})}{dV} \frac{d\lambda}{dV} d\mathbf{r} = -2\rho(R) \frac{d\lambda}{dV}, \end{aligned} \quad (3.7)$$

gives a vanishing contribution. We have used in the preceding equation the relation (2.12). The last term (3.3f) is zero since Ω is linear on λ . Finally, the inverse compressibility may be cast in the form

$$\begin{aligned} \chi^{-1} &= -V \left(\frac{\partial p}{\partial V} \right)_{T, \mu_i} \\ &= V \frac{d^2 \Omega}{dV^2} \\ &= V \int_{\mathcal{R}^2} \sum_{\alpha\gamma} \frac{\delta^2 \Omega}{\delta n_\alpha(\mathbf{r}) \delta n_\gamma(\mathbf{r}')} \frac{dn_\alpha(\mathbf{r})}{dV} \frac{dn_\gamma(\mathbf{r}')}{dV} d\mathbf{r} d\mathbf{r}'. \end{aligned} \tag{3.8}$$

From Eq. (2.1) we have

$$\begin{aligned} \frac{\delta^2 \Omega}{\delta n_\alpha(\mathbf{r}) \delta n_\gamma(\mathbf{r}')} &= \frac{\partial \omega(\{n_\delta(\mathbf{r})\})}{\partial n_\alpha \partial n_\gamma} \delta(\mathbf{r} - \mathbf{r}') \\ &\quad + q_\alpha q_\beta G(\mathbf{r}, \mathbf{r}'). \end{aligned} \tag{3.9}$$

The second term, the Coulomb contribution, when replaced into Eq. (3.8), gives

$$\begin{aligned} &\int_{\mathcal{R}^2} \sum_{\alpha\gamma} q_\alpha q_\gamma G(\mathbf{r}, \mathbf{r}') \frac{dn_\alpha(\mathbf{r})}{dV} \frac{dn_\gamma(\mathbf{r}')}{dV} d\mathbf{r} d\mathbf{r}' \\ &= -\frac{1}{S_\nu} \int_{\mathcal{R}} \phi(\mathbf{r}) \Delta \phi(\mathbf{r}) d\mathbf{r} \end{aligned} \tag{3.10a}$$

$$= -R^{\nu-1} \phi(R) \partial_n \phi(R) + \frac{1}{S_\nu} \int_{\mathcal{R}} |\nabla \phi(\mathbf{r})|^2 d\mathbf{r}, \tag{3.10b}$$

where we have defined the ‘‘electric potential’’ created by the charge variation

$$\phi(\mathbf{r}) = \int_{\mathcal{R}} G(\mathbf{r}, \mathbf{r}') \sum_\alpha q_\alpha \frac{dn_\alpha(\mathbf{r}')}{dV} d\mathbf{r}', \tag{3.11}$$

and performed an integration by parts. The boundary term in (3.10b) vanishes because, from Eq. (A10), one has

$$\phi(R) = \int_{\mathcal{R}} \sum_\alpha q_\alpha \frac{dn_\alpha(\mathbf{r}')}{dV} G(\mathbf{R}, \mathbf{r}') d\mathbf{r}' = 0, \tag{3.12}$$

thus showing that the Coulomb contribution term is always positive, and

$$\begin{aligned} \chi^{-1} &= V \int_{\mathcal{R}} \sum_{\alpha\gamma} \frac{\partial^2 \omega}{\partial n_\alpha \partial n_\gamma} \frac{dn_\alpha(\mathbf{r})}{dV} \frac{dn_\gamma(\mathbf{r})}{dV} \\ &\quad + \frac{V}{S_\nu} \int_{\mathcal{R}} \left| \nabla_{\mathbf{r}} \left[\int_{\mathcal{R}} G(\mathbf{r}, \mathbf{r}') \sum_\alpha q_\alpha \frac{dn_\alpha(\mathbf{r}')}{dV} d\mathbf{r}' \right] \right|^2 d\mathbf{r}. \end{aligned} \tag{3.13}$$

B. Discussion

From Eq. (3.13), the positive definiteness of the integral operator whose kernel is defined by

$$\frac{\partial^2 \omega(\{n_\delta(\mathbf{r})\})}{\partial n_\alpha \partial n_\gamma} \delta(\mathbf{r} - \mathbf{r}') \tag{3.14}$$

ensures that the compressibility is positive (this is a sufficient but not necessary condition). This is the case for Poisson–Boltzmann theory, where ω is simply the ideal gas grand potential density, and it may be checked that it also holds for the theories presented in Refs. 4–6.

More generally, in any well-constructed approximate theory for the colloid based on density functionals for the grand potential of the form (2.1) (that is, a local density term plus an ‘‘interaction term’’ given by the mean-field Coulomb electrostatic energy), the solution of the variational problem should be a minimum, i.e., the quadratic form

$$\frac{\delta^2 \Omega}{\delta n_\alpha(\mathbf{r}) \delta n_\gamma(\mathbf{r}')} \tag{3.15}$$

should be positive definite to ensure thermodynamic stability. From expression (3.8), it then follows that the compressibility will always be positive in such a theory.

Equation (3.8) for the compressibility can be seen as a generalization for nonuniform fluids of the compressibility sum rule for uniform fluids^{13,14}

$$\beta(n\chi)^{-1} = 1 - n \int c^{(2)}(r) dr, \tag{3.16}$$

written here for a one-component system. In this relation, $c^{(2)}(r)$ is the direct correlation function defined, in the more general situation of a mixture, from

$$\frac{\delta^2 \Omega}{\delta n_\alpha(\mathbf{r}) \delta n_\gamma(\mathbf{r}')} = \frac{\delta^2 \mathcal{F}_{id}}{\delta n_\alpha(\mathbf{r}) \delta n_\gamma(\mathbf{r}')} - k_B T c_{\alpha\gamma}^{(2)}(\mathbf{r}, \mathbf{r}'), \tag{3.17}$$

where \mathcal{F}_{id} is the ideal gas contribution to the free-energy functional. When one replaces (3.17) into (3.8) for a uniform fluid [$c_{\alpha\gamma}^{(2)}(\mathbf{r}, \mathbf{r}') = c_{\alpha\gamma}^{(2)}(|\mathbf{r} - \mathbf{r}'|)$], and knowing that for a uniform fluid $dn_\alpha(\mathbf{r})/dV = -N_\alpha/V^2 = -n_\alpha/V$, one recovers the compressibility sum rule

$$\beta\chi^{-1} = \sum_\alpha n_\alpha - \int_{\mathcal{R}} \sum_{\alpha\gamma} n_\alpha n_\gamma c_{\alpha\gamma}^{(2)}(r) dr. \tag{3.18}$$

Although Eq. (3.8) is a natural generalization of the compressibility sum rule and similar expressions exist in the literature (see, for instance, Ref. 14), we included here the derivation of this result in the context of the Poisson–Boltzmann and other generic local density functional theories because these theories are approximate (nonexact) and nothing guarantees in advance the validity of Eq. (3.8) for nonexact theories.

IV. CONCLUSION

Within the cell model and a generic local density functional theory, we have considered a suspension of charged spherical macromolecules of arbitrary dimension. We have cast the corresponding compressibility in a form where the sign of this quantity is positive under a (weak) sufficient condition: the grand potential ω appearing in Eq. (2.1) should be a convex-up function on densities $\{n_\alpha\}$. This proves that the stability requirement of a positive compressibility is fulfilled by Poisson–Boltzmann theory as well as several improvements upon this mean-field approach.^{4–7} Our results show that such theories yield stable suspensions, and cannot exhibit a critical point associated with a gas–liquid phase separation.

This result should be put in perspective with the recent proofs that within PB theory, the effective interactions be-

tween two identical colloids confined in a cylinder of infinite length is necessarily positive.^{15,16} This proof has been extended to the more general family of local density functional theories (2.1) in Refs. 3 and 17. It was shown that the positive definiteness of the local free-energy density (or equivalently of the grand potential density in the semi-grand-canonical situation) was a sufficient condition for repulsive interactions. The results derived in this article show that under the same circumstances exactly, the bulk modulus within a cell model is also a positive quantity.

We explicitly considered the semi-grand-canonical situation where the macroions suspension is dialyzed against an electrolyte reservoir. Our results may, however, be extended to other electrostatic situations, such as the canonical one where the mean salt content in the suspension is fixed, or to the situation where the macroions are held at constant potential rather than constant charge.

APPENDIX: ON THE CHOICE OF THE GREEN'S FUNCTION

We consider the Green's function $G(\mathbf{r}, \mathbf{r}')$ satisfying

$$\nabla_{\mathbf{r}}^2 G(\mathbf{r}, \mathbf{r}') = -S_\nu \delta(\mathbf{r} - \mathbf{r}'), \quad (\text{A1})$$

with yet unspecified boundary conditions. From a standard identity (Green second identity), the solution of Poisson's equation $\nabla_{\mathbf{r}}^2 \psi = -S_\nu \rho(\mathbf{r})$ obeys the relation¹¹

$$\begin{aligned} \psi(\mathbf{r}) &= \int_{\mathcal{R}} \rho(\mathbf{r}') G(\mathbf{r}, \mathbf{r}') d\mathbf{r}' \\ &+ \frac{1}{S_\nu} \int_{\partial\mathcal{R}} \frac{\partial \psi(\mathbf{r}')}{\partial n'} G(\mathbf{r}, \mathbf{r}') dS' \\ &- \frac{1}{S_\nu} \int_{\partial\mathcal{R}} \psi(\mathbf{r}') \frac{\partial G}{\partial n'}(\mathbf{r}, \mathbf{r}') dS', \end{aligned} \quad (\text{A2})$$

where $\partial_n \equiv \partial/\partial n$ denotes the normal derivative and $\partial\mathcal{R}$ is the surface delimiting the region \mathcal{R} .

The Dirichlet G_D and Neumann G_N Green's function satisfy the boundary conditions

$$G_D(\mathbf{r}, \mathbf{r}') = 0 \quad \text{and} \quad \partial_n G_N(\mathbf{r}, \mathbf{r}') = -1/R^{\nu-1} \quad \text{for } \mathbf{r}' \in \partial\mathcal{R}. \quad (\text{A3})$$

For Dirichlet boundary conditions, we therefore have

$$\begin{aligned} \psi(\mathbf{r}) &= \int_{\mathcal{R}} \rho(\mathbf{r}') G_D(\mathbf{r}, \mathbf{r}') d\mathbf{r}' \\ &- \frac{1}{S_\nu} \int_{\partial\mathcal{R}} \psi(\mathbf{r}') \frac{\partial G_D}{\partial n'}(\mathbf{r}, \mathbf{r}') dS'. \end{aligned} \quad (\text{A4})$$

For the isotropic situation considered here and from Gauss law, the last term in Eq. (A4) may be written as

$$-\psi(R) \frac{1}{S_\nu} \int_{\partial\mathcal{R}} \frac{\partial G_D}{\partial n'}(\mathbf{r}, \mathbf{r}') dS' = \psi(R). \quad (\text{A5})$$

So far, the choice $G_D(\mathbf{r}, \mathbf{r}') = 0$ for $\mathbf{r}' \in \partial\mathcal{R}$ does not ensure that $\psi(R) = 0$. We chose to fix the zero of the electric poten-

tial at the boundary of the cell $\psi(R) = 0$ so that we recover Eq. (2.4).

For Neumann boundary conditions

$$\begin{aligned} \psi(\mathbf{r}) &= \langle \psi \rangle_S + \int_{\mathcal{R}} \rho(\mathbf{r}') G_N(\mathbf{r}, \mathbf{r}') d\mathbf{r}' \\ &+ \frac{1}{S_\nu} \int_{\partial\mathcal{R}} \frac{\partial \psi(\mathbf{r}')}{\partial n'} G_N(\mathbf{r}, \mathbf{r}') dS', \end{aligned} \quad (\text{A6})$$

where the first term $\langle \psi \rangle_S = \psi(R)$ is the average of the electric potential on the surface of the cell and we chose it to vanish. The last term in Eq. (A6) is

$$\begin{aligned} \frac{1}{S_\nu} \partial_n \psi(R) \int_{\partial\mathcal{R}} G_N(\mathbf{r}, \mathbf{r}') dS' &= -\frac{1}{R^{\nu-1}} \int_{\mathcal{R}} \rho(\mathbf{r}') d\mathbf{r}' \\ &\times \int_{\partial\mathcal{R}} G_N(\mathbf{r}, \mathbf{r}'') dS''. \end{aligned} \quad (\text{A7})$$

We have used Gauss law: $-\partial_n \psi(R) = \int \rho(\mathbf{r}') d\mathbf{r}' / R^{\nu-1}$. A proper choice of the Green's function ensures that the surface integral on the right-hand side of (A7) is independent of \mathbf{r} , and vanishes (one can shift G_N by an arbitrary constant). Explicitly, in the three-dimensional case, the choice

$$\begin{aligned} G_N(\mathbf{r}, \mathbf{r}') &= -\frac{1}{R} + \frac{1}{r_>} + \sum_{\ell=1}^{\infty} \left[\frac{r_<^\ell}{r_>^{\ell+1}} + \frac{\ell+1}{\ell} \frac{(rr')^\ell}{R^{2\ell+1}} \right] \\ &\times P_\ell(\cos \theta), \end{aligned} \quad (\text{A8})$$

with $r_> = \max(r, r')$ and $r_< = \min(r, r')$, θ the angle between \mathbf{r} and \mathbf{r}' and P_ℓ the Legendre polynomial of order ℓ , makes the term (A7) vanish. Finally, with this choice for the Green's function and for the reference potential, we have in both cases of boundary conditions

$$\psi(\mathbf{r}) = \int_{\mathcal{R}} \rho(\mathbf{r}') G(\mathbf{r}, \mathbf{r}') d\mathbf{r}' \quad \text{and} \quad \psi(R) = 0. \quad (\text{A9})$$

A useful property that follows from these considerations is that for *any* isotropic charge distribution $\rho(r)$ (eventually nonglobally neutral) we have in both cases of boundary conditions

$$\int_{\mathcal{R}} \rho(r') G(\mathbf{R}, \mathbf{r}') d\mathbf{r}' = 0, \quad (\text{A10})$$

where $\mathbf{R} \in \partial\mathcal{R}$. This follows directly in the Dirichlet boundary conditions case from $G(\mathbf{R}, \mathbf{r}') = 0$ and in the Neumann boundary conditions case from the particular choice (A8). Finally, we emphasize that the symmetry property $G(\mathbf{r}, \mathbf{r}') = G(\mathbf{r}', \mathbf{r})$ is not necessarily fulfilled by a generic Green's function,¹² but may be imposed as a separate requirement, and holds for the functions considered here.

ACKNOWLEDGMENTS

The visit of G.T. at LPT Orsay was supported by ECOS Nord/COLCIENCIAS-ICETEX-ICFES action C00P02 of French and Colombian cooperation. G.T. acknowledge partial financial support from COLCIENCIAS and BID through Project No. 1204-05-10078.

- ¹R. A. Marcus, J. Chem. Phys. **23**, 1057 (1955).
- ²M. J. Stevens, M. L. Falk, and M. O. Robbins, J. Chem. Phys. **104**, 5209 (1996).
- ³E. Trizac, Phys. Rev. E **62**, R1465 (2000).
- ⁴M. Eigen and E. Wicke, J. Phys. Chem. **58**, 702 (1954); V. Kralj-Iglič and A. Iglič, J. Phys. II **6**, 477 (1996); I. Borukhov, D. Andelman, and H. Orland, Phys. Rev. Lett. **79**, 435 (1997).
- ⁵L. Lue, N. Zoeller, and D. Blankschtein, Langmuir **15**, 3726 (1999).
- ⁶M. C. Barbosa, M. Deserno, and C. Holm, Europhys. Lett. **52**, 80 (2000).
- ⁷M. C. Barbosa, J. Phys.: Condens. Matter **14**, 2461 (2002).
- ⁸R. M. Fuoss, A. Katchalsky, and S. Lifson, Proc. Natl. Acad. Sci. U.S.A. **37**, 579 (1951). See also T. Alfrey, P. Berg, and H. J. Morawetz, J. Polym. Sci. **7**, 543 (1951).
- ⁹E. Trizac and J.-P. Hansen, Phys. Rev. E **56**, 3137 (1997).
- ¹⁰M. Deserno and H.-H. von Grünberg, Phys. Rev. E **66**, 011401 (2002).
- ¹¹J. D. Jackson, *Classical Electrodynamics* (Wiley, New York, 1962).
- ¹²K.-J. Kim and J. D. Jackson, Am. J. Phys. **61**, 1144 (1993).
- ¹³H. Wennerström, B. Jönsson, and P. Linse, J. Chem. Phys. **76**, 4665 (1982).
- ¹⁴See, e.g., D. Henderson in *Fundamentals of Inhomogeneous Fluids* edited by D. Henderson (Dekker, New York, 1992).
- ¹⁵J. C. Neu, Phys. Rev. Lett. **82**, 1072 (1999).
- ¹⁶J. E. Sader and D. Y. Chan, Langmuir **16**, 324 (2000).
- ¹⁷E. Trizac, Langmuir **17**, 4793 (2001).

Chapitre E

Macroions anisotropes et effet d'écran

Effective interactions and phase behaviour for a model clay suspension in an electrolyte

E Trizac¹, L Bocquet², R Agra¹, J-J Weis¹ and M Aubouy³

¹ Laboratoire de Physique Théorique, UMR CNRS 8627, Bâtiment 210, Université Paris-Sud, 91405 Orsay Cedex, France

² Laboratoire de Physique de l'Ens Lyon, UMR CNRS 5672, 46 Allée d'Italie, 69364 Lyon Cedex, France

³ SI3M, DRFMC, CEA-DSM Grenoble, 17 rue des Martyrs, 38054 Grenoble Cedex 9, France

Received 2 May 2002

Published 27 September 2002

Online at stacks.iop.org/JPhysCM/14/9339

Abstract

Since the early observation of nematic phases of disc-like clay colloids by Langmuir in 1938, the phase behaviour of such systems has resisted theoretical understanding. The main reason is that there is no satisfactory generalization for charged discs of the isotropic DLVO (Derjaguin, Landau, Verwey and Overbeek) potential describing the effective interactions between a pair of spherical colloids in an electrolyte. In this paper, we show how to construct such a pair potential, incorporating approximately both the non-linear effects of counter-ion condensation (charge renormalization) and the anisotropy of the charged platelets. We discuss the consequences for the phase behaviour of laponite dispersions (thin discs of 30 nm diameter and 1 nm thickness), and we present an investigation into the mesostructure via Monte Carlo simulations.

1. Introduction

With the possibility of forming an orientational ordering, the phase behaviour of anisotropic colloids is richer than its counterpart for spherical particles. Surprisingly, the isotropic–nematic transition expected on purely entropic grounds (excluded volume effects) has been extensively reported for rod-like colloids in the last 60 years [1]. However, it could only be observed recently for discotic particles in apolar media [2]. This experimental work directly points to the subtle effect of electrostatic interactions, given that in the widely studied model system of colloidal platelets, namely aqueous clay dispersions, the isotropic/nematic phase separation is hindered by a ubiquitous ‘fluid–solid’ transition.

In spite of an important experimental and theoretical effort in the last ten years, triggered by the emergence of laponite as a model system for disc-like colloidal suspensions⁴, the above

⁴ Laponite particles may be considered as approximately monodisperse charged discs with a radius of 150 Å and a thickness of 10 Å.

transition is far from being well understood [3–30]. In particular, the precise nature of the phases observed experimentally is debated [3, 13, 23], so that the relevance of the traditional terminology ‘sol–gel’ to describe the transition is somewhat controversial.

On the other hand, theoretical approaches to describe the phase behaviour of charged disc-like particles in an electrolyte are in their infancy [4, 8, 16, 21], essentially because there is no satisfactory generalization for discs of the isotropic DLVO (Derjaguin, Landau, Verwey and Overbeek) potential [31] describing the effective interactions between a pair of spherical colloids. In the simplest situation of two coaxial and parallel uniformly charged platelets, the effective Coulomb force has been computed within linear [10] and non-linear [20] Poisson–Boltzmann (PB) theory. A screened electrostatic pair potential has been worked out [32], allowing us to compute analytically the interaction energy for discs of arbitrary orientation; this approach holds at the level of linearized PB theory (weak electrostatic coupling), and is expressed as a perturbative expansion in the parameter κr_0 , r_0 being the disc radius and κ the inverse Debye length in the electrolyte. It consequently becomes less reliable when κr_0 becomes of the order of one or larger (the typical situation for laponite solutions), or when the charge on the platelets becomes too large (high electrostatic coupling, also typical of clay systems). The latter limitation may be circumvented by introducing the concept of charge renormalization [31, 33–35], while the former requires the re-summation of all the powers of κr_0 involved in the ‘multi-polar’ expansion propounded in [32]. In this paper, we discuss how to take both aspects into account and investigate the consequences on the phase behaviour. Our goal is to understand the effect of colloid anisotropy on a possible phase transition. We show that considering electrostatic effects only and discarding van der Waals interactions yields qualitative differences between spherical and discotic colloids. We also show that the equivalent of the fluid–solid transition for spheres is nevertheless reminiscent of the ‘sol–gel’ transition reported in [3].

The paper is organized as follows. In section 2, we obtain a pair potential for discs valid at large distances within linearized PB theory. We show that, at asymptotically large separations, this potential remains strongly anisotropic, unlike its counterpart in vacuum or in a plain dielectric medium (no salt). The approach is generalized in section 3 to an arbitrary ‘one-dimensional’ or ‘two-dimensional’ colloid (i.e. with vanishing internal volume). The non-linear phenomenon of counter-ion ‘condensation’ leading to a renormalization of the bare platelet charge is then considered in section 4, and the resulting effective charge successfully tested against ‘exact’ numerical simulations reported in the literature. In section 5, we propose a first and simplified investigation into the phase behaviour by mapping the interaction energy on to an isotropic Yukawa potential. Finally, the full anisotropic potential, including charge renormalization, is used to investigate the mesostructure of an assembly of interacting discs by means of Monte Carlo computer simulations (section 6). Conclusions are drawn in section 7.

2. Large distance screened electrostatic potential

We consider first a unique platelet \mathcal{P} of radius r_0 and surface charge σ in a 1:1 electrolyte of bulk density n (infinite dilution limit). The solvent is assumed to be a dielectric continuum of permittivity ε . Within linearized Poisson–Boltzmann (LPB) theory, the dimensionless electrostatic potential obeys the following Poisson equation

$$\nabla^2 \phi = \kappa^2 \phi, \quad (1)$$

where $\kappa^2 = 8\pi \ell_B n$ is the inverse Debye length squared and $\ell_B = e^2/(kT\varepsilon)$ denotes the Bjerrum length corresponding to the distance where the bare Coulomb potential felt by two

elementary point charges becomes equal to the thermal energy kT ($\ell_B \simeq 7 \text{ \AA}$ in water at room temperature). The potential is chosen to vanish at infinity and e denotes the elementary charge.

We are interested in the behaviour of ϕ at large distances, which is relevant to describe the interactions in dilute suspensions. The solution of equation (1) has been worked out in the form of an integral representation in [10, 36], or as a multi-polar-like expansion [32]. It is however more convenient to obtain an explicit expression, which is a good starting point to derive the pair interaction. This can be achieved by writing the solution as a convolution of the surface charge of the platelets with the screened Coulomb potential:

$$\phi(\mathbf{r}) = \ell_B \int_P \frac{\sigma \exp(-\kappa|\mathbf{r} - \mathbf{s}|)}{e |\mathbf{r} - \mathbf{s}|} d^2s. \quad (2)$$

It is important to realize that such a convolution procedure would give incorrect results for polyions of non-vanishing excluded volume (e.g. spheres or rods of non-zero radii, see the appendix). Introducing the unit vector $\hat{\mathbf{n}}$ normal to the disc surface, and the angle $\theta \in [0, \pi/2]$ between the corresponding direction and the position vector \mathbf{r} with the origin at the platelet centre, we obtain the leading contribution

$$\phi(\mathbf{r}) \stackrel{\kappa r \gg 1}{\sim} \ell_B Z_{bare} 2 \frac{I_1(\kappa r_0 \sin \theta) e^{-\kappa r}}{\kappa r_0 \sin \theta r} \quad \text{with } Z_{bare} e = \pi r_0^2 \sigma, \quad (3)$$

where I_1 denotes the modified Bessel function of the first kind, such that $I_1(x) \sim x/2$ for $|x| \ll 1$. A peculiarity of the screened Coulomb potential appears at this point: whereas the large r potential becomes isotropic and behaves as Z_{bare}/r in vacuum (a situation corresponding to the limit $\kappa \rightarrow 0$), the anisotropy is present at all distances in an electrolyte ($\kappa \neq 0$); the θ and r dependences factorize in equation (3). In practice, the anisotropy of the potential is generically significant when the size of the object under consideration is larger than the Debye length (i.e. $\kappa r_0 > 1$ here). For laponite discs of radius 150 \AA this crossover corresponds to an ionic strength $I^* = 10^{-4} \text{ M}$. As noted in [17], I^* corresponds experimentally to a threshold value delimiting qualitatively different phase behaviours. At fixed distance r , the potential (3) is minimum for $\theta = 0$ which corresponds to the configuration where the ‘average’ distance between the point where ϕ is computed and the platelet is maximal. On the other hand, the potential is maximum for $\theta = \pi/2$. From equation (3) the ratio between these extremal values is r -independent, and reads $2I_1(\kappa r_0)/(\kappa r_0)$ which can be as large as 10 for $\kappa r_0 = 5$ (important anisotropy).

This result may be used to compute the potential energy of interactions between two platelets A and B with arbitrary relative orientations, as shown in figure 1. This energy is obtained by integrating the screened potential created by disc A defined by equation (3) over the surface charge distribution of the second disc (B)

$$V_{AB}(r, \theta_A, \theta_B) = \int_B \frac{\sigma}{e} \phi_A(\mathbf{r} + \mathbf{s}) d^2s, \quad (4)$$

where V_{AB} is the dimensionless potential expressed in kT units. Again, such a procedure would not give the proper interactions in the case of polyions with internal volume. At large distances, we obtain

$$V_{AB}(r, \theta_A, \theta_B) \sim Z_{bare}^2 \ell_B^4 \frac{I_1(\kappa r_0 \sin \theta_A) I_1(\kappa r_0 \sin \theta_B) e^{-\kappa r}}{\kappa r_0 \sin \theta_A \kappa r_0 \sin \theta_B r}. \quad (5)$$

Clearly, the relative orientation of the platelets is not completely specified by the three parameters r , θ_A and θ_B , but the omitted Euler angles only appear in higher-order terms, such as $\exp(-\kappa r)/r^2$, $\exp(-\kappa r)/r^3 \dots$. In particular, the energy (5) appears insensitive to a precession of the discs around their centre-to-centre direction.

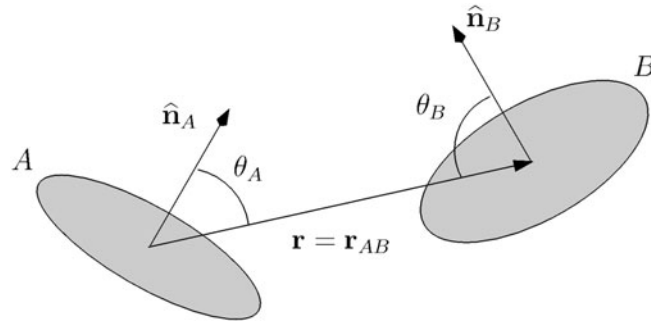


Figure 1. Definition of the coordinates used in the two-body problem.

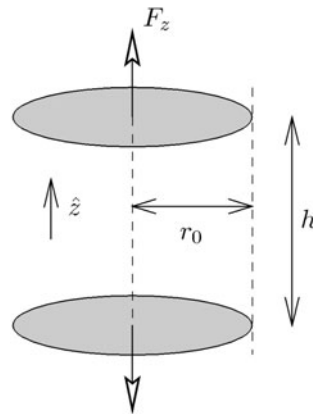


Figure 2. Geometry used to compute the force between two discs in section 4.

At fixed centre-to-centre distance, the above energy (always repulsive [37]) is maximized for co-planar discs ($\theta_A = \theta_B = \pi/2$, which corresponds to the maximum overlap of electric double layers) and minimized when the discs are co-axial and parallel ($\theta_A = \theta_B = 0$, see the configuration represented in figure 2). A situation of intermediate electrostatic energy is that of T-shape perpendicular discs ($\theta_A = 0$ and $\theta_B = \pi/2$). These results are consistent with the numerical LPB pair potential reported in [36], where it was also shown that the interactions between platelets at constant surface charge or constant potential were qualitatively very similar.

In [32], the potential energy V_{AB} was obtained in the form of a multi-polar expansion. Unlike its unscreened counterpart where the multipole of order l has a $1/r^{l+1}$ large distance contribution to the potential, this expansion is such that the multipole of order l contributes to orders $\exp(-\kappa r)/r$, $\exp(-\kappa r)/r^2 \dots \exp(-\kappa r)/r^{l+1}$. The large r potential can, in principle, be obtained by re-summation of all multi-polar contributions, which should lead to expression (5). Alternatively, truncating the multi-polar expansion at a given order amounts to expanding (5) in powers of κr_0 . Including monopole–monopole, monopole–quadrupole and quadrupole–quadrupole interactions, the following expression was obtained in [32]:

$$V_{AB}(r, \theta_A, \theta_B) = Z_{bare}^2 \ell_B \left[1 + \frac{\kappa^2 r_0^2}{8} (\sin^2 \theta_A + \sin^2 \theta_B) + \frac{\kappa^4 r_0^4}{64} (\sin^2 \theta_A \sin^2 \theta_B) \right] \frac{e^{-\kappa r}}{r}. \quad (6)$$

From equation (5), we obtain

$$V_{AB}(r, \theta_A, \theta_B) = Z_{bare}^2 \ell_B \left[1 + \frac{\kappa^2 r_0^2}{8} (\sin^2 \theta_A + \sin^2 \theta_B) + \frac{\kappa^4 r_0^4}{64} \left(\sin^2 \theta_A \sin^2 \theta_B + \frac{1}{3} \sin^4 \theta_A \sin^4 \theta_B \right) + \mathcal{O}(\kappa^6 r_0^6) \right] \frac{e^{-\kappa r}}{r}. \quad (7)$$

Both expressions agree at order $(\kappa r_0)^2$, and the difference at order $(\kappa r_0)^4$ is the monopole-hexadecapole contribution which has not been included in equation (6). This comparison illustrates the perturbative nature of the potential derived in [32], and the fact that the corresponding multi-polar contributions are implicitly re-summed in expression (5).

3. Generalization to a polyion of arbitrary shape

The method used in the previous section may be generalized to find the far-field electrostatic potential of an arbitrary polyion with vanishing internal volume and bare charge $Z = \int_{polyion} \sigma(\mathbf{s}) d^2 s$. In general, the convolution solution (2) admits the large distance behaviour:

$$\phi(\mathbf{r}) \sim Z \ell_B f(\hat{\mathbf{r}}, \kappa) \frac{e^{-\kappa r}}{r} + \mathcal{O}\left(\frac{e^{-\kappa r}}{r^2}\right) \quad \text{for } \kappa r \gg 1. \quad (8)$$

In this expression, the anisotropic part of the potential again factorizes from the r -dependence and is given by

$$f(\hat{\mathbf{r}}, \kappa) = \int_{polyion} \frac{\sigma(\mathbf{s})}{Ze} \exp(-\kappa \hat{\mathbf{r}} \cdot \mathbf{s}) d^2 s, \quad (9)$$

where $\hat{\mathbf{r}}$ denotes a unit vector in the direction of the position \mathbf{r} where the potential is computed, and $\sigma(\mathbf{s})$ is the surface charge density at point \mathbf{s} on the colloid. As expected, the isotropic bare Coulomb potential is recovered in the limit of low electrolyte density

$$\lim_{\kappa \rightarrow 0} f(\hat{\mathbf{r}}, \kappa) = 1, \quad (10)$$

where Z is the bare charge.

For a circle of radius r_0 and uniform line charge, we find

$$f(\theta, \kappa r_0) = I_0(\kappa r_0 \sin \theta), \quad (11)$$

where θ is the angle between \mathbf{r} and the normal to the plane containing the circle. Finally, for a uniformly charged rod of vanishing radius and length $2l$

$$f(\theta, \kappa l) = \frac{\sinh(\kappa l \cos \theta)}{\kappa l \cos \theta}, \quad (12)$$

where θ is now the angle between \mathbf{r} and the rod direction.

4. Towards charge renormalization for platelets

The bare charge of laponite platelets can be considered to be of the order of $Z_{bare} = 700$ – 1000 negative elementary charges [22, 23]. At the level of the PB approximation, this corresponds to a high electrostatic coupling (ϕ larger than unity [12, 20]), where the linearization procedure underlying equation (1) fails. However, a few Debye lengths away from the colloid, the potential has sufficiently decreased so that equation (1) is recovered and the one-body potential takes the form

$$\phi(r, \theta) = Z_{eff} f(\theta, \kappa r_0) \frac{e^{-\kappa r}}{r}.$$

The effective charge Z_{eff} is (in absolute value) smaller than the bare one [33–35]. Within PB theory, it saturates to a value independent of Z_{bare} if the latter quantity is large enough. The contribution embodied in $f(\theta, \kappa r_0)$ results from the anisotropy of the colloid, and is *a priori* an unknown function. In the limit of small electrostatic coupling (small Z_{bare}) where $Z_{eff}/Z_{bare} \rightarrow 1$ by definition, the results of section 2 show that $f(\theta, X) = 2I_1(X \sin \theta)/(X \sin \theta)$. On the other hand, at higher Z_{bare} corresponding to the saturation regime, the functional form of $f(\theta, X)$ is the signature of the effective charge distribution on the platelet and is related to possible differences in counter-ion condensation around the centre of the discs or in the vicinity of the edges.

It has been shown within PB theory that, in the colloidal limit $\kappa r_0 > 1$, highly charged colloids behave, as far as their far field is concerned, as constant potential particles whose value is close to $4kT/e$ (i.e. $\phi = 4$), irrespective of shape (planar, cylindrical, spherical) [38]. This prescription may be applied to the present case, with the restriction that, to our knowledge, the LPB problem cannot be solved analytically with the boundary condition of constant surface potential. However, the potential associated with the constant surface charge boundary condition provides a reasonable first approximation providing the correct qualitative variation of the effective charge with physico-chemical parameters. The corresponding anisotropic contribution to the large distance field is that computed in section 2 and the calculation of Z_{eff} follows from the knowledge of $\phi(r = 0)$. From the analytical expression reported in [10], we obtain the saturation value of Z_{eff}

$$Z_{eff}^{saturation} = Z_{sat} = \frac{r_0}{\ell_B} \frac{2\kappa r_0}{1 - \exp(-\kappa r_0)}. \quad (13)$$

It is worth noting that for a typical salt concentration corresponding to $\kappa r_0 = 1$, $Z_{sat} \simeq 100$, which is an order of magnitude smaller than the bare charge. This asymmetry guarantees that the effective charge is in the saturation regime where it no longer depends on the value of Z_{bare} [33, 38] (the precise experimental determination of Z_{bare} is therefore not required). This saturation picture is expected to be reliable in a 1:1 electrolyte (the PB mean-field approximation generally fails in electrolytes of higher valence), when there is a clear scale separation between the Bjerrum length and the size of the charged object (this constraint being fulfilled for laponite) [39].

The above prediction may be checked by inserting Z_{sat} into the analytical expression giving the LPB force between two parallel platelets [10] (configuration depicted in figure 2)

$$\frac{r_0 F_z}{kT} = \frac{4\pi \ell_B}{r_0} Z_{sat}^2 \int_0^\infty J_1^2(x) \frac{1}{x} \exp\left\{-\frac{h}{r_0} \sqrt{x^2 + \kappa^2 r_0^2}\right\} dx \quad (14)$$

and by comparing the results with the Monte Carlo simulations of Meyer *et al* [22], who considered the situation of vanishing salt. In this limit, where the quality of our prescription for Z_{eff} is expected to deteriorate, we obtain from equation (13) $Z_{sat} \rightarrow 2r_0/\ell_B \simeq 42$. The comparison is displayed in figure 3 which shows good agreement. Neglect of charge renormalization effects leads to an overestimation of the force by more than two orders of magnitude (more precisely, by a factor of $(Z_{bare}/Z_{sat})^2$ —see the difference between the dashed and dotted curves in figure 3), which points to the prime importance of such a phenomenon.

5. Tentative investigation into the phase behaviour

At this point, it is interesting to investigate at least qualitatively the difference in the phase behaviour between spherical and disc-like charge stabilized colloids. For spheres, the fluid–solid transition driven by repulsive electrostatic interactions favours the isotropic fluid upon

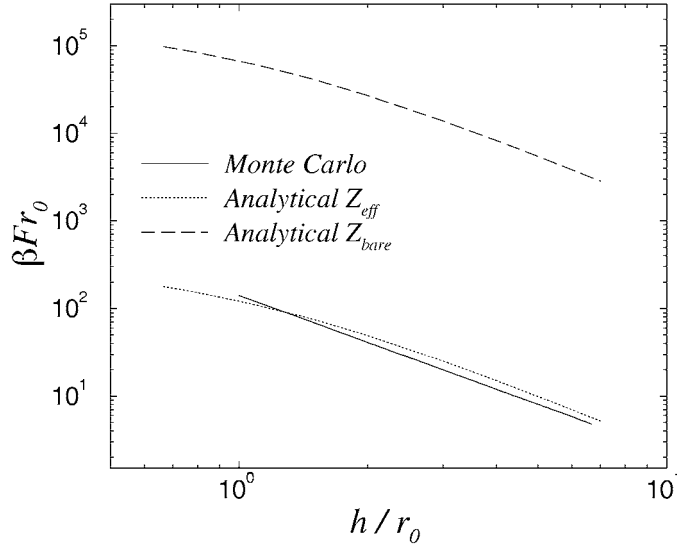


Figure 3. Comparison of the effective force between two parallel and coaxial platelets obtained by (N, V, T) Monte Carlo simulations in [22], with the general expression for the LPB force supplemented with the effective charge given by equation (13). h is the distance between the two plates (see figure 2). The same results are shown neglecting charge renormalization, which amounts to considering $Z_{eff} = Z_{bare}$ (upper dashed curve).

addition of salt in the solution [40]. The opposite is observed for laponite dispersions, where an increase of the ionic strength lowers the density where the ‘solid’ phase appears [3, 11]. Given that van der Waals interactions are believed to be irrelevant in the corresponding parameter range [11], this effect (illustrated in figure 4) appears at first to contradict standard DLVO phenomenology, where a screening of electrostatic repulsion (decrease of Debye length κ^{-1}) is expected to promote the simple fluid phase (sol), as occurs for spheres. However, the effective charge of an arbitrary charged object is generically a growing function of salt concentration (see, for instance, expression (13), which increases with κ), as a result of an enhanced screening of colloid/micro-ion attraction which diminishes the amount of counter-ion ‘condensation’. This increase of the effective charge favours the solid phase and is thus antagonistic to the above-mentioned decrease of the range of electrostatic repulsion driven by the decrease of κ^{-1} . The competition between the increase of the amplitude of repulsion and the decrease of its range upon adding salt is a possible scenario to interpret the phase behaviour of discs, within the DLVO picture and without any attractive interactions. More quantitative results are given below.

In the following analysis, we treat spheres and discs on an equal footing (both are considered to have the same radius r_0). From the above analysis, we consider the following pair potential for discs

$$V_{AB}(r, \theta_A, \theta_B) = Z_{sat}^2 \ell_B^4 \frac{I_1(\kappa r_0 \sin \theta_A)}{\kappa r_0 \sin \theta_A} \frac{I_1(\kappa r_0 \sin \theta_B)}{\kappa r_0 \sin \theta_B} \frac{e^{-\kappa r}}{r}, \quad (15)$$

where Z_{sat} is given by equation (13). Its counterpart for charged spheres is the standard isotropic DLVO expression [31, 35]

$$V_{AB}(r) = Z_{sat}^2 \ell_B \left(\frac{e^{\kappa r_0}}{1 + \kappa r_0} \right)^2 \frac{e^{-\kappa r}}{r}, \quad (16)$$

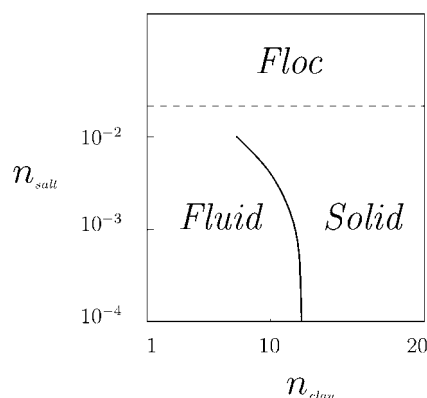


Figure 4. Schematic phase diagram of laponite suspensions, reproduced from [3], where the fluid–solid transition was referred to as a sol–gel transition. The salt concentration on the y-axis is expressed in mol (dm)^{−3}, and the scale for laponite concentrations on the x-axis is in g l^{−1}. The solid under consideration is isotropic but, at higher clay densities, a nematic solid may be formed [6]. The corresponding diagram for spherical colloids would exhibit a fluid/solid line of opposite (positive) slope [40].

where the saturation value of the effective charge has been derived analytically in [38] as a function of salt concentration (we again consider colloids with a high bare charge such that Z_{eff} coincides with its saturation value).

Given that the phase behaviour of particles interacting through Yukawa-like potentials has been extensively explored by computer simulations [41–43], we can readily obtain the melting density corresponding to a given salt concentration for the potential (16). The results (corresponding to spherical colloids) are shown in figure 5. A related procedure may be used to estimate qualitatively the position of the melting or freezing line for discs by assuming that, at low clay density (typically where the fluid/solid transition takes place for laponite suspensions), the rotational motion of the platelets occurs on a shorter timescale than the translational motion. Thus, these objects feel an effective potential resulting from the angular average of the expression given in equation (15), namely

$$\begin{aligned} V_{AB}^{average}(r) &= \langle V_{AB}(r, \theta_A, \theta_B) \rangle_{\theta_A, \theta_B} = \frac{1}{4} \int_0^\pi \sin \theta_A d\theta_A \int_0^\pi \sin \theta_B d\theta_B V_{AB}(r, \theta_A, \theta_B) \\ &= Z_{sat}^2 \ell_B^4 \left(\frac{\cosh(\kappa r_0) - 1}{\kappa^2 r_0^2} \right)^2 \frac{e^{-\kappa r}}{r}. \end{aligned} \quad (17)$$

In doing so, we obtain an isotropic Yukawa potential where the energy scale—the term in parentheses in equation (17)—reflects the original anisotropy of the pair potential. In the standard DLVO potential (16) for spheres, the energy scale (the term $\exp(\kappa r_0)/(1 + \kappa r_0)$) also depends on Debye length, but has a different physical origin and results from the exclusion of micro-ions from the interior of the spheres. Making use of the numerical Yukawa phase diagram [41–43], we obtain the melting line represented in figure 5 for the averaged potential (17), where the threshold density decreases when the salt concentration (or equivalently κ) increases, at least for $\kappa d < 4$. At the same level of description, spherical colloids show the opposite behaviour, for all values of κd . (We also emphasize that, for the spherical colloids used in the experiments of Monovoukas and Gast [40], the equivalent of the melting line reported in figure 5 is in excellent agreement with its experimental counterpart [38].)

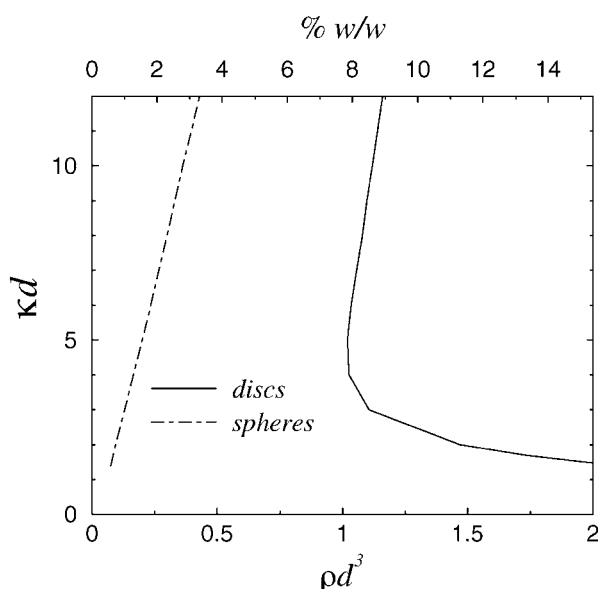


Figure 5. Tentative phase diagram of highly charged colloids in a 1:1 electrolyte, as obtained for particles interacting through a Yukawa potential in [41–43]. The equivalent of the fluid–solid transition for spheres (i.e. the underlying Yukawa potential is given by equation (16) for spheres and by equation (17) for discs). Discs and spheres have the same radius $r_0 = 150 \text{ \AA}$ (reasonable for laponite clays), and $d = 2r_0$ denotes the diameter. The bottom x -label corresponds to the dimensionless number density, while the upper x -scale converts this quantity in terms of the ratio of clay mass over solvent mass for laponite platelets (this scale is consequently irrelevant for spherical colloids). In both cases, the line shown is the melting curve delimiting a solid at high density and a fluid for more dilute suspensions.

For both spheres and discs, the pre-factor of the Yukawa term $\exp(-\kappa r)/r$ is an increasing function of κ (see equations (16) and (17)). The subtle interplay between this increase and the decrease of Debye length is nevertheless able to produce a ‘re-entrant’ melting line for discs only. In the limit of low κr_0 , both expressions (16) and (17) become $\ell_B Z_{sat}^2 \exp(-\kappa r)/r$; the melting lines for spheres and discs however do not merge in this limit in figure 5, due to the difference in the limiting values of Z_{sat} for both geometries.

This approach, which consists of averaging the two-body platelet potential over angular degrees of freedom, predicts a qualitative change in the phase behaviour of platelet systems for a reduced density $\rho^* = \rho d^3$ of the order of one, which corresponds to a clay mass fraction of 8% for laponite with diameter $d = 300 \text{ \AA}$; see the upper x -label of figure 5. This density is approximately four times higher than the maximum density delimiting the fluid and solid regions in the phase diagram of laponite suspensions (see figure 4 and [3, 11]). So the present approach does not allow a quantitative comparison with experiments. It is however worth noting that a density $\rho^* \simeq 1$ is much smaller than the isotropic/nematic coexistence density for uncharged plates ($\rho^* \simeq 4$, [44, 45]). At this stage, it is impossible to be more specific concerning the nature of the ‘solid’ phase supplementing the fluid phase at high densities. This question is addressed in the following section using computer simulations.

6. Mesostructure: Monte Carlo simulations

We have implemented standard Monte Carlo simulations with typically $N = 500$ platelets interacting through the potential (15) where Z_{sat} is given by equation (13). This allows us to

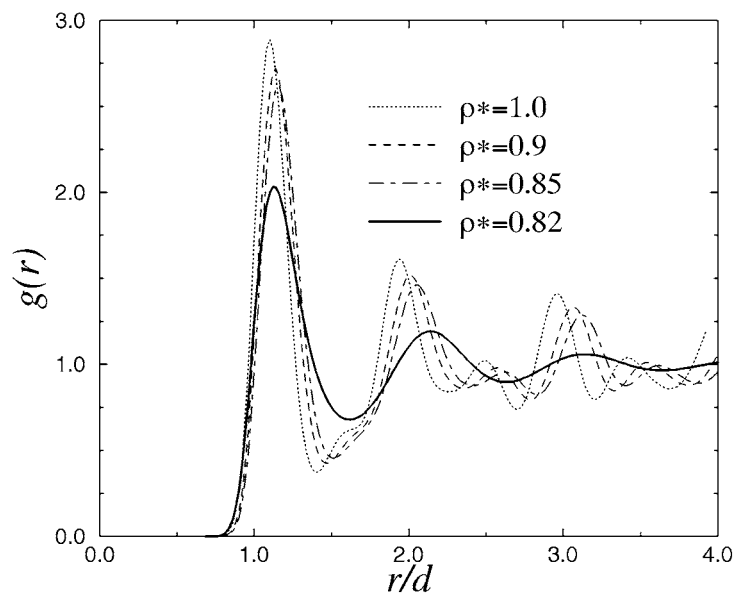


Figure 6. Centre-to-centre pair correlation function as a function of distance for $\kappa d = 1$.

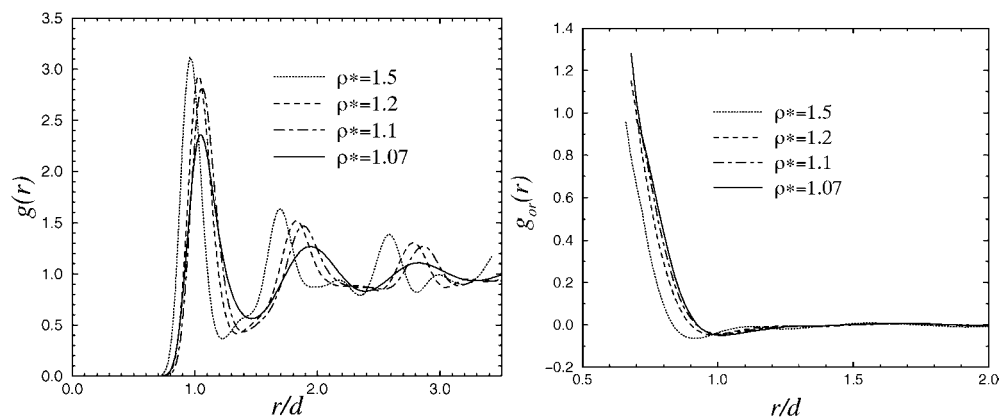


Figure 7. Same as figure 6 for a higher salt concentration ($\kappa d = 3$). The structureless orientational distribution is shown for completeness in the graph on the right.

test the validity of the approach proposed in section 5, where the initial anisotropic potential was mapped on to the isotropic Yukawa function (17). A typical run consisted of 10^5 cycles (both random displacement and rotation of the N particles).

For different values of salt concentration and platelet density, two diagnostics were used to characterize the simulated samples. Firstly, the centre-to-centre pair distribution function $g(r)$ was computed. Secondly, the orientational ordering was quantified through the statistical average of (twice) the second Legendre polynomial $P(\psi) = 3 \cos^2 \psi - 1$ at a given centre-to-centre distance r , where ψ is the angle formed by the normals to the two discs. The orientational pair correlation function denoted $g_{or}(r)$ follows from averaging over all pairs of platelets.

The corresponding information on the mesostructure is displayed in figures 6 and 7 for different densities and two values of κ . A striking observation is that a slight increase of the

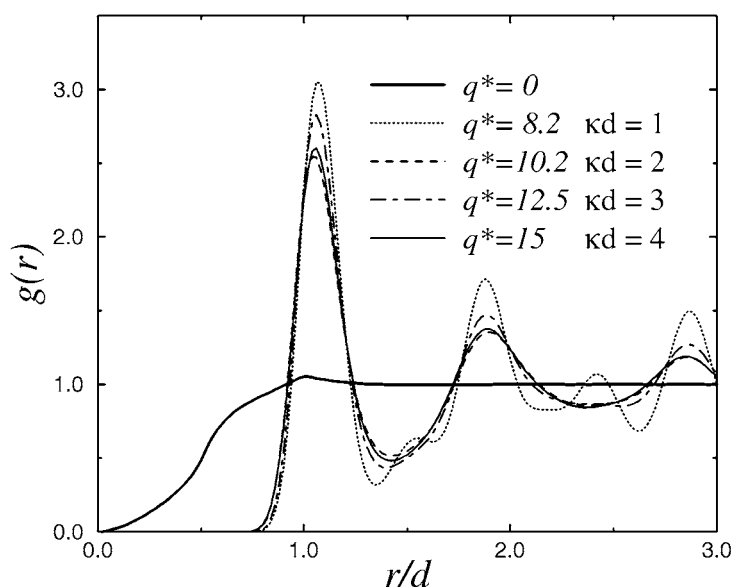


Figure 8. Pair distribution function for $\rho^* = 1.1$. The reduced charges defined as $q^* = Z_{sat} \sqrt{\ell_B/d}$ have been computed from equation (13) and are given for completeness for every κ . Also shown is $g(r)$ for an uncharged platelet system at the same density (only excluded volume effects).

density induces an important increase of the structure (see the differences between the curves at $\rho^* = 0.82$ and 0.85 in figure 6; the same is seen at $\kappa d = 3$ in figure 7 when the reduced density changes from 1.07 to 1.10). Such values of ρ^* lie close to the threshold $\rho^* = 1$ estimated in section 5. The associated orientational distributions (not shown) are structureless for the densities considered here. These results indicate a qualitative change in the structure of the fluid phase upon increasing the density, but it is still difficult to characterize the new ‘phase’ emerging without a thermodynamical study.

We have tested the relevance of the scenario propounded at the beginning of section 5 (competition between an increase of the amplitude and a decrease of the range of the pair potential when κ —or equivalently n_{salt} —increases). For a given density ($\rho^* = 1.1$), the pair correlation functions are monitored for various values of κ . The corresponding charges change with κ , according to equation (13). Figure 8 shows an interesting feature. As expected, the structure is most pronounced for the lowest κ , and decreases when κ increases (see the difference between the curves for $\kappa d = 1$ and 2). However, when salt concentration is further raised to $\kappa d = 3$, the maximum of $g(r)$ and the whole structure are enhanced, before decreasing again when $\kappa d = 4$. The effect evidenced in figure 8 is reminiscent of the ‘anomalous’ slope of the phase diagram reproduced in figure 4, and is in qualitative agreement with the simplified phase diagram drawn in figure 5.

Finally, we have performed exploratory runs at higher densities where a nematic phase would be observed in the uncharged system. The results of figure 9 for a high density $\rho^* = 5.0$ show a rich local structure both for the $g(r)$ and the orientational $g_{or}(r)$, very different from that observed at lower densities. The reference uncharged system ($q^* = 0$) with its strong nematic plateau is displayed for comparison. The inclusion of electrostatic interactions preserves the long-range nematic order, but decreases its strength (the height of the plateau). Such a nematic order was clearly absent at lower densities (see figure 7). The peaks of $g(r)$ appear correlated to those of $g_{or}(r)$, which points to the existence of oriented micro-domains with parallel platelets, and a higher nematic order than the mean one. The complex behaviour of

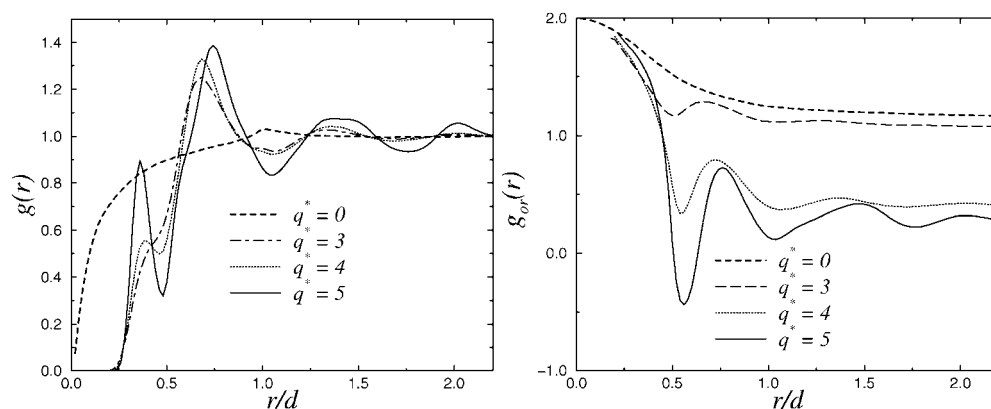


Figure 9. Effect of charge on the distributions $g(r)$ and $g_{or}(r)$, for $\rho^* = 5.0$ and a fixed screening length $\kappa d = 8$.

the distribution functions of figure 9 calls for more thorough investigations at high densities. In particular, the validity of the large distance expansion (15) may be questionable at high ρ^* .

7. Conclusion

In this paper, we have devised an electrostatic pair potential for both highly anisotropic and highly charged objects (of vanishing internal volume) based on LPB theory. For the example of infinitely thin platelets, we show that the anisotropic shape of the object results in an anisotropic Yukawa potential even at large distances. The anisotropy is an increasing function of κr_0 and becomes very marked in the colloidal limit $\kappa r_0 > 1$. To account for the non-linearities in the PB theory, when the bare charge of the platelets is large, we introduce an effective or renormalized charge. This approximation yields an effective pair potential for highly charged platelets.

The addition of salt generically results in two antagonistic effects, irrespective of colloid geometry: the range of the effective potential decreases, but its amplitude increases. This interplay appears to be quite subtle, and is able to discriminate between spherical and disc-like colloids by producing a re-entrant melting line for discs. This phenomenon appears at first incompatible with the naive DLVO expectation. Moreover, the corresponding threshold density for discs is smaller than the isotropic/nematic coexistence for uncharged plates, but still higher than its experimental ‘fluid/solid’ counterpart.

Preliminary results of Monte Carlo simulations for particles interacting through an anisotropic potential provide information on the mesoscopic structure of the dense phase. In particular, we show that the resulting structure is very sensitive upon increasing the density. We have also observed a ‘re-entrant’ melting curve. These effects are in qualitative agreement with the experimental phase diagram of laponite suspensions found in the literature, even if this topic is still under debate.

Our approach suffers from several weaknesses:

- the non-linearities in the PB theory are accounted for at the level of charge renormalization;
- in this framework, we expect the effective charge to be better approximated with an ansatz where the particle effectively behaves as a constant electrostatic potential object [38], whereas we considered the platelets to be of constant surface charge;
- we work at the level of pair potential, and correlation effects beyond the mean-field PB approach might play a role;

(d) the precise role of van der Waals forces has not been assessed, and remains obscure for clay platelets.

Further theoretical and numerical work is needed, but we hope that the arguments presented here provide a first hint at the full problem. At least, our results strongly suggest that the combined effect of anisotropy and charge condensation have a significant and non-trivial qualitative influence on the phase diagram of highly charged colloids. These features could well be of prime importance in our understanding of the thermodynamics of clay suspensions.

Acknowledgments

We thank J-P Hansen, H Lekkerkerker, P Levitz, A Delville, D Bonn, T Nicolai, B Jancovici and F van Wijland for fruitful discussions.

Appendix

In this appendix, we show that the solution of equation (1) is not given by convolution product (2) for polyions having a non-zero internal volume. For simplicity, we consider a charged hard sphere of radius r_0 (which consequently excludes micro-ions from its interior), with a uniform surface charge σ . The solution of equation (1) takes the well-known DLVO form

$$\phi(r) = Z\ell_B \frac{e^{\kappa r_0}}{1 + \kappa r_0} \frac{e^{-\kappa r}}{r}, \quad (\text{A.1})$$

where $Ze = 4\pi r_0^2 \sigma$ denotes the total bare charge. Alternatively, the convolution route of equation (2) yields

$$\phi_{\text{convol}}(r) = \ell_B \int_{\mathcal{P}} \frac{\sigma \exp(-\kappa|\mathbf{r} - \mathbf{s}|)}{e^{|\mathbf{r} - \mathbf{s}|}} d^2 \mathbf{s} \quad (\text{A.2})$$

$$= Z\ell_B \frac{\sinh(\kappa r_0)}{\kappa r_0} \frac{e^{-\kappa r}}{r} \quad \text{for } r \geq r_0. \quad (\text{A.3})$$

The origin of this discrepancy comes from the fact that upon summing up the elementary surface contributions in equation (A.2), the micro-ions are allowed to enter the 'interior' region $r \leq r_0$. The field created is thus that of the shell with charge Z (the colloid) plus that of the 'plasma' inside. The corresponding interior charge Z_{in} is easily computed from the expression of the electrostatic potential for $r \leq r_0$, which follows from a simple permutation of r and r_0 in expression (A.3)

$$\phi_{\text{convol}}^{\text{inside}}(r) = Z\ell_B \frac{\sinh(\kappa r)}{\kappa r} \frac{e^{-\kappa r_0}}{r_0}. \quad (\text{A.4})$$

We obtain

$$Z_{in} = -\frac{\kappa^2}{4\pi\ell_B} \int_0^{r_0} \phi_{\text{convol}}^{\text{inside}}(r) d^3 \mathbf{r} \quad (\text{A.5})$$

$$= -Ze^{-\kappa r_0} \left[\cosh(\kappa r_0) - \frac{\sinh(\kappa r_0)}{\kappa r_0} \right]. \quad (\text{A.6})$$

Gathering results, a straightforward calculation allows us to rewrite equation (A.3) in the form

$$\phi_{\text{convol}}(r) = Z\ell_B \frac{\sinh(\kappa r_0)}{\kappa r_0} \frac{e^{-\kappa r}}{r} = (Z + Z_{in})\ell_B \frac{e^{\kappa r_0}}{1 + \kappa r_0} \frac{e^{-\kappa r}}{r}, \quad (\text{A.7})$$

so that the DLVO structure of expression (A.1) is recovered.

The argument given here bears some similarities with the proof of the equivalence between two charged hard spheres models with a uniform background [46] (note that the equivalent of the background, the micro-ion density, is not uniform in the present situation). Finally, a related remark is that application of expression (4) for spheres does not give the DLVO pair potential (16) even if the correct one body potential (A.1) is used (use of expression (A.2) is equally incorrect). A simple way to recover (16) is through the stress tensor [31].

References

- [1] Bernal J D and Fankuchen I 1941 *J. Gen. Physiol.* **25** 111
- [2] Van der Kooij F M and Lekkerkerker H N W 1998 *J. Phys. Chem. B* **102** 7829
- [3] Mourchid A, Delville A, Lambard J, Lécolier E and Levitz P 1995 *Langmuir* **11** 1942
- [4] Dijkstra M, Hansen J-P and Madden P 1995 *Phys. Rev. Lett.* **75** 2236
- [5] Trizac E and Hansen J-P 1996 *J. Phys.: Condens. Matter* **8** 9191
- [6] Gabriel J-C, Sanchez C and Davidson P 1996 *J. Phys. Chem.* **100** 11 139
- [7] Pignon F, Piau J M and Magnin A 1996 *Phys. Rev. Lett.* **56** 3281
- [8] Dijkstra M, Hansen J-P and Madden P 1997 *Phys. Rev. E* **55** 3044
- [9] Hansen J P and Trizac E 1997 *Physica A* **235** 257
- [10] Trizac E and Hansen J-P 1997 *Phys. Rev. E* **56** 3137
- [11] Mourchid A, Lécolier E, van Damme H and Levitz P 1998 *Langmuir* **14** 4718
- [12] Leote de Carvalho R J F, Trizac E and Hansen J-P 1998 *Europhys. Lett.* **43** 369
- [13] Bonn D, Kellay H, Tanaka H, Wegdam G and Meunier J 1999 *Langmuir* **15** 7534
- [14] Fossum J O 1999 *Physica A* **270** 270
- [15] Saunders J M, Goodwin J W, Richardson R M and Vincent B 1999 *J. Phys. Chem. B* **103** 9211
- [16] Kutter S, Hansen J-P, Sprik M and Boek E 2000 *J. Chem. Phys.* **112** 311
- [17] Levitz P, Lécolier E, Mourchid A, Delville A and Lyonnard S 2000 *Europhys. Lett.* **49** 672
- [18] Nicolai T and Coccoard S 2000 *Langmuir* **16** 8189
- [19] Knaebel A, Bellour M, Munch J-P, Viasnoff V, Lequeux F and Harden J L 2000 *Europhys. Lett.* **52** 73
- [20] Leote de Carvalho R J F, Trizac E and Hansen J-P 2000 *Phys. Rev. E* **61** 1634
- [21] Harnau L, Costa D and Hansen J-P 2001 *Europhys. Lett.* **53** 729
- [22] Meyer S, Levitz P and Delville A 2001 *J. Phys. Chem. B* **105** 10 684
- [23] Nicolai T and Coccoard S 2001 *Eur. Phys. J. E* **5** 221
- [24] Nicolai T and Coccoard S 2001 *J. Colloid Interface Sci.* **244** 51
- [25] Bellon L, Ciliberto S and Laroche C 2001 *Europhys. Lett.* **53** 511
- [26] Abou B, Bonn D and Meunier J 2001 *Phys. Rev. E* **64** 021510
- [27] Léger D and Levesque D 2002 *J. Chem. Phys.* **116** 2251
- [28] Cousin F, Cabuil V and Levitz P 2002 *Langmuir* **18** 1466
- [29] Michot L J, Ghanbaja J, Tirtaatmadja V and Scales P J 2001 *Langmuir* **17** 2100
- [30] Rowan D and Hansen J-P 2002 *Langmuir* **18** 2063
- [31] Belloni L 2000 *J. Phys.: Condens. Matter* **12** R549
- [32] Rowan D, Hansen J-P and Trizac E 2000 *Mol. Phys.* **98** 1369
- [33] Alexander S, Chaikin P M, Grant P, Morales G J and Pincus P 1984 *J. Chem. Phys.* **80** 5776
- [34] Belloni L 1998 *Colloids Surf. A: Physicochem. Eng. Aspects* **140** 227
- [35] Hansen J-P and Löwen H 2000 *Ann. Rev. Phys. Chem.* **51** 209
- [36] Hsu J-P and Tseng M T 1997 *Langmuir* **13** 1810
- [37] Trizac E 2000 *Phys. Rev. E* **62** R1465
- [38] Trizac E, Bocquet L and Aubouy M 2002 *Preprint cond-mat/0201510* submitted
- [39] Groot R D 1991 *J. Chem. Phys.* **95** 9191
- [40] Monovoukas Y and Gast A P 1989 *J. Colloid Interface Sci.* **128** 533
- [41] Robbins M O, Kremer K and Grest G S 1988 *J. Chem. Phys.* **88** 3286
- [42] Meijer E J and Frenkel D 1991 *J. Chem. Phys.* **94** 2269
- [43] Bitzer F, Palberg T, Löwen H, Simon R and Leiderer P 1994 *Phys. Rev. E* **50** 2821
- [44] Eppenga R and Frenkel D 1984 *Mol. Phys.* **52** 1303
- [45] Veerman J A C and Frenkel D 1992 *Phys. Rev. A* **45** 5632
- [46] Hansen J-P 1981 *J. Phys. C: Solid State Phys.* **14** L151